THE JOURNAL OF PHYSICAL CHEMISTRY C

Article

pubs.acs.org/JPCC

Investigating the Relative Influences of Molecular Dimensions and Binding Energies on Diffusivities of Guest Species Inside Nanoporous Crystalline Materials

Rajamani Krishna* and Jasper M. van Baten

Van't Hoff Institute for Molecular Sciences, University of Amsterdam, Science Park 904, 1098 XH Amsterdam, The Netherlands

Supporting Information

ABSTRACT: The primary objective of this article is to investigate the relative influences of molecular dimensions and adsorption binding energies on unary diffusivities of guest species inside nanoporous crystalline materials such as zeolites and metal−organic frameworks (MOFs). The investigations are based on molecular dynamics (MD) simulations of unary diffusivities, along with configurational-bias Monte Carlo (CBMC) simulations of the isosteric heats of adsorption ($-Q_{st}$) of a wide variety of guest molecules (CO_2, H_2, N_2, He, Ne, Ar, Kr, CH_4, C_2H_4, C_2H_6, C_3H_6, C_3H_8, and nC_4H_{10}) in 24 different host materials spanning a wide range of pore sizes, topologies, and connectivities. For cage-type materials with narrow windows, in the 3.2−4.2 Å size range, separating adjacent cages (e.g., LTA, CHA, DDR, and ZIF-8), the diffusivities are primarily dictated by the molecular dimensions, bond lengths, and bond angles. However, for channel structures (e.g., AFI, MFI, MgMOF-74, NiMOF-74, MIL-47, MIL-53, and BTP-COF) and "open" frameworks with large windows separating adjacent cavities (NaY, NaX, CuBTC, IRMOF-1, MOF-177, and MIL-101), the diffusivities of guest species in any given host material are strongly dependent on the binding energies of the guest species that can be quantified by $-Q_{st}$. The stronger the binding energy, the higher the "sticking tendency", and the lower the corresponding diffusivity. The insights gained from our study are used to rationalize published experimental data on diffusivities and trans-membrane permeances. The results of our study will be valuable in choosing the right material with the desired diffusion characteristics for a given separation application.

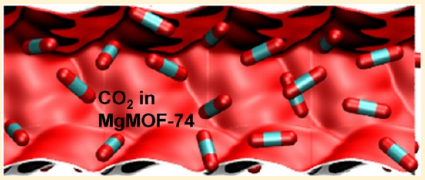

1. INTRODUCTION

Ordered crystalline nanoporous materials such as zeolites (crystalline aluminosilicates), metal−organic frameworks (MOFs), zeolitic imidazolate frameworks (ZIFs), covalent organic frameworks (COFs), UMCM-1, MCM-41, and SBA-15 offer considerable potential for separation of a variety of mixtures: CO_2/N_2, CO_2/CH_4, $CO_2/CO/CH_4/H_2$, CO_2/H_2, CH_4/H_2, O_2/N_2, natural gas, alkane/alkenes, alkyne/alkene, and hydrocarbon isomers.[1−13] The technologies used in such separations are either pressure swing adsorption (PSA) units or membrane permeation devices. The separation performance of such technologies is dictated by a combination of adsorption and diffusion characteristics that are dictated by a wide variety of factors that include pore size, pore topology, connectivity, and interactions (both van der Waals and electrostatic) of the guest species with the framework atoms. To illustrate these differences, Figure 1 provides a comparison of CO_2/CH_4 adsorption selectivities

$$S_{ads} = \frac{q_1/q_2}{f_1/f_2} \quad (1)$$

and CO_2/CH_4 diffusion selectivities

$$S_{diff} = \frac{D_1}{D_2} \quad (2)$$

for CO_2/CH_4 mixtures for selected materials culled from the published literature. There appear to be two fundamentally

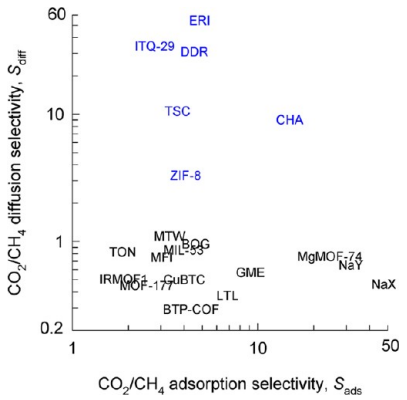

Figure 1. Comparison of diffusion selectivities, S_{diff} (obtained from MD simulations for binary mixtures), and adsorption selectivities, S_{ads} (obtained from CBMC simulations for binary mixtures), for $CO_2(1)/CH_4(2)$ mixtures. The conditions correspond to partial fugacities $f_1 = f_2 = 0.5$ MPa and 300 K. The data on S_{diff} and S_{ads} are collected from earlier published material.[8,14,51] For MgMOF-74, the S_{ads} data are from experimental isotherms.[48] The S_{diff} data for ZIF-8 are obtained for the infra-red microscopy measurements.[25,52] The symbols marked blue are cage-type structures with narrow windows, falling in the first category of materials.

Received: September 10, 2012
Revised: October 17, 2012
Published: October 19, 2012

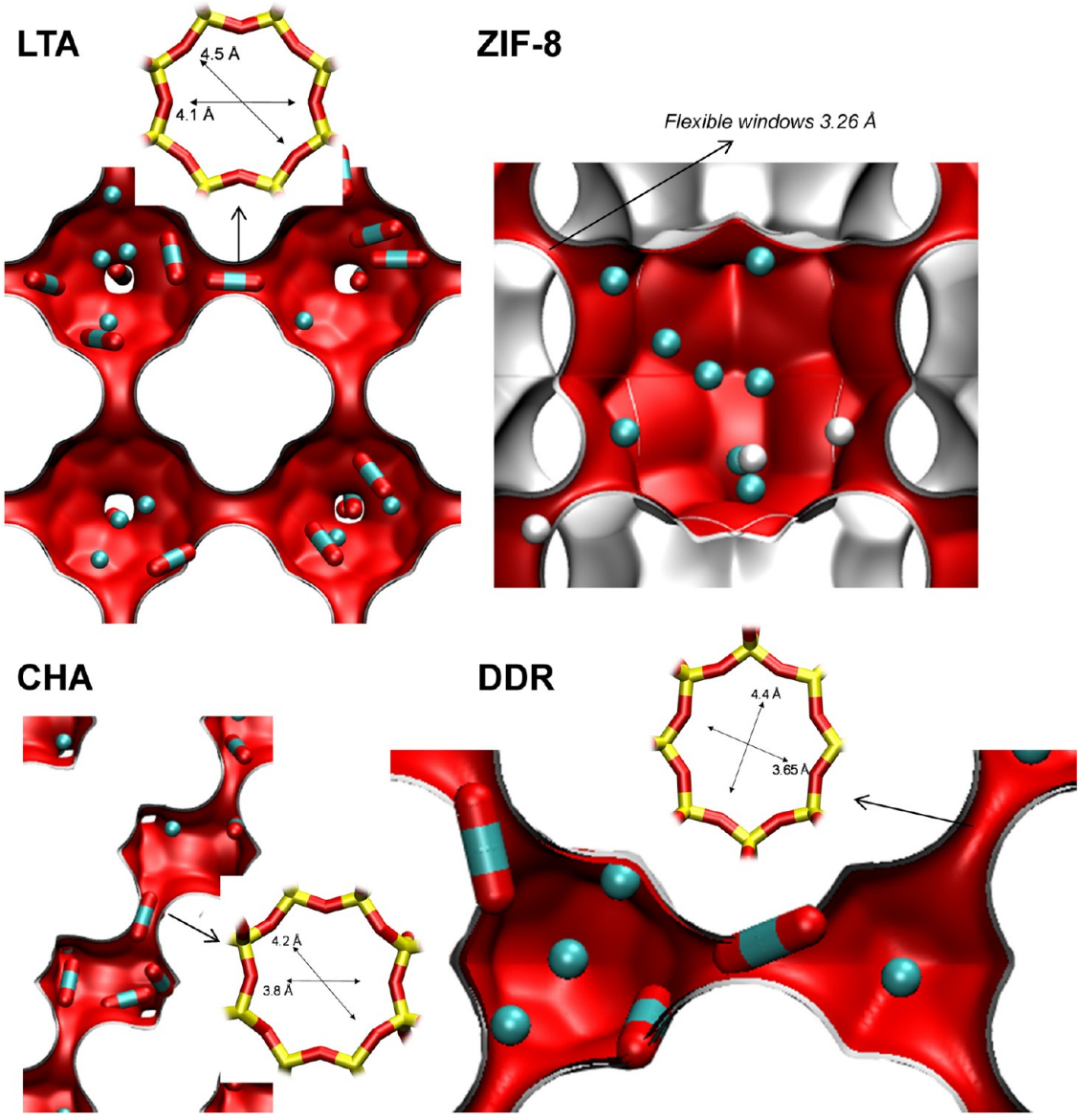

Figure 2. Structures consisting of cages separated by narrow windows: LTA, ZIF-8, CHA, and DDR.

different categories of behaviors. The adsorption and diffusion selectivities of CHA, DDR, ERI, ITQ-29, ZIF-8, and TSC serve to complement each other; we obtain $S_{ads} > 1$ and $S_{diff} > 1$, leading to enhanced permeation selectivities

$$S_{perm} = \frac{N_1/N_2}{f_1/f_2} \tag{3}$$

in membrane separation because of the relation: $S_{perm} = S_{diff} \times S_{ads}$.[14] These materials have cage-type topologies in which adjacent cages are separated by narrow windows in the 3.2−4.2 Å size range; see Figure 2 for pore landscapes of four commonly used cage-type materials.

In the second category of materials, we find $S_{ads} > 1$ but $S_{diff} \leq 1$; that is, the diffusion selectivity favors the more poorly adsorbing CH_4 that has the larger kinetic diameter (see Table 1); these materials fall into three subclasses

1. One-dimensional (1D) channels (e.g., TON, LTL, MTW, BTP-COF, MgMOF-74, and MIL-53)

Table 1. Molar Mass and Kinetic Diameter of a Variety of Guest Molecules

guest molecule	molar mass, M_i (g mol^{-1})	kinetic diameter (Å)
He	4.0	2.6
H_2	2.0	2.8
CH_4	16.0	3.8
Ne	20.2	2.75
N_2	28.0	3.64
C_2H_4	28.1	3.9
C_2H_6	30.1	3.85
O_2	32.0	3.46
Ar	39.9	3.4
C_3H_6	42.1	4.5
CO_2	44.0	3.3
C_3H_8	44.1	4.3
n-C4	58.1	4.3
i-C4	58.1	5
Kr	83.8	3.6

dx.doi.org/10.1021/jp308971w | J. Phys. Chem. C 2012, 116, 23556−23568

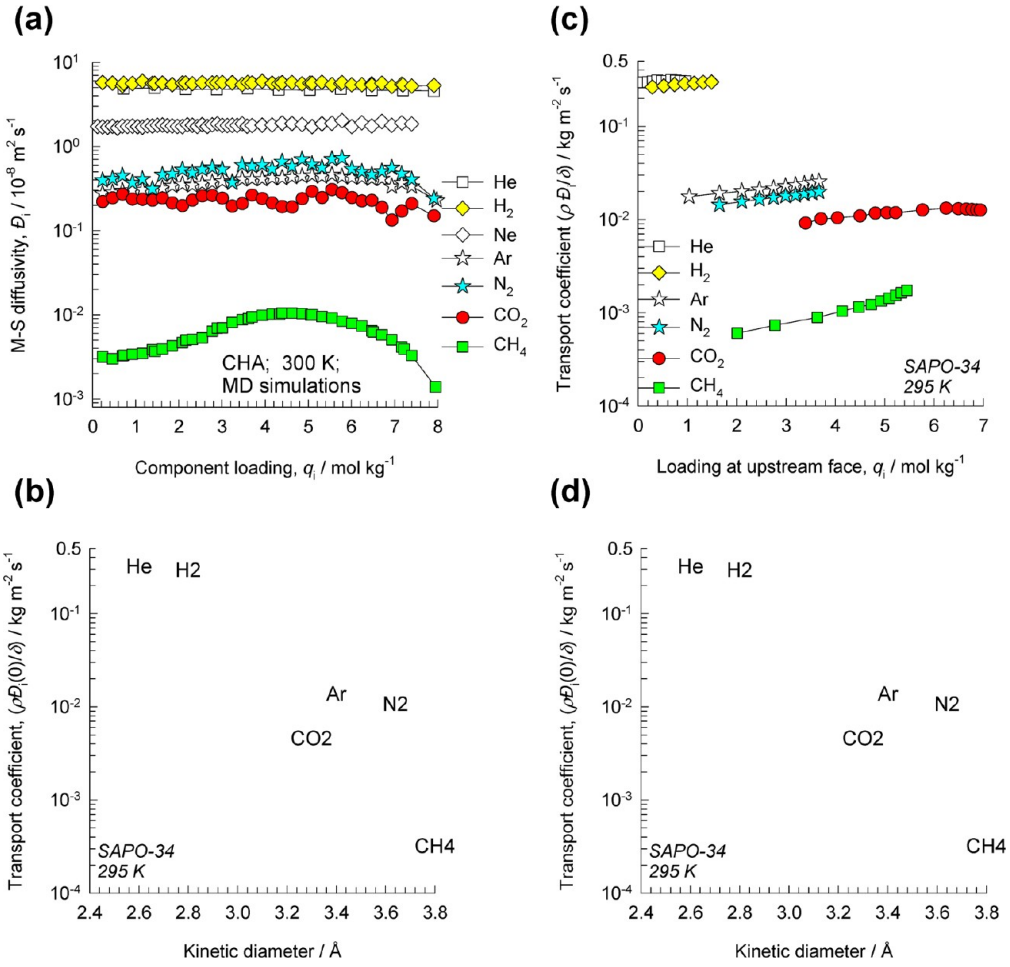

Figure 3. (a) MD simulations of the loading dependence of M−S diffusivities, $Đ_i$, for a variety of guest molecules in CHA at 300 K. (b) Plot of $Đ_i(0)$ versus kinetic diameter. (c) The transport coefficient, $\rho Đ_i/\delta$, as a function of molar loadings at the upstream face of a SAPO-34 membrane operating at 295 K. The experimental data are from Li et al.[19,20] (d) The transport coefficient, $\rho Đ_i/\delta$, for SAPO-34 membrane as a function of kinetic diameter.

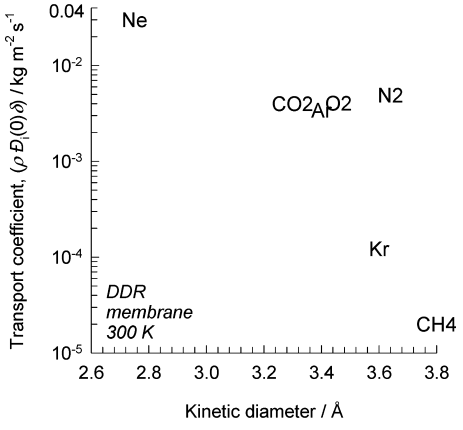

Figure 4. Transport coefficient, $\rho Đ_i/\delta$, for DDR membrane as a function of kinetic diameters of the guest species. The calculations are obtained from a reanalysis[21,53,54] of the experimental data on permeation fluxes in van den Bergh et al.[55,56]

2. Intersecting channels (e.g., MFI, BOG, and GME).
3. "Open" structures with large cavities (e.g., NaY, NaX, IRMOF-1, CuBTC, and MOF-177)

The fundamental rationalization of the data presented in Figure 1 is one of the aims of this article, whose major objective is to highlight the strong and direct influence of binding energies on the guest diffusivities in the second category of materials. The realization and quantification of the subtle interplay between adsorption and diffusion, along with the appropriate modeling, is of importance in selection of the proper material for use in PSA or membrane devices.

For obtaining the necessary fundamental insights, we need a consistent set of data on diffusivities, adsorption strengths and binding energies for a wide variety of guest molecules for each host material. There are three different diffusivities that can be determined from either experimental measurements or from molecular dynamics (MD) simulations. The Fick diffusivity, D_i, is defined by the Fick's law of diffusion[1,15,16]

$$N_i = -\rho D_i \frac{dq_i}{dz} \tag{4}$$

The D_i is related, by means of the thermodynamic correction factor Γ_i, to the Maxwell−Stefan (M-S) or "corrected" diffusivity $Đ_i$

$$D_i = Đ_i \Gamma_i;\ \Gamma_i \equiv \frac{c_i}{f_i}\frac{\partial f_i}{\partial c_i} \tag{5}$$

The factor Γ_i can be determined directly from molecular simulations or by analytic differentiation of the adsorption isotherm fits. Usually, but not always, $\Gamma_i \geq 1$ and $Đ_i \leq D_i$.[16] The M-S diffusivity $Đ_i$ is obtained from MD simulations by

dx.doi.org/10.1021/jp308971w | J. Phys. Chem. C 2012, 116, 23556−23568

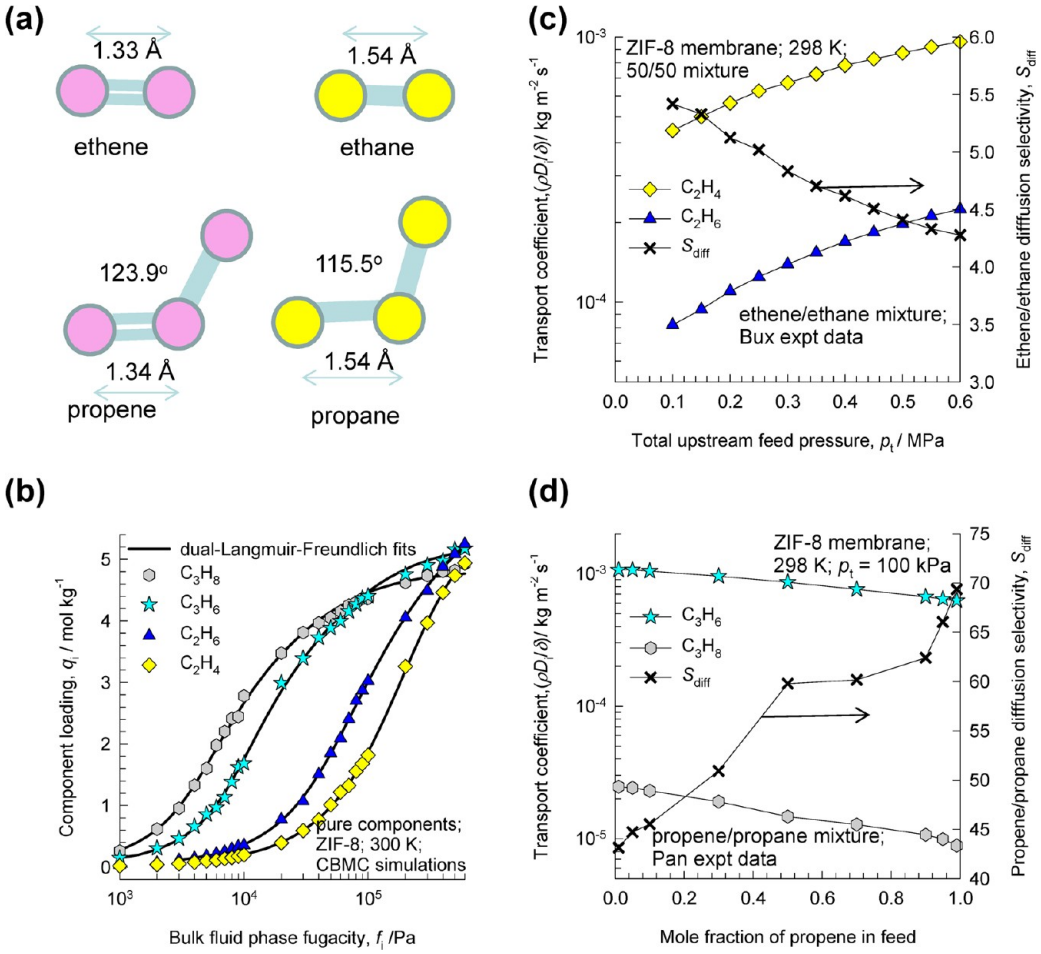

Figure 5. (a) Cartoon showing the bond lengths and bond angles of ethene, ethane, propene, and propane. (b) CBMC simulations of the pure component adsorption isotherms of alkanes and alkenes in ZIF-8 at 300 K. (c and d) The transport coefficients, $\rho Đ_i/\delta$, of ethene, ethane, propene, and propane for ZIF-8 membrane permeation, backed out from the experimental data. The backing-out of the transport coefficients $\rho Đ_i/\delta$ is based on the ideal adsorbed solution theory (IAST) calculations of mixture adsorption equilibrium using dual-Langmuir-Freundlich fits of the pure component isotherms, shown by the continuous solid lines in panel b. The ethene/ethane permeation data in panel c are from Bux et al.[23] The propene/propane mixture permeation data in panel d are from Pan et al.[24] Further details of isotherm fits, IAST calculations, and backing-out procedures are provided in the Supporting Information.

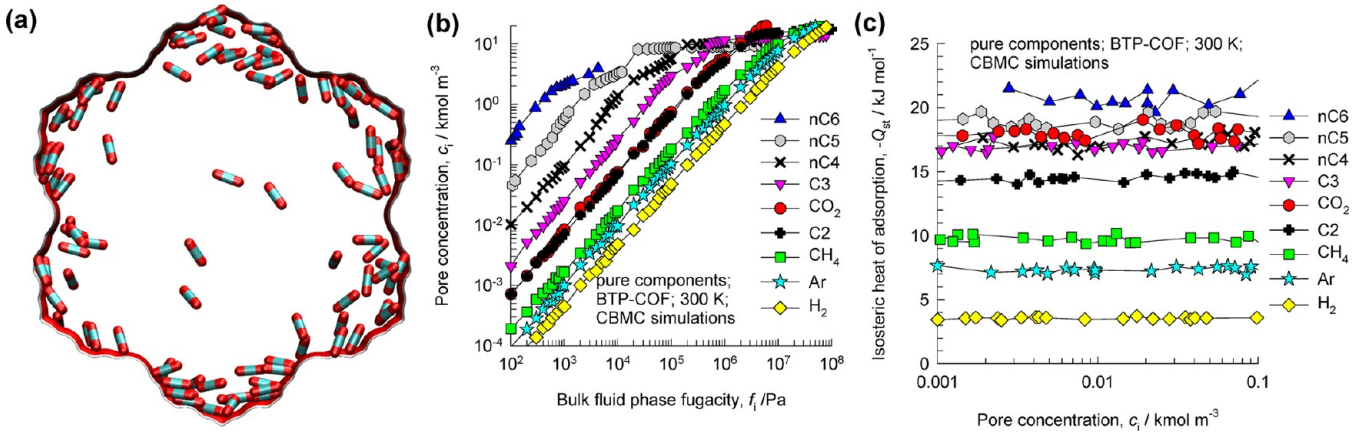

Figure 6. (a) Pore landscape of BTP-COF, showing adsorbed CO_2 molecules. (b) CBMC simulations of the pure component adsorption isotherms in BTP-COF at 300 K, expressed as a function of the fugacity in the bulk gas phase. (c) CBMC simulations of $-Q_{st}$, for a variety of guest molecules in BTP-COF at 300 K, expressed as a function of the pore concentration, c_i, expressed in terms of the accessible pore volume.

monitoring the mean square displacement of an ensemble of molecules.[1] The self-diffusivity, $D_{i,self}$, is determined by analyzing the mean square displacement of individual molecules.[1] At any adsorbate loading, $D_{i,self} \leq Đ_i$; this is because individual jumps of molecules are correlated due to revisitation of sites that have been recently vacated. The following relationship

dx.doi.org/10.1021/jp308971w | J. Phys. Chem. C 2012, 116, 23556−23568

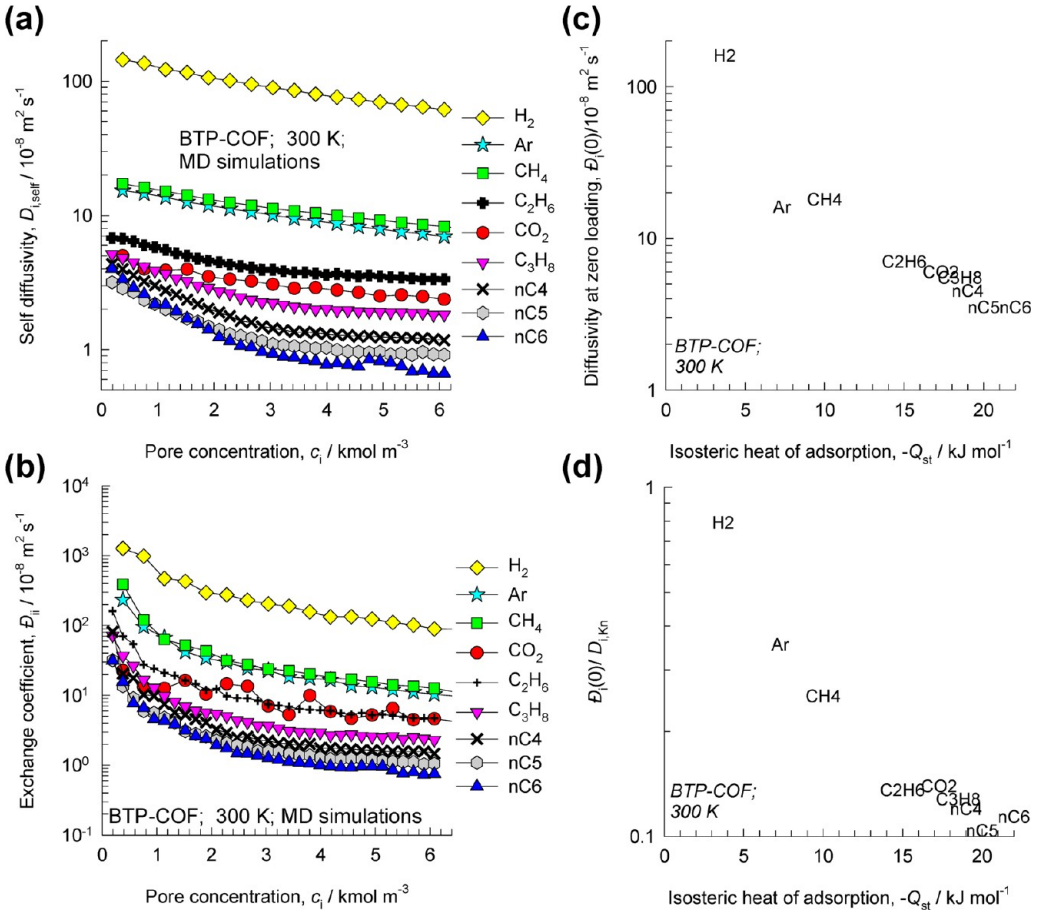

Figure 7. (a and b) MD simulations of (a) self-diffusivities, $D_{i,self}$, and (b) exchange coefficients, $Đ_{ii}$, for variety of guest molecules in BTP-COF at 300 K, expressed as a function of the concentrations c_i within the pores. (c and d) Plots of (c) $Đ_i(0)$ and (d) $Đ_i(0)/D_{i,Kn}$, for variety of guest molecules in BTP-COF at 300 K as function of $-Q_{st}$ of the corresponding species.

between $D_{i,self}$ and $Đ_i$ can be derived on the basis of the M-S equations[16]

$$1/D_{i,self} = 1/Đ_i + 1/Đ_{ii} \quad (6)$$

wherein the exchange coefficient, $Đ_{ii}$, serves to quantify the facility with which the revisitation of sites occurs; such quantification is essential for describing mixture diffusion.

The magnitudes of $D_{i,self}$, $Đ_i$, and D_i vary with the adsorbate loading q_i. For a fair comparison of guest diffusivities in a given host material, we shall examine the diffusivities in the limit $q_i \to 0$, for which we have $D_{i,self} = Đ_i = D_i$; this limiting value is termed the "zero loading" diffusivity, noted by $Đ_i(0)$. In the current study we use MD simulations of diffusivities $D_{i,self}$, and $Đ_i$ for a range of loadings and obtain the $Đ_i(0)$ by careful extrapolation to "zero loading" conditions. Additionally, we performed CBMC simulations to determine adsorption isotherms and isosteric heats of adsorption, $-Q_{st}$, for quantification of binding energies. The MD and CBMC data sets were obtained for several guest molecules (CO_2, H_2, N_2, He, Ne, Ar, Kr, CH_4, C_2H_4, C_2H_6, C_3H_6, C_3H_8, nC_4H_{10}, nC_5H_{12}, and nC_6H_{14}) in any given host material. The chosen structures, 24 in number, span a wide range of characteristic pore dimensions ranging from 3.26 Å (corresponding to windows of ZIF-8) to 34 Å 1D channels of BTP-COF. Published experimental data, on transient uptake and membrane permeation, are used to test and verify the important concepts and conclusions that emerge from the MD data.

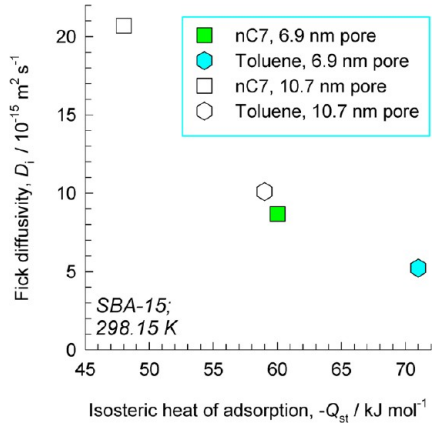

Figure 8. Diffusivities of nC7 and toluene in SBA-15 materials with pore sizes of 6.9 nm (SBA-15−80) and 10.7 nm (SBA-15−130), determined at 298 K by Huang et al.[32].

The entire database of simulation results is available in the Supporting Information accompanying this publication; this material includes details of the CBMC and MD simulation methodologies, details of the porous structures investigated (pore landscapes, unit cell dimensions, accessible pore volume, characteristic pore dimensions), specification of the force fields used, simulation data on self- and M-S diffusivities, and isosteric heats of adsorption.

dx.doi.org/10.1021/jp308971w | J. Phys. Chem. C 2012, 116, 23556−23568

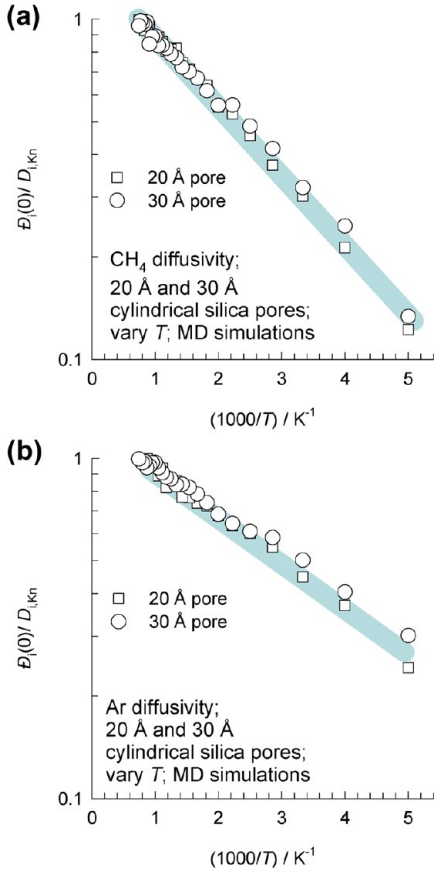

Figure 9. Arrhenius plots for data on $Đ_i(0)/D_{i,Kn}$ for (a) CH_4 and (b) Ar in cylindrical silica pores of 20 and 30 Å size at 300 K.

We begin our discussions with the first category of materials to be found in the upper region of Figure 1 (marked blue).

2. DIFFUSIVITIES IN CAGE-TYPE STRUCTURES WITH NARROW WINDOWS SEPARATING ADJACENT CAGES

Figure 3a presents MD data on $Đ_i$ vs q_i for a variety of guest molecules in CHA, that has windows of 3.8 Å × 4.2 Å size. The narrow windows offer high free-energy barriers for intercage hopping. This energy barrier is higher for guest species with a larger kinetic diameter; this is due to the higher degree of constraint, or confinement, at the window regions. The energy barrier often decreases with the intracage loading, resulting in a dependence of $Đ_i$ on q_i as observed in Figure 3a.[17,18] On extrapolation of the MD data to low loadings, we find that the $Đ_i(0)$ follows the hierarchy He ≈ H_2 > Ne > Ar ≈ N_2 > CO_2 > CH_4. Broadly speaking, the hierarchy is dictated by the kinetic diameters; see Figure 3b. The CO_2 diffusivity is significantly higher, by about 1 order of magnitude, than that of CH_4. CO_2 is a pencil-shaped molecule, with a significantly smaller cross-section than CH_4 and hops lengthwise across the windows; this is also qualitatively evident in the snapshots shown in Figure 2. The correlation of $Đ_i(0)$ with the kinetic diameter is, however, not perfect because molecular lengths are also of importance. This explains why the $Đ_i(0)$ value of CO_2 is lower than that of Ar or N_2.

Experimental verification of the MD simulations for CHA is provided by the data of Li et al.[19,20] for permeation across a thin layer of SAPO-34, a structural analog of CHA. Precise information on the thickness of the membrane layer, δ, is usually not available, and therefore. it is more commonplace to back-out the transport coefficients, $\rho Đ_i/\delta$, from membrane permeation experiments; this set of data for a variety of gases as a function of molar loadings at the upstream face of the membrane are shown in Figures 3c. The corresponding plot of $\rho Đ_i(0)/\delta$, vs kinetic diameter is provided in Figure 3d. There is good agreement with MD data for CHA, in both the hierarchy of diffusivity values, and its dependence on the kinetic diameter. As in Figure 3b, the correlation of $\rho Đ_i/\delta$ with the kinetic diameter is not perfect; the CO_2 lies below that of Ar and N_2.

The 3.65 Å × 4.4 Å windows of DDR have a more oblong shaped aperture compared to that of CHA. Consequently, the experimental values of the membrane transport coefficient $\rho Đ_i/\delta$ show a similar, but not identical, dependence on the kinetic diameter; see Figure 4. The spherical CH_4 molecule is more strongly constrained at the window regions than in CHA, and therefore the diffusivity of CH_4 is more than 2 orders of magnitude below that of CO_2. Due to the oblong shaped aperture the window regions are also preferred adsorption sites for CO_2; this has been established by CBMC simulations.[21]

Zhang et al.[22] have systematically analyzed the diffusivities of a wide variety of guest molecules in ZIF-8 to also conclude that the diffusivities are not simply correlated by the molecular diameters. A good illustration of the influence of differences in molecular *configuration* is provided by diffusion-selective separation of alkane/alkene mixtures using ZIF-8 membranes. There are subtle differences in the bond lengths and bond angles; see cartoons in Figure 5a. The bond length of the alkenes is slightly smaller than that of the corresponding alkane of the same C number. The bond angle for propene is larger than that of propane. Alkene/alkane mixtures separations across ZIF-8 membranes is dictated by a combination of S_{diff} and S_{ads}. CBMC simulations of the pure component adsorption isotherms show that the adsorption selectivity S_{ads} is in favor or the saturated alkane molecule; see Figure 5b. The value of S_{diff}, on the other hand, is strongly in favor of the unsaturated alkenes for both mixtures. This is evidenced in the data for the transport coefficients, $\rho D_i/\delta$, backed-out from ZIF-8 permeation experiments of Bux et al.[23] and Pan et al.;[24] see Figure 5, panels c and d. The diffusivity of ethene is about a factor 5 higher than that of ethane; this must be ascribed to the shorter bond length. Measurements of the Fick diffusivity of ethene and ethane using infra-red microscopy,[23,25] confirms the value of $S_{diff} \approx 5$. The diffusivity of propene is 45−70 times that of propane, reflecting differences in both bond lengths and bond angles. A further confirmation of the subtle influence of bond lengths and bond angles is provided by Ruthven and Reyes,[26] who report S_{diff} values in excess of 10^3 for propene/propene mixtures in CHA and DDR. The propene/propene diffusion selectivity in CHA is about a factor of 2 higher than that in DDR, reaffirming the subtle influence of windows shapes.

Lattice flexibility has little influence on the intercage hopping across narrow 8-ring windows of zeolites.[18,27] In contrast, the flexibility of the windows of ZIF-8 has distinctively different characteristics, illustrated by the video animations provided as Supporting Information, causing the effective aperture size to be higher than the crystallographic value of 3.26 Å.

3. DIFFUSIVITIES IN 1D MESOPOROUS CHANNELS, LARGER THAN 20 Å

In contrast to hopping across narrow windows, the other extreme in the spectrum of diffusion behaviors corresponds to diffusion inside mesoporous channels. Let us examine the

dx.doi.org/10.1021/jp308971w | J. Phys. Chem. C 2012, 116, 23556−23568

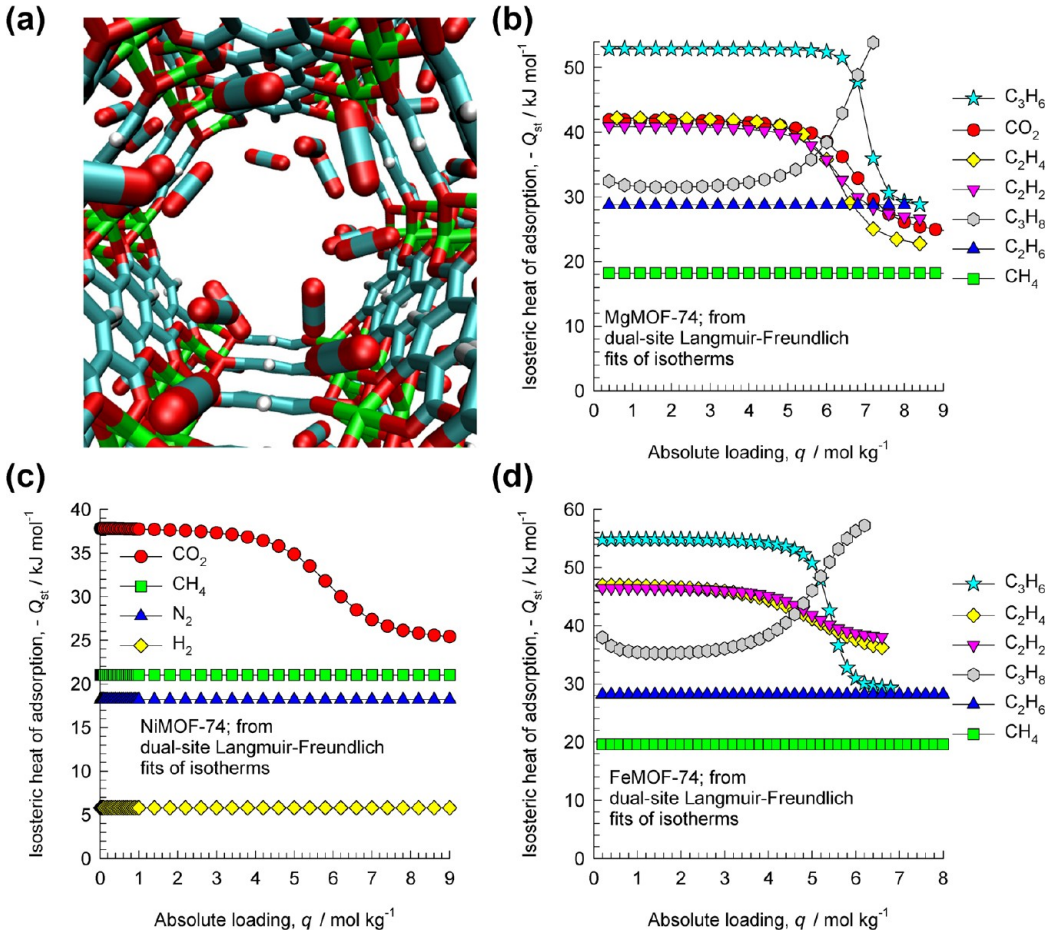

Figure 10. (a) Snapshot showing adsorbed CO_2 molecules within the 1D hexagonal-shaped channels of MgMOF-74. (b, c, d) Isosteric heats of adsorption, $-Q_{st}$, as a function of molar loadings for a variety of guest molecules in (b) MgMOF-74, (c) NiMOF-74, and (d) FeMOF-74. The data in panels b–d are obtained from experiment data on pure component isotherms for a variety of temperatures; details of the fits are provided in the Supporting Information.

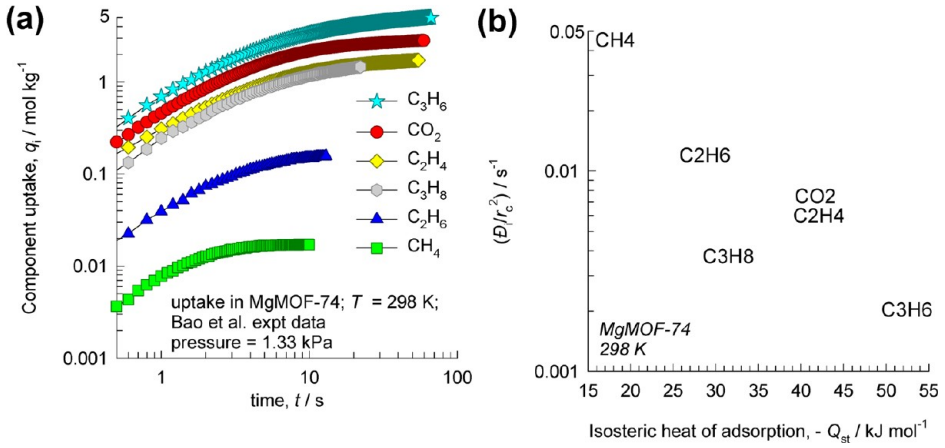

Figure 11. (a) Transient uptake of CO_2, CH_4, C_2H_4, C_2H_6, C_3H_6, and C_3H_8 in MgMOF-74 at 298 K and 1.33 kPa. The plotted data are from the experiments reported by Bao et al.;[4,41] the reported fractional uptake data are multiplied by the loadings corresponding to 298 K and 1.33 kPa; these values are determined from the pure component isotherm fits to be 2.9, 0.017, 1.8, 0.17, 5.9, and 2 mol kg^{-1}, respectively, for CO_2, CH_4, C_2H_4, C_2H_6, C_3H_6, and C_3H_8; details are provided in the Supporting Information. (b) The values of $Đ_i/r_c^2$ for CO_2, CH_4, C_2H_4, C_2H_6, C_3H_6, and C_3H_8 in MgMOF-74 plotted as a function of $-Q_{st}$; the $-Q_{st}$ corresponds to the loadings of the species at the end of the equilibration process in panel a.

adsorption and diffusion of CO_2, H_2, Ar, CH_4, C_2H_6, C_3H_8, nC_4H_{10}, nC_5H_{12}, and nC_6H_{14} in BTP-COF that has an effective pore diameter of 34 Å; see Figure 6a for the pore landscape.

Figure 6, panels b and c, shows the CBMC simulation results for the adsorption isotherms and $-Q_{st}$ for a variety of guest molecules in BTP-COF. Both the adsorbed phase

dx.doi.org/10.1021/jp308971w | J. Phys. Chem. C 2012, 116, 23556–23568

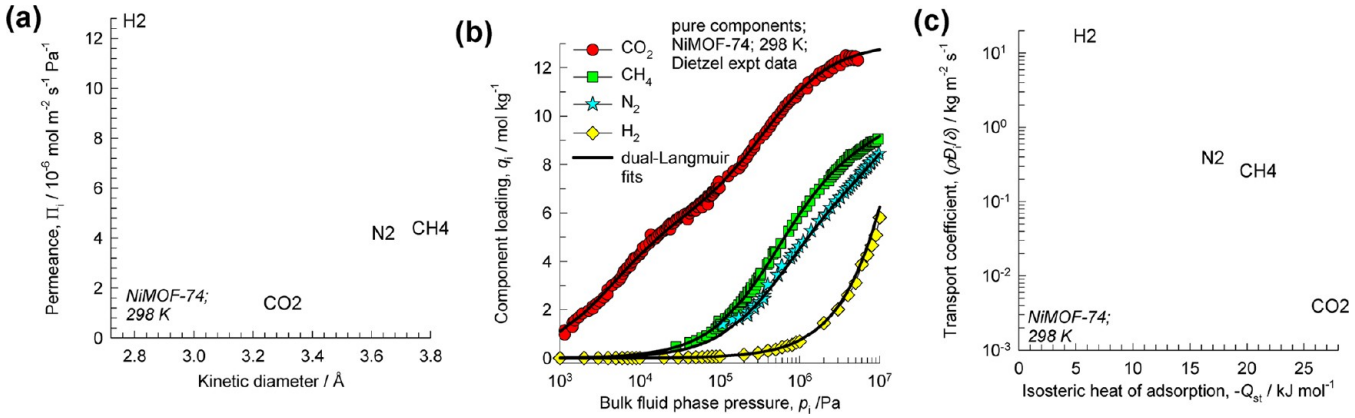

Figure 12. (a) Permeances, Π_i, and of CO_2, H_2, N_2, and CH_4 across a NiMOF-74 membrane operating at 298 K and 100 kPa upstream pressure; the experimental data are from Lee et al.[44] (b) Experimental isotherm data for adsorption of N_2, CH_4, and CO_2 in NiMOF-74 from Dietzel et al.[57] The isotherm data for H_2 are from CBMC simulations. The continuous solid lines are dual-Langmuir fits; the fit parameters are provided in the Supporting Information. (c) The membrane transport coefficient, $\rho Đ_i/\delta$, as a function of $-Q_{st}$; the $-Q_{st}$ values are determined at component loadings of 7.16, 1.43, 0.95, and 0.075 mol kg^{-1} for CO_2, CH_4, N_2, and H_2, respectively.

pore concentrations c_i and $-Q_{st}$ follow the hierarchy H_2 < Ar < CH_4 < C_2H_6 < CO_2 < C_3H_8 < nC_4H_{10} < nC_5H_{12} < nC_6H_{14}. The values of $-Q_{st}$ in the limit of low pore concentrations, $c_i \to 0$, may be taken as a measure of the binding energies for each species.

The MD simulations of the self-diffusivities, $D_{i,self}$, are plotted in Figure 7a as a function of c_i. With increasing pore concentration, the $D_{i,self}$ tend to decrease due to increased contribution of molecule−molecule interactions. The exchange coefficients, $Đ_{ii}$, backed-out from MD data on $D_{i,self}$ and $Đ_i$, eq 6 are plotted in Figure 7b. For both $D_{i,self}$, and $Đ_{ii}$, the observed hierarchy of values at any loading is H_2 > CH_4 ≈ Ar > C_2H_6 ≈ CO_2 ≈ C_3H_8 > nC_4H_{10} > nC_5H_{12} ≈ nC_6H_{14}. This hierarchy does not seem to follow the trends dictated by either the values of the kinetic diameters or molar masses that are listed in Table 1. If we choose the kinetic diameter as the appropriate determinant for diffusivities, we should expect CO_2 to diffuse faster than CH_4. On the basis of molar masses, we would expect C_2H_6 to have a lower diffusivity than Ar. Neither expectation is fulfilled by the MD data; a closer scrutiny is therefore required.

Extrapolation to low pore concentrations, $c_i \to 0$, we obtain $Đ_i(0)$. The values of $Đ_i(0)$ are plotted in Figure 7c as a function of the corresponding values of $-Q_{st}$. Broadly speaking, the data show that the higher the binding energy, the lower is the magnitude of $Đ_i(0)$. Also, the higher the binding energy the lower is the value of the exchange coefficient, $Đ_{ii}$; the interpretation of these will be provided in a later section in comparison with other structures.

For theoretical interpretation of the observed trend of $Đ_i(0)$ values in Figure 7c, let us consider the gas-translation model of Xiao and We,[28]

$$Đ_i(0) = \frac{1}{3} u\lambda \exp\left(-\frac{E_A}{RT}\right); \quad u = \sqrt{\frac{8RT}{\pi M_i}} \tag{7}$$

In eq 7, u is the characteristic velocity at which the molecule travels, E_A represents the energy barrier for hopping of molecule from one adsorption site to an adjacent one, and λ is the average distance of jumps. Taking the values of $\lambda = d_p$ and $E_A = 0$, we recover the Knudsen diffusivity formula

$$D_{i,Kn} = \frac{1}{3} u\lambda = \frac{d_p}{3}\sqrt{\frac{8RT}{\pi M_i}} \tag{8}$$

The Knudsen diffusivity formula holds when the reflection following molecule-wall collisions are purely diffuse in nature; that is, the angle of reflection bears no relation to the angle of incidence at which the molecule strikes the pore wall. Adsorption causes the molecules to bind to the wall and perhaps hop to a neighboring adsorption site, rather than return to the bulk after collision.[15,29,30] Consequently, adsorption at the pore wall introduces a bias in molecular hops; this bias increases with increasing binding strength. A quantification of the bias in molecular hops is obtained by dividing $Đ_i(0)$ by $D_{i,Kn}$. The plot of $Đ_i(0)/D_{i,Kn}$ versus $-Q_{st}$ in Figure 7d indicates the strong influence of $-Q_{st}$ on deviations from the Knudsen formula. In the limiting case for which the binding energy is negligibly small, as is the case for H_2, $D_{i,Kn}$ provides a good estimate of the diffusivity at zero-loading, $Đ_i(0)$. At the other extreme, for nC5 and nC6 alkanes, $Đ_i(0)/D_{i,Kn} \approx 0.1$, indicating that the Knudsen formula will overestimate the diffusivities by about 1 order of magnitude. In the experimental study of Katsanos et al.,[31] the measured diffusivities of nC5, nC6, and nC7 in α-alumina (d_p = 216 Å) and γ-alumina (d_p = 106 Å) were found to be in the range of 10−27% of the values anticipated by the Knudsen formula. Results analogous to those presented in Figure 7 are obtained for cylindrical silica mesopores of 20 and 30 Å (see the Supporting Information).

Figure 8 presents the experimental data of Huang et al.[32] for diffusivities of nC7 (*n*-heptane) and toluene in SBA-15 materials of two different pore sizes, 69 and 107 Å, as a function of $-Q_{st}$. The molar masses of the two guest species are nearly equal, 0.1 and 0.092 kg mol^{-1}, respectively. However, the diffusivities of toluene are found to be significantly lower than that of nC7; the rationale for this is attributable to the much higher binding energy for toluene.

The gas-translation formulation (7) also indicates that the influence of the binding energies on diffusivities should diminish with increasing T. To test this expectation, Figure 9, panels a and b, presents Arrhenius plots for data on $Đ_i(0)/D_{i,Kn}$ for CH_4 and Ar in cylindrical silica pores of 20 and 30 Å. As anticipated, the departures from the Knudsen prescription decrease with increasing T. At the highest temperatures, $Đ_i(0)/D_{i,Kn}$ approaches unity. The values of E_A for CH_4 and Ar are determined to be 3.5 and 2.4 kJ mol^{-1}.

dx.doi.org/10.1021/jp308971w | J. Phys. Chem. C 2012, 116, 23556−23568

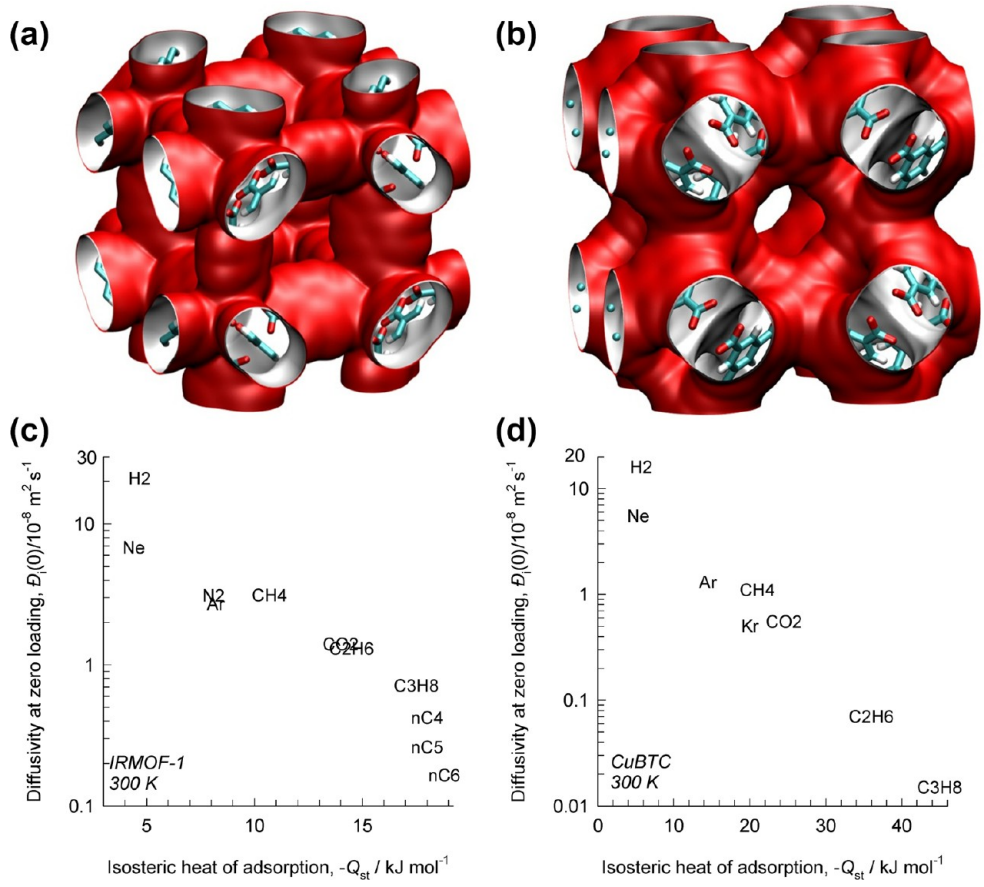

Figure 13. (a and b) Pore landscapes of (a) IRMOF-1 and (b) CuBTC. (c and d) The zero-loading diffusivities $Đ_i(0)$ for (c) IRMOF-1 and (d) CuBTC as a function of $-Q_{st}$, of the corresponding species.

Ruthven and co-workers[33,34] have questioned the conclusions reached in the MD simulations regarding the influence of pore adsorption and have reanalyzed published experimental data[35,36] to conclude that the Knudsen formula remains valid even for gases that have strong adsorption. This debate on the validity of the Knudsen formula is complicated by the fact that the tortuosity factors are not known precisely and there is still disagreement on what tortuosity factors can be considered to be reasonable.[29] Furthermore, there is often a distribution of pore diameters that makes the application of eq 8 not entirely straightforward.

4. DIFFUSIVITIES IN MICROPOROUS 1D CHANNELS

M-MOF-74, also denoted as M_2(dobdc) and CPO-27-M, where M represents the exposed metal atoms Mg, Ni, Co, Zn, or Fe are iso-structural MOFs with 1D hexagonal shaped channels of approximately 11 Å size. Figure 10a shows a snapshot of adsorbed CO_2 molecules within the channels of MgMOF-74. With the aid of neutron diffraction measurements, Wu et al.[37] have established that there is strong Mg−CO_2 binding, attributed to enhanced electrostatic interactions. The adsorbed CO_2 molecule is strongly attached through one of its O atoms. Neutron diffraction measurements also demonstrate that alkynes and alkenes attach strongly, side-on, to the metal atoms of FeMOF-74.[5] In order to quantify the strong binding of CO_2, alkynes, and alkenes to metal atoms, Figure 10b−d presents $-Q_{st}$. data for guest molecules in MgMOF-74, NiMOF-74, and FeMOF-74 as function of the molar loadings. At low loadings, the $-Q_{st}$ values for CO_2, ethyne, ethene, and propene are in excess of 37 kJ mol^{-1}, confirming the strong binding energies of these guest molecules. Saturated alkanes have significantly lower binding energies, in the 18−32 kJ mol^{-1} range. Consequently, M-MOF-74 offers high adsorption selectivities for separation of CO_2/N_2,[38,39] CO_2/CH_4,[40] CO_2/H_2,[6] alkane/alkenes,[3−5,9] and alkyne/alkene[5,9] mixtures.

Let us now investigate the extent to which the high binding energies of CO_2 and alkenes serve to reduce the corresponding diffusivities within the 1D channels. Bao et al.[4,41] report measurements of the transient uptake of CO_2, CH_4, C_2H_4, C_2H_6, C_3H_6, and C_3H_8 in MgMOF-74 crystals. As illustration, the transient uptake data at 298 K and 1.33 kPa are shown in Figure 11a. The transient uptake of species i within the crystallites is described by

$$\frac{\partial q_i}{\partial t} = -\frac{1}{\rho}\frac{1}{r^2}\frac{\partial}{\partial r}(r^2 N_i) \tag{9}$$

The set of eqs 9, 4, and 5 need to be solved numerically in order to obtain values of $Đ_i/r_c^2$.[42] The fitted $Đ_i/r_c^2$ values for CO_2, CH_4, C_2H_4, C_2H_6, C_3H_6, and C_3H_8 are 0.0075, 0.045, 0.006, 0.012, 0.00203, and 0.00375 s^{-1}, respectively. Figure 11b presents a plot of $Đ_i/r_c^2$ as a function of $-Q_{st}$. It is remarkable to note that the diffusivity of the alkene is a factor of 2 lower than that of the corresponding alkane; this trend is opposite to that suggested by both molar masses and kinetic diameters in Table 1; the reduction in the alkenes diffusivities must be attributed to the higher binding energies. If we were to adopt the Knudsen formula 8 as a guideline, we should expect the diffusivity of CO_2 to be a factor of $(44/16)^{1/2} = 1.66$ lower than that of CH_4; the experimental uptakes show a reduction by a

dx.doi.org/10.1021/jp308971w | J. Phys. Chem. C 2012, 116, 23556−23568

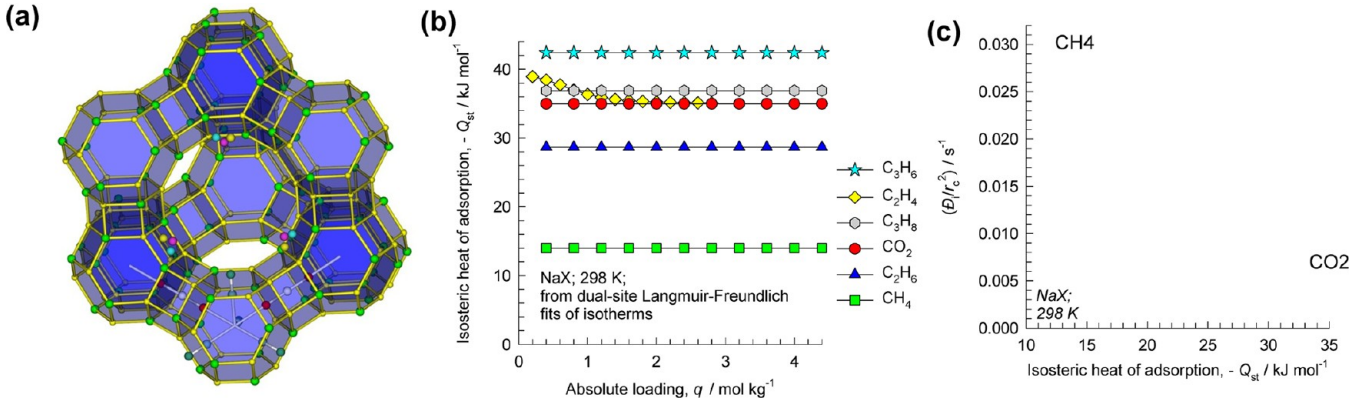

Figure 14. (a) Framework structure of NaX zeolite, also showing the location of Na^+ cations. (b) Isosteric heats of adsorption, $-Q_{st}$, as a function of molar loadings. These are based on the dual-Langmuir−Freundlich fits of the isotherms; details are provided in the Supporting Information. (c) The values of $Đ_i/r_c^2$ of CO_2, and CH_4 in NaX zeolite, plotted as a function of $-Q_{st}$. The data for $Đ_i/r_c^2$ are obtained from by dividing values of the corresponding Fick diffusivities in Table 4 of Bao et al.[41] at T = 298 K by the thermodynamic correction factor Γ_i determined from the isotherm fits.

factor of 6. The significantly lower CO_2 diffusivity must be ascribable to its higher binding energy 42 kJ mol^{-1}, compared to only 20.5 kJ mol^{-1} for CH_4. Furthermore, the recent experimental NMR study of Kong et al.[43] demonstrates a rotational motion of CO_2 molecules within the channels of MgMOF-74. Video animations of the MD simulations of CO_2 motion, uploaded as Supporting Information, provide a visual appreciation of rotational motion that reduces transversal mobility within the channels.

The correlation of diffusivities with $-Q_{st}$ is not perfect, suggesting that the molecular sizes and configurations do additionally influence the velocity, u, and the jump distance, λ, in eq 7; the precise nature of such influences needs further investigation.

A layer-by-layer seeding technique has been developed for preparation of NiMOF-74 membranes,[44] opening up the possibility of the use of M-MOF-74 membranes for a variety of separations. Lee et al.[44] report data on unary permeances for CO_2, CH_4, N_2, and H_2 across a NiMOF-74 membrane; the permeance of species i is defined as the permeation flux N_i divided by the trans-membrane partial pressure difference, Δp_i

$$\Pi_i \equiv \frac{N_i}{\Delta p_i} \tag{10}$$

The permeance of CO_2 is the lowest and does not seem to correlate with the kinetic diameters of the molecules; see Figure 12a. The downstream pressures are negligible in comparison with the upstream partial pressures, $\Delta p_i \approx p_i$, and we obtain from eqs 4 and 10

$$\Pi_i \equiv \frac{N_i}{p_i} \approx \frac{\rho D_i}{\delta}\frac{q_i}{p_i} = \frac{\rho Đ_i \Gamma_i}{\delta}\frac{q_i}{p_i} \tag{11}$$

where q_i is the molar loading of component i at the upstream face. The molar loadings q_i and correction factor Γ_i can be determined from the adsorption isotherms. From the pure component isotherm data (Figure 12b), we determine the molar loadings for CO_2, CH_4, N_2, and H_2 to be 7.16, 1.43, 0.95, and 0.075 mol kg^{-1}, respectively. The corresponding values of $-Q_{st}$ can be obtained from the data on the adsorption isotherms for each of the species (Figure 12c). The transport coefficient, $\rho Đ_i/\delta$, backed-out from the experimental membrane

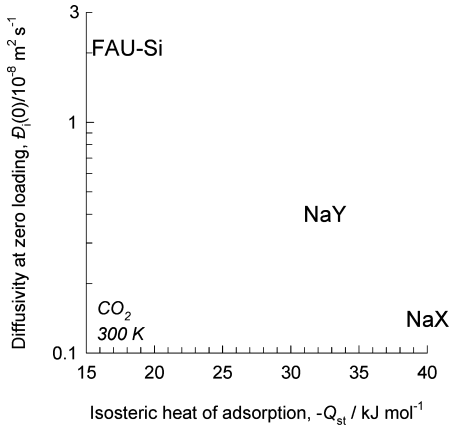

Figure 15. Comparison of zero-loading diffusivities $Đ_i(0)$ of CO_2 in FAU-Si (all silica), NaY (54 Na^+/u.c.), and NaX (86 Na^+/u.c.) zeolites, plotted with the corresponding values of $-Q_{st}$. These data are based on CBMC and MD simulations.

permeances Π_i, is seen to correlate well with $-Q_{st}$ (cf. Figure 12c) and confirms the strong influence on binding energies on diffusivities.

Results analogous to that for MgMOF-74 and NiMOF-74 are obtained for other 1D channel structures (AFI and MOR) and MOFs (MIL-47 and MIL-53); see the Supporting Information.

5. "OPEN" STRUCTURES WITH LARGE CAVITIES

Figure 13, panels a and b, shows the pore landscapes of two well-researched MOFs: IRMOF-1 and CuBTC that have "open" structures with 11−12 Å sized cavities. The hierarchy of $Đ_i(0)$ diffusivities correlates reasonably well with $-Q_{st}$ for both MOFs; see Figure 13, panels c and d. For both MOFs, diffusivities of CO_2 are more than a factor of 2 lower than that of CH_4; this data is not explainable by either differences in kinetic diameter or molar masses. Analogous data hold for MOF-177.

Consider now the diffusivities in the industrially important NaX zeolite, also known commonly by its trade name 13X zeolite. This material has the FAU topology, and contains typically 86 Na^+ extra-framework cations per unit cell; see Figure 14a. The structure has cavities that are about 11 Å in size. Adjacent cavities are separated by 10-ring windows of 7.3 Å size; the window aperture does not offer significant free-energy

dx.doi.org/10.1021/jp308971w | J. Phys. Chem. C 2012, 116, 23556−23568

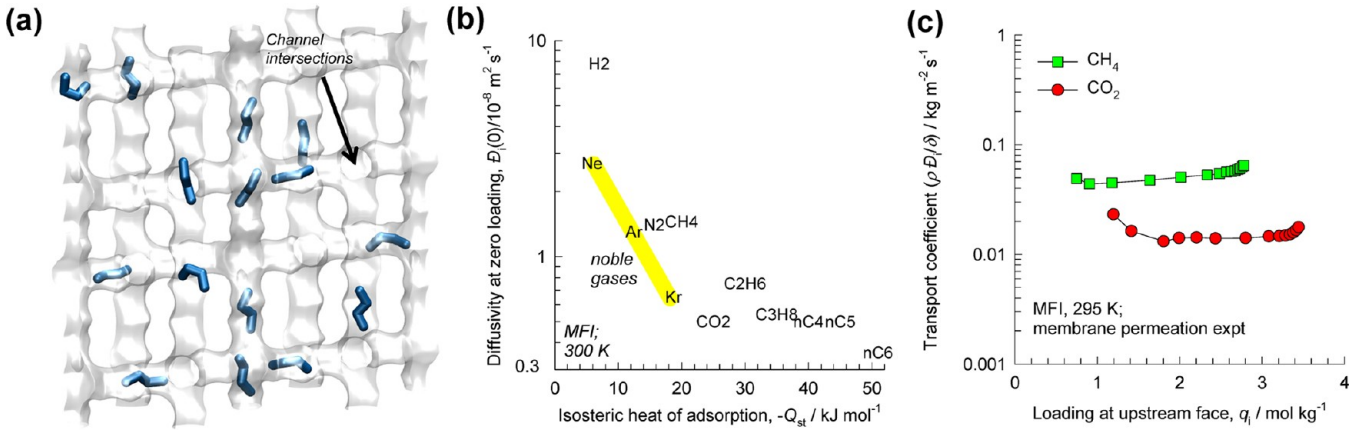

Figure 16. (a) Snapshot showing the location of adsorbed n-C_4H_{10} molecules within the intersecting framework structure of MFI zeolite. (b) MD data on $Đ_i(0)$ as function of $-Q_{st}$. (c) The membrane transport coefficient, $\rho Đ_i/\delta$, as a function of molar loading at the upstream face of the membrane; data from Krishna et al.[45]

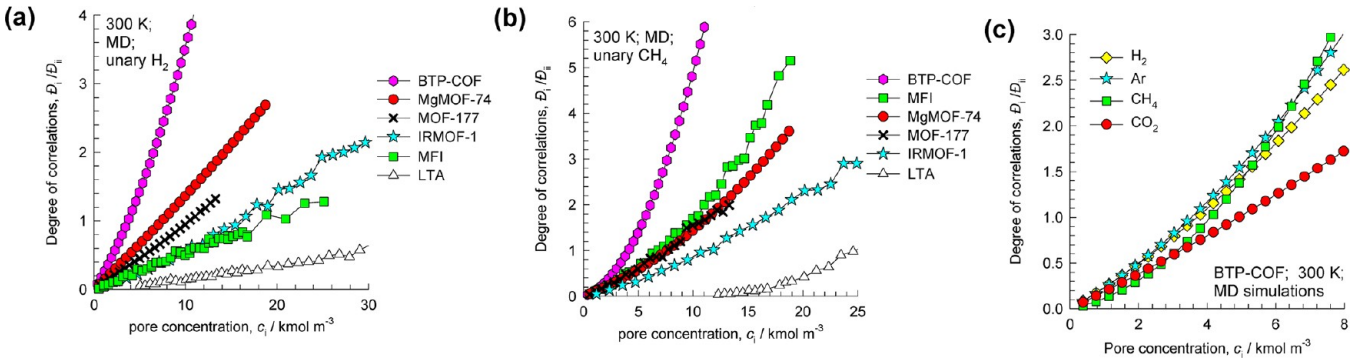

Figure 17. (a and b) Degree of correlations, $Đ_i/Đ_{ii}$, for diffusion of (a) H_2 and (b) CH_4 in a variety of porous host materials. (c) The degree of correlations, $Đ_i/Đ_{ii}$, for diffusion of H_2, CH_4, Ar, and CO_2 in BTP-COF. The x axis is the pore concentration, $c_i = q_i/V_p$, where V_p is the accessible pore volume.

barriers for intercage hopping. Due to electrostatic interactions of Na^+ cations with CO_2, the binding energies are significantly higher than that of CH_4; see data in Figure 14b which also demonstrates that electrostatic interactions with alkenes result in higher $-Q_{st}$ values than the corresponding alkanes. On the basis of the $-Q_{st}$ data we should expect the CO_2 diffusivity to be significantly lower than that of CH_4. The uptake data of Bao et al.[41] show that the diffusivities of CO_2 are lower than that for CH_4 by a factor 4; see Figure 14c.

A further demonstration of the strong influence of binding energy is provided by a comparison of CO_2 diffusivities in FAU-Si (all silica), NaY (with 54 Na^+/u.c.), and NaX (86 Na^+/u.c.). Increasing the number of cations has the effect of increasing the binding energy of CO_2. Concomitantly, however, there is a reduction in the diffusivities as shown in the $Đ_i(0)$ versus $-Q_{st}$ plot in Figure 15. The $Đ_i(0)$ values are 2.1×10^{-8}, 0.4×10^{-8}, and 0.14×10^{-8} m^2 s^{-1}, for FAU-Si, NaY, and NaX, respectively. The diffusivity of CH_4, on the other hand, is hardly influenced by the presence of cations. In the context of CO_2/CH_4 separations using FAU membranes, this implies that increasing the number of cations will increases S_{ads} but at the expense of S_{diff}.

6. DIFFUSIVITIES IN INTERSECTING CHANNEL STRUCTURES

MFI zeolite consists of a set of intersecting channels that are approximately 5.5 Å in size; Figure 16a illustrates the channel topology and shows the location of adsorbed n-butane molecules. The molecular simulation results for the zero-loading diffusivities $Đ_i(0)$ as function of $-Q_{st}$ are provided in Figure 16b. For monatomic noble gases, the $Đ_i(0)$ correlate well with $-Q_{st}$. The diffusivity of CO_2 is lower than that of CH_4 and N_2, despite having a lower kinetic diameter than either species; the rationale for the lower CO_2 mobility is to be ascribed to its higher binding energy. In MFI membrane permeation experiments,[45] the transport coefficient, $\rho Đ_i/\delta$, for CO_2, was determined to be a factor 3 lower than that of CH_4, in agreement with the MD data; see Figure 16c. The experimental diffusivity data of Sun et al.[46] provides further confirmation of the lower mobility of CO_2 compared to CH_4.

7. DEGREE OF CORRELATIONS

Data on the exchange coefficients $Đ_{ii}$ such as those presented in Figure 7b for BTP-COF were obtained for all guest/host combinations. It is convenient, and useful, to define the degree of correlations as the ratio $Đ_i/Đ_{ii}$. Figure 17, panels a and b, provides comparisons of $Đ_i/Đ_{ii}$ for H_2 and CH_4 diffusion in a variety of host materials. Broadly speaking, the highest degree of correlations is for 1D channel structures, such as MgMOF-74 and BTP-COF, because of the difficulty of bypassing of molecules. The smallest degree of correlations is realized in cage-type structures, typified by LTA; here, intercage hops across the windows occur one molecule at a time and correlations are practically negligible at pore concentrations $c_i < 10$ kmol m^{-3}.

dx.doi.org/10.1021/jp308971w | J. Phys. Chem. C 2012, 116, 23556−23568

The correlations within the intersecting channels of MFI lie in between the above two extremes.

Figure 17c compares the degrees of correlation for H_2, CH_4, Ar, and CO_2 in BTP-COF; the value of $Đ_i/Đ_{ii}$ for CO_2 that has the highest binding energy is lower than for the other guest species. For mixture diffusion in structures such as BTP-COF, MgMOF-74, and MFI, correlation effects will have the effect of slowing-down the more mobile partner species.[45,47,48] Broadly speaking, slowing-down effects are of greater importance for more mobile species with lower adsorption strengths.

Correlation effects are of lesser importance in cage-type structures with narrow windows. For CH_4/H_2 mixture permeation across the ZIF-8 membrane, the S_{diff} values can be estimated reasonably accurately on the basis of pure component diffusivity values because of negligible degree of correlations.[49,50] However, experimental data for CO_2/H_2 permeation across a SAPO-34 membrane indicate that correlation effects cannot be completely ignored.[45]

8. CONCLUSIONS

With the aid of an extensive database of simulations and experiments, we have attempted to obtain insights into the variety of factors that determine the magnitudes and hierarchy , of diffusivities in nanoporous crystalline materials. Our investigations have revealed that there are two broad categories of materials with two distinct different diffusion behaviors.

(1) In the first category, we have cage-type structures with narrow windows. Here, molecular sizes, bond lengths, and bond angles are important determinants of the diffusivities. Subtle differences in molecular sizes result in differences in diffusivities by 1−3 orders of magnitude. Such materials are usefully employed in membrane devices, for which the permeation selectivities, $S_{perm} = S_{diff} \times S_{ads}$, are primarily, but not exclusively, driven by S_{diff}. Correlation effects are generally of negligible importance in such structures.

(2) All other materials fall into the second category in which the diffusivities are significantly influenced by the binding energies. This category of materials is also characterized by high of correlations, quantified by the ratio $Đ_i/Đ_{ii}$.

(3) For 1D mesoporous channels, with well-defined and uniform pore sizes (>20 Å), the gas translation model, described by eq 7, provides a reasonable, albeit qualitative, description of the diffusion process. The activation energy E_A in eq 7 is relatable to the binding energy, which in turn can be quantified by the isosteric heat of adsorption, $-Q_{st}$. For guest species that have negligible binding energy, such as H_2, the zero-loading diffusivities $Đ_i(0)$ correspond with the values determined from the Knudsen formula 8. However, for molecules with significantly high binding energies, the Knudsen formula overestimates the diffusivities by about a factor of 10.

(4) Diffusivities within 1D microporous channels of M-MOF-74, with channel sizes of 11 Å, can also be qualitatively described by the gas translation model. Due to strong interactions of CO_2 and alkenes with the exposed metal atoms, these molecules have extremely high binding energies with concomitant lower diffusivity values. An important consequence of this is that CO_2/CH_4 and alkene/alkane separations across M-MOF-74 membranes will be driven by adsorption, with S_{ads} over-riding the disadvantage of S_{diff}.

(5) Diffusivities in intersecting channel structures, such as MFI, and "open" structures with large cavities, such as FAU and IRMOF-1, are qualitatively similar to those for 1D microporous channels. The diffusivities are strongly influenced by binding energies. For chain molecules, the chain length is also an important determinant.

(6) The presence of extra-framework cations in NaY and NaX zeolites have the effect of enhancing adsorption binding energies of CO_2, due to strong electrostatic interactions with the Na^+ cations. An important consequence is that there is a concomitant reduction in the CO_2 diffusivity; this has consequences for membrane separations.

The data and discussions in this paper are primarily focused on unary diffusivities and the influence of molecular dimensions and binding energies thereon. The influence of binding energies on mixture diffusion characteristics needs further detailed investigation.

■ ASSOCIATED CONTENT

Supporting Information

(a) Structural details (unit cell dimensions, accessible pore volume, and characteristic pore dimensions) of a wide variety of porous materials; (b) information on force fields and simulation methodologies; (c) CBMC and MD simulation data for isotherms, iso-steric heats of adsorption, and unary diffusivities; and (d) video animations illustrating the rotational motion of CO_2 molecules with 1D channel of MgMOF-74 and framework dynamics of ZIF-8. This material is available free of charge via the Internet at http://pubs.acs.org.

■ AUTHOR INFORMATION

Corresponding Author

*Tel: +31 20 6270990. Fax: + 31 20 5255604. E-mail: r.krishna@uva.nl.

Notes

The authors declare no competing financial interest.

■ NOTATION

c_i pore concentration of species i, $c_i = q_i/V_p$, mol m^{-3}
d_p pore diameter, m
D_i Fick diffusivity of species i, m^2 s^{-1}
$D_{i,self}$ self-diffusivity of species i, m^2 s^{-1}
$Đ_i$ M-S diffusivity, m^2 s^{-1}
$Đ_{ii}$ self-exchange coefficient, m^2 s^{-1}
$Đ_i(0)$ zero-loading M-S diffusivity, m^2 s^{-1}
$D_{i,Kn}$ Knudsen diffusivity of species i, m^2 s^{-1}
E_A activation energy for diffusion, J mol^{-1}
f_i partial fugacity of species i, Pa
M_i molar mass of species i, kg mol^{-1}
N_i molar flux of species i, mol m^{-2} s^{-1}
p_i partial pressure of species i, Pa
p_t total system pressure, Pa
q_i molar loading species i
$-Q_{st}$ isosteric heat of adsorption, J mol^{-1}
r radial distance coordinate, m
r_c radius of crystallite, m
R gas constant, 8.314 J mol^{-1} K^{-1}
S_{ads} adsorption selectivity, dimensionless
S_{diff} diffusion selectivity, dimensionless
S_{perm} permeation selectivity, dimensionless
t time, s
T temperature, K

u characteristic velocity for motion of molecules, m s^{-1}
V_p accessible pore volume, m^3 kg^{-1}
z distance coordinate, m

Greek letters

δ thickness of membrane, m
Γ_i thermodynamic factor, dimensionless
λ molecular jump distance, m
Π_i membrane permeance of species i, mol m^{-2} s^{-1} Pa^{-1}
ρ framework density, kg m^{-3}

Subscripts

i referring to component i
t referring to total mixture

REFERENCES

(1) Kärger, J.; Ruthven, D. M.; Theodorou, D. N. *Diffusion in Nanoporous Materials;*; Wiley-VCH: Weinheim, Germany, 2012.
(2) Bloch, E. D.; et al. *J. Am. Chem. Soc.* **2011**, *133*, 14814−14822.
(3) Bae, Y.-S.; Lee, C. Y.; Kim, K. C.; Farha, O. K.; Nickias, P.; Hupp, J. T.; Nguyen, S. T.; Snurr, R. Q. *Angew. Chem., Int. Ed.* **2012**, *51*, 1857−1860.
(4) Bao, Z.; Alnemrat, S.; Vasiliev, I.; Ren, Q.; Yu, L.; Lu, X.; Deng, S. *Langmuir* **2011**, *27*, 13554−13562.
(5) Bloch, E. D.; Queen, W. L.; Krishna, R.; Zadrozny, J. M.; Brown, C. M.; Long, J. R. *Science* **2012**, *335*, 1606−1610.
(6) Herm, Z. R.; Swisher, J. A.; Smit, B.; Krishna, R.; Long, J. R. *J. Am. Chem. Soc.* **2011**, *133*, 5664−5667.
(7) Das, M. C.; et al. *J. Am. Chem. Soc.* **2012**, *134*, 8708−8710.
(8) Krishna, R.; van Baten, J. M. *Phys. Chem. Chem. Phys.* **2011**, *13*, 10593−10616.
(9) He, Y.; Krishna, R.; Chen, B. *Energy Environ. Sci.* **2012**, *5*, 9107−9120.
(10) Xiang, S. C.; He, Y.; Zhang, Z.; Wu, H.; Zhou, W.; Krishna, R.; Chen, B. *Nat. Commun.* **2012**, http://dx.doi.org/doi:10.1038/ncomms1956.
(11) He, Y.; Zhou, W.; Krishna, R.; Chen, B. *Chem. Commun.* **2012**, http://dx.doi.org/doi:10.1039/c2cc35418g.
(12) Wu, H.; Yao, K.; Zhu, Y.; Li, B.; Shi, Z.; Krishna, R.; Li, J. *J. Phys. Chem. C* **2012**, *116*, 16609−16618.
(13) Dubbeldam, D.; Krishna, R.; Calero, S.; Yazaydın, A. Ö. *Angew. Chem., Int. Ed.* **2012**, http://dx.doi.org/doi:10.1002/anie.201205040.
(14) Krishna, R.; van Baten, J. M. *J. Membr. Sci.* **2010**, *360*, 323−333.
(15) Krishna, R. *J. Phys. Chem. C* **2009**, *113*, 19756−19781.
(16) Krishna, R. *Chem. Soc. Rev.* **2012**, *41*, 3099−3118.
(17) Dubbeldam, D.; Calero, S.; Maesen, T. L. M.; Smit, B. *Phys. Rev. Lett.* **2003**, *90* (24), 245901.
(18) Krishna, R.; van Baten, J. M. *Microporous Mesoporous Mater.* **2011**, *137*, 83−91.
(19) Li, S.; Falconer, J. L.; Noble, R. D.; Krishna, R. *Ind. Eng. Chem. Res.* **2007**, *46*, 3904−3911.
(20) Li, S.; Falconer, J. L.; Noble, R. D.; Krishna, R. *J. Phys. Chem. C* **2007**, *111*, 5075−5082.
(21) Krishna, R.; van Baten, J. M. *Sep. Purif. Technol.* **2008**, *61*, 414−423.
(22) Zhang, C.; Lively, R. P.; Zhang, K.; Johnson, J. R.; Karvan, O.; Koros, W. J. *J. Phys. Chem. Lett.* **2012**, *3*, 2130−2134.
(23) Bux, H.; Chmelik, C.; Krishna, R.; Caro, J. *J. Membr. Sci.* **2011**, *369*, 284−289.
(24) Pan, Y.; Li, T.; Lestari, G.; Lai, Z. *J. Membr. Sci.* **2012**, *390−391*, 93−98.
(25) Chmelik, C.; van Baten, J. M.; Krishna, R. *J. Membr. Sci.* **2012**, *397−398*, 87−91.
(26) Ruthven, D. M.; Reyes, S. C. *Microporous Mesoporous Mater.* **2007**, *104*, 59−66.
(27) Krishna, R.; van Baten, J. M. *J. Phys. Chem. C* **2010**, *114*, 18017−18021.
(28) Xiao, J. R.; Wei, J. *Chem. Eng. Sci.* **1992**, *47*, 1123−1141.
(29) Bhatia, S. K.; Nicholson, D. *Chem. Eng. Sci.* **2011**, *66*, 284−293.
(30) Krishna, R.; van Baten, J. M. *Microporous Mesoporous Mater.* **2011**, *138*, 228−234.
(31) Katsanos, N. A.; Bakaoukas, N.; Koliadima, A.; Karaiskakis, G. *J. Phys. Chem. B* **2005**, *109*, 11240−11246.
(32) Huang, Q.; Qamar, R. A.; Eić, M. *Adsorption* **2011**, *17*, 27−38.
(33) Ruthven, D. M.; DeSisto, W.; Higgins, S. *Chem. Eng. Sci.* **2009**, *64*, 3201−3203.
(34) Ruthven, D. M. *Chem. Eng. Sci.* **2010**, *65*, 4521−4522.
(35) Higgins, S.; DeSisto, W.; Ruthven, D. M. *Microporous Mesoporous Mater.* **2009**, *117*, 268−277.
(36) Reyes, S. C.; Sinfelt, J. H.; DeMartin, G. J.; Ernst, R. H.; Iglesia, E. *J. Phys. Chem. B* **1997**, *101*, 614−622.
(37) Wu, H.; Simmons, J. M.; Srinivas, G.; Zhou, W.; Yildrim, T. *J. Phys. Chem. Lett.* **2010**, *1*, 1946−1951.
(38) Yazaydın, A. Ö.; et al. *J. Am. Chem. Soc.* **2009**, *131*, 18198−18199.
(39) Mason, J. A.; Sumida, K.; Herm, Z. R.; Krishna, R.; Long, J. R. *Energy Environ. Sci.* **2011**, *3*, 3030−3040.
(40) Herm, Z. R.; Krishna, R.; Long, J. R. *Microporous Mesoporous Mater.* **2012**, *151*, 481−487.
(41) Bao, Z.; Yu, L.; Ren, Q.; Lu, X.; Deng, S. *J. Colloid Interface Sci.* **2011**, *353*, 549−556.
(42) Krishna, R.; Baur, R. *Sep. Purif. Technol.* **2003**, *33*, 213−254.
(43) Kong, X.; Scott, E.; Ding, W.; Mason, J. A.; Long, J. R.; Reimer, J. A. *J. Am. Chem. Soc.* **2012**, *134*, 14341−14344.
(44) Lee, D. J.; Li, Q.; Kim, H.; Lee, K. *Microporous Mesoporous Mater.* **2012**, *163*, 169−177.
(45) Krishna, R.; Li, S.; van Baten, J. M.; Falconer, J. L.; Noble, R. D. *Sep. Purif. Technol.* **2008**, *60*, 230−236.
(46) Sun, M. S.; Talu, O.; Shah, D. B. *AIChE J.* **1996**, *42*, 3001−3007.
(47) Krishna, R.; van Baten, J. M. *J. Membr. Sci.* **2011**, *383*, 289−300.
(48) Krishna, R.; van Baten, J. M. *J. Membr. Sci.* **2011**, *377*, 249−260.
(49) Bux, H.; Liang, F.; Li, Y.; Cravillon, J.; Wiebcke, M.; Caro, J. *J. Am. Chem. Soc.* **2009**, *131*, 16000−16001.
(50) Krishna, R.; van Baten, J. M. *J. Membr. Sci.* **2011**, *367*, 204−210.
(51) Krishna, R.; van Baten, J. M. *Ind. Eng. Chem. Res.* **2011**, *50*, 7083−7087.
(52) Bux, H.; Chmelik, C.; Van Baten, J. M.; Krishna, R.; Caro, J. *Adv. Mater.* **2010**, *22*, 4741−4743.
(53) Krishna, R.; van Baten, J. M. *Chem. Eng. Sci.* **2008**, *63*, 3120−3140.
(54) Krishna, R.; van Baten, J. M. *Microporous Mesoporous Mater.* **2009**, *125*, 126−134.
(55) van den Bergh, J.; Zhu, W.; Groen, J. C.; Kapteijn, F.; Moulijn, J. A.; Yajima, K.; Nakayama, K.; Tomita, T.; Yoshida, S. *Stud. Surf. Sci. Catal.* **2007**, *170*, 1021−1027.
(56) van den Bergh, J.; Tihaya, A.; Kapteijn, F. *Microporous Mesoporous Mater.* **2010**, *132*, 137−147.
(57) Dietzel, P. D. C.; Besikiotis, V.; Blom, R. *J. Mater. Chem.* **2009**, *19*, 7362−7370.

Supplementary Information (SI) to accompany:

Investigating the Relative Influences of Molecular Dimensions and Binding Energies on Diffusivities of Guest Species Inside Nanoporous Crystalline Materials

Rajamani Krishna* and Jasper M. van Baten

Van 't Hoff Institute for Molecular Sciences, University of Amsterdam, Science Park 904,

1098 XH Amsterdam, The Netherlands

*CORRESPONDING AUTHOR Tel +31 20 6270990; Fax: + 31 20 5255604;

email: r.krishna@uva.nl

Table of Contents

1. Force field for guest molecules

The force fields for He, Ne and Ar are taken from the paper by Skoulidas and Sholl[1].

The force field for Kr is from Talu and Myers [2].

The force field for H_2 corresponds to that given by Kumar et al.[3] In implementing this force field, quantum effects for H_2 have been ignored because the work of Kumar et al.[3] has shown that quantum effects are of negligible importance for temperatures above 200 K; all our simulations were performed at 300 K. The force field of Kumar et al.[3] is quite similar to that used by Gallo et al. [4].

For CO_2 and N_2 we use the 3LJ3CB.EPM2 and 2LJ3CB.MSKM potentials [5]. The Lennard-Jones parameters for CO_2 and N_2 are essentially those of Makrodimitris et al.[6]; see also García-Pérez et al.[7].

CH_4 molecules are described with a united atom model, in which each molecule is treated as a single interaction center [8].The interaction between adsorbed molecules is described with Lennard-Jones terms.

For simulations with linear alkanes with two or more C atoms, the beads in the chain are connected by harmonic bonding potentials. A harmonic cosine bending potential models the bond bending between three neighboring beads, a Ryckaert-Bellemans potential controls the torsion angle. The force fields of Dubbeldam et al.[9] was used for the variety of potentials.

The alkene force field corresponds to that of Ban et al. [10]

2. Force field for framework structures

All-silica zeolites

The force field for zeolite frameworks are taken from Dubbeldam et al.[9] The zeolite lattices are rigid during simulations, with static atomic charges that are assigned by choosing q_{Si} = +2.05 and q_O = -1.025, following the work of Calero et al.[11]

Zeolite structures with cations present

The following structures were investigated

NaX (106 Si, 86 Al, 86 Na^+, Si/Al=1.23),

NaY (138 Si, 54 Al, 54 Na^+, Si/Al=2.55),

The force field information for the simulations with cations are taken from García-Sanchez et al.[12]. In the MC simulations, the cations were allowed to move within the framework and both Lennard-Jones and Coulombic interactions are taken into consideration.

The cations were maintained in their preferred locations.

MOFs and ZIFs

The metal organic framework structures are considered to be rigid in the simulations.

For the atoms in the host metal organic framework, Lennard-Jones potentials along with the framework charges used are based on available literature sources.

In cases, where no literature data are available, the generic UFF [13] and DREIDING [14] force fields were used for the Lennard-Jones potential. For estimation of the framework charges we use the group-contribution procedure based on quantum mechanical calculations described in the papers by Xu and Zhong [15] and Zheng and Zhong [16].

For all MOFs, ZIFs, and COFs, the information on the force fields for the framework atoms is provided, per framework structure, in the Figures accompanying this document.

The Lorentz-Berthelot mixing rules were applied for calculating σ and ε/k_B for guest-host interactions.

Mesoporous BTP-COF

The crystallographic structural information for the covalent organic framework BTP-COF was obtained from the paper of Dogru et al.[17]. The original structure is monoclinic structure $\alpha = \beta = 90^o$,

$\gamma = 120^o$. For convenience in simulations this monoclinic structure was transformed to the orthogonal form for simulation purposes. The transformed orthogonal structure has twice the number of framework atoms. The unit cell dimensions of the transformed orthogonal structure are a = 43.65 Å; b = 75.604 Å; c = 3.52 Å, with angles $\alpha = \beta = \gamma = 90^o$. The paper by Dogru et al.[17] quotes the pore diameter as being 4 nm; this is a "nominal" value. We determined the actual pore diameter following the method of Delaunay triangulation, described in the work by Foster et al.[18] The value obtained is 3.4 nm, and this represents maximum hard-sphere diameter that can pass through the 1D channels; this value was used in the calculations for the Knudsen diffusivity. All simulations were performed with 1×1×7 unit cells.

For estimation of the framework charges we use the group-contribution procedure based on quantum mechanical calculations described in the papers by Xu and Zhong [15] and Zheng and Zhong [16].

The details of the force fields used for the BTP-COF framework are given in our earlier publication [19]. The information on the force fields is also provided in the accompanying Figure for this structure.

Mesoporous cylindrical silica pores

Cylindrical silica pores of 20 Å, and 30 Åpore sizes were prepared using a method based on Coasne et al.[20]. An initial β-cristobalite (unit cell of 8 Si and 16 O atoms, at glass density of 2200 kg/m^3, with a box size of 7.132 Å) structure was considered. The total number of β-cristobalite unit cells in the complete box was determined by a minimum of 24 Å in the z-direction, and a minimum of 24 Å plus target pore diameter in the remaining two directions. A cylindrical cavity was cut out of the initial geometry. Subsequently, all Si atoms that was not bound to 4 O atoms were removed. Any non-bound O atoms were removed after that. This causes singly bound O atoms to remain in the structure. Half of these need to be removed to ensure electro-neutrality of the system. Pairs of singly-bound O-atoms were detected for which the O-O distance is less than 2.7 Å. These combinations where replaced by a single O atom to form a Siloxane bridge. The single O atom was placed at the geometric mean location of the two removed O atoms. Half of the remaining singly bound O atoms were removed at random, introducing one bond defect per O atom. Of the remaining structure, all atoms were displaced on a

random sphere with 0.7 Å radius to form the amorphous structure. The structure data files we used in our simulations are available on our website [21].

The interaction between the guest molecules and the silica surface is assumed to be dominated by interactions between guest molecules and the O atoms in the silica. The force field for the guest-host interactions are those used in our earlier works [22, 23].

3. Determination of pore volume

The pore volume is determined using a simulation of a single helium molecule at the reference temperature T [24-26]

$$V_p = \frac{1}{m}\int_0^{V_{pore}} \exp\left(-\frac{U(\mathbf{r})}{k_B T}\right) d\mathbf{r} \qquad (1)$$

where U is the interaction energy between a single helium atom and the framework, and m is the mass of the framework. The pore volume can be readily computed from Monte Carlo sampling using Widom particle insertion [27]. Basically, the average Boltzmann factor associated with the random insertion of a probe molecule is computed. This value is averaged over all generated trial positions. In equation (1) the integration is over the entire volume of the sample and yields the value of the accessible pore volume per unit mass of the framework; the units of V_p are m^3/kg, or in more commonly used units mL/(g framework). The volume fraction, ϕ, is then given by V_p/V_{total} where V_{total} is the total volume of the unit cell. Usually, a reference temperature of 298.15 K is chosen for the experimental determination of the helium void volume; this value is also used in the simulations.

The force field for He-He interactions are taken from Table 1 of Talu and Myers [28]; these are listed also in Table 1. For zeolites the He-O interaction parameters were also taken from their Table 1. For determination of the pore volume fraction we have switched to the Talu and Myers force field parameters that has been tuned to represent experimental data on pore volumes in MFI.

For MOFs, the interaction between He and the atoms of the MOF structures were then determined using the Lorentz-Berthelot mixing rules.

For determination of the accessible pore volumes of FAU, NaX, NaY, TSC, ITQ-29, and LTA the sodalite cages were blocked and no He probe atoms could enter these cages. Only the supercage volumes are determined for these structures. For DDR, NaRhoZMOF, CHA, AWW, CuBTT, the appropriate blocking strategy was used for the inaccessible pockets.

4. Determination of pore surface area

The surface area of various structures were determined using the method described by Düren et al.[29].

5. Characteristic diameter using Delaunay triangulation

In many cases, the characteristic size of the channels or windows of microporous structures were determined following the method of Delaunay triangulation, described in the work by Foster et al.[18] These values represent the maximum hard-sphere diameter that can pass through the structure. The values quoted are obtained by subtracting the Lennard-Jones sigma parameter of the framework atom.

6. Surface area vs pore dimension

Additionally, the accompanying Figures present plots of surface area vs pore dimensions, using a combination of the procedures of Düren et al.[29], and the Delaunay triangulation described in the work by Foster et al.[18]. The methodology used for this purpose is described in detail in the attached document entitled *Characterization of Ordered Nanoporous Crystalline Materials by Determination of the Surface Areas as a function of the corresponding Pore Dimensions*.

7. CBMC simulation methodology

The Lennard-Jones potentials are shifted and cut at 12 Å.

The number of unit cells in the simulation box was chosen such that the minimum length in each of the coordinate directions was larger than 24 Å. Periodic boundary conditions were employed. Further CBMC simulation details are available in earlier publications [9, 11, 30, 31].

The CBMC simulations were performed using the BIGMAC code developed by T.J.H. Vlugt[32] as basis. The code was modified to handle rigid molecular structures and charges.

8. Heat of adsorption

We determined the isosteric heats of adsorption, ΔQ_{st}, from CBMC simulations using the fluctuation formula

$$Q_{st} = RT - \frac{< U_i n_i > - < U_i >< n_i >}{\left\langle n_i^2 \right\rangle - \left\langle n_i \right\rangle^2} \qquad (2)$$

where n_i represents the number of molecules in the simulation box and $\langle \ldots \rangle$ denotes ensemble averaging.

9. MD simulation methodology

Diffusion is simulated using Newton's equations of motion until the system properties, on average, no longer change in time. The Verlet algorithm is used for time integration. A time step of 1 fs was used in all simulations. For each simulation, *initializing* CBMC moves are used to place the molecules in the domain, minimizing the energy. Next, follows an *equilibration* stage. These are essentially the same as the production cycles, only the statistics are not yet taken into account. This removes any initial large disturbances in the system that do not affect statistics on molecular displacements. After a fixed number of initialization and equilibrium steps, the MD simulation *production* cycles start. For every cycle, the statistics for determining the mean square displacements (MSDs) are updated. The MSDs are determined for time intervals ranging from 2 fs to 1 ns. In order to do this, an order-*N* algorithm, as detailed in Chapter 4 of Frenkel and Smit[27] is implemented. The Nosé-Hoover thermostat is applied to all the diffusing particles.

The DLPOLY code[33] was used along with the force field implementation as described in the previous section. DL_POLY is a molecular dynamics simulation package written by W. Smith, T.R.

Forester and I.T. Todorov and has been obtained from CCLRCs Daresbury Laboratory via the website.[33]

The MD simulations were carried out for a variety of loadings within the various structures. All simulations were carried out on the LISA clusters of PCs equipped with Intel Xeon processors running at 3.4 GHz on the Linux operating system[34]. Each MD simulation, for a specified loading, was run for 120 h, determined to be long enough to obtain reliable statistics for determination of the diffusivities. In several cases the campaigns were replicated and the results averaged.

The self-diffusivities $D_{\mathrm{i,self}}$ for each species in binary mixtures are computed from MD simulations by analyzing the mean square displacement of each species i for each coordinate direction

$$D_{i,self} = \frac{1}{2n_i} \lim_{\Delta t \to \infty} \frac{1}{\Delta t} \left\langle \left(\sum_{l=1}^{n_i} \left(\mathbf{r}_{l,i}(t+\Delta t) - \mathbf{r}_{l,i}(t) \right)^2 \right) \right\rangle \tag{3}$$

For three-dimensional pore networks (e.g. MFI, FAU-Si, NaX, NaY, LTA, CHA, IRMOF-1, CuBTC, ZIF-8, MOF-177) the arithmetic average of the diffusivities in the three coordinate directions were used in further analysis and reported in the Figures accompanying this Supplementary material. For one-dimensional pore structures (e.g. AFI, MOR, FER, MIL-47, MIL-53(Cr), MgMOF-74, ZnMOF-74) the diffusivities along the direction of diffusion are reported and analyzed. For DDR the reported diffusivities are the averages in x- and y- directions.

The pure component $Đ_{\mathrm{i}}$ is obtained from MD simulations of molecular displacements using the formula in each of the coordinate direction

$$Đ_i = \frac{1}{2} \lim_{\Delta t \to \infty} \frac{1}{n_i} \frac{1}{\Delta t} \left\langle \left(\sum_{l=1}^{n_i} \left(\mathbf{r}_{l,i}(t+\Delta t) - \mathbf{r}_{l,i}(t) \right) \right)^2 \right\rangle \tag{4}$$

10. Acknowledgements

We are grateful to T.J.H. Vlugt, Delft, for providing the BIGMAC code. This code was modified to handle rigid molecular structures and charges, with generous assistance and technical inputs from S. Calero, Seville.

The calculation of the accessible pore volume using the Widom insertion of He probe atoms is implemented within the BIGMAC code.

11. Notation

c_i	pore concentration of species i, $c_i = q_i / V_p$, mol m^{-3}
d_p	pore diameter, m
D_i	Fick diffusivity of species i, m^2 s^{-1}
$D_{i,self}$	self-diffusivity of species i, m^2 s^{-1}
$Đ_i$	Maxwell-Stefan diffusivity, m^2 s^{-1}
$Đ_{ii}$	self-exchange coefficient, m^2 s^{-1}
$Đ_i(0)$	zero-loading M-S diffusivity, m^2 s^{-1}
$D_{i,Kn}$	Knudsen diffusivity of species i, m^2 s^{-1}
E_A	activation energy for diffusion, J mol^{-1}
f_i	partial fugacity of species i, Pa
k_B	Boltzmann constant, 1.38×10^{-23} J molecule^{-1} K^{-1}
M_i	molar mass of species i, kg mol^{-1}
N_i	molar flux of species i, mol m^{-2} s^{-1}
n_i	number of molecules of species i in simulation box, dimensionless
p_i	partial pressure of species i, Pa
p_t	total system pressure, Pa
q_i	molar loading species i, mol kg^{-1}
$-Q_{st}$	isosteric heat of adsorption, J mol^{-1}
r	radial distance coordinate, m
r_c	radius of crystallite, m
R	gas constant, 8.314 J mol^{-1} K^{-1}
S_{ads}	adsorption selectivity, $S_{ads} = \frac{c_1/c_2}{f_1/f_2}$, dimensionless
S_{diff}	diffusion selectivity, $S_{diff} = \frac{D_{1,self}}{D_{2,self}}$, dimensionless

S_{perm}	permeation selectivity, $S_{perm} = \dfrac{N_1/N_2}{f_1/f_2}$, dimensionless
t	time, s
T	temperature, K
u	characteristic velocity for motion of molecules, m s^{-1}
V_p	accessible pore volume, m^3 kg^{-1}
z	distance coordinate, m

Greek letters

δ	thickness of membrane, m
ε	Lennard-Jones interaction energy parameter, J $molecule^{-1}$
Γ_i	thermodynamic factor, dimensionless
λ	molecular jump distance, m
Π_i	membrane permeance of species *i*, mol m^{-2} s^{-1} Pa^{-1}
ρ	framework density, kg m^{-3}
σ	Lennard-Jones size parameter, m

Subscripts

i	referring to component *i*
t	referring

12. References

[1] A.I. Skoulidas, D.S. Sholl, Transport diffusivities of CH_4, CF_4, He, Ne, Ar, Xe, and SF_6 in silicalite from atomistic simulations, J. Phys. Chem. B 106 (2002) 5058-5067.

[2] O. Talu, A.L. Myers, Reference potentials for adsorption of helium, argon, methane and krypton in high-silica zeolites, Colloids Surf., A 187-188 (2001) 83-93.

[3] A.V.A. Kumar, H. Jobic, S.K. Bhatia, Quantum effects on adsorption and diffusion of hydrogen and deuterium in microporous materials J. Phys. Chem. B 110 (2006) 16666-16671.

[4] M. Gallo, T.M. Nenoff, M.C. Mitchell, Selectivities for binary mixtures of hydrogen/methane and hydrogen/carbon dioxide in silicalite and ETS-10 by Grand Canonical Monte Carlo techniques, Fluid Phase Equilib. 247 (2006) 135-142.

[5] J.G. Harris, K.H. Yung, Carbon Dioxide's Liquid-Vapor Coexistence Curve And Critical Properties as Predicted by a Simple Molecular Model, J. Phys. Chem. 99 (1995) 12021-12024.

[6] K. Makrodimitris, G.K. Papadopoulos, D.N. Theodorou, Prediction of permeation properties of CO_2 and N_2 through silicalite via molecular simulations, J. Phys. Chem. B 105 (2001) 777-788.

[7] E. García-Pérez, J.B. Parra, C.O. Ania, A. García-Sánchez, J.M. Van Baten, R. Krishna, D. Dubbeldam, S. Calero, A computational study of CO_2, N_2 and CH_4 adsorption in zeolites, Adsorption 13 (2007) 469-476.

[8] J.P. Ryckaert, A. Bellemans, Molecular dynamics of liquid alkanes, Faraday Discuss. Chem. Soc. 66 (1978) 95-106.

[9] D. Dubbeldam, S. Calero, T.J.H. Vlugt, R. Krishna, T.L.M. Maesen, B. Smit, United Atom Forcefield for Alkanes in Nanoporous Materials, J. Phys. Chem. B 108 (2004) 12301-12313.

[10] S. Ban, A. van Laak, P.E. de Jongh, J.P.J.M. van der Eerden, T.J.H. Vlugt, Adsorption Selectivity of Benzene and Propene Mixtures for Various Zeolites, J. Phys. Chem. C 111 (2007) 17241-17248.

[11] S. Calero, D. Dubbeldam, R. Krishna, B. Smit, T.J.H. Vlugt, J.F.M. Denayer, J.A. Martens, T.L.M. Maesen, Understanding the role of sodium during adsorption. A force field for alkanes in sodium exchanged faujasites, J. Am. Chem. Soc. 126 (2004) 11377-11386.

[12] A. García-Sánchez, C.O. Ania, J.B. Parra, D. Dubbeldam, T.J.H. Vlugt, R. Krishna, S. Calero, Development of a Transferable Force Field for Carbon Dioxide Adsorption in Zeolites, J. Phys. Chem. C 113 (2009) 8814-8820.

[13] A.K. Rappé, C.J. Casewit, K.S. Colwel, W.A. Goddard, W.M. Skiff, UFF, a Full Periodic Table Force Field for Molecular Mechanics and Molecular Dynamics Simulations, J. Am. Chem. Soc. 114 (1992) 10024-10035.

[14] S.L. Mayo, B.D. Olafson, W.A. Goddard, DREIDING: A Generic Force Field for Molecular Simulations, J. Phys. Chem. 94 (1990) 8897-8909.

[15] Q. Xu, C. Zhong, A General Approach for Estimating Framework Charges in Metal-Organic Frameworks, J. Phys. Chem. C 114 (2010) 5035-5042.

[16] C. Zheng, C. Zhong, Estimation of Framework Charges in Covalent Organic Frameworks Using Connectivity-Based Atom Contribution Method, J. Phys. Chem. C 114 (2010) 9945-9951.

[17] M. Dogru, A. Sonnauer, A. Gavryushin, P. Knochel, T. Bein, A Covalent Organic Framework with 4 nm open pores, Chem. Commun. 47 (2011) 1707-1709.

[18] M.D. Foster, I. Rivin, M.M.J. Treacy, O.D. Friedrichs, A geometric solution to the largest-free-sphere problem in zeolite frameworks, Microporous Mesoporous Mater. 90 (2006) 32-38.

[19] R. Krishna, J.M. van Baten, Investigating the validity of the Knudsen prescription for diffusivities in a mesoporous covalent organic framework, Ind. Eng. Chem. Res. 50 (2011) 7083-7087.

[20] B. Coasne, F. Di Renzo, A. Galarneau, R.J.M. Pellenq, Adsorption of Simple Fluid on Silica Surface and Nanopore: Effect of Surface Chemistry and Pore Shape, Langmuir 24 (2008) 7285-7293.
[21] J.M. van Baten, R. Krishna, MD animations of diffusion in nanoporous materials, University of Amsterdam, Amsterdam, http://www.science.uva.nl/research/cr/animateMD/, 7 April 2009.
[22] R. Krishna, J.M. van Baten, An investigation of the characteristics of Maxwell-Stefan diffusivities of binary mixtures in silica nanopores, Chem. Eng. Sci. 64 (2009) 870-882.
[23] R. Krishna, J.M. van Baten, Unified Maxwell-Stefan description of binary mixture diffusion in micro- and meso- porous materials, Chem. Eng. Sci. 64 (2009) 3159-3178.
[24] A.L. Myers, P.A. Monson, Adsorption in Porous Materials at High Pressure: Theory and Experiment, Langmuir 18 (2002) 10261-10273.
[25] R. Babarao, Z. Hu, J. Jiang, S. Chempath, S.I. Sandler, Storage and separation of CO_2 and CH_4 in silicalite, C_{168} schwarzite, and IRMOF-1: A comparative study from Monte Carlo simulation, Langmuir 23 (2007) 659-666.
[26] R. Babarao, J. Jiang, Exceptionally high CO_2 storage in covalent-organic frameworks: Atomistic simulation study, Energy Environ. Sci. 1 (2008) 139-143.
[27] D. Frenkel, B. Smit, Understanding molecular simulations: from algorithms to applications, Academic Press, 2nd Edition, San Diego, 2002.
[28] O. Talu, A.L. Myers, Molecular Simulation of Adsorption: Gibbs Dividing Surface and Comparison with Experiment, A.I.Ch.E.J. 47 (2001) 1160-1168.
[29] T. Düren, F. Millange, G. Férey, K.S. Walton, R.Q. Snurr, Calculating Geometric Surface Areas as a Characterization Tool for Metal-Organic Frameworkss, J. Phys. Chem. C 111 (2007) 15350-15356.
[30] T.J.H. Vlugt, R. Krishna, B. Smit, Molecular simulations of adsorption isotherms for linear and branched alkanes and their mixtures in silicalite, J. Phys. Chem. B 103 (1999) 1102-1118.
[31] D. Dubbeldam, R. Krishna, S. Calero, A.Ö. Yazaydın, Computer-Assisted Screening of Ordered Crystalline Nanoporous Adsorbents for Separation of Alkane Isomers, Angew. Chem. Int. Ed. XXX (2012) XXX-XXX. (http://dx.doi.org/doi:10.1002/anie.201205040)
[32] T.J.H. Vlugt, BIGMAC, University of Amsterdam, http://molsim.chem.uva.nl/bigmac/, 1 November 2000.
[33] W. Smith, T.R. Forester, I.T. Todorov, The DL_POLY Molecular Simulation Package, Warrington, England, http://www.cse.clrc.ac.uk/msi/software/DL_POLY/index.shtml, March 2006.
[34] SARA, Computing & Networking Services, Amsterdam, https://subtrac.sara.nl/userdoc/wiki/lisa/description, 16 January 2008.
[35] E. García-Pérez, D. Dubbeldam, T.L.M. Maesen, S. Calero, Influence of cation Na/Ca ratio on adsorption in LTA 5A: A systematic molecular simulations study of alkane chain length, J. Phys. Chem. B 110 (2006) 23968-23976.
[36] A. García-Sánchez, E. García-Pérez, D. Dubbeldam, R. Krishna, S. Calero, A Simulation Study of Alkanes in Linde Type A Zeolites, Adsorpt. Sci. Technol. 25 (2007) 417-427.

Table 1. Lennard-Jones parameters used to determine the pore volume in zeolites in which cations are present. The Na^+ - Na^+ parameters are from Calero et al. [11, 35, 36]. The He-He parameters are from Table 1 of the paper.by Talu and Myers [28]. The interaction parameters for interaction of He with the O atoms of zeolite frameworks is from Table 1 of Talu and Myers [28]

(pseudo-) atom	**Atom-atom** σ **/ Å**	**Atom-atom** ε/k_B **/ K**
He - He	2.64	10.9
He - Na^+	2.4	36.8
He - O	2.952	28
Na^+ - Na^+	2.16	124.4

13. Listing of Sequence of Figures with Simulation results, along with experimental data, for each structure

The structural details, pore landscapes, Surface area vs pore size distributions, CBMC and MD simulation results are presented in the accompanying Figures in the following order: The arrangement of the information is according to the pore topologies, zeolites followed by MOFs. Note that for some materials only structural data is provided, no diffusivity data.

Cage-type structures with narrow windows

CHA

SAPO-34 experimental data on membrane permeation

DDR

ERI

ITQ-29

LTA-Si (all-silica)

SOD

TSC

ZIF-8: CBMC and MD data along

ZIF-8 membrane experimental data and analysis

1D meso-porous channels

BTP-COF

20 Å cylindrical pore

30 Å cylindrical pore

1D micro-porous channels

AFI

MTW

TON

MgMOF-74

ZnMOF-74

NiMOF-74

FeMOF-74

MIL-47

MIL-53(Cr)-lp

1D micro-porous channels with side pockets

FER

MOR

“Open” structures with large cavities

FAU-Si

NaY

NaX

FAU-Si vs NaY vs NaX

CuBTC

IRMOF-1

MOF-177

Intersecting channels

BEA

BOG

ISV

MFI

Zn(bdc)dabco

14. Figures, a total of 161

15. Characterization of Ordered Nanoporous Crystalline Materials by Determination of the Surface Areas as a function of the corresponding Pore Dimensions

Cage-type structures with narrow windows

CHA landscape

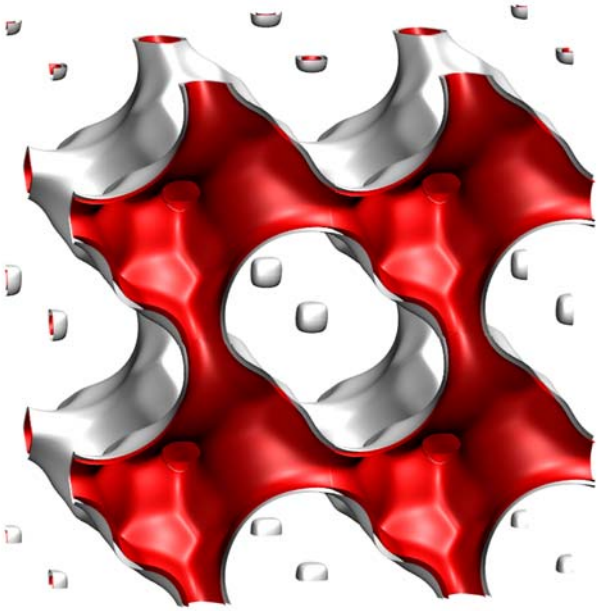

There are 6 cages per unit cell. The volume of one CHA cage is 316.4 Å^3, slightly larger than that of a single cage of DDR (278 Å^3), but significantly lower than FAU (786 Å^3).

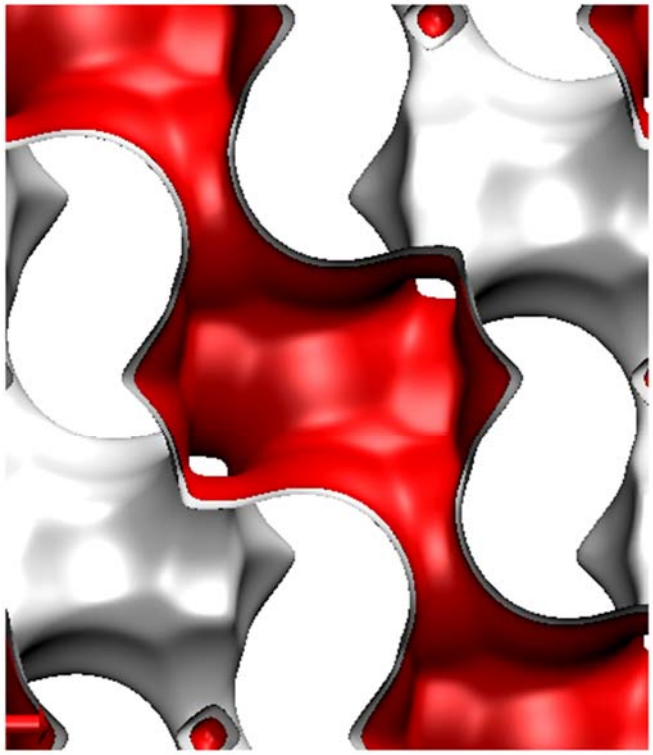

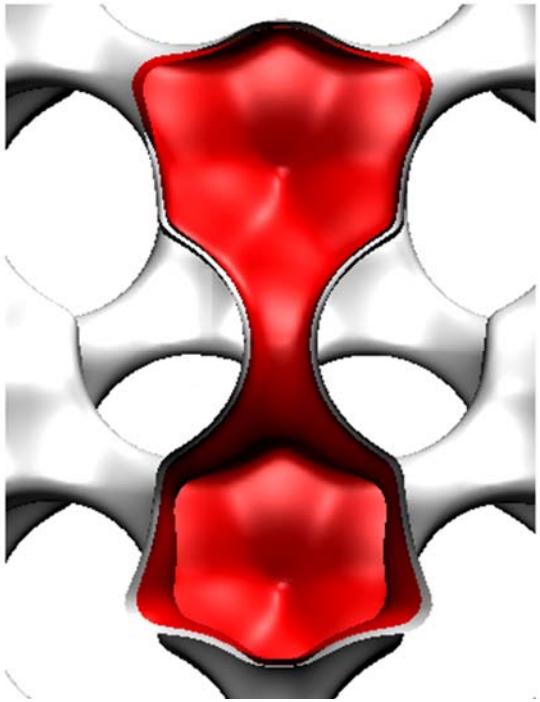

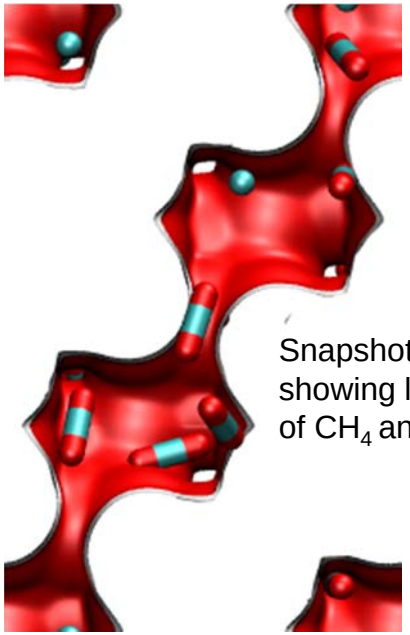

Snapshots showing location of CH_4 and CO_2

Snapshots showing location of CH_4

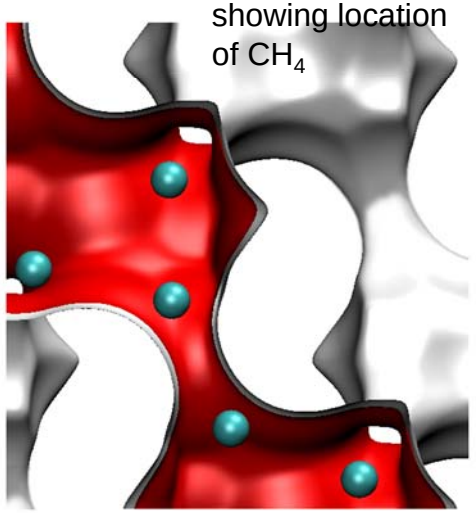

Structural information from: C. Baerlocher, L.B. McCusker, Database of Zeolite Structures, International Zeolite Association, http://www.iza-structure.org/databases/

CHA window and pore dimensions

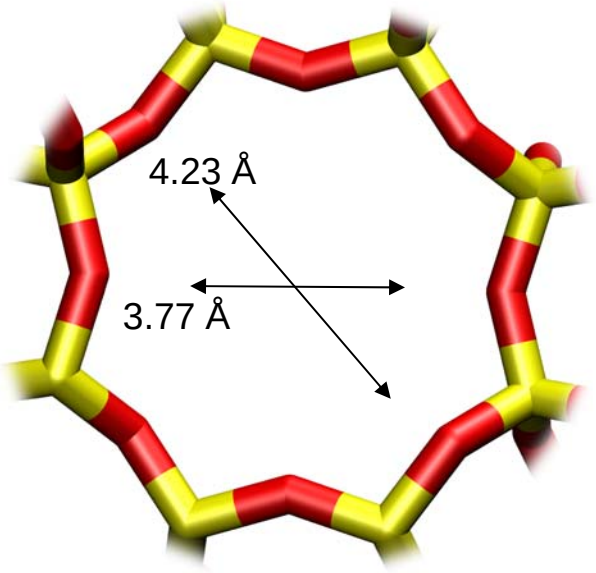

CHA

The window dimensions calculated using the van der Waals diameter of framework atoms = 2.7 Å are indicated above by the arrows.

This plot of surface area versus pore dimension is determined using a combination of the DeLaunay triangulation method for pore dimension determination, and the procedure of Düren for determination of the surface area.

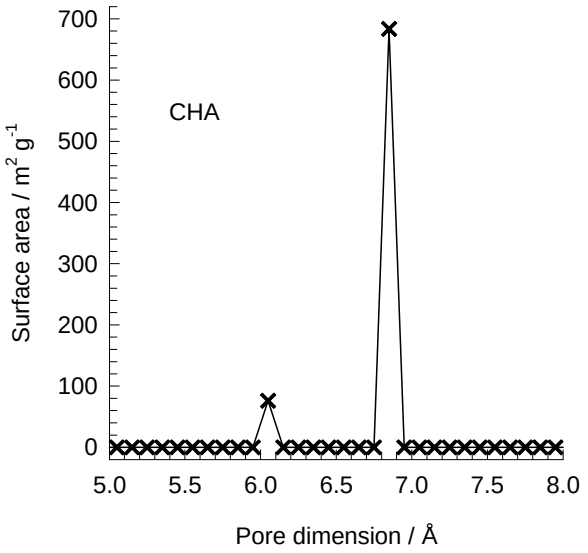

	CHA
a /Å	15.075
b /Å	23.907
c /Å	13.803
Cell volume / Å^3	4974.574
conversion factor for [molec/uc] to [mol per kg Framework]	0.2312
conversion factor for [molec/uc] to [kmol/m^3]	0.8747
ρ [kg/m3]	1444.1
MW unit cell [g/mol(framework)]	4326.106
ϕ, fractional pore volume	0.382
open space / Å^3/uc	1898.4
Pore volume / cm^3/g	0.264
Surface area /m^2/g	758.0
DeLaunay diameter /Å	3.77

CHA CBMC simulations of isotherms, and isosteric heats of adsorption

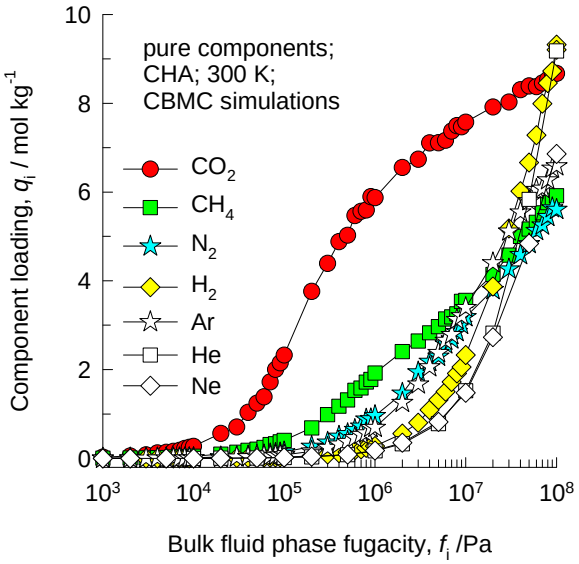

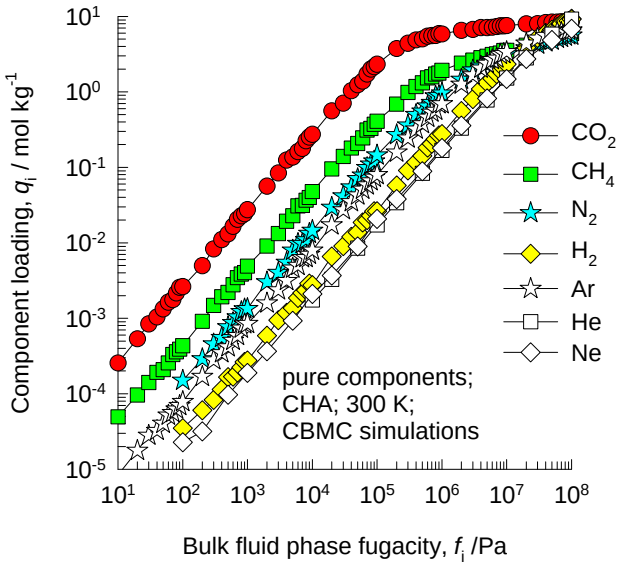

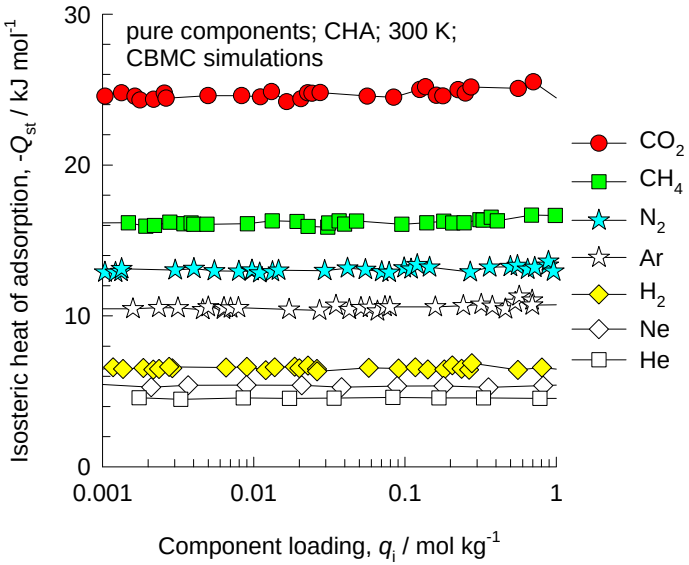

CHA MD simulations of unary self- , and M-S diffusivities

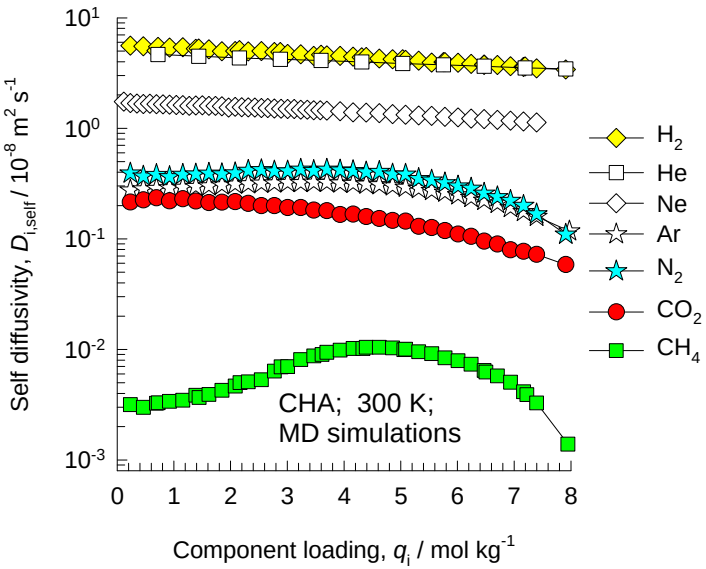

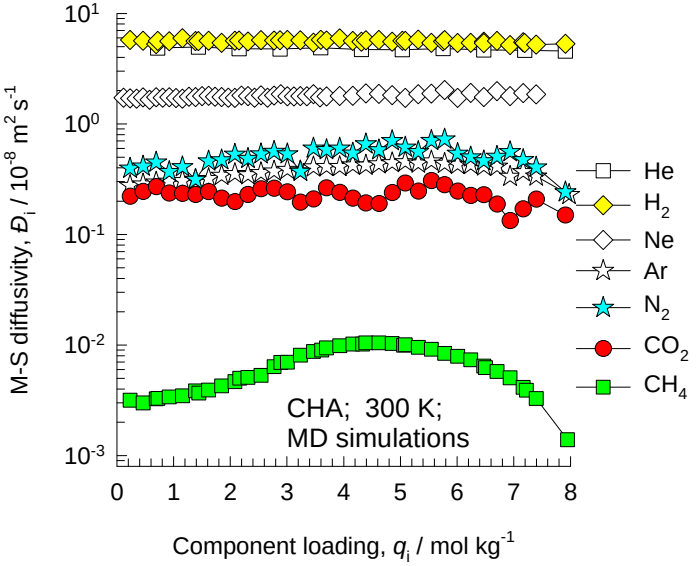

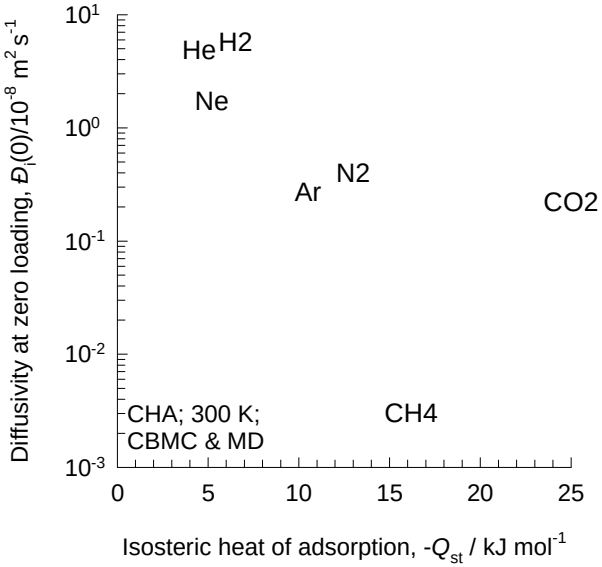

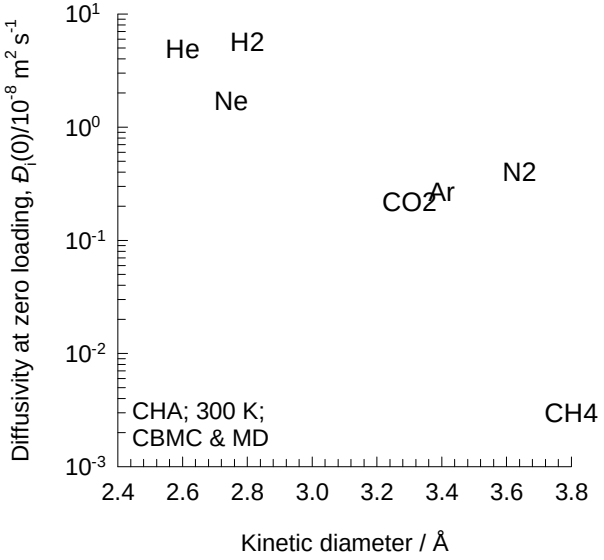

CHA pure component isotherms; comparison with experiments

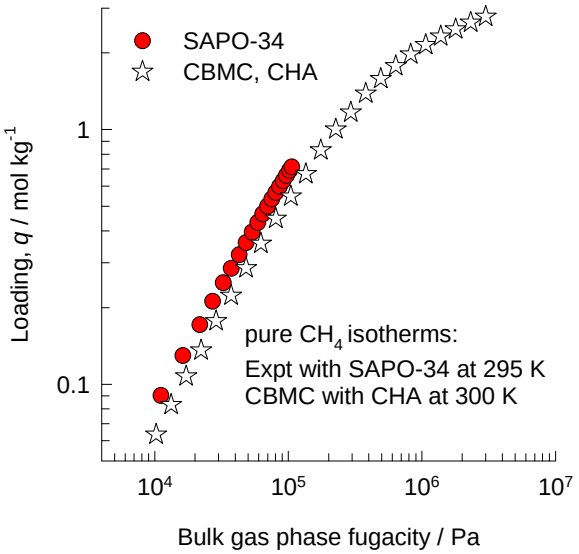

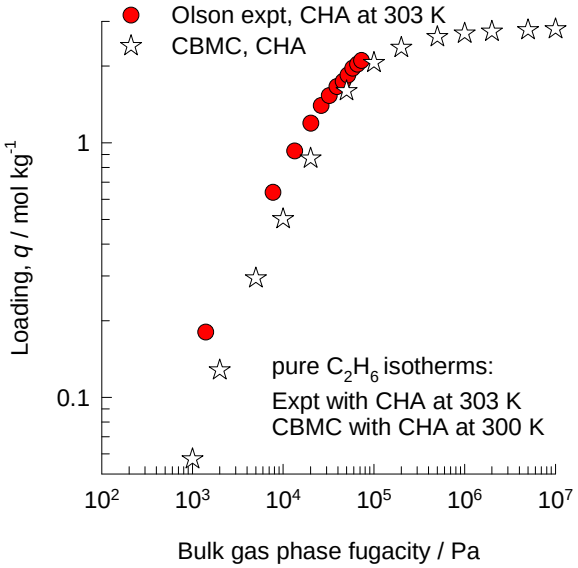

The experimental data for SAPO-34 are from the following sources:

Li, S.; Martinek, J. G.; Falconer, J. L.; Noble, R. D.; Gardner, T. Q., High-Pressure CO2/CH4 separation using SAPO-34 membranes, Ind. Eng. Chem. Res. 2005, 44, 3220-3228.

Li, S.; Falconer, J. L.; Noble, R. D., SAPO-34 membranes for CO2/CH4 separation, J. Membr. Sci. 2004, 241, 121-135.

The experimental data for CHA are from:

D.H. Olson, M.A. Camblor, L.A. Vallaescusa, G.H. Kuehl, Light hydrocarbon sorption properties of pure silica Si-CHA and ITQ-3 and high silica ZSM-58, Microporous Mesoporous Mater. 67 (2004) 27-33.

SAPO-34 transport coefficients, backed out from unary membrane permeation experiments

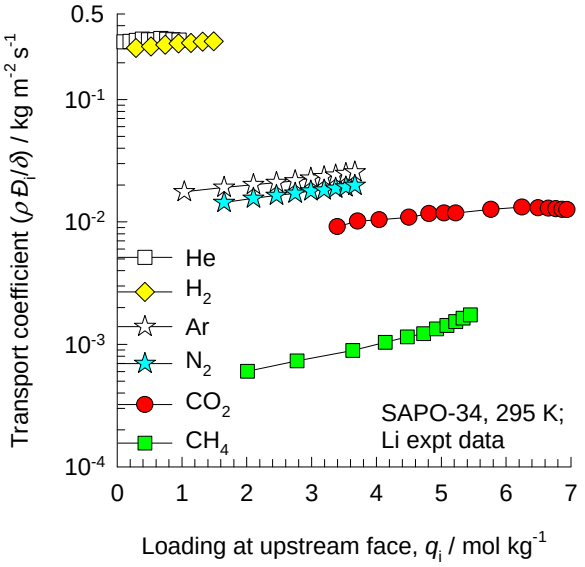

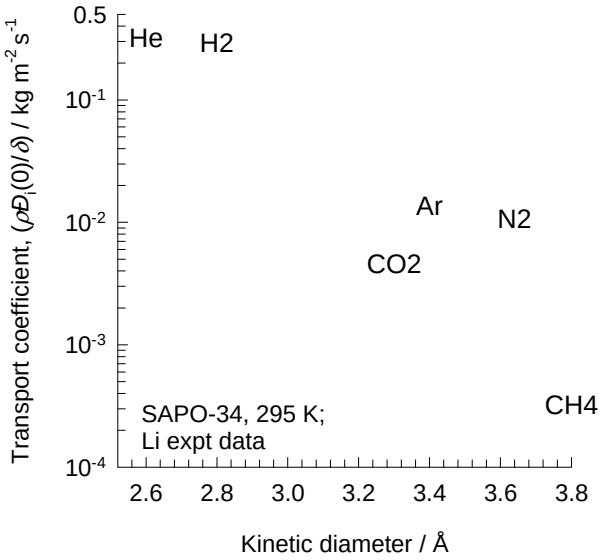

The data are re-plotted using the information provided in:
S. Li, J.L. Falconer, R.D. Noble, R. Krishna, Interpreting unary, binary and ternary mixture permeation across a SAPO-34 membrane with loading-dependent Maxwell-Stefan diffusivities, J. Phys. Chem. C 111 (2007) 5075-5082.

DDR landscape

There are 12 cages per unit cell. The volume of one DDR cage is 278 Å^3, significantly smaller than that of a single cage of FAU (786 Å^3), or ZIF-8 (1168 Å^3).

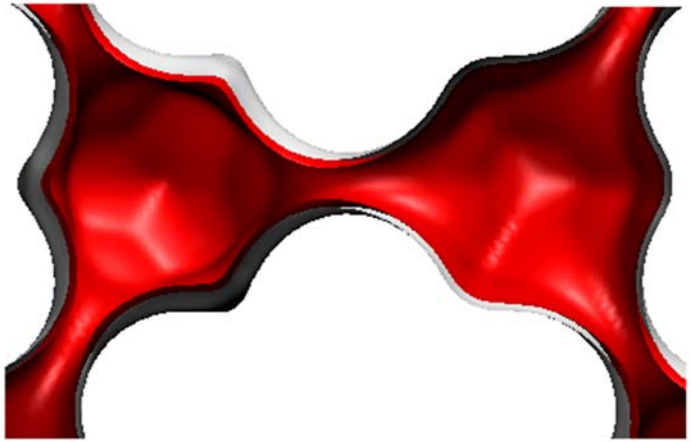

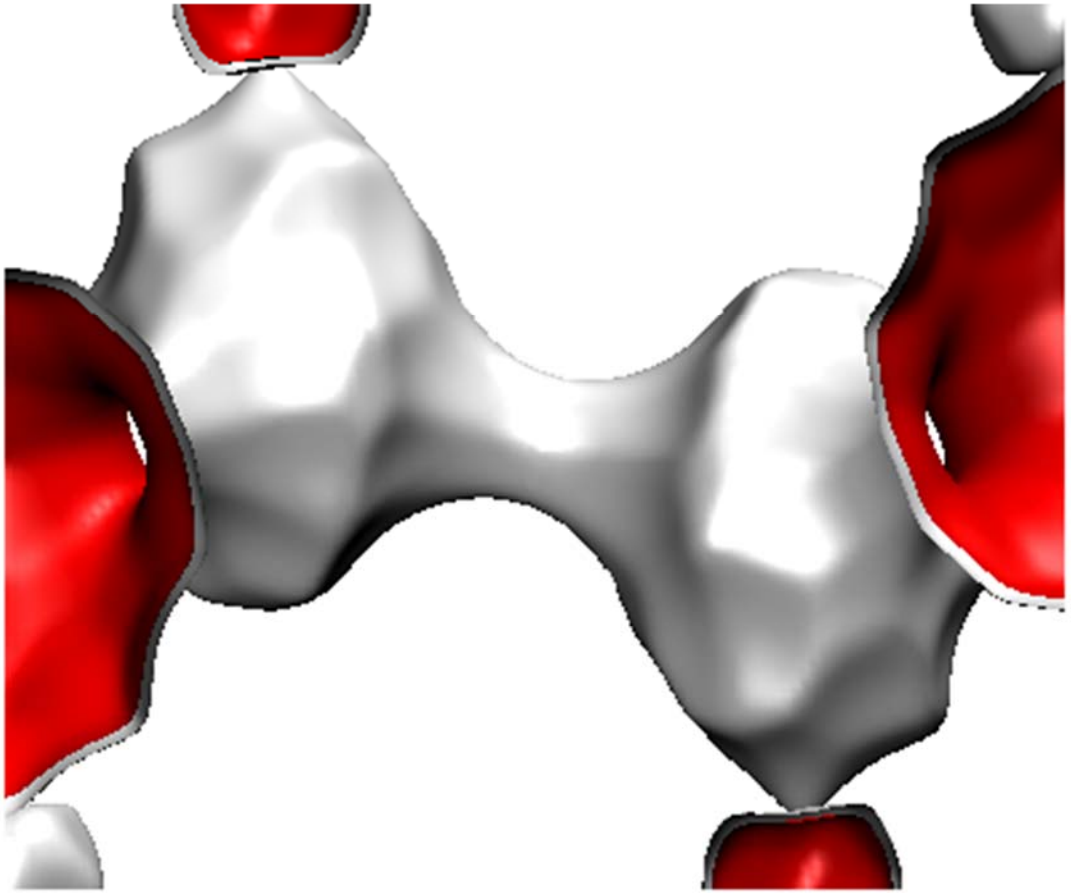

Structural information from: C. Baerlocher, L.B. McCusker, Database of Zeolite Structures, International Zeolite Association, http://www.iza-structure.org/databases/

To convert from molecules per unit cell to mol kg^{-1}, multiply by 0.06936.
The pore volume is 0.182 cm^3/g.

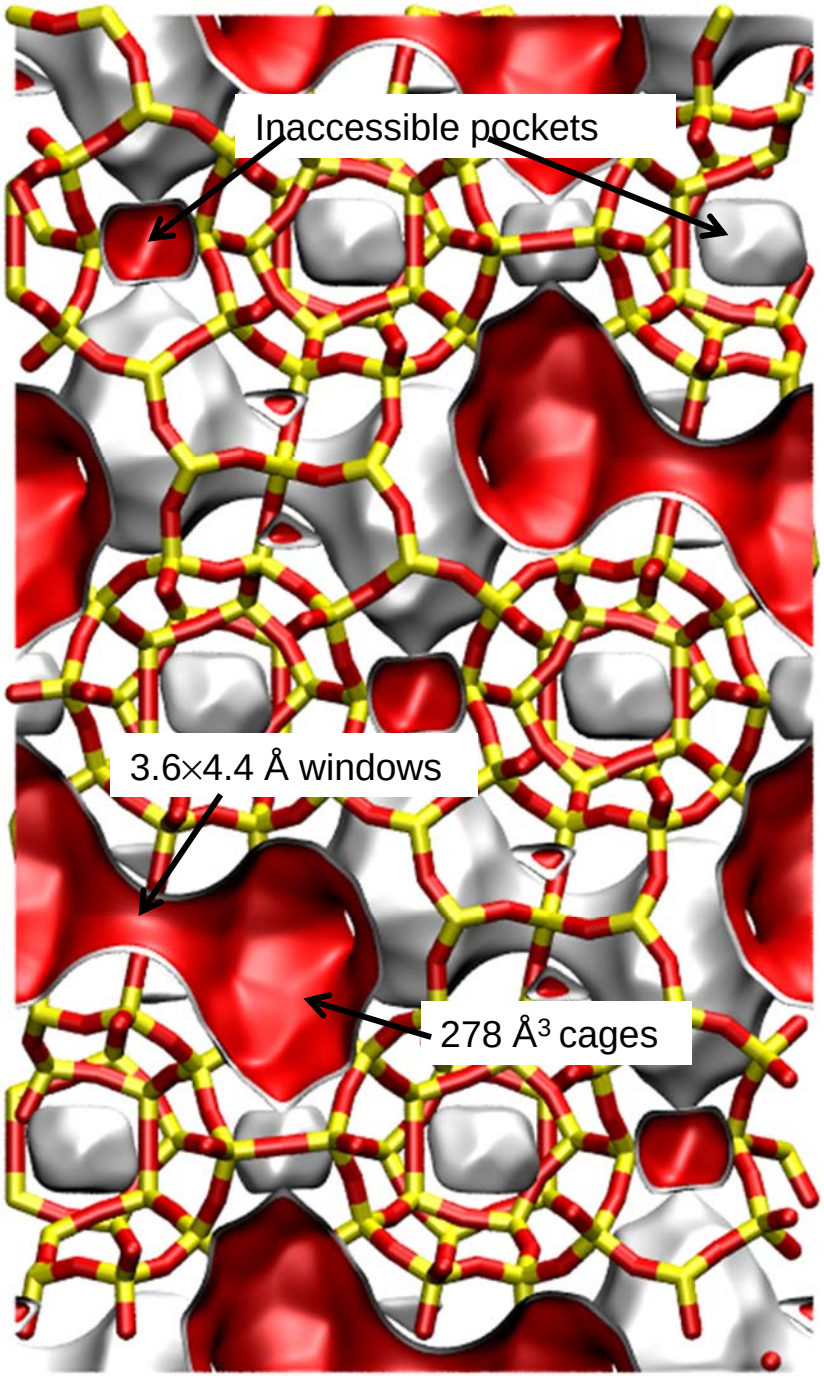

DDR landscapes without blocking

In all our simulations the inaccessible pockets of DDR were blocked. This aspect is explained in our paper
R. Krishna and J.M. van Baten, Comment on Comparative Molecular Simulation Study of CO2/N2 and CH4/N2 Separation in Zeolites and Metal-Organic Frameworks, Langmuir, 26 (2010) 2975-2978

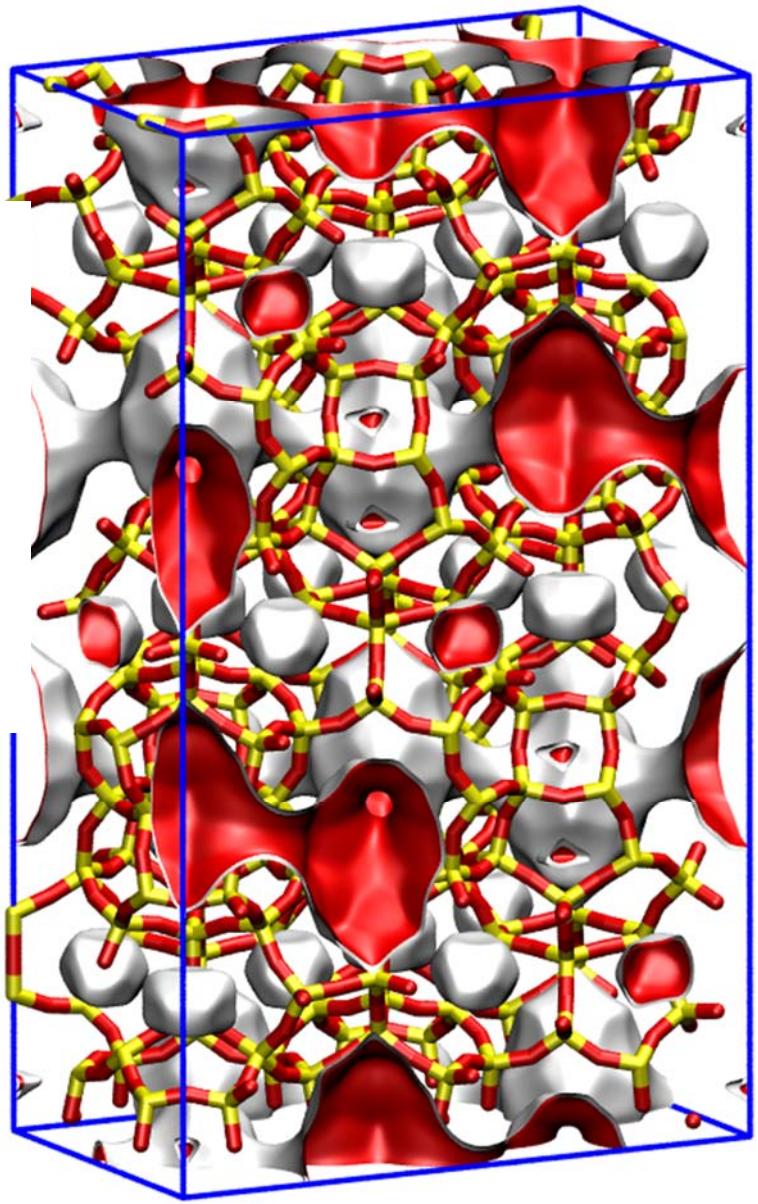

DDR window and pore dimensions

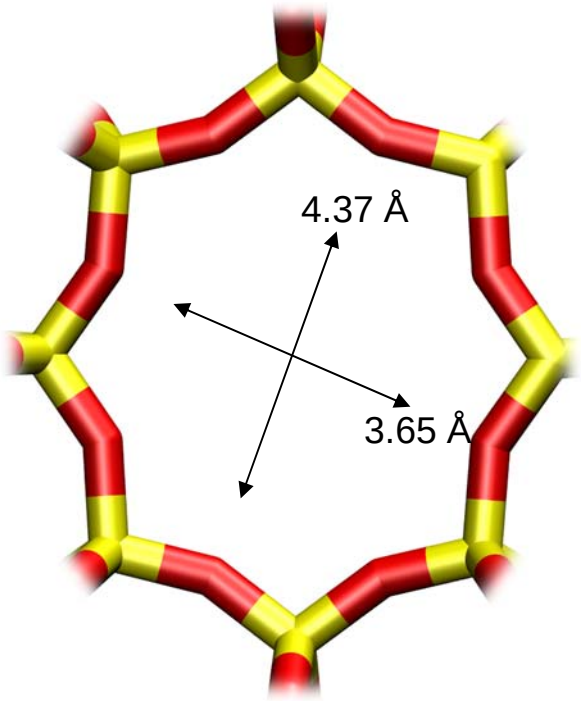

DDR

The window dimensions calculated using the van der Waals diameter of framework atoms = 2.7 Å are indicated above by the arrows.

This plot of surface area versus pore dimension is determined using a combination of the DeLaunay triangulation method for pore dimension determination, and the procedure of Düren for determination of the surface area.

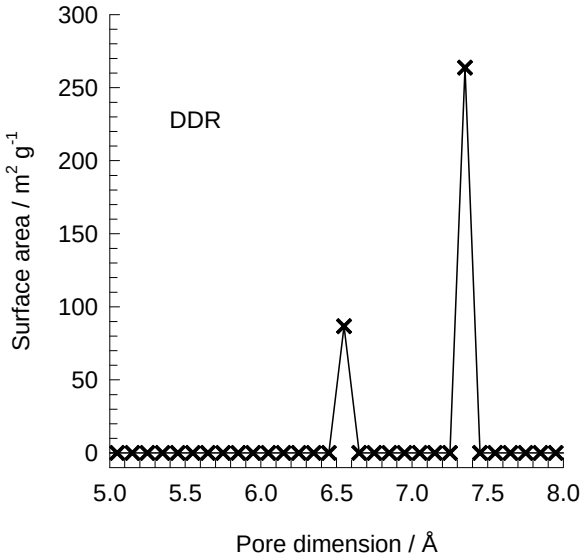

	DDR
a /Å	24.006
b /Å	13.86
c /Å	40.892
Cell volume / Å^3	13605.72
conversion factor for [molec/uc] to [mol per kg Framework]	0.0693
conversion factor for [molec/uc] to [kmol/m^3]	0.4981
ρ [kg/m3]	1759.991
MW unit cell [g/mol(framework)]	14420.35
ϕ, fractional pore volume	0.245
open space / Å^3/uc	3333.5
Pore volume / cm^3/g	0.139
Surface area /m^2/g	350.0
DeLaunay diameter /Å	3.65

DDR CBMC simulations of isotherms, and isosteric heats of adsorption

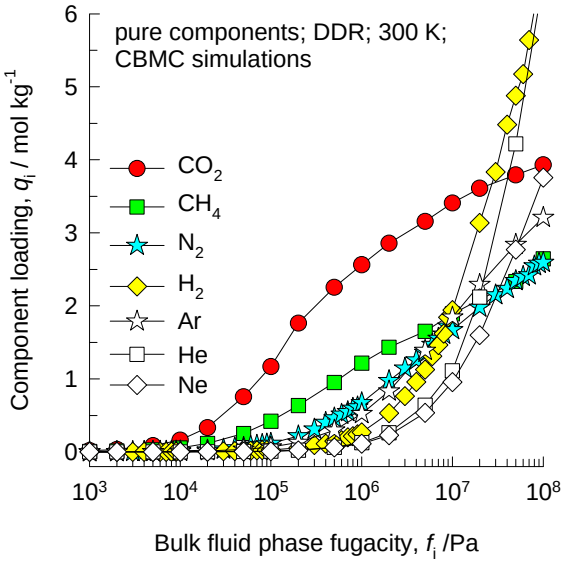

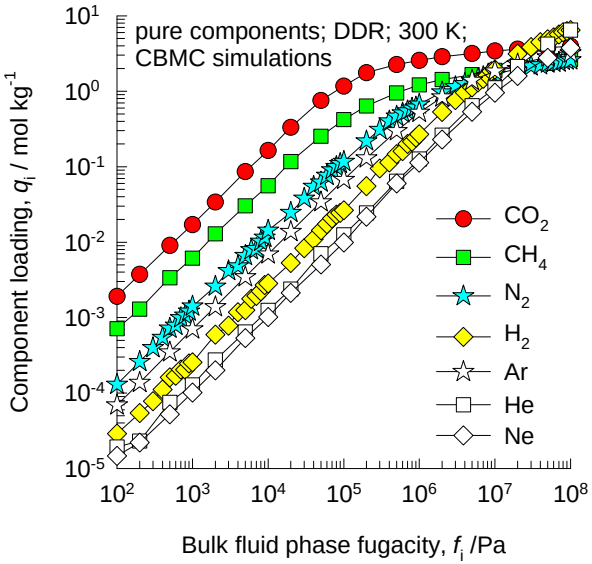

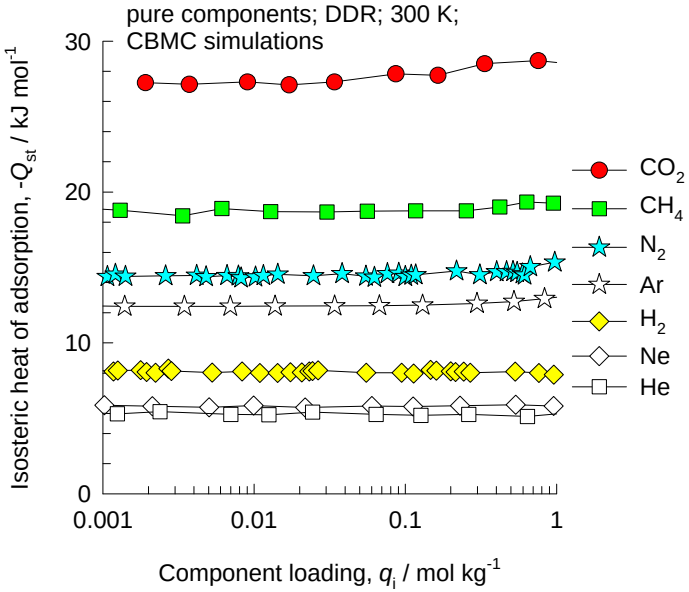

DDR MD simulations of unary self- , and M-S diffusivities

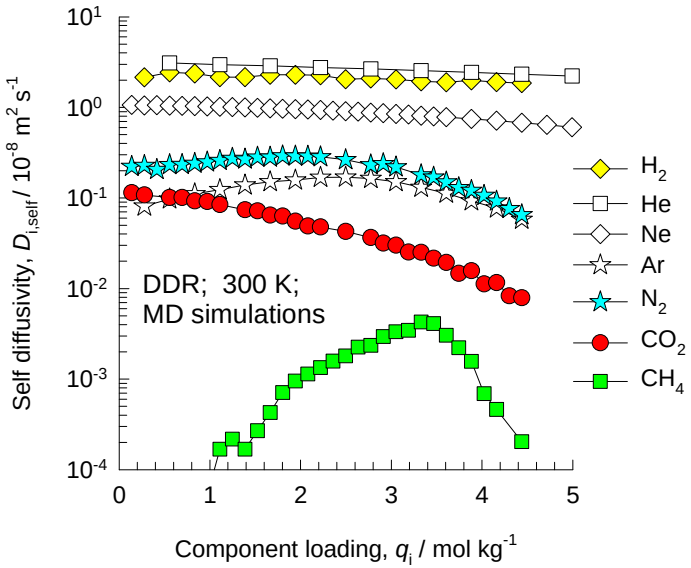

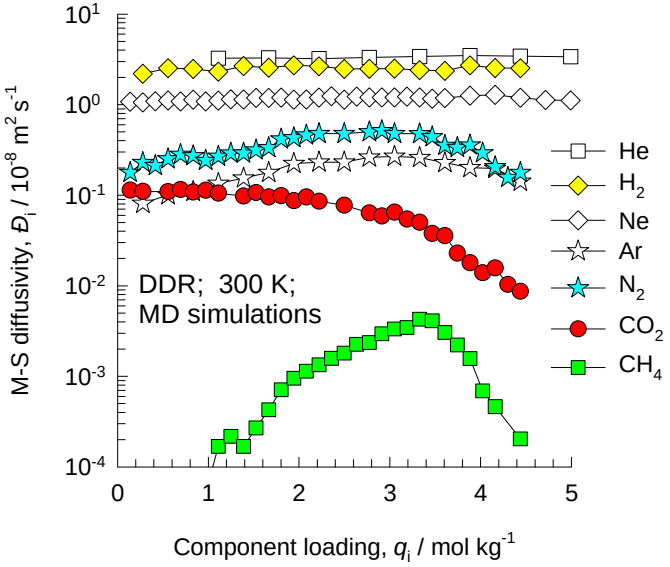

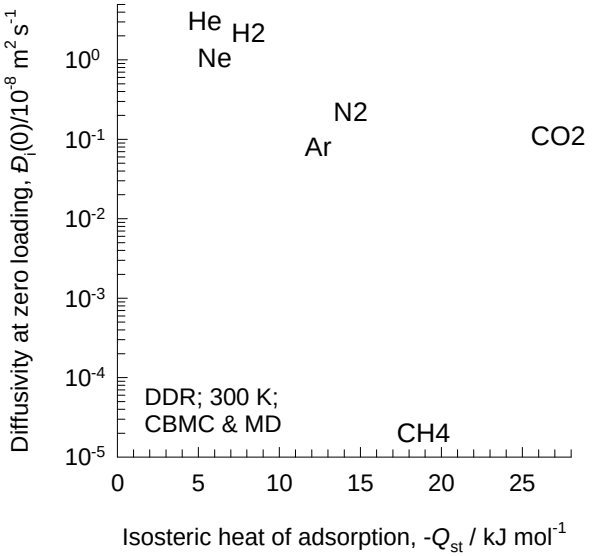

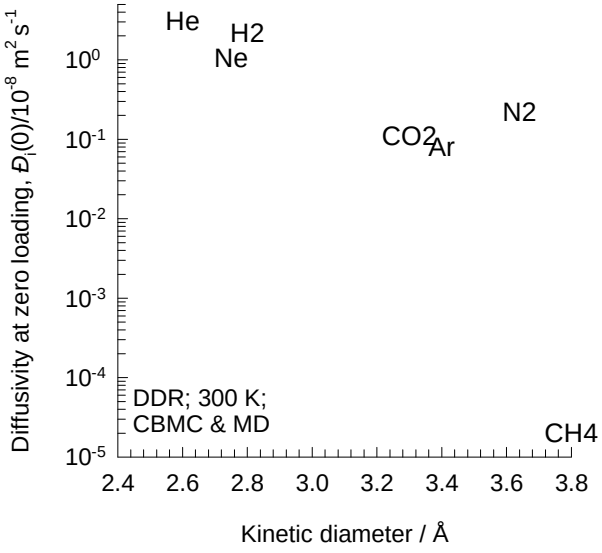

DDR Transport coefficients obtained from membrane permeation experiments

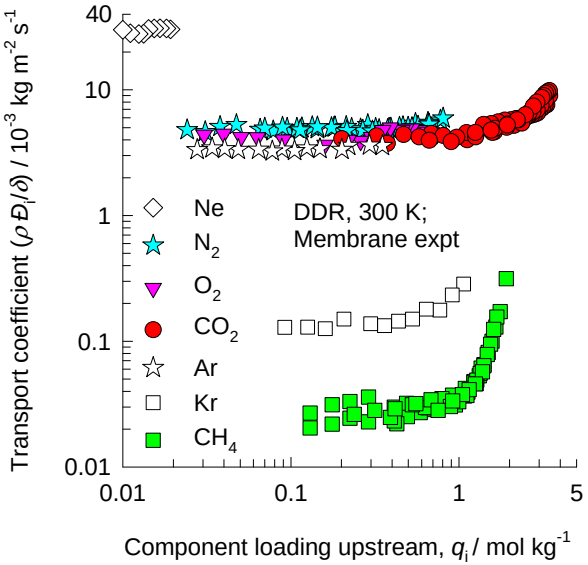

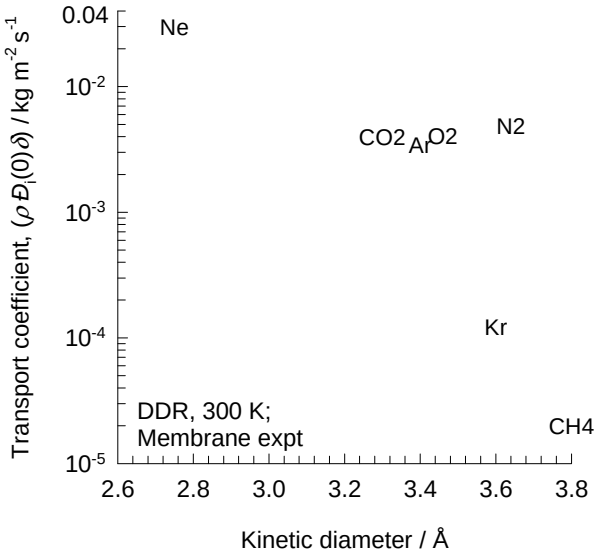

The experimental data are from:
J. van den Bergh, W. Zhu, J. Gascon, J.A. Moulijn, F. Kapteijn, Separation and Permeation Characteristics of a DD3R Zeolite Membrane, J. Membr. Sci. 316 (2008) 35-45.
J. van den Bergh, W. Zhu, J.C. Groen, F. Kapteijn, J.A. Moulijn, K. Yajima, K. Nakayama, T. Tomita, S. Yoshida, Natural Gas Purification with a DDR Zeolite Membrane; Permeation Modelling with Maxwell-Stefan Equations, Stud. Surf. Sci. Catal. 170 (2007) 1021-1027.

These data were re-analysed and interpreted to obtain the transport coefficients at 300 K. The re-analysis is provided in the following publications.
R. Krishna, J.M. van Baten, Onsager coefficients for binary mixture diffusion in nanopores, Chem. Eng. Sci. 63 (2008) 3120-3140.
R. Krishna, J.M. van Baten, Segregation effects in adsorption of CO2 containing mixtures and their consequences for separation selectivities in cage-type zeolites, Sep. Purif. Technol. 61 (2008) 414-423.
R. Krishna, J.M. van Baten, A molecular dynamics investigation of a variety of influences of temperature on diffusion in zeolites, Microporous Mesoporous Mater. 125 (2009) 126-134.

DDR Transport coefficients: MD vs Experiments obtained from membrane permeation experiments

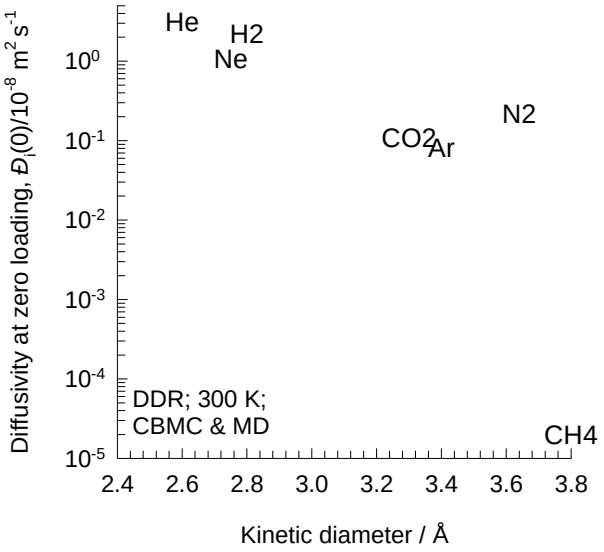

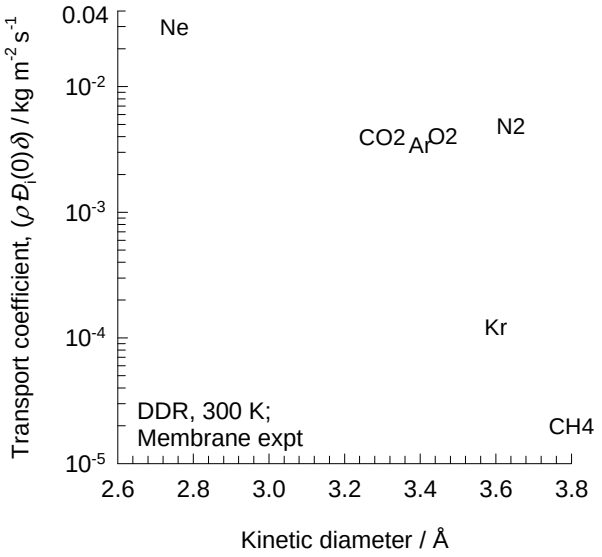

There is reasonable agreement between the two data sets

ERI pore landscape

There are 4 cages per unit cell.
The volume of one ERI cage is 408.7 Å^3, significantly smaller than that of a single cage of FAU-Si (786 Å^3), or ZIF-8 (1168 Å^3).

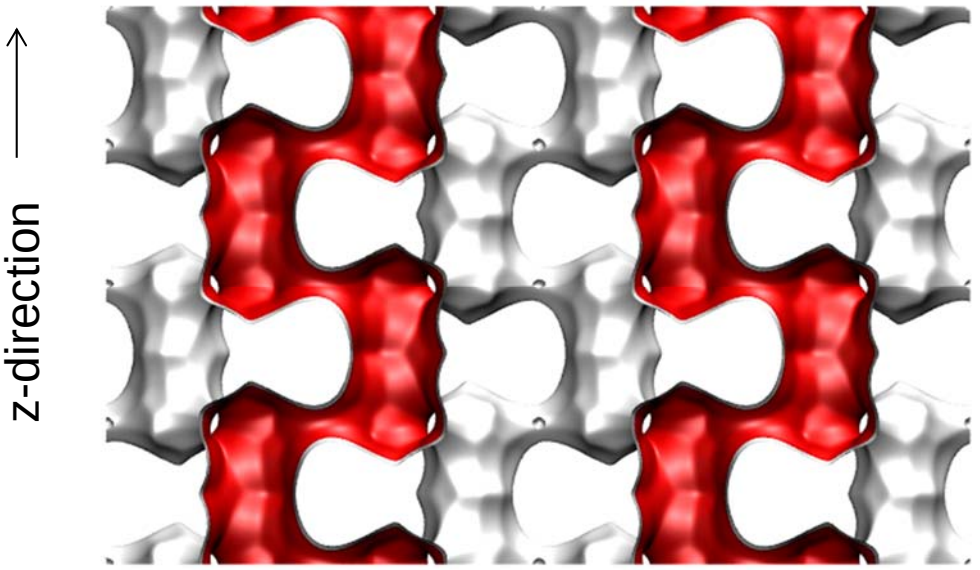

x-y projection

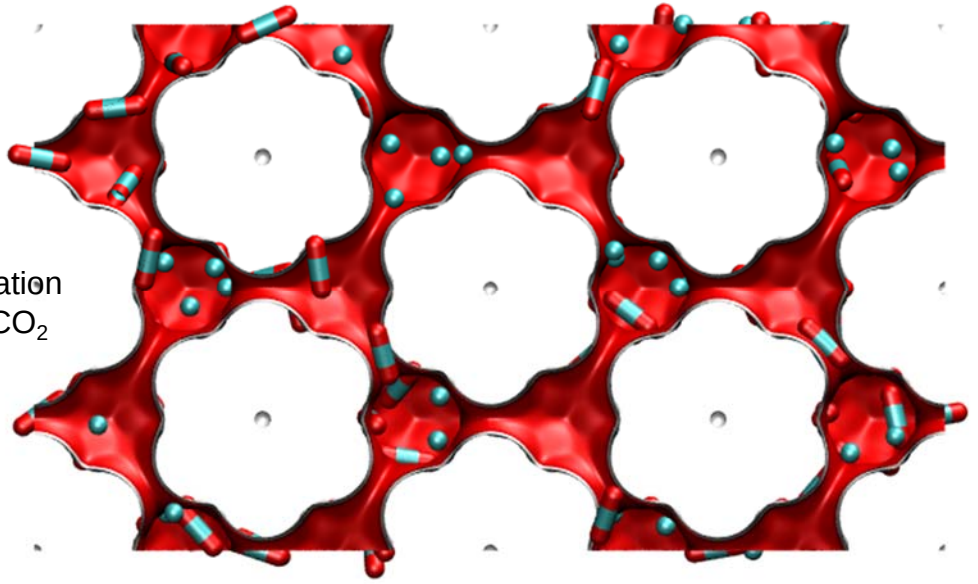

Snapshots showing location of CH_4 and CO_2

Structural information from: C. Baerlocher, L.B. McCusker, Database of Zeolite Structures, International Zeolite Association, http://www.iza-structure.org/databases/

ERI window and pore dimensions

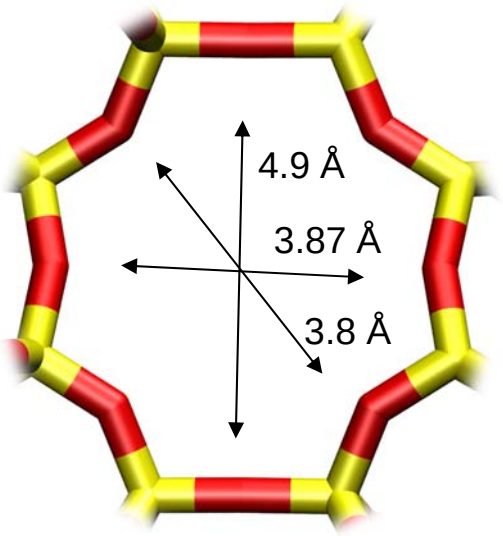

ERI

The window dimensions calculated using the van der Waals diameter of framework atoms = 2.7 Å are indicated above by the arrows.

This plot of surface area versus pore dimension is determined using a combination of the DeLaunay triangulation method for pore dimension determination, and the procedure of Düren for determination of the surface area.

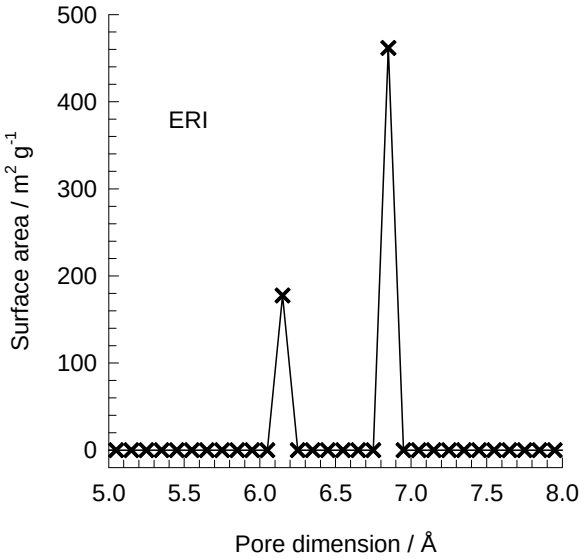

	ERI
a /Å	22.953
b /Å	13.252
c /Å	14.81
Cell volume / Å^3	4504.804
conversion factor for [molec/uc] to [mol per kg Framework]	0.2312
conversion factor for [molec/uc] to [kmol/m^3]	1.0156
ρ [kg/m3]	1594.693
MW unit cell [g/mol(framework)]	4326.106
ϕ, fractional pore volume	0.363
open space / Å^3/uc	1635.0
Pore volume / cm^3/g	0.228
Surface area /m^2/g	635.0
DeLaunay diameter /Å	3.81

ERI MD simulations of unary self- diffusivities

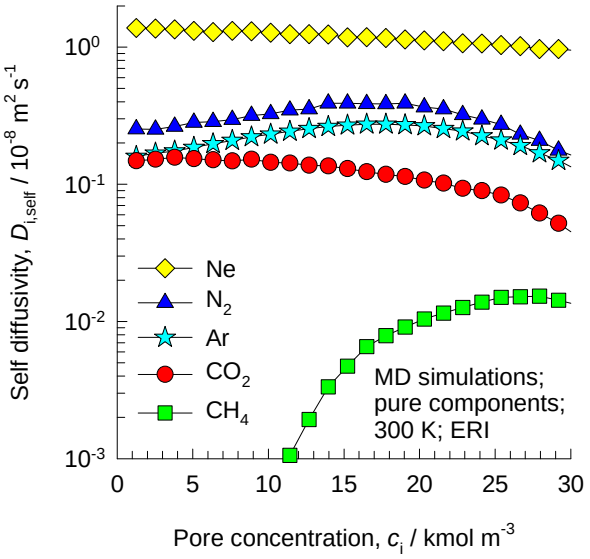

ITQ-29 pore landscape

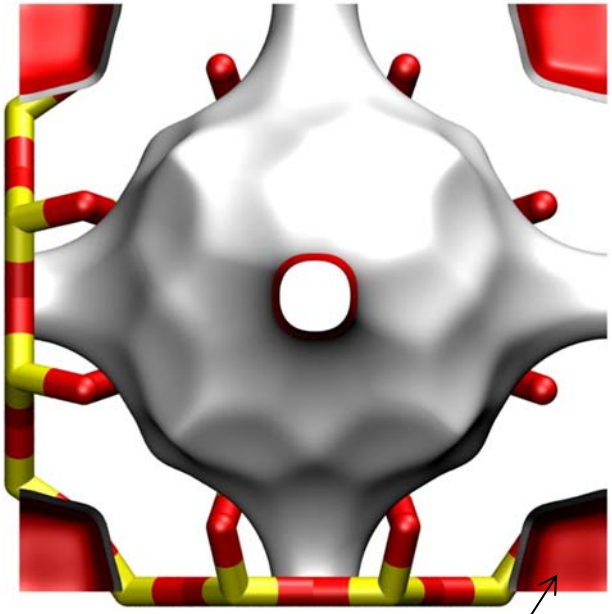

There is 1 cage per unit cell.
The volume of one ITQ-29 cage is 677.6 Å^3, intermediate in size between a single cage of ZIF-8 (1168 Å^3) and of DDR (278 Å^3).

The structural information for ITQ-29 is not available in the IZA atlas and is taken from Corma, Nature, 437 (2004) 287. The window size is slightly smaller than that of LTA Si.

Inaccessible sodalite cages have been blocked in these simulations

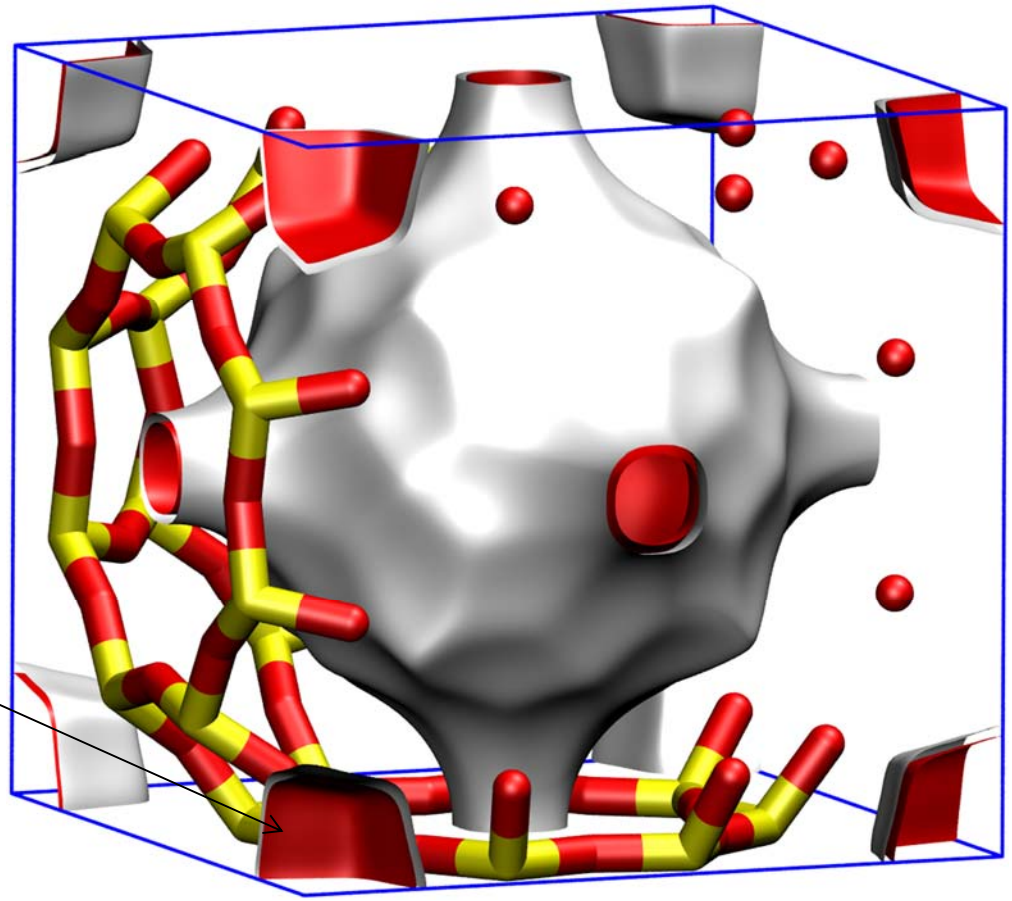

ITQ-29 window and pore dimensions

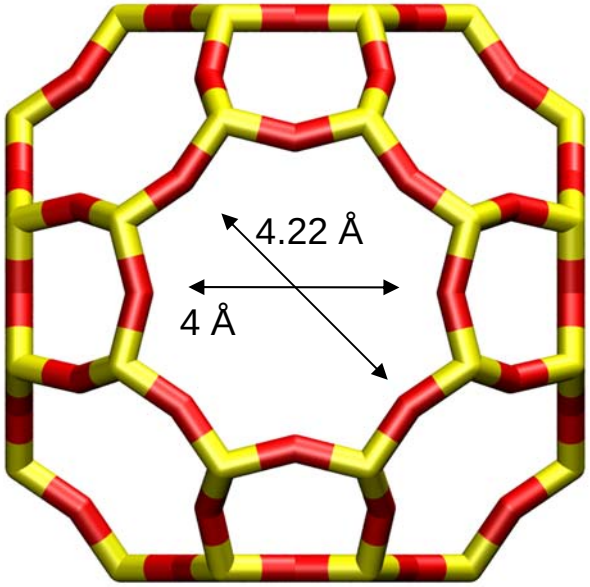

The window dimension calculated using the van der Waals diameter of framework atoms = 2.7 Å is indicated above by the arrows.

This plot of surface area versus pore dimension is determined using a combination of the DeLaunay triangulation method for pore dimension determination, and the procedure of Düren for determination of the surface area.

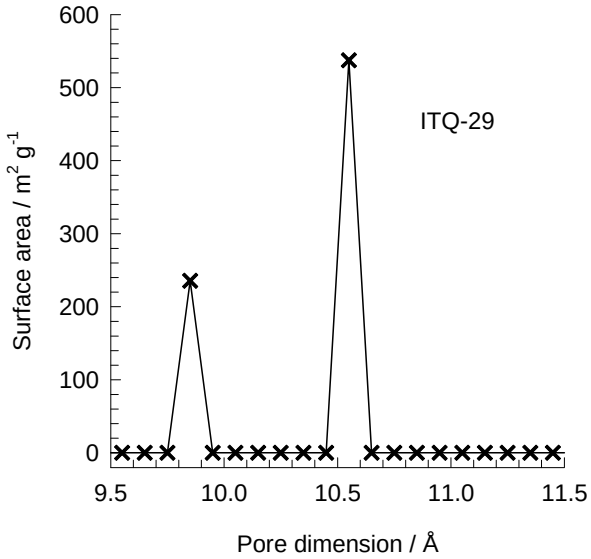

	ITQ-29
a /Å	11.867
b /Å	11.867
c /Å	11.867
Cell volume / Å^3	1671.178
conversion factor for [molec/uc] to [mol per kg Framework]	0.6935
conversion factor for [molec/uc] to [kmol/m^3]	2.4508
ρ [kg/m3]	1432.877
MW unit cell [g/mol(framework)]	1442.035
ϕ, fractional pore volume	0.405
open space / Å^3/uc	677.6
Pore volume / cm^3/g	0.283
Surface area /m^2/g	773.0
DeLaunay diameter /Å	3.98

ITQ-29 MD simulations of unary self- diffusivities

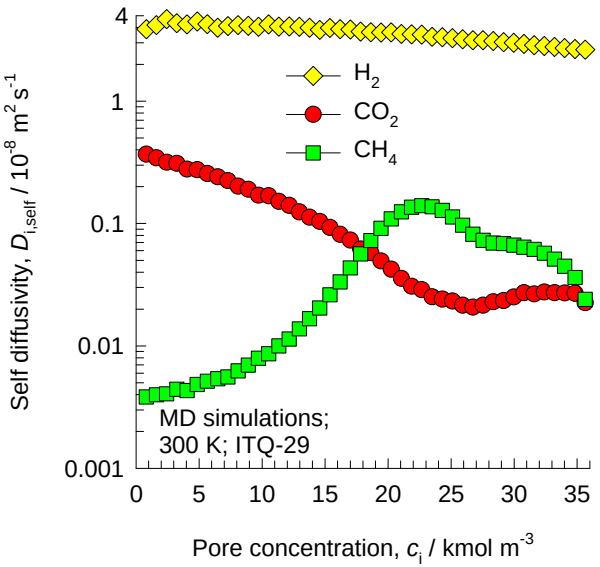

LTA-Si landscapes

This is a *hypothetical* structure constructed from dealuminized LTA-5A structure

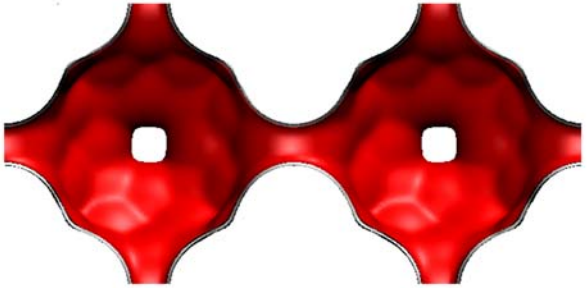

There are 8 cages per unit cell.
The volume of one LTA cage is 743 Å^3, intermediate in size between a single cage of ZIF-8 (1168 Å^3) and of DDR (278 Å^3).

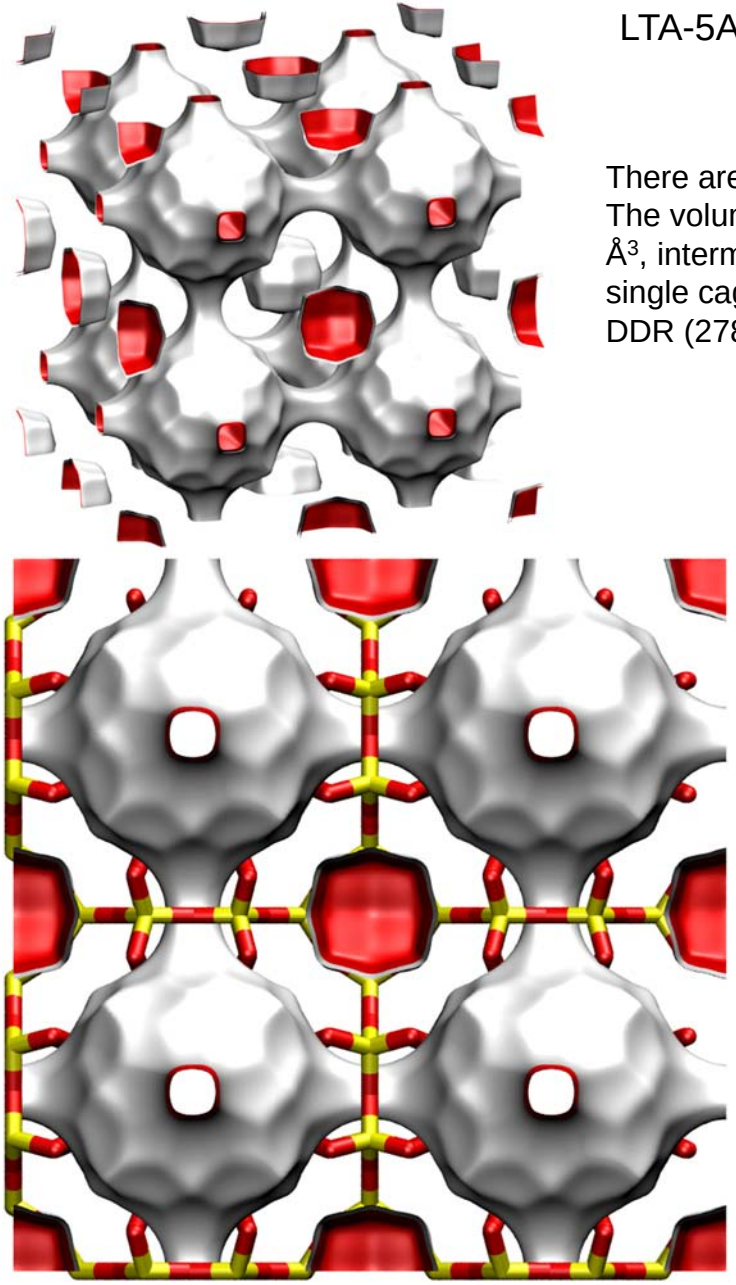

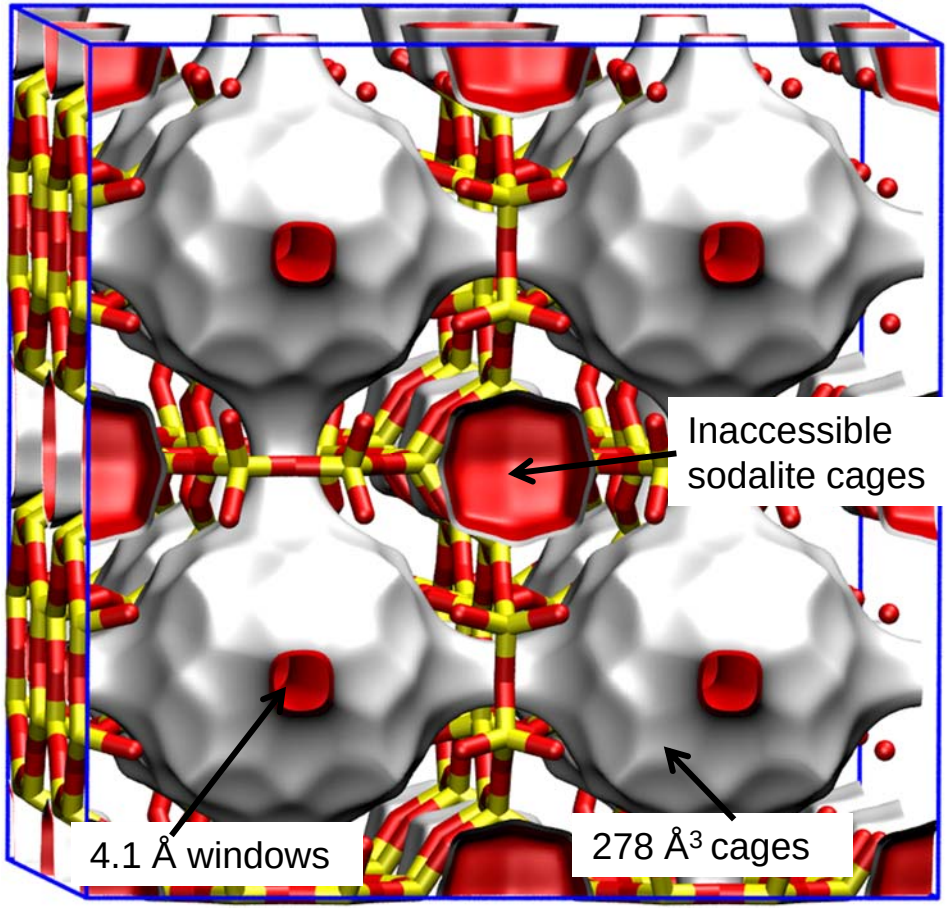

LTA-Si window and pore dimensions

8-ring window of LTA

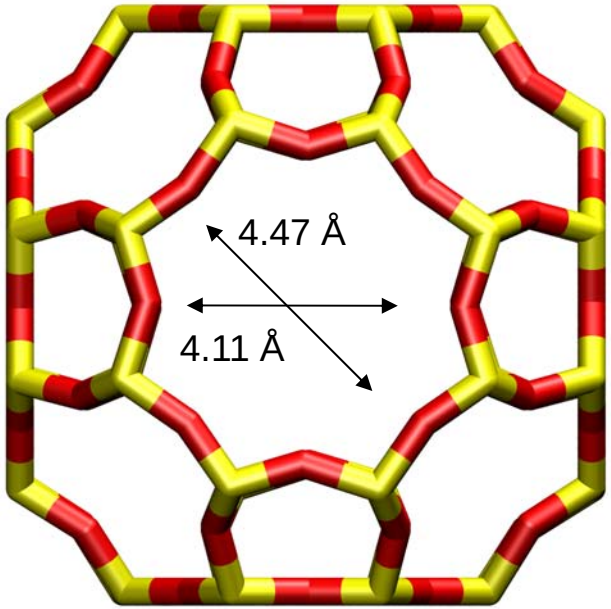

The window dimension calculated using the van der Waals diameter of framework atoms = 2.7 Å is indicated above by the arrows.

This plot of surface area versus pore dimension is determined using a combination of the DeLaunay triangulation method for pore dimension determination, and the procedure of Düren for determination of the surface area.

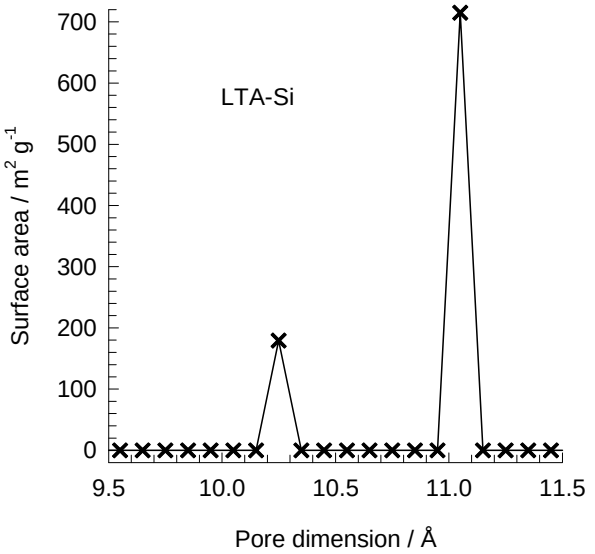

	LTA-Si
a /Å	24.61
b /Å	24.61
c /Å	24.61
Cell volume / Å^3	14905.1
conversion factor for [molec/uc] to [mol per kg Framework]	0.0867
conversion factor for [molec/uc] to [kmol/m^3]	0.2794
ρ [kg/m3]	1285.248
MW unit cell [g/mol(framework)]	11536.28
ϕ, fractional pore volume	0.399
open space / Å^3/uc	5944.4
Pore volume / cm^3/g	0.310
Surface area /m^2/g	896.0
DeLaunay diameter /Å	4.10

LTA-Si CBMC simulations of isotherms, and isosteric heats of adsorption

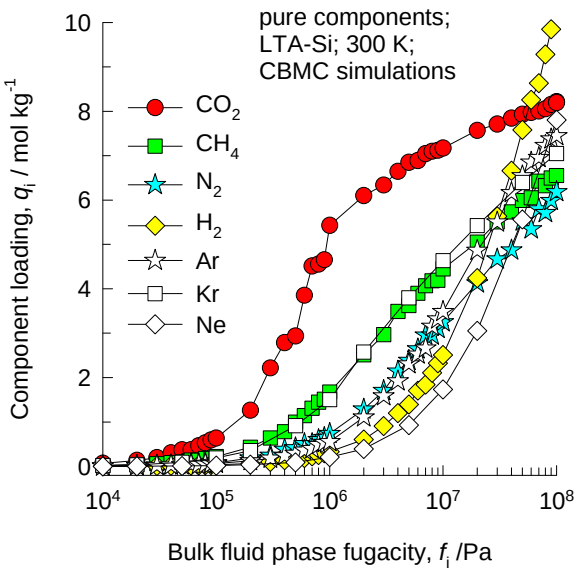

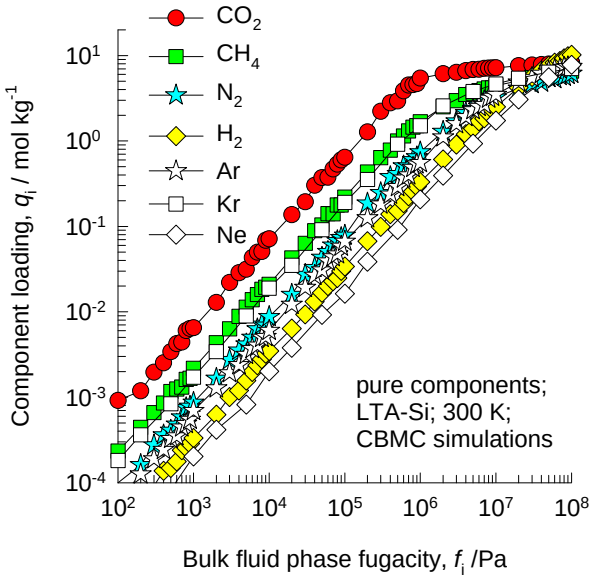

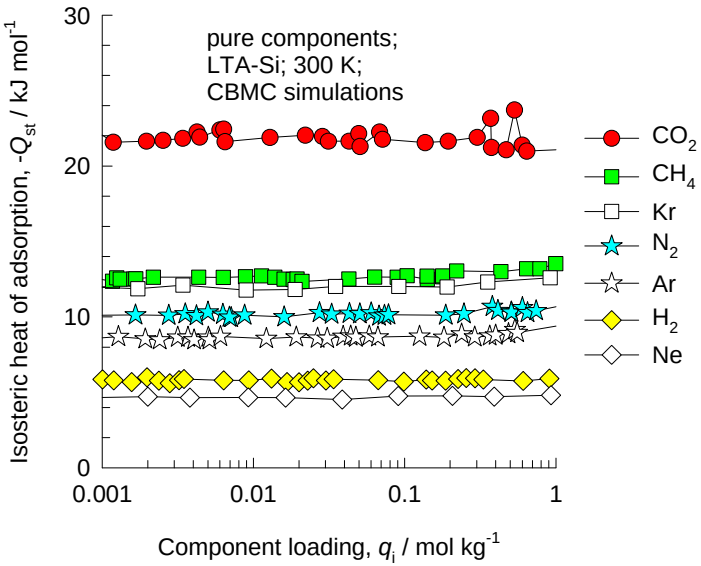

LTA-Si MD simulations of unary self- , and M-S diffusivities

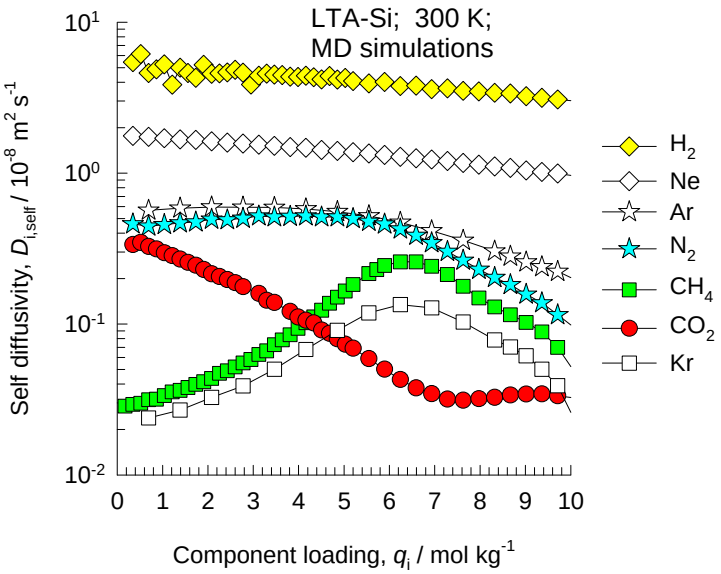

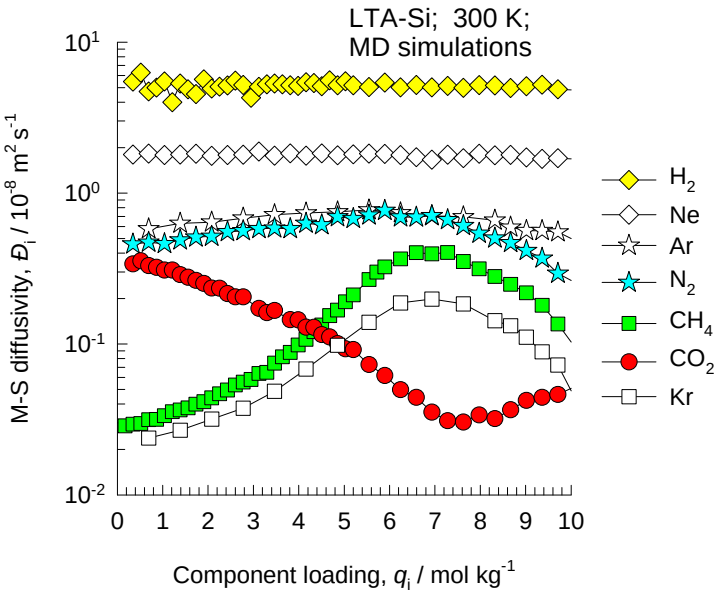

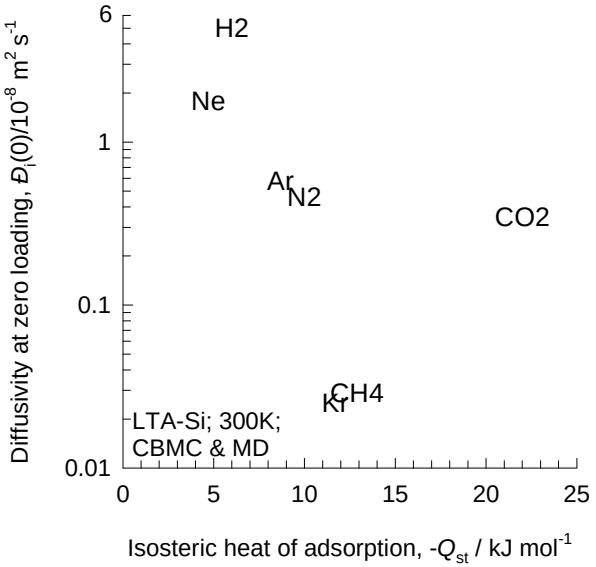

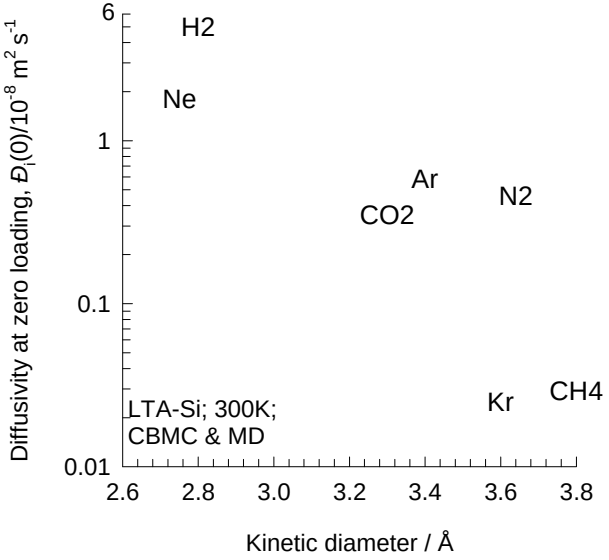

SOD-Si pore landscape

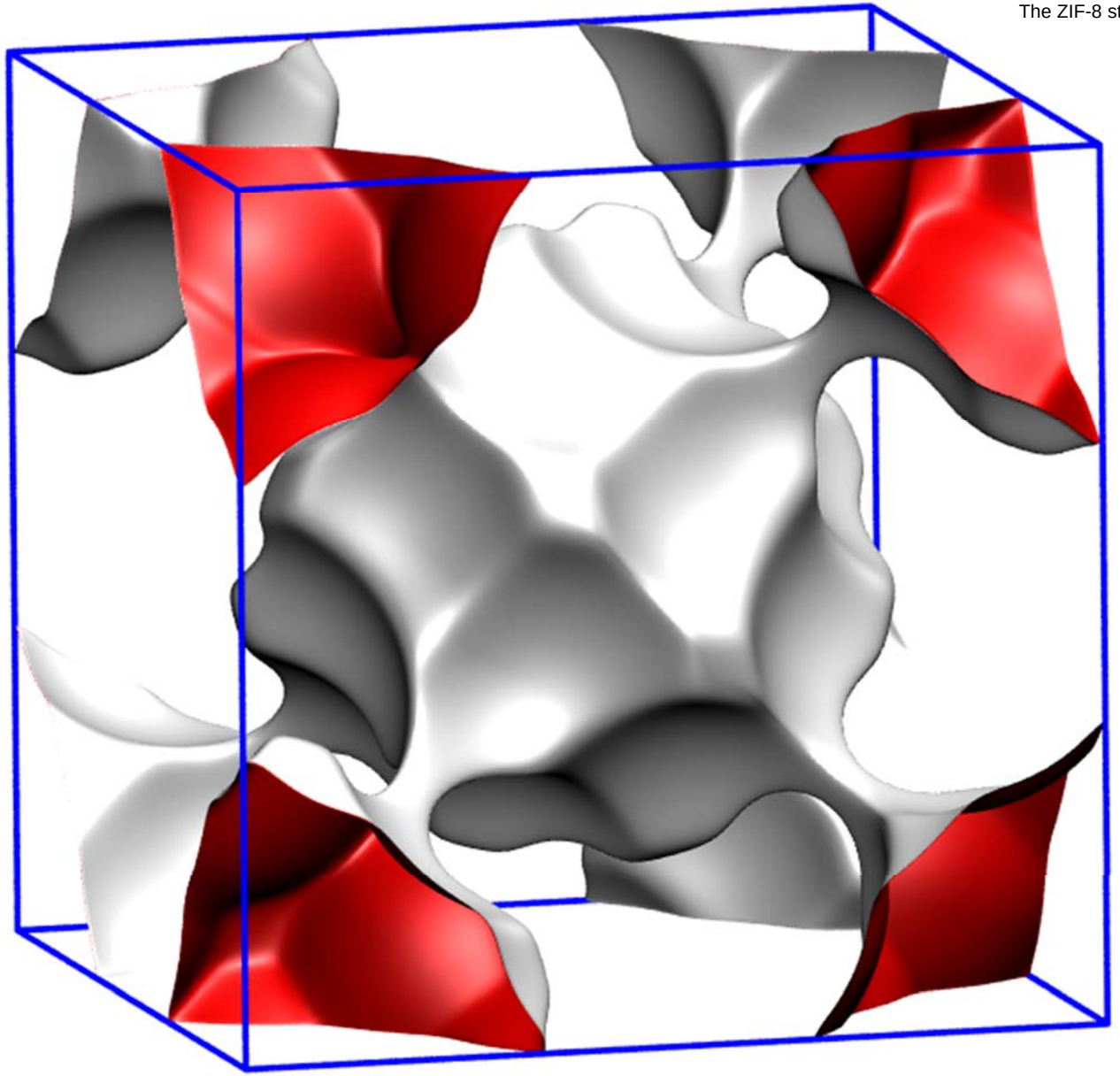

The ZIF-8 structure is analogous to that of SOD.

There are 2 cages per unit cell. The volume of one SOD cage is 84.8 $Å^3$, significantly smaller than that of ZIF-8 (1168 $Å^3$), its structural analog.

Structural information from: C. Baerlocher, L.B. McCusker, Database of Zeolite Structures, International Zeolite Association, http://www.iza-structure.org/databases/

SOD-Si dimensions

	SOD-Si
a /Å	8.89
b /Å	8.89
c /Å	8.89
Cell volume / Å^3	702.5954
conversion factor for [molec/uc] to [mol per kg Framework]	1.3869
conversion factor for [molec/uc] to [kmol/m^3]	9.7908
ρ [kg/m3]	1704.106
MW unit cell [g/mol(framework)]	721.0176
ϕ, fractional pore volume	0.241
open space / Å^3/uc	169.6
Pore volume / cm^3/g	0.142
Surface area /m^2/g	
DeLaunay diameter /Å	2.47

TSC landscape

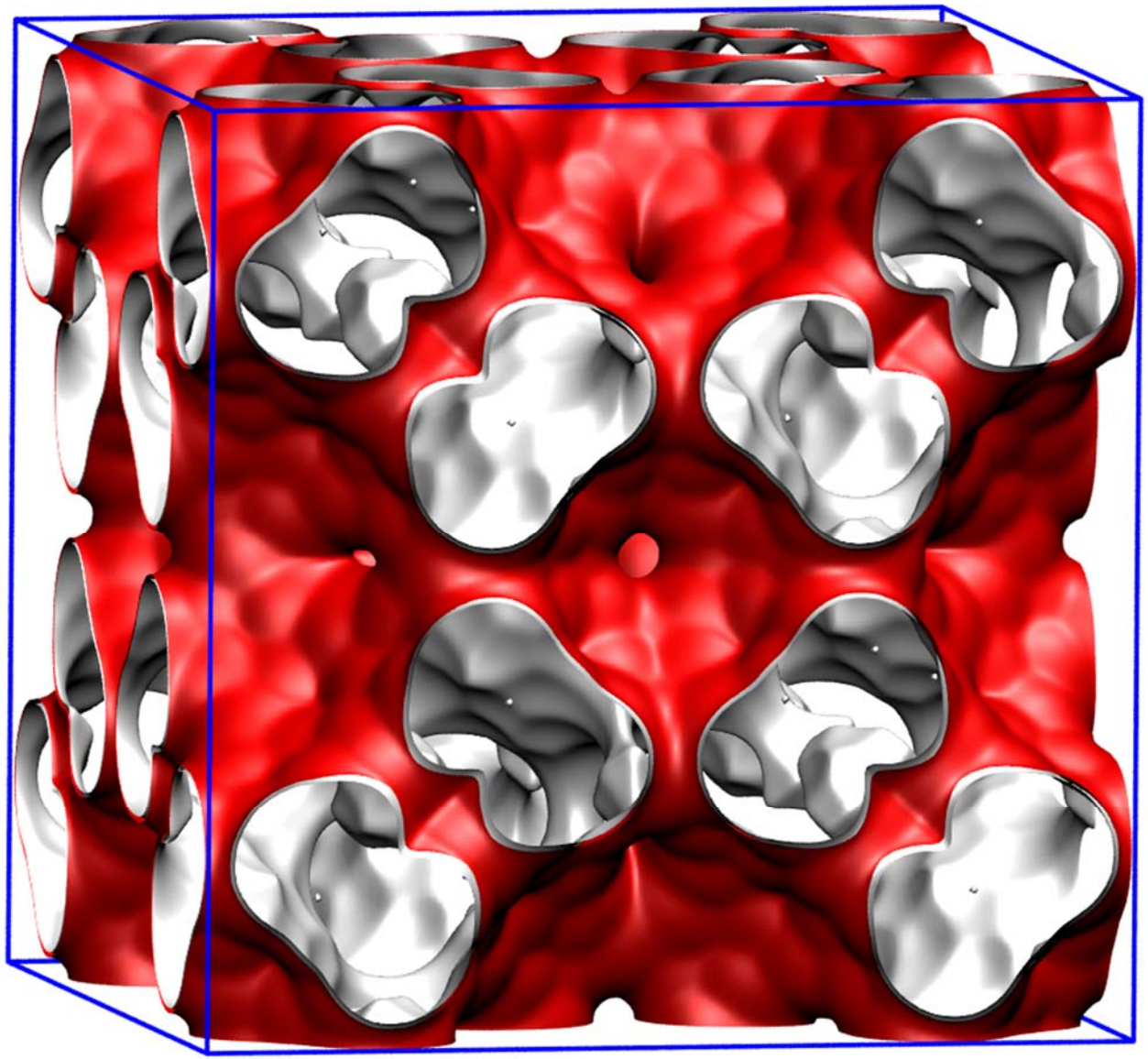

Unit cell of TSC

Structural information from: C. Baerlocher, L.B. McCusker, Database of Zeolite Structures, International Zeolite Association, http://www.iza-structure.org/databases/

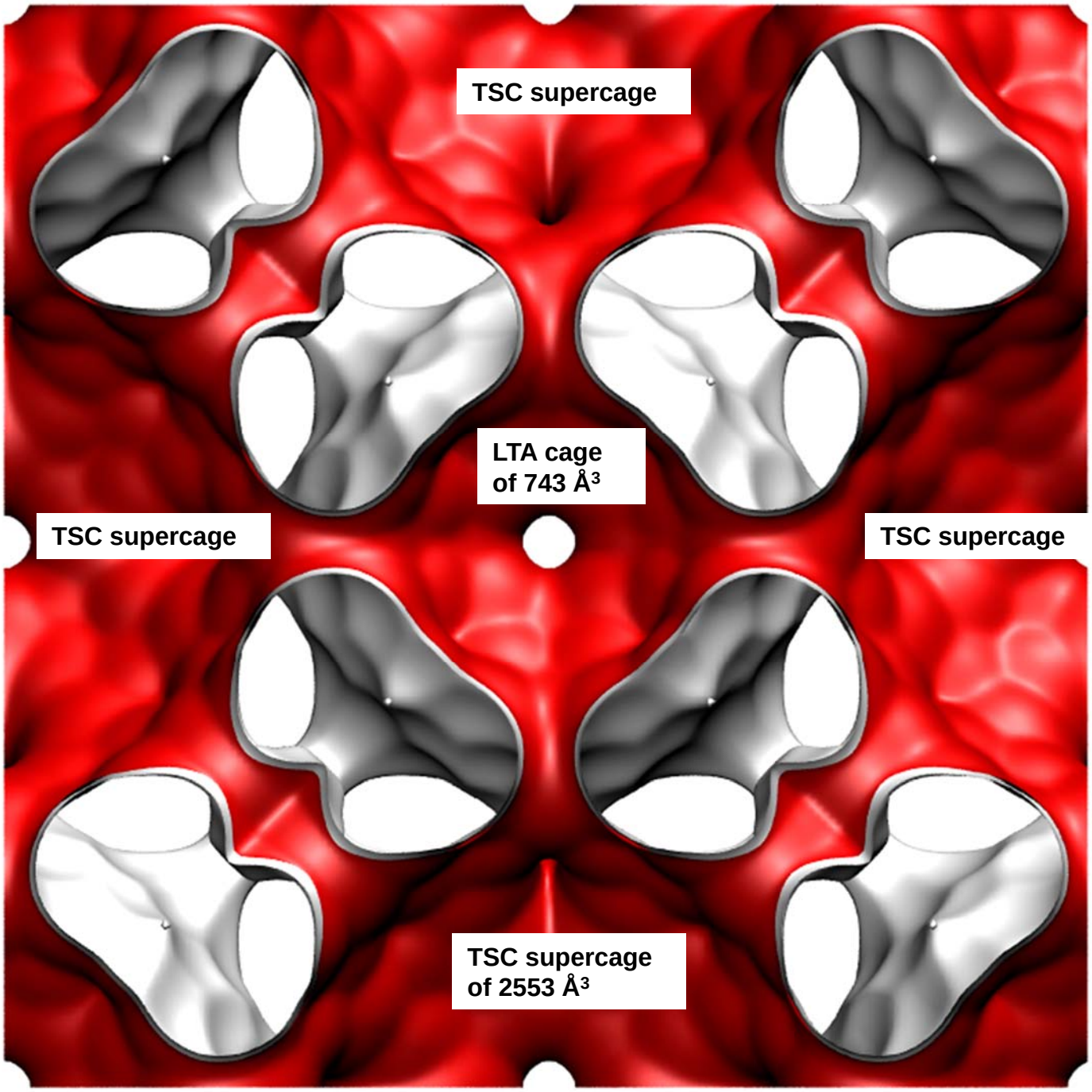

8-ring windows of two sizes:
4.2x4.2 Å along [100]
3.1x5.6 Å along [110]

Front plane of unit cell of TSC

TSC window and pore dimensions

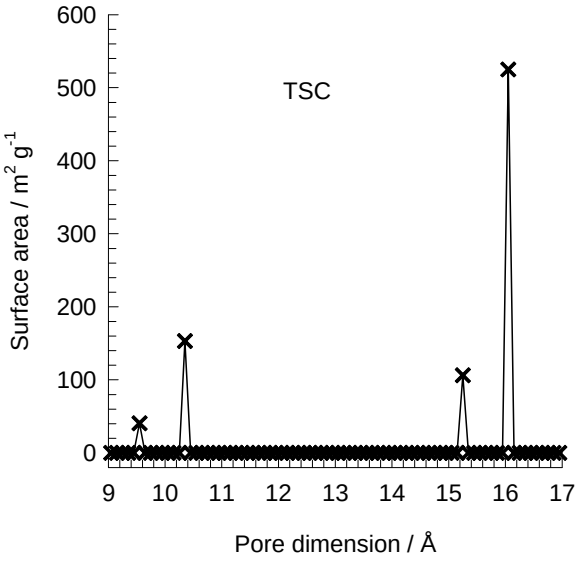

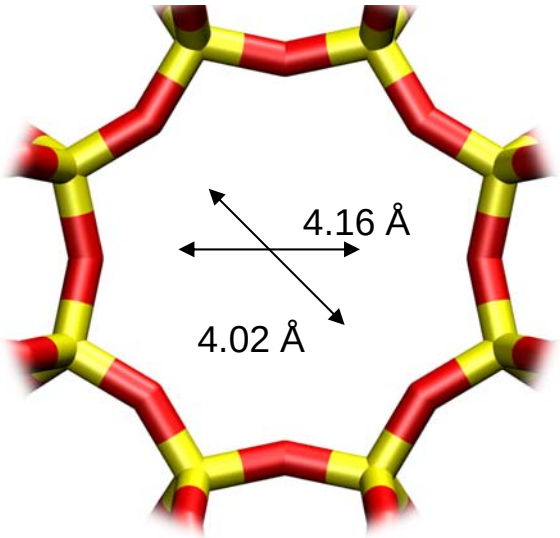

TSC
(supercage - cage)

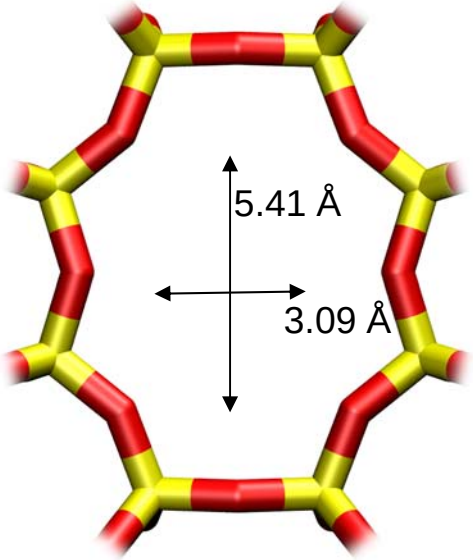

TSC
(supercage - pocket)

	TSC
a /Å	30.742
b /Å	30.742
c /Å	30.742
Cell volume / Å^3	29053.36
conversion factor for [molec/uc] to [mol per kg Framework]	0.0433
conversion factor for [molec/uc] to [kmol/m^3]	0.1260
ρ [kg/m3]	1318.729
MW unit cell [g/mol(framework)]	23072.56
ϕ, fractional pore volume	0.454
open space / Å^3/uc	13182.6
Pore volume / cm^3/g	0.344
Surface area /m^2/g	829.0
DeLaunay diameter /Å	4.02

The window dimension calculated using the van der Waals diameter of framework atoms = 2.7 Å are indicated above by the arrows. It is likely that the pockets are inaccessible due to the narrow constriction of 3.092 Å. Another point to note is that the dimensions provided in the IZA website do not appear to be correct for the window on the left.

TSC MD simulations of unary self- diffusivities

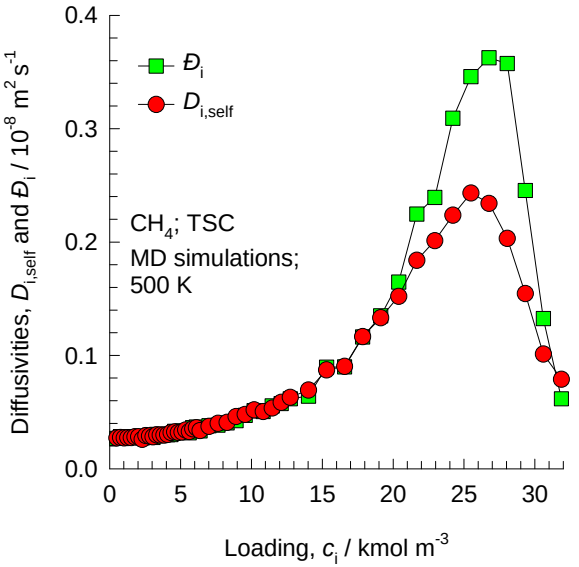

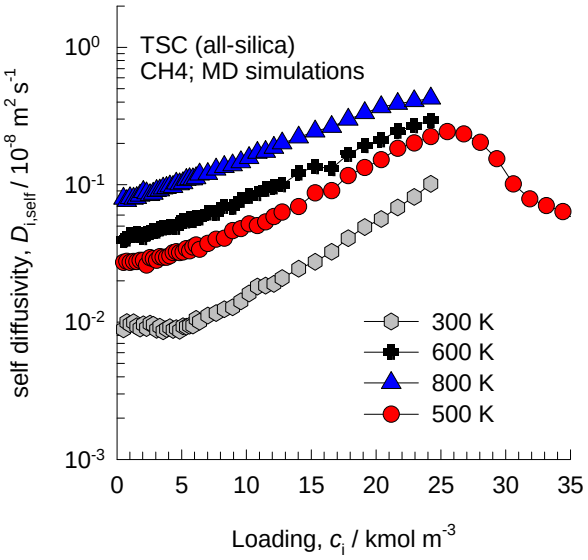

Comparing CH_4 diffusivities in 8-ring zeolites

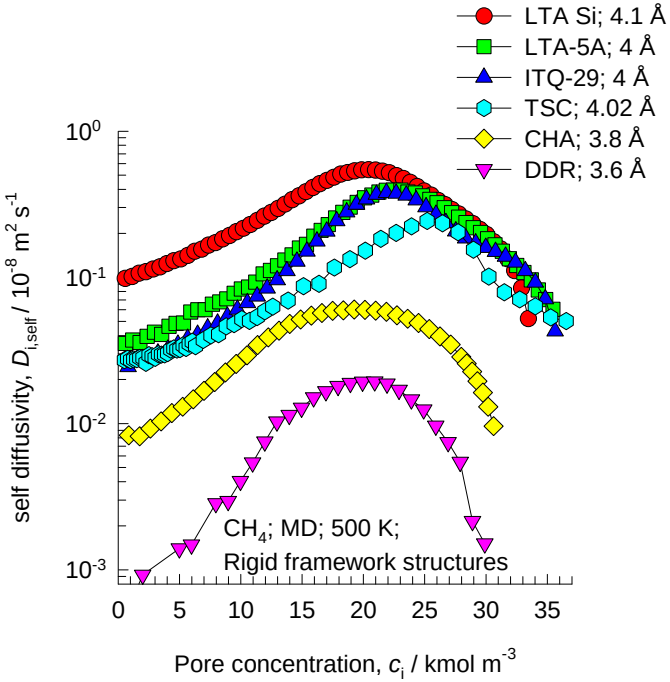

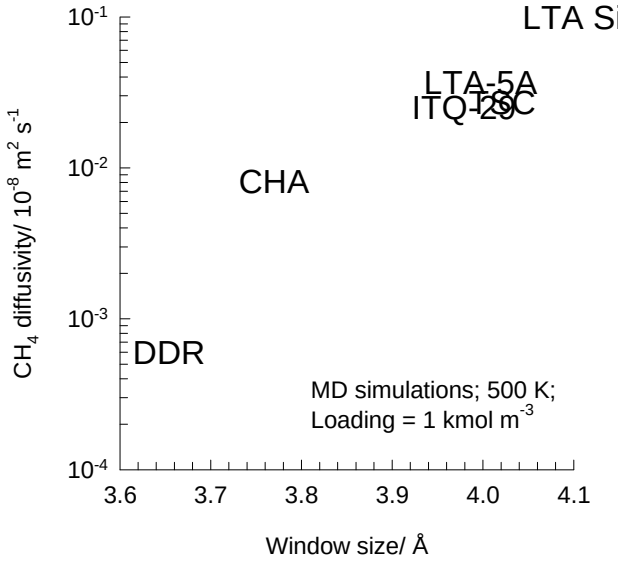

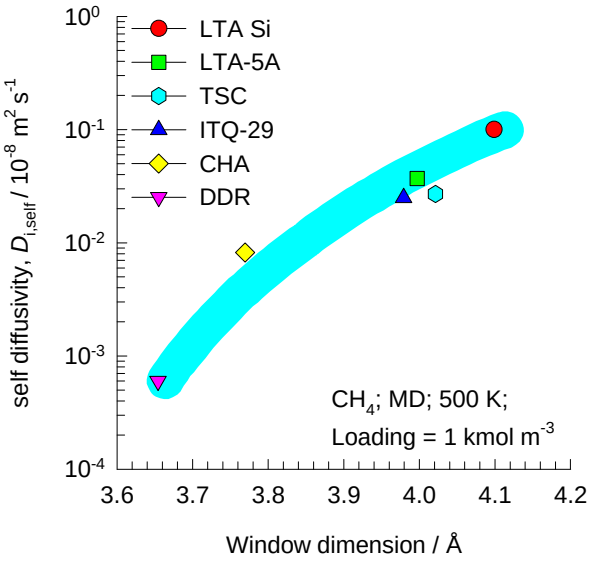

ZIF-8 pore landscapes

The ZIF-8 = Zn(methylimidazole)$_2$ structure was taken from
R. Banerjee, A. Phan, B. Wang, C. Knobler, H. Furukawa, M. O'Keeffe, O.M. Yaghi, High-Throughput Synthesis of Zeolitic Imidazolate Frameworks and Application to CO_2 Capture, Science 319 (2008) 939-943.
The original structural data (cif file) contains solvent molecules; these were removed and the solvent-free structures were simulated.

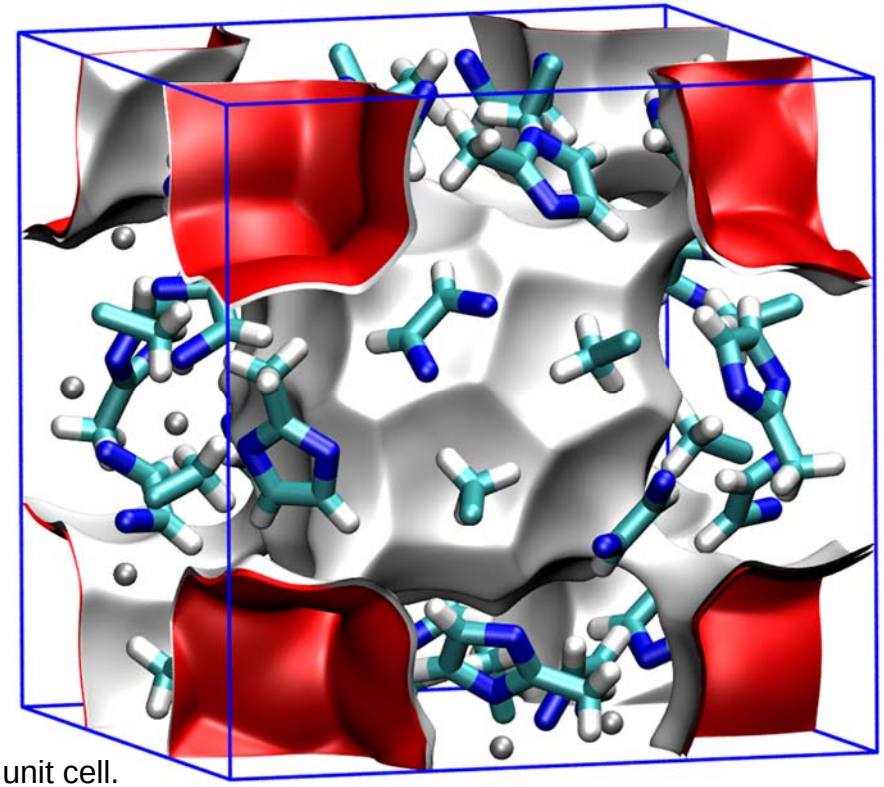

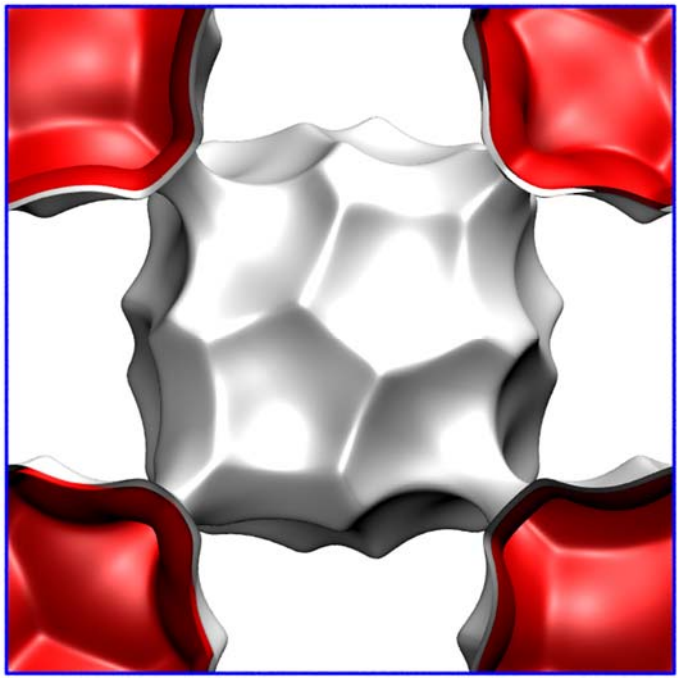

There are 2 cages per unit cell. The volume of one ZIF-8 cage is 1168 Å^3, significantly larger than that of a single cage of DDR (278 Å^3), or FAU (786 Å^3).

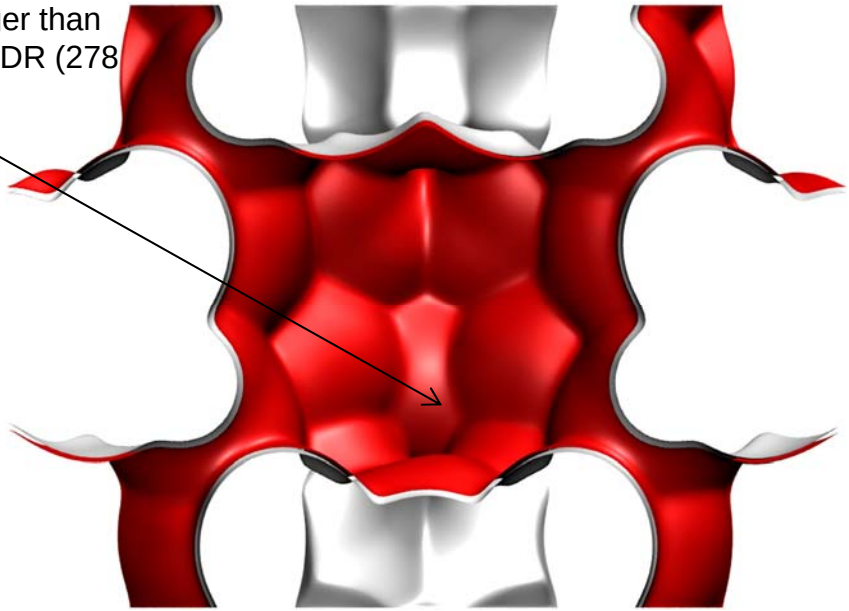

ZIF-8 dimensions

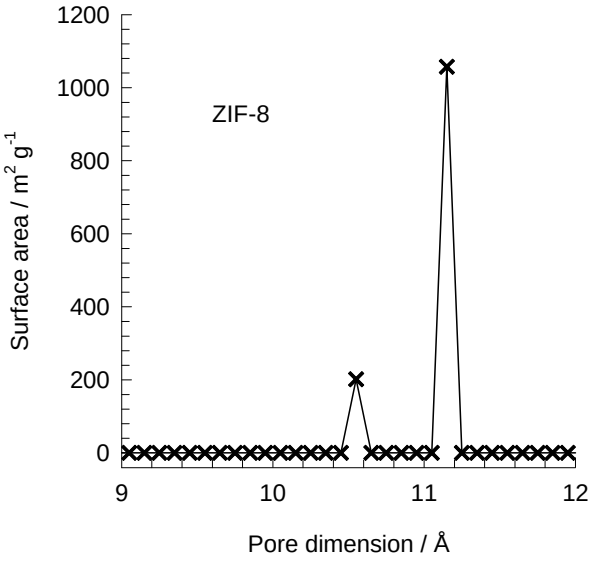

This plot of surface area versus pore dimension is determined using a combination of the DeLaunay triangulation method for pore dimension determination, and the procedure of Düren for determination of the surface area.

	ZIF-8
a /Å	16.991
b /Å	16.991
c /Å	16.991
Cell volume / Å^3	4905.201
conversion factor for [molec/uc] to [mol per kg Framework]	0.3663
conversion factor for [molec/uc] to [kmol/m^3]	0.7106
ρ [kg/m3]	924.253
MW unit cell [g/mol(framework)]	2730.182
ϕ, fractional pore volume	0.476
open space / Å^3/uc	2337.0
Pore volume / cm^3/g	0.515
Surface area /m^2/g	1164.7
DeLaunay diameter /Å	3.26

ZIF-8 snapshot of CO_2/CH_4 mixture

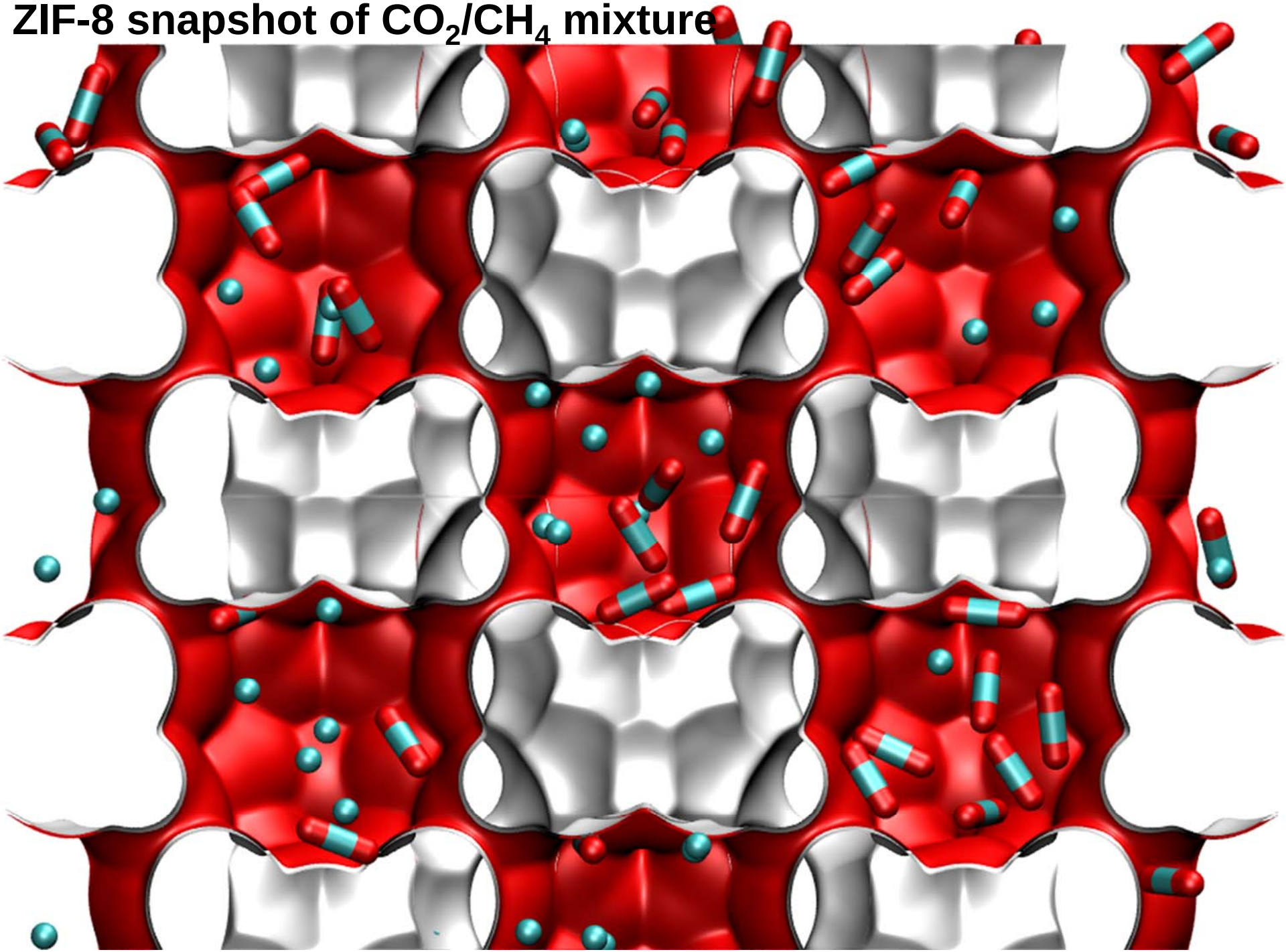

ZIF-8 force-field for framework atoms

The Lennard-Jones potentials for the framework atoms of ZIF-8 were taken from the combined works of S.L. Mayo, B.D. Olafson, W.A. Goddard (DREIDING: A Generic Force Field for Molecular Simulations, J. Phys. Chem. 94 (1990) 8897-8909), Q. Yang, C. Zhong, (Understanding Hydrogen Adsorption in Metal-Organic Frameworks with Open Metal Sites: A Computational Study, J. Phys. Chem. B 110 (2006) 655-658) and W.L. Jorgensen, D.S. Maxwell, J. Tirado-Rives(Development and Testing of the OPLS All-Atom Force Field on Conformational Energetics and Properties of Organic Liquids, J. Am. Chem. Soc. 118 (1996) 11225-11236), as was reported in the computational study of M. Zhou, Q. Wang, L. Zhang, Y.C. Liu, Y. Kang (Adsorption Sites of Hydrogen in Zeolitic Imidazolate Frameworks, J. Phys. Chem. B 113 (2009) 11049-11053). The framework charges of ZIF-8 were estimated using the group-contribution procedure based on quantum mechanical calculations described by Q. Xu, C. Zhong (A General Approach for Estimating Framework Charges in Metal-Organic Frameworks, J. Phys. Chem. C 114 (2010) 5035-5042).

(pseudo-) atom	σ / Å	ε/k_B / K	charge
Zn	4.54	27.59	0.749
N	3.25	85.29	-0.387
Ca	2.25	25.08	0.698
Cb	3.55	35.12	-0.0093
Cc	3.5	20.03	0.0117
Ha	2.5	15.05	-0.139
Hb	3.19	7.53	0.0627

ZIF-8

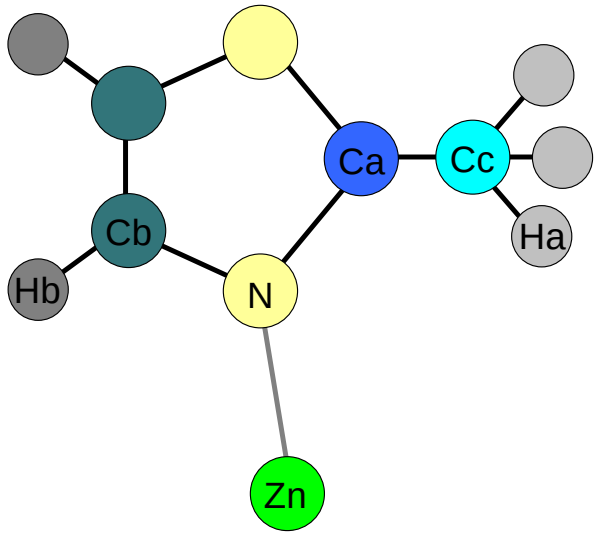

ZIF-8 pure component isotherms; comparison with experiments

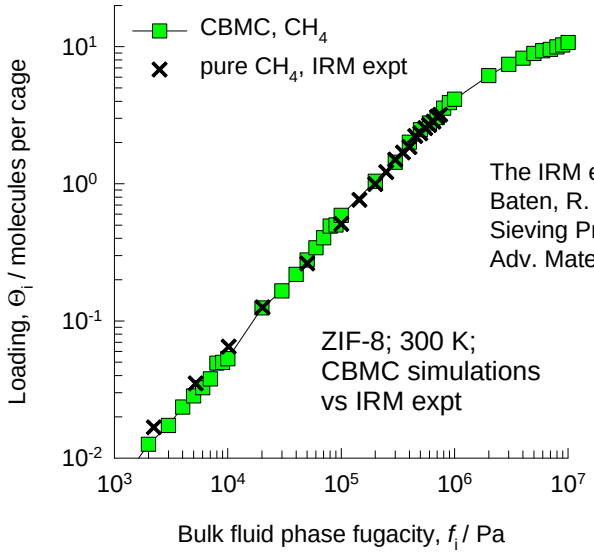

The IRM experimental data is from H. Bux, C. Chmelik, J.M. Van Baten, R. Krishna, J. Caro, Novel MOF-Membrane for Molecular Sieving Predicted by IR-Diffusion Studies and Molecular Modeling, Adv. Mater. 22 (2010) 4741-4743.

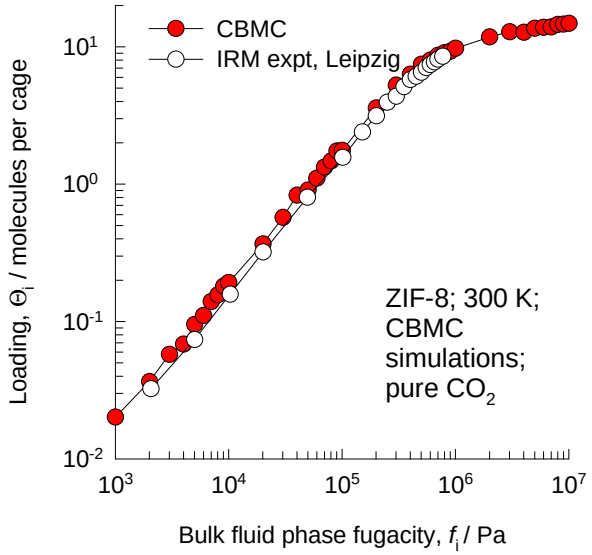

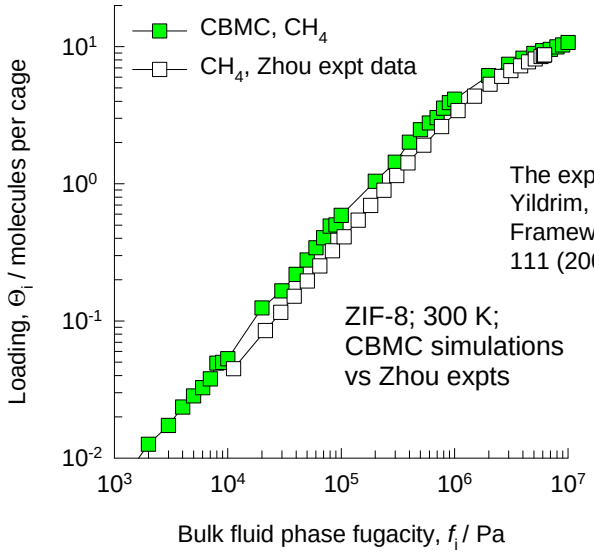

The experimental data is from W. Zhou, H. Wu, M.R. Hartman, T. Yildrim, Hydrogen and Methane Adsorption in Metal-Organic Frameworks: A High-Pressure Volumetric Study, J. Phys. Chem. C 111 (2007) 16131-16137.

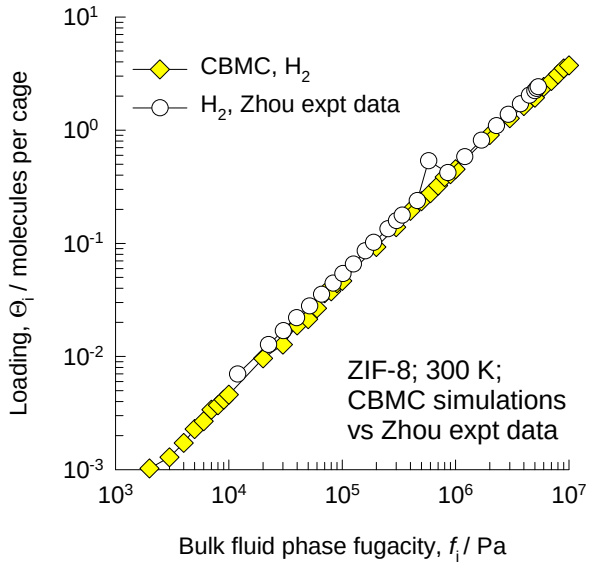

ZIF-8 pure component isotherms; comparison with experiments

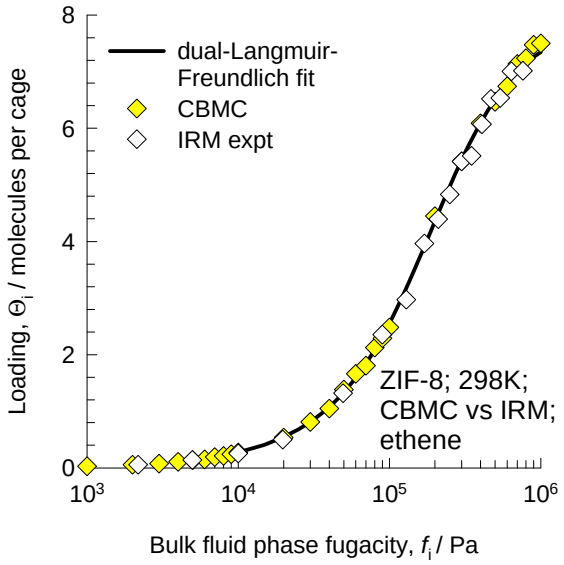

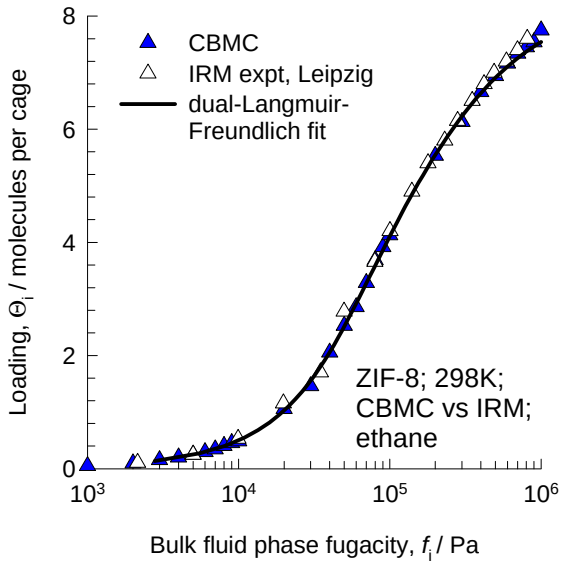

The IRM experimental data is from H. Bux, C. Chmelik, R. Krishna, J. Caro, Ethene/Ethane Separation by the MOF Membrane ZIF-8: Molecular Correlation of Permeation, Adsorption, Diffusion, J. Membr. Sci. 369 (2011) 284-289.

ZIF-8 CBMC simulations of isotherms, and isosteric heats of adsorption

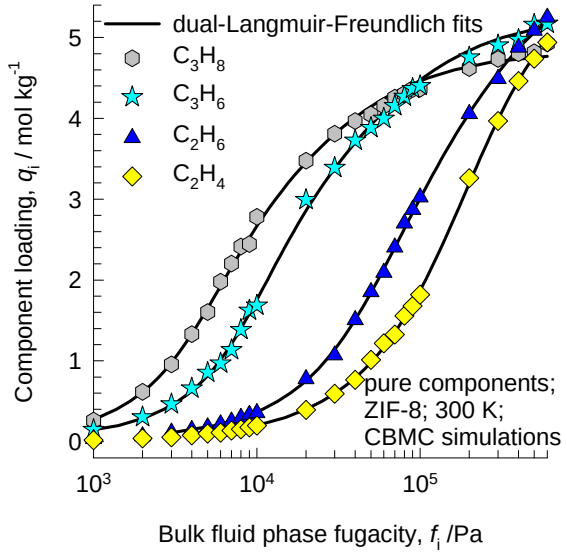

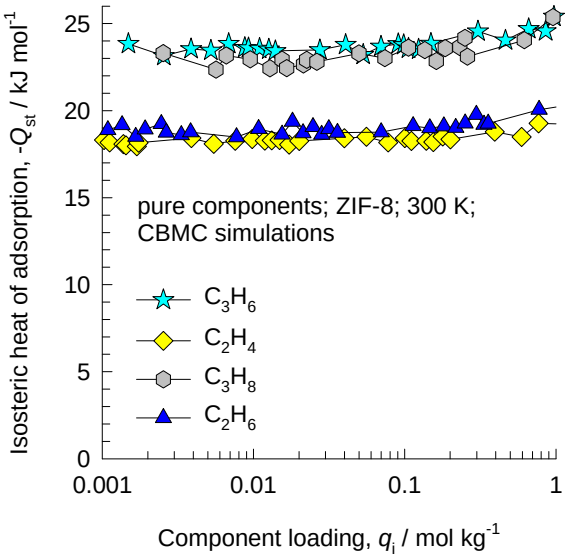

Dual-site Langmuir parameters for ethene, ethane, propene and propane isotherms in ZIF-8 at 300 K. These fits are based on CBMC simulations.

$$q_i = q_{i,A,sat}\frac{b_{i,A} f_i^{\nu_A}}{1+b_{i,A} f_i^{\nu_A}} + q_{i,B,sat}\frac{b_{i,B} f_i^{\nu_B}}{1+b_{i,B} f_i^{\nu_B}}$$

	Site A			Site B		
	$q_{i,A,sat}$ mol/kg	$b_{i,A}$ $Pa^{-\nu_i}$	$\nu_{i,A}$ dimensionless	$q_{i,B,sat}$ mol/kg	$b_{i,B}$ $Pa^{-\nu_i}$	$\nu_{i,B}$ dimensionless
ethene	0.9	2.04×10^{-5}	1	4.9	6.97×10^{-9}	1.54
ethane	4.8	17.4×10^{-6}	1	1.3	2.89×10^{-10}	2
propene	1.5	2.45×10^{-10}	2.4	3.8	3.63×10^{-5}	1
propane	1.55	1.22×10^{-8}	2.13	3.3	7.57×10^{-5}	1

ZIF-8 ethene/ethane mixture permeances and transport coefficients

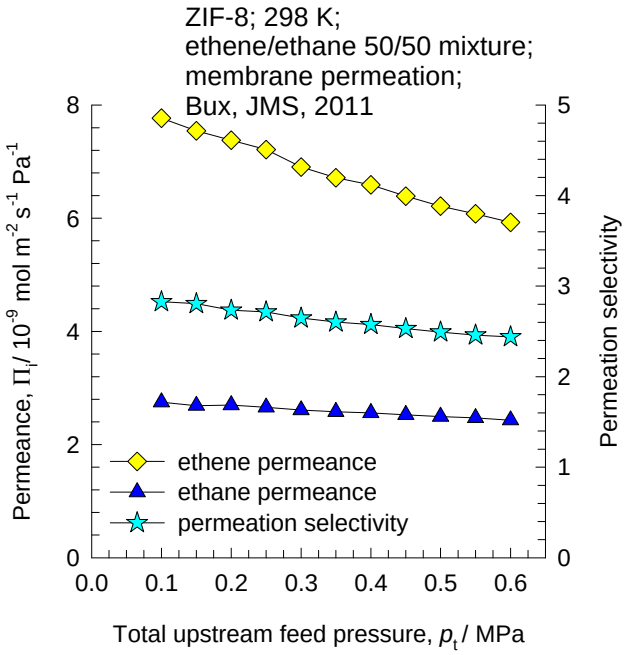

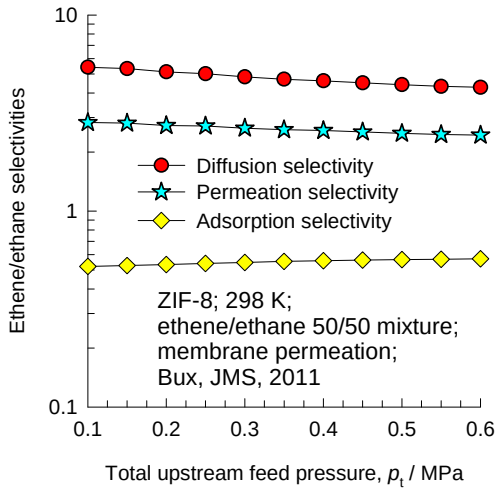

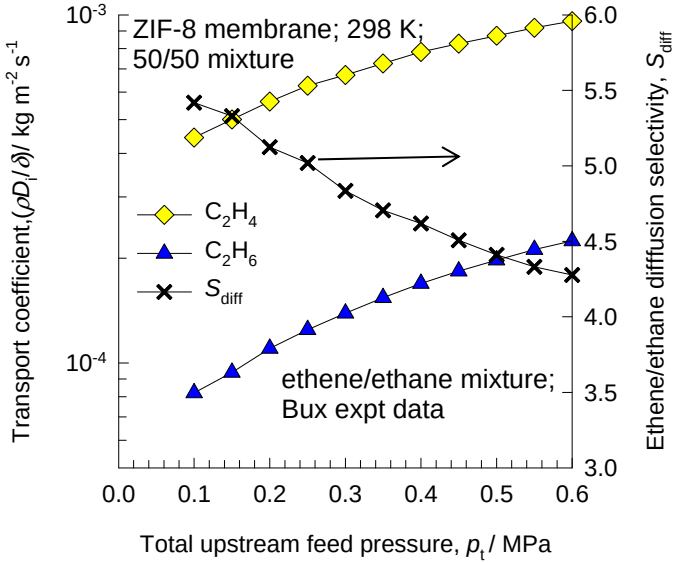

The data on membrane permeances are obtained from:

H. Bux, C. Chmelik, R. Krishna, J. Caro, Ethene/Ethane Separation by the MOF Membrane ZIF-8: Molecular Correlation of Permeation, Adsorption, Diffusion, J. Membr. Sci. 369 (2011) 284-289.

The calculations of S_{ads} are on the basis of IAST, with dual-Langmuir-Freundlich fits of pure component isotherms.

The transport coefficients are calculated from $$\frac{\rho D_i}{\delta} = \frac{\Pi_i}{\frac{q_i}{p_i}}$$

with the molar loadings q_i at the upstream face determined from IAST calculations.

ZIF-8 propene/propane mixture permeances and transport coefficients

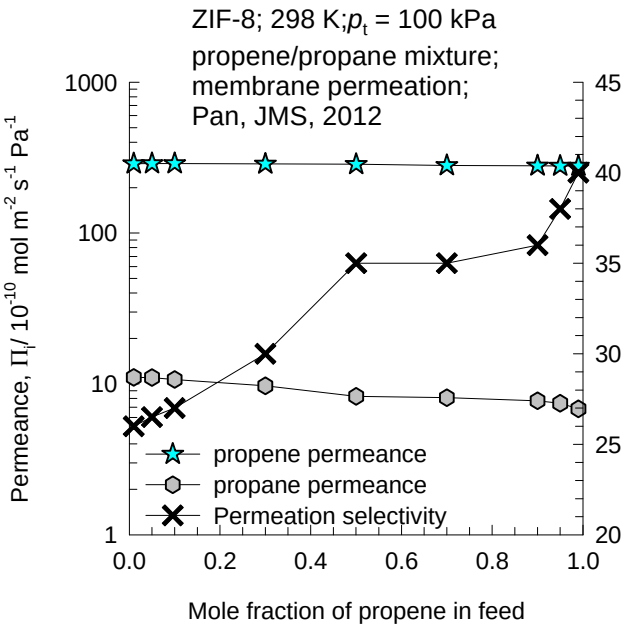

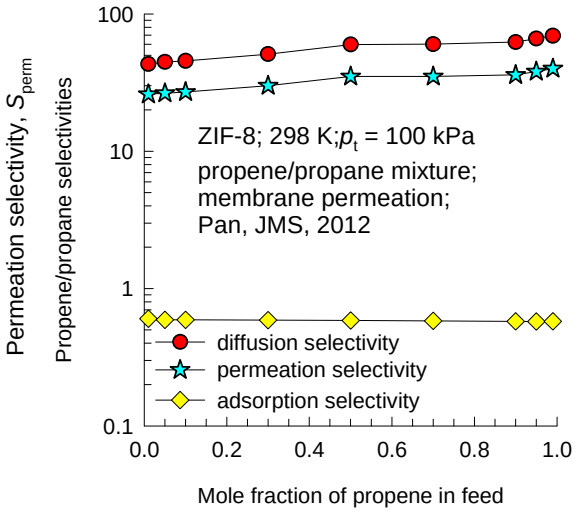

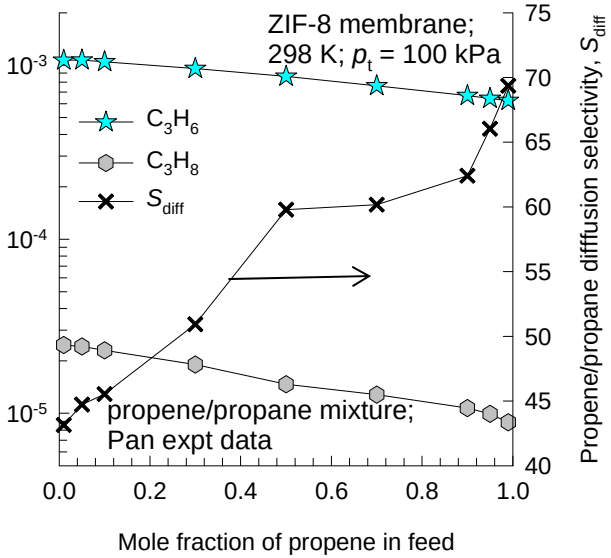

The data on membrane permeances are obtained from:

Y. Pan, T. Li, G. Lestari, Z. Lai, Effective Separation of Propylene/Propane Binary Mixtures by ZIF-8 Membranes, J. Membr. Sci. 390-391 (2012) 93-98.

The calculations of S_{ads} are on the basis of IAST, with dual-Langmuir-Freundlich fits of pure component isotherms.

The transport coefficients are calculated from $$\frac{\rho D_i}{\delta} = \frac{\Pi_i}{\frac{q_i}{p_i}}$$

with the molar loadings q_i at the upstream face determined from IAST calculations.

ZIF-8 ethane/ethane diffusion at 298 K: IRM experimental data

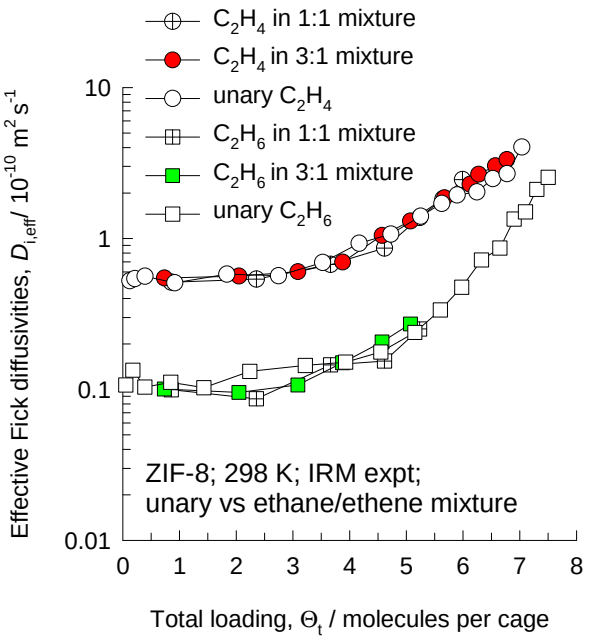

The IRM experimental data are re-plotted using the information in:

H. Bux, C. Chmelik, R. Krishna, J. Caro, Ethene/Ethane Separation by the MOF Membrane ZIF-8: Molecular Correlation of Permeation, Adsorption, Diffusion, J. Membr. Sci. 369 (2011) 284-289.

1D mesoporous channels

BTP-COF landscape

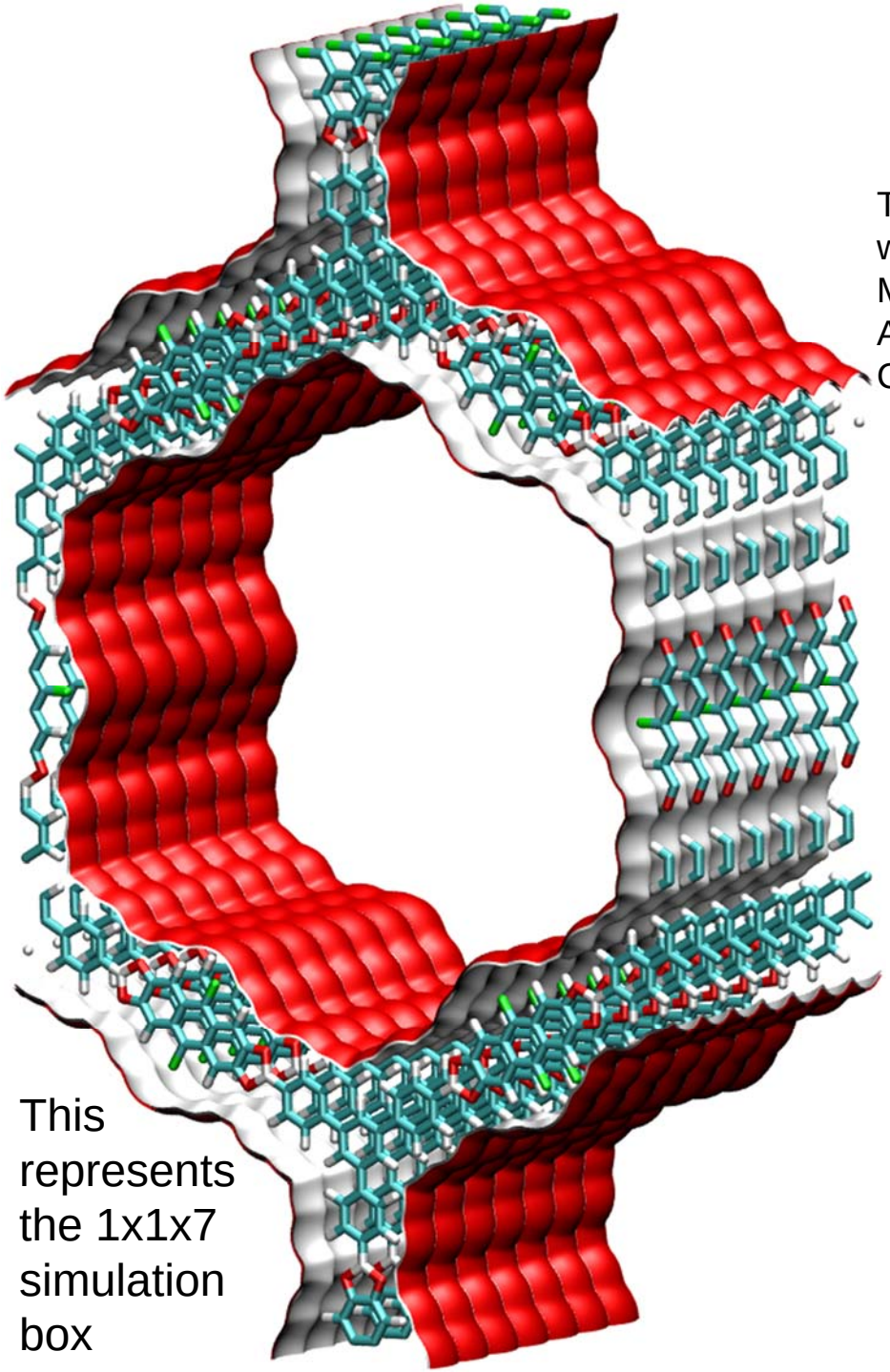

This represents the 1x1x7 simulation box

The crystallographic structural information for BTP-COF was obtained from
M. Dogru, A. Sonnauer, A. Gavryushin, P. Knochel, T. Bein, A Covalent Organic Framework with 4 nm open pores, Chem. Commun. 47 (2011) 1707-1709.

	BTP-COF
a /Å	43.65
b /Å	75.604
c /Å	3.52
Cell volume / Å^3	11616.4
conversion factor for [molec/uc] to [mol per kg Framework]	0.3403
conversion factor for [molec/uc] to [kmol/m^3]	0.1900
ρ [kg/m3]	420.0831
MW unit cell [g/mol(framework)]	2938.67
ϕ, fractional pore volume	0.752
open space / Å^3/uc	8738.7
Pore volume / cm^3/g	1.791
Surface area /m^2/g	
DeLaunay diameter /Å	34.26

BTP-COF force field for framework atoms

. Lennard-Jones parameters for the framework atoms of BTP-COF. The framework charges of BTP-COF were estimated using the group-contribution procedure based on quantum mechanical calculations described by Q. Xu, C. Zhong (A General Approach for Estimating Framework Charges in Metal-Organic Frameworks, J. Phys. Chem. C 114 (2010) 5035-5042), and C. Zheng, C. Zhong, (Estimation of Framework Charges in Covalent Organic Frameworks Using Connectivity-Based Atom Contribution Method, J. Phys. Chem. C 114 (2010) 9945-9951).

(pseudo-) atom	σ / Å	ε/k_B / K	charge
B	47.81	3.58	0.661
CA	47.86	3.47	-0.198
CB	47.86	3.47	0.198
CC	47.86	3.47	0.027
CD	47.86	3.47	-0.153
H	7.65	2.85	0.086
Methyl	108.00	3.76	0.335
O	48.16	3.03	-0.425

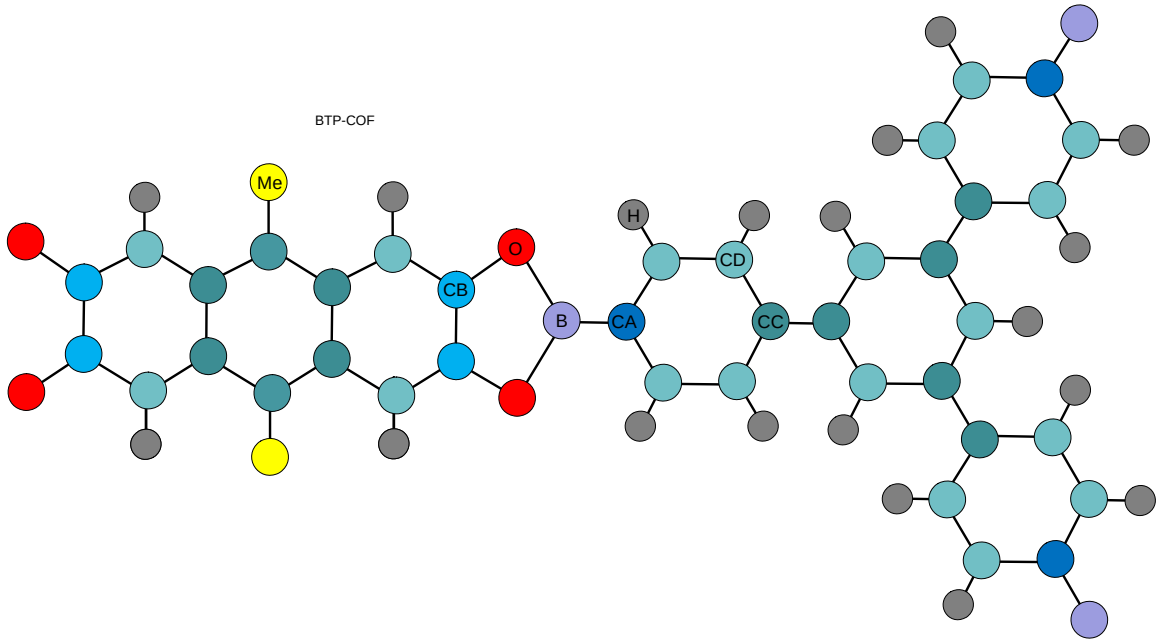

BTP-COF CBMC simulations of isotherms, and isosteric heats of adsorption

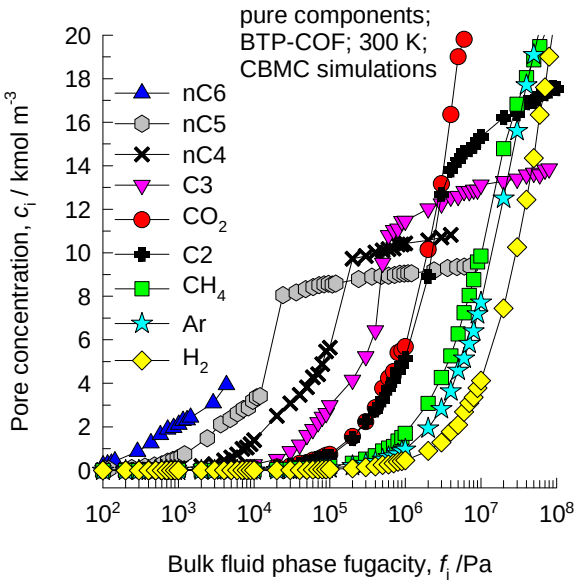

Note that C2 and C3 refer to saturated alkanes

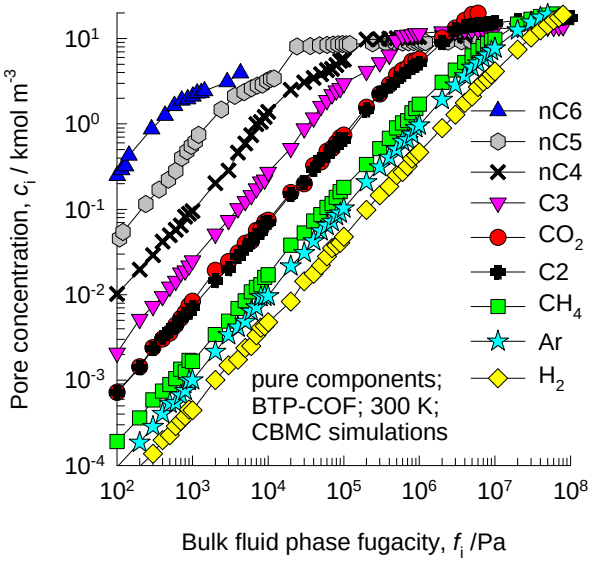

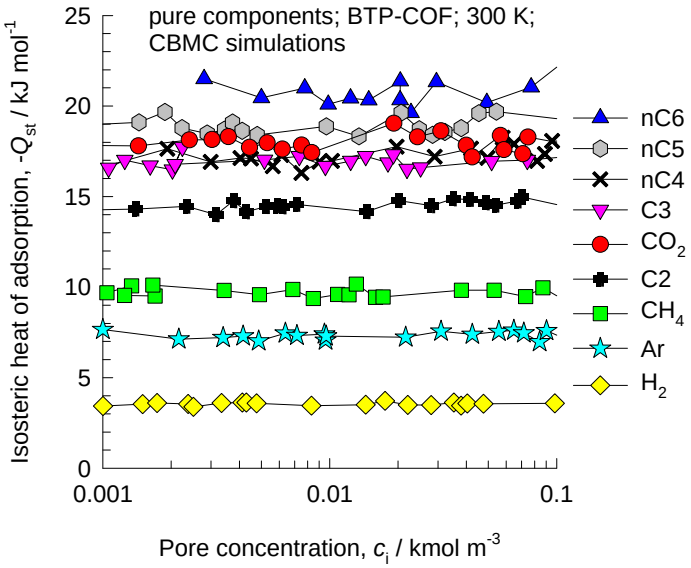

The isosteric heats of adsorption correlate with the Henry coefficients determined from CBMC

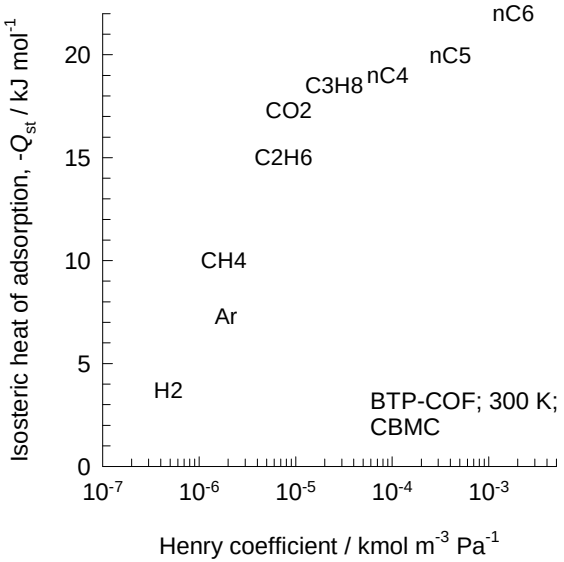

BTP-COF MD simulations of unary self- , and M-S diffusivities

Note that C2 and C3 refer to saturated alkanes

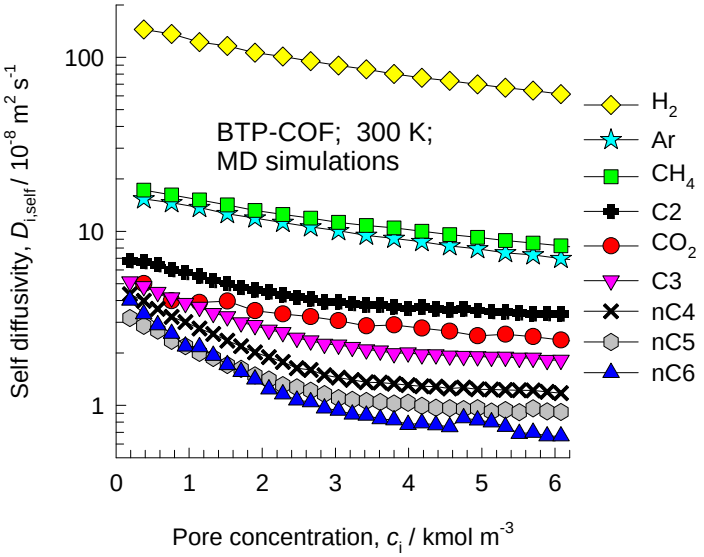

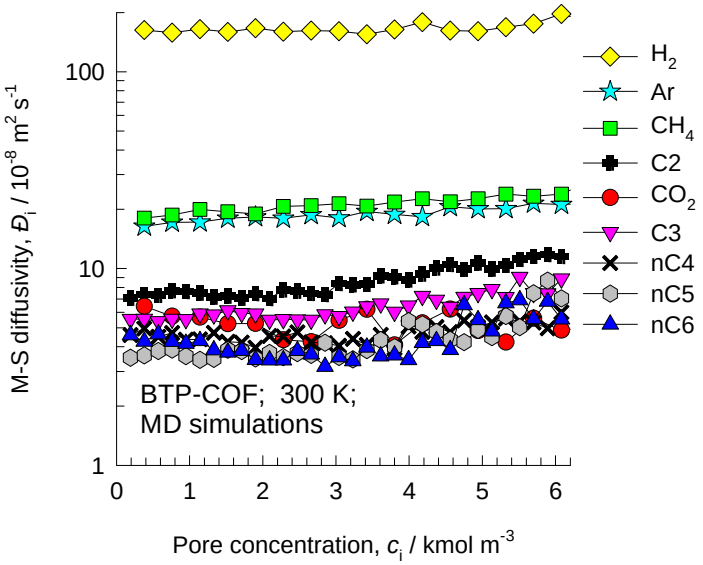

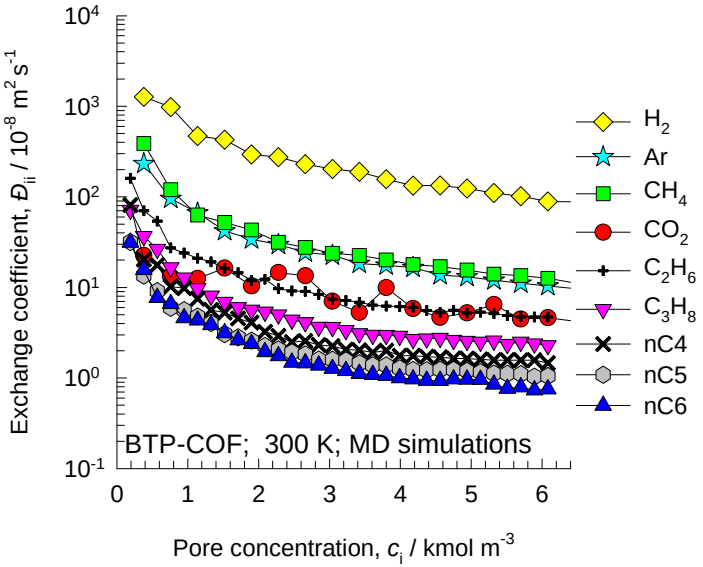

BTP-COF diffusivity vs binding energy

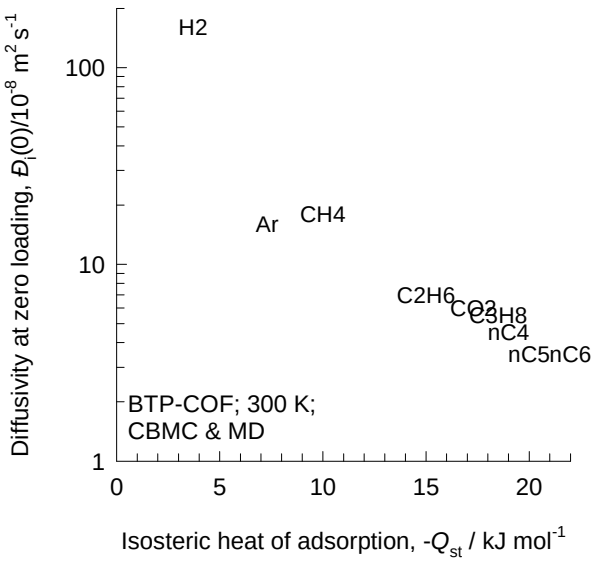

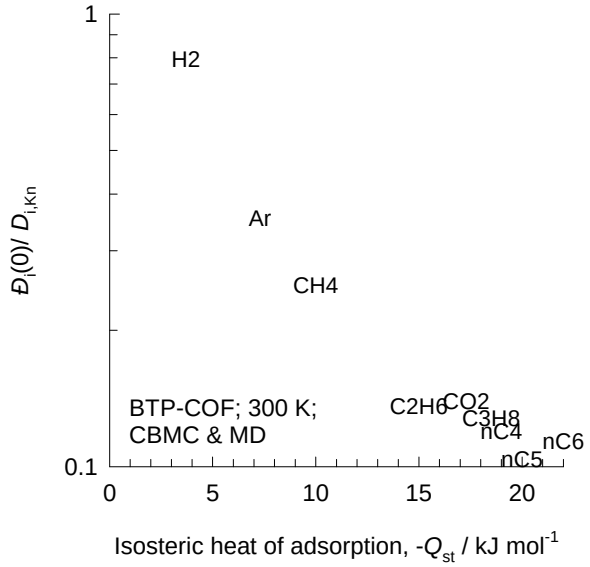

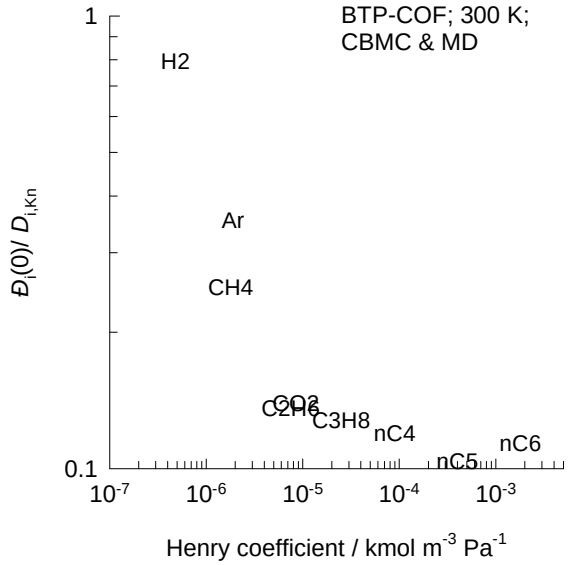

2 nm pore

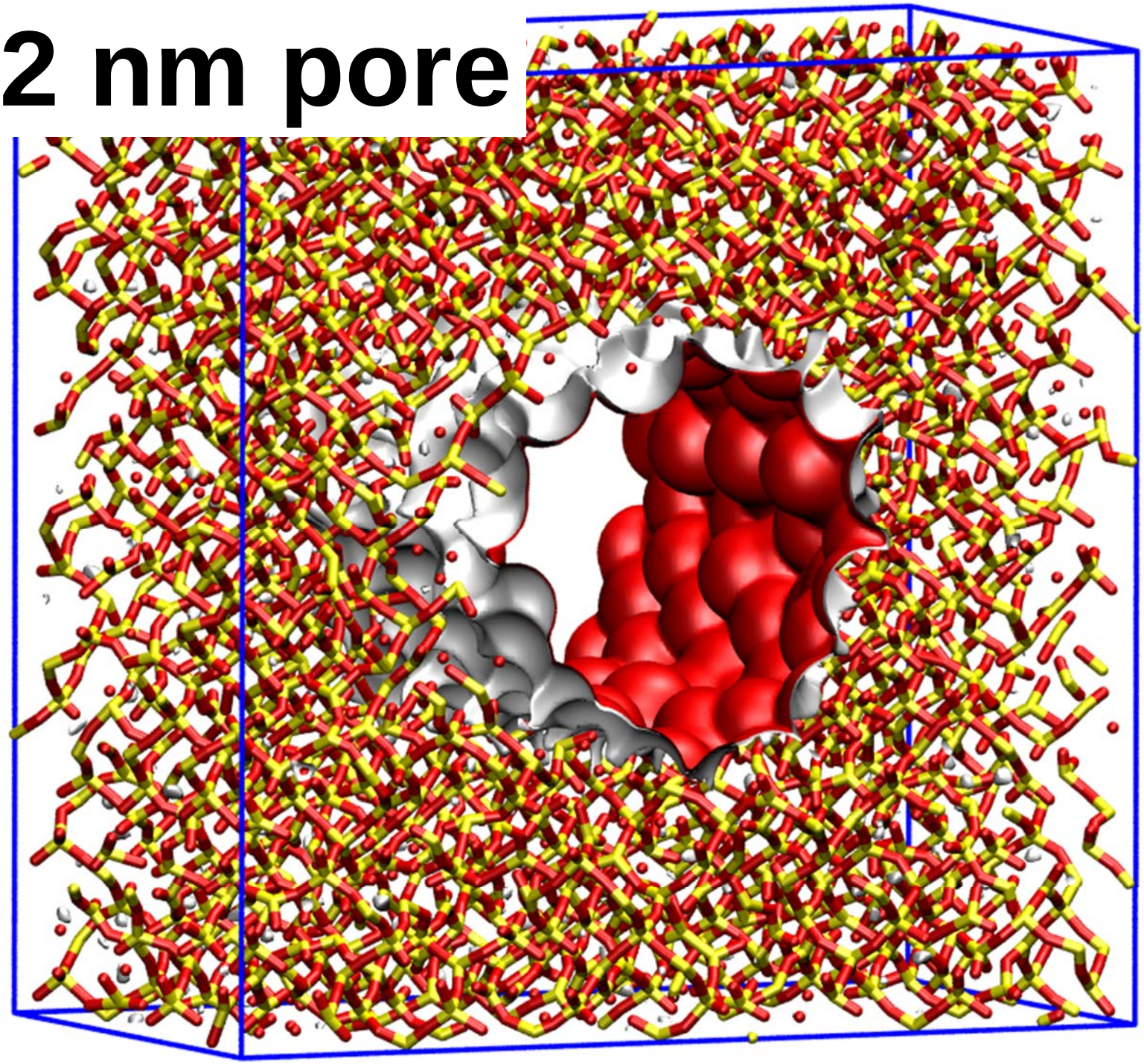

20 Å silica pore CBMC simulations of isotherms, and thermodynamic factors

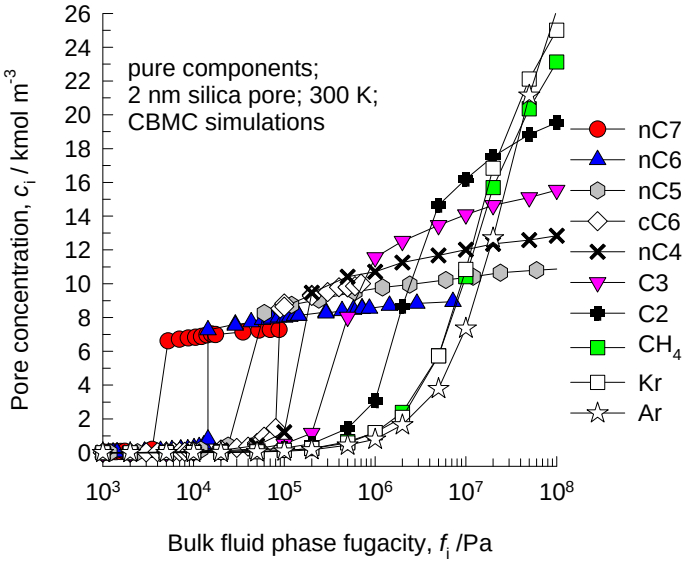

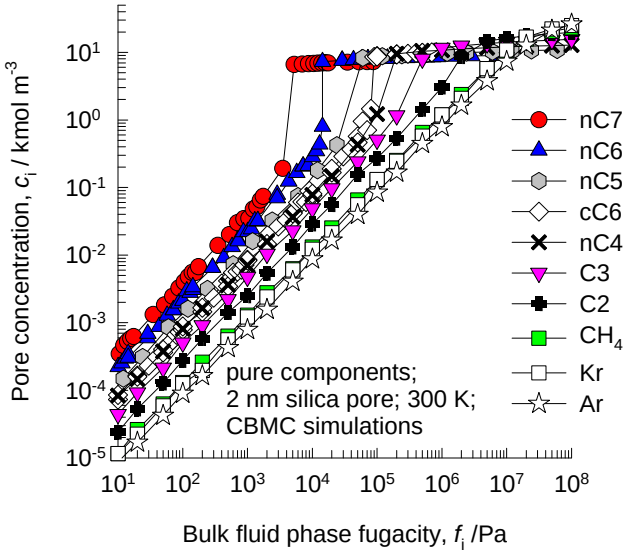

Note that C2 and C3 above refer to saturated alkanes
cC6 refers to cyclohexane

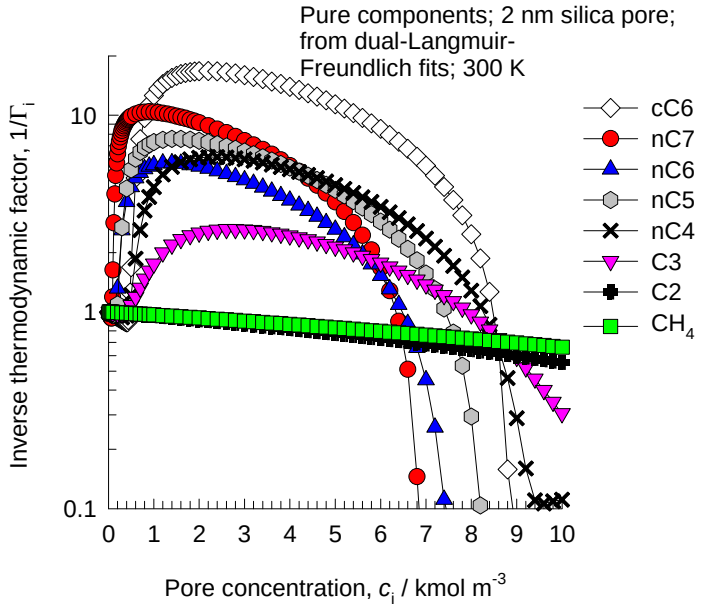

20 Å silica pore MD simulations of unary self- , and M-S diffusivities

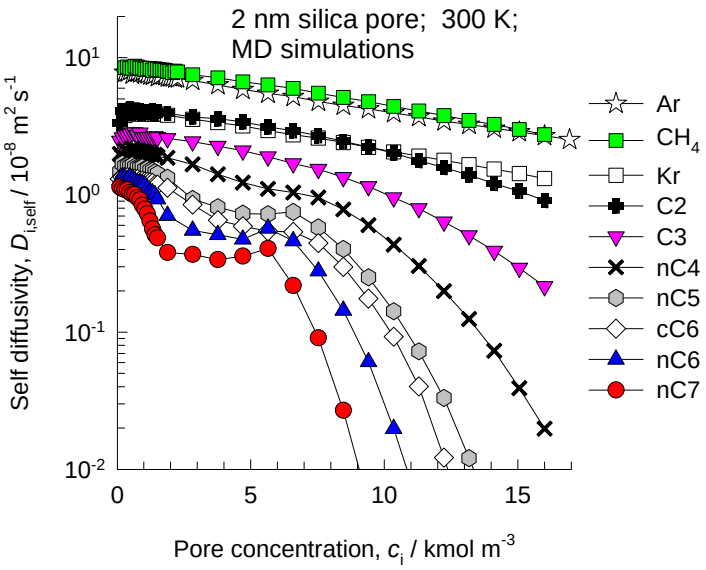

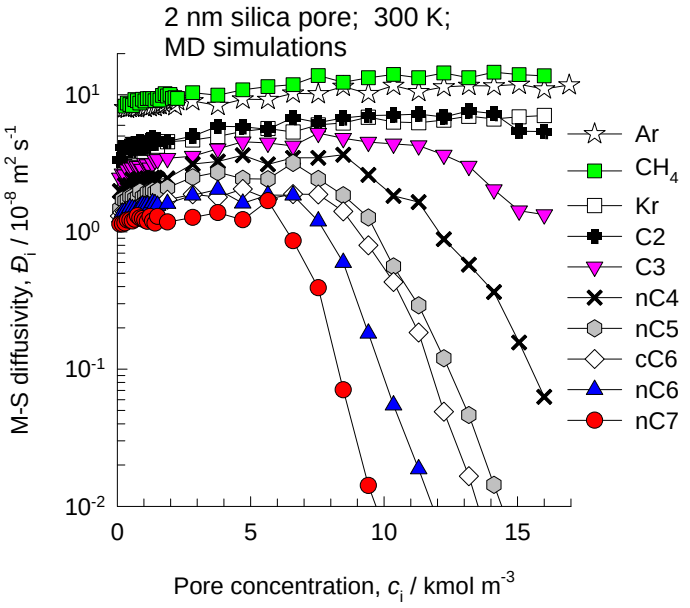

Note that C2 and C3 above refer to saturated alkanes

cC6 refers to cyclohexane

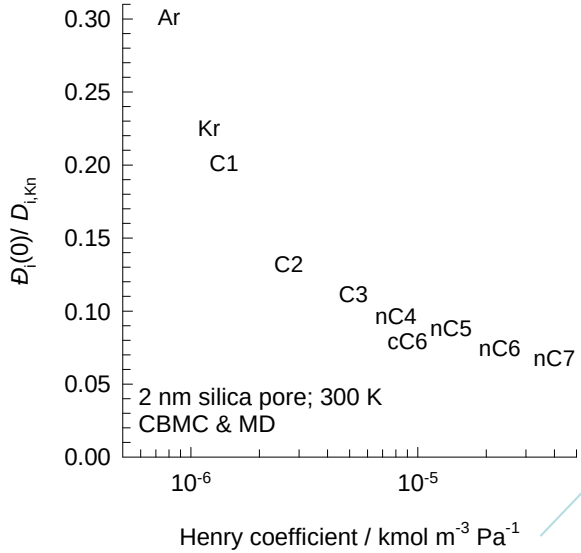

The Henry coefficients are determined from the isotherm data, at low fugacities.

The Henry coefficients are used here in place of the isosteric heats of adsorption.

Diffusivity of CH_4 and Ar in 20 Å and 30 Å silica pores

MD simulations of zero-loading diffusivities at various *T*

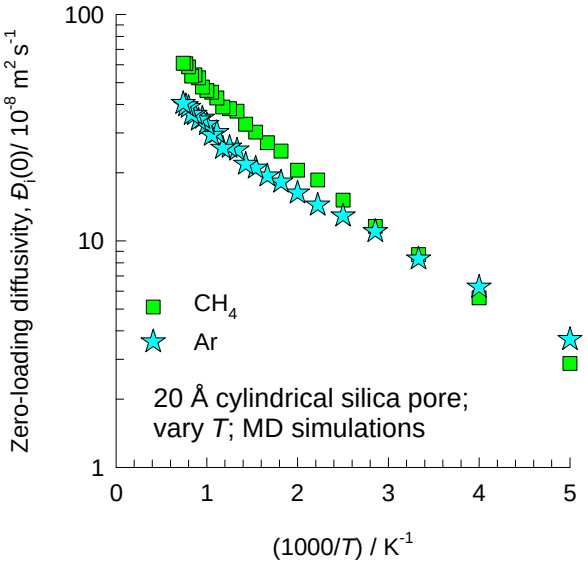

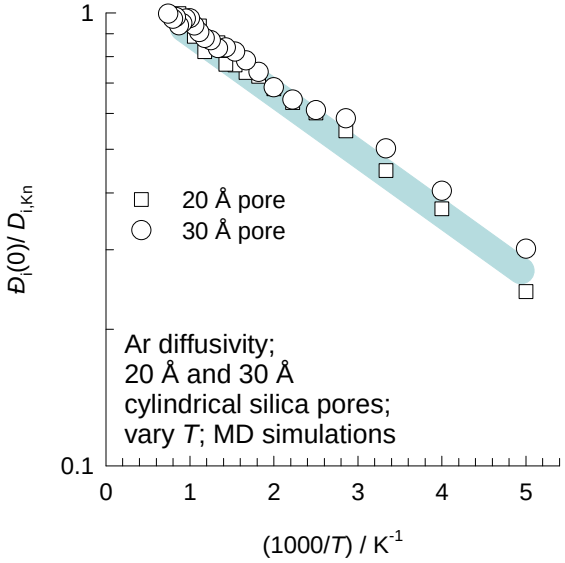

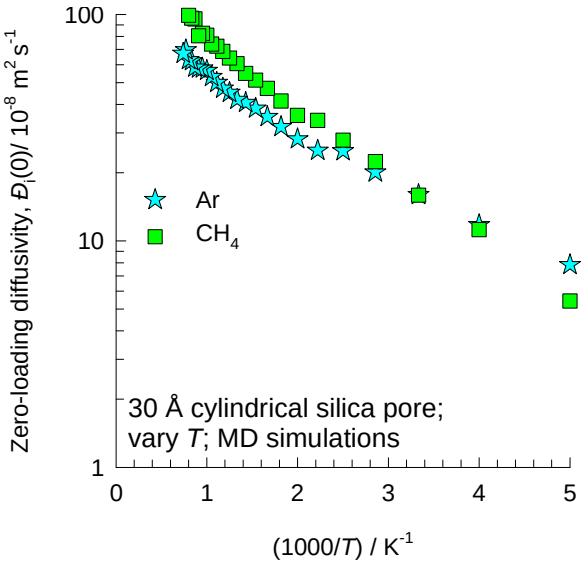

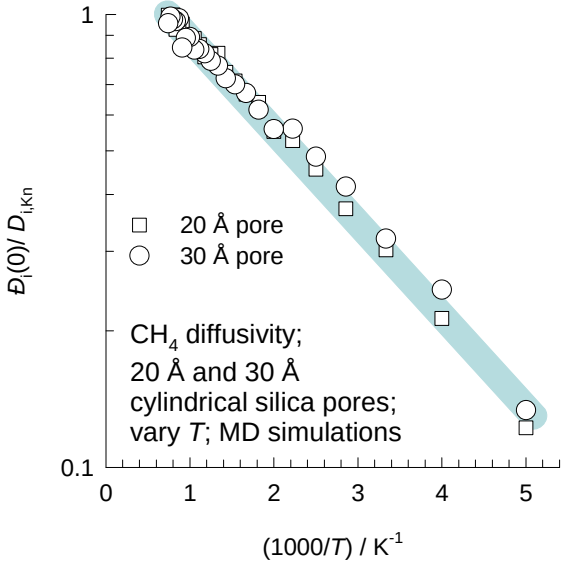

1D micro-porous channels

AFI landscapes

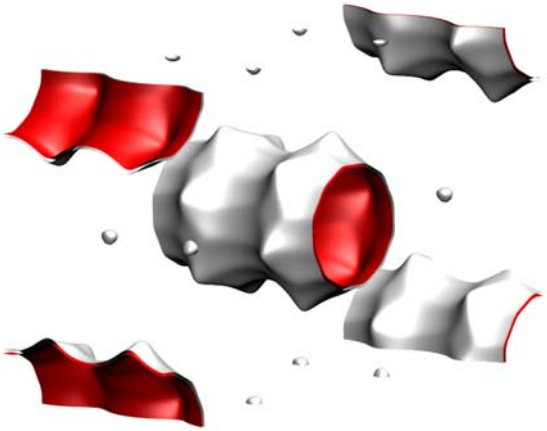

12-ring
1D channel of AFI

Snapshots showing location of CH_4 and CO_2

Structural information from: C. Baerlocher, L.B. McCusker, Database of Zeolite Structures, International Zeolite Association, http://www.iza-structure.org/databases/

AFI pore dimensions

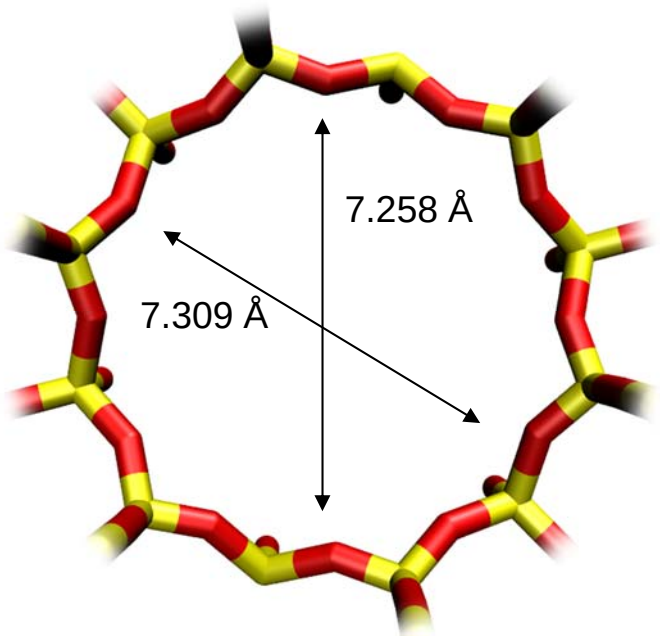

	AFI
a /Å	23.774
b /Å	13.726
c /Å	8.484
Cell volume / Å^3	2768.515
conversion factor for [molec/uc] to [mol per kg Framework]	0.3467
conversion factor for [molec/uc] to [kmol/m^3]	2.1866
ρ [kg/m3]	1729.876
MW unit cell [g/mol(framework)]	2884.07
ϕ, fractional pore volume	0.274
open space / Å^3/uc	759.4
Pore volume / cm^3/g	0.159
Surface area /m^2/g	466.0
DeLaunay diameter /Å	7.26

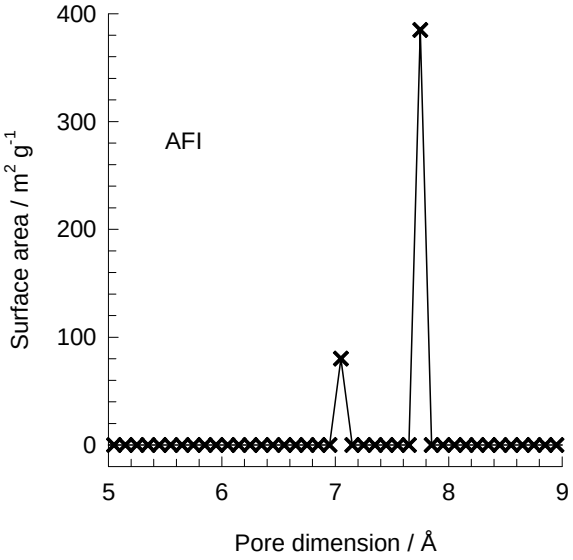

This plot of surface area versus pore dimension is determined using a combination of the DeLaunay triangulation method for pore dimension determination, and the procedure of Düren for determination of the surface area.

AFI CBMC simulations of isotherms, and isosteric heats of adsorption

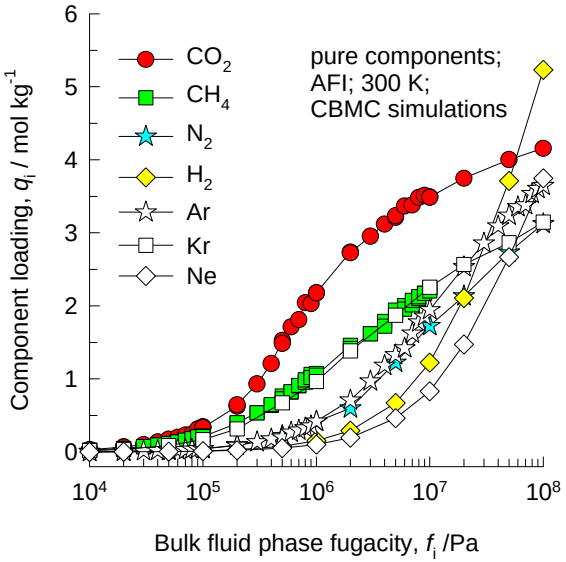

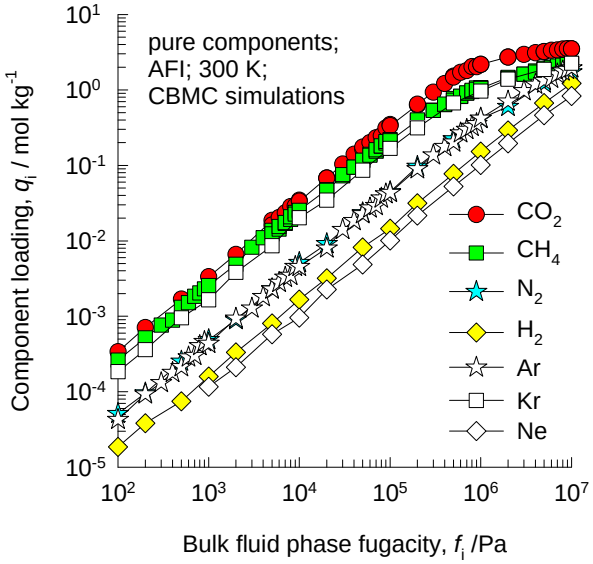

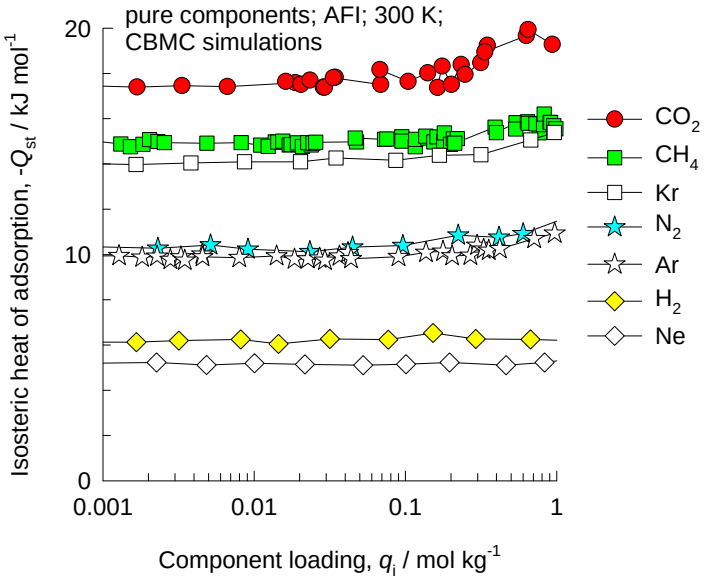

AFI MD simulations of unary self- , and M-S diffusivities

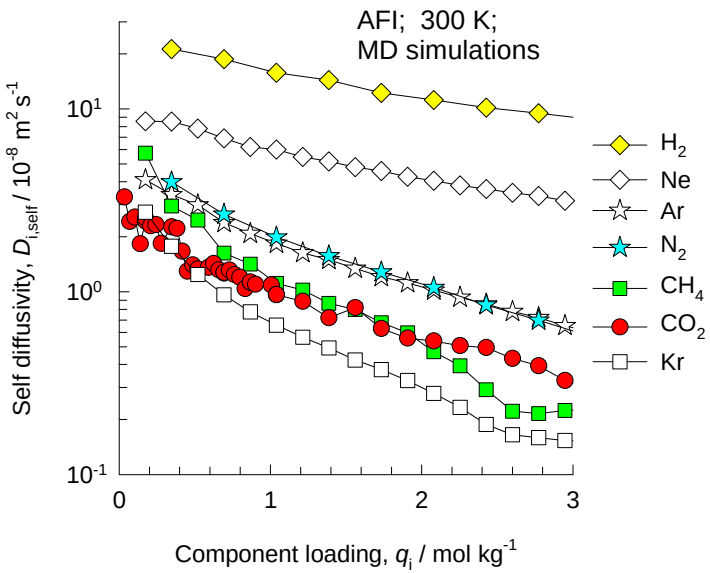

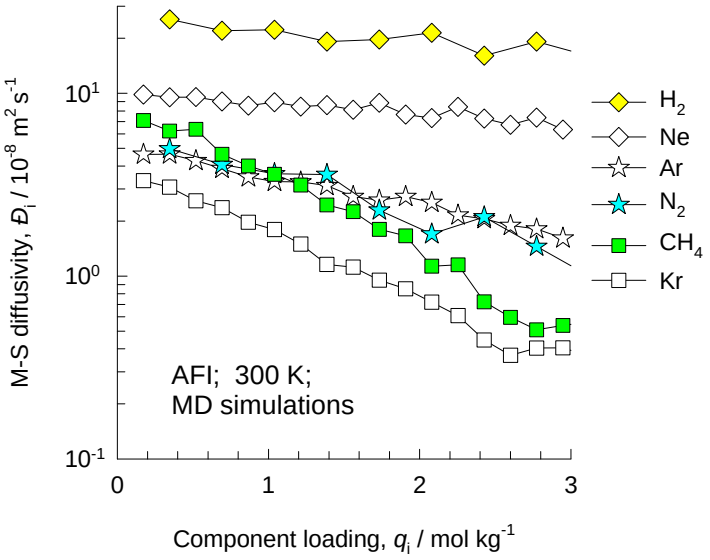

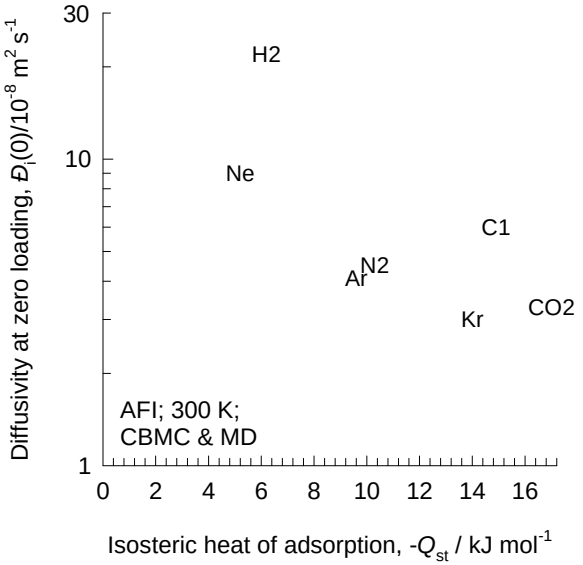

MTW pore landscape

MTW has 1D 12-ring channels

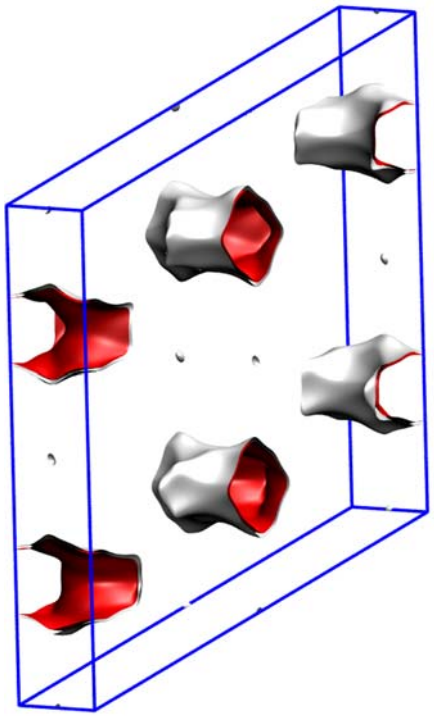

Structural information from: C. Baerlocher, L.B. McCusker, Database of Zeolite Structures, International Zeolite Association, http://www.iza-structure.org/databases/

MTW pore dimensions

This plot of surface area versus pore dimension is determined using a combination of the DeLaunay triangulation method for pore dimension determination, and the procedure of Düren for determination of the surface area.

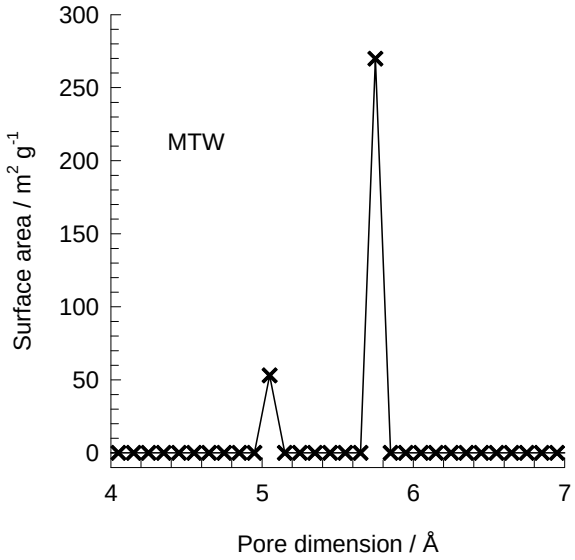

MTW has 1D, 12-ring channels

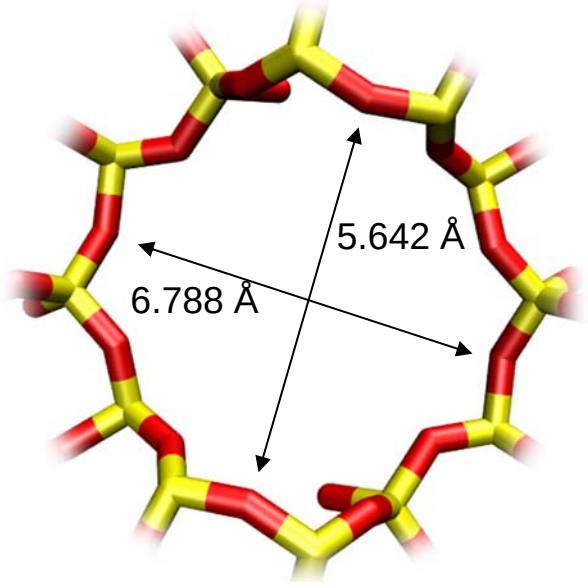

	MTW
a /Å	24.863
b /Å	5.012
c /Å	24.326
Cell volume / Å^3	2887.491
conversion factor for [molec/uc] to [mol per kg Framework]	0.2972
conversion factor for [molec/uc] to [kmol/m^3]	2.6759
ρ [kg/m3]	1935.031
MW unit cell [g/mol(framework)]	3364.749
ϕ, fractional pore volume	0.215
open space / Å^3/uc	620.6
Pore volume / cm^3/g	0.111
Surface area /m^2/g	323.0
DeLaunay diameter /Å	5.69

MTW MD simulations of unary self- , and M-S diffusivities

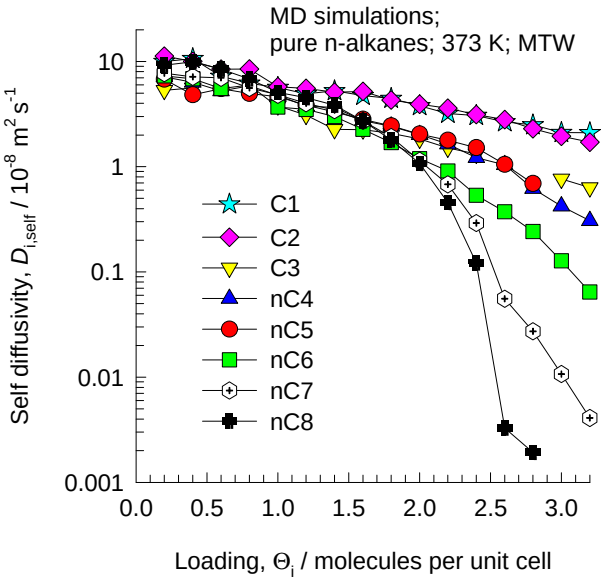

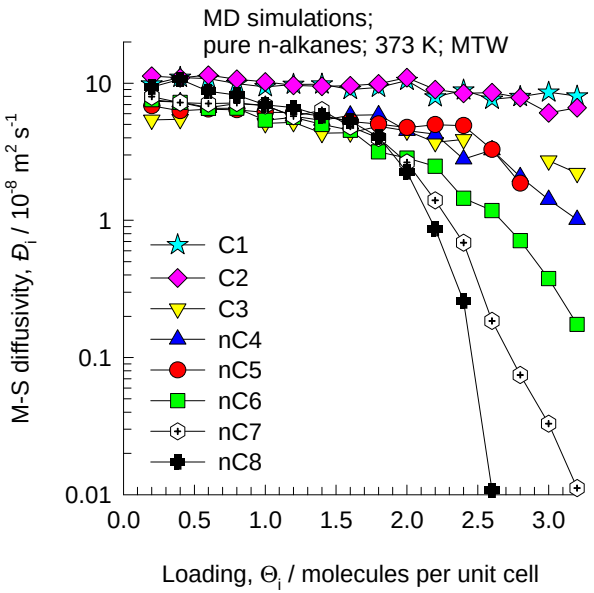

TON pore landscape

10-ring 1D channel of TON

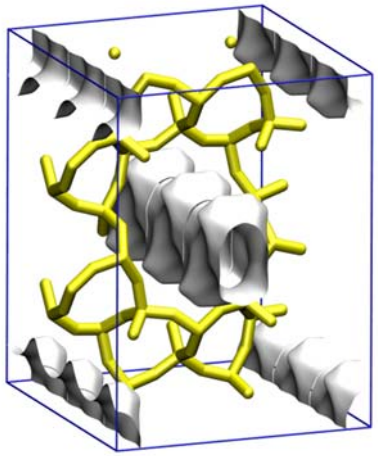

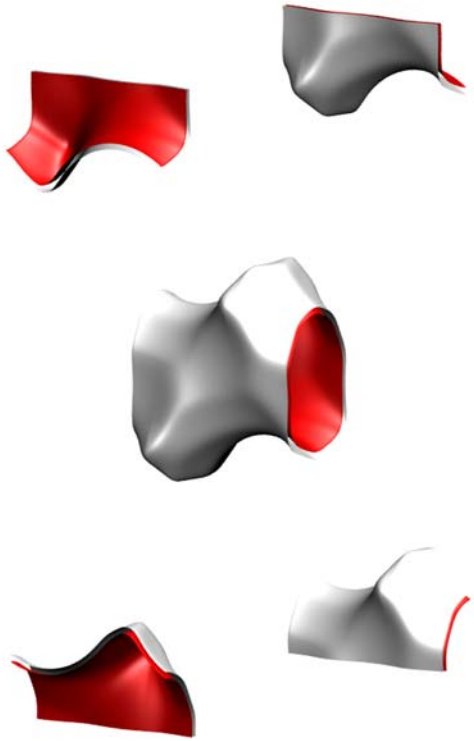

Structural information from: C. Baerlocher, L.B. McCusker, Database of Zeolite Structures, International Zeolite Association, http://www.iza-structure.org/databases/

TON pore dimensions

This plot of surface area versus pore dimension is determined using a combination of the DeLaunay triangulation method for pore dimension determination, and the procedure of Düren for determination of the surface area.

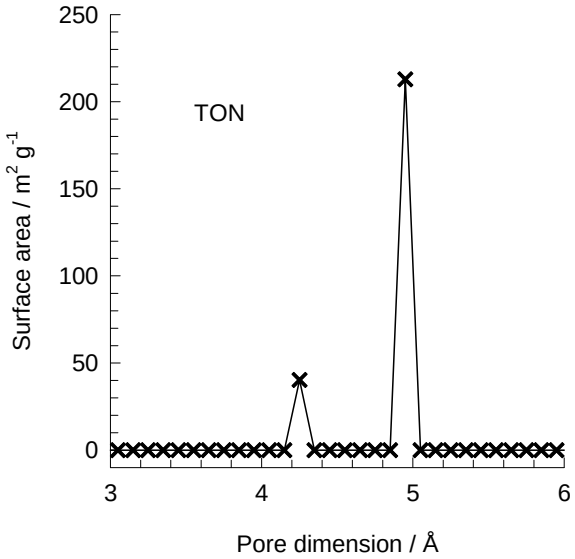

10-ring channel of TON

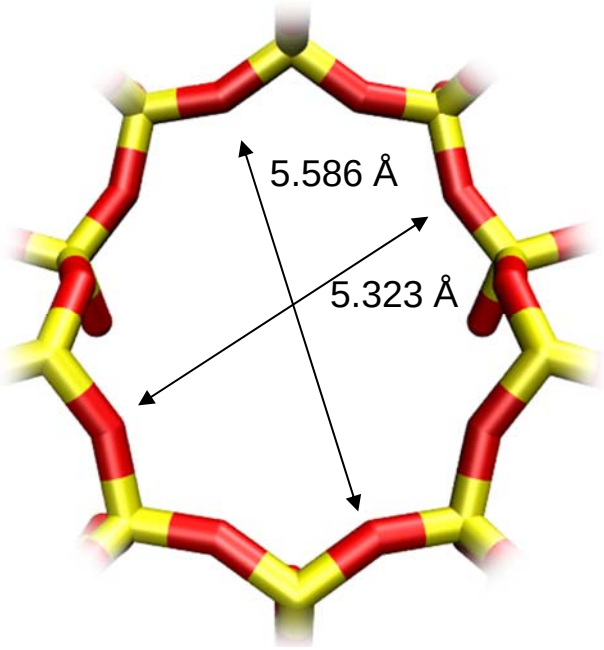

	TON
a /Å	13.859
b /Å	17.42
c /Å	5.038
Cell volume / Å^3	1216.293
conversion factor for [molec/uc] to [mol per kg Framework]	0.6935
conversion factor for [molec/uc] to [kmol/m^3]	7.1763
ρ [kg/m3]	1968.764
MW unit cell [g/mol(framework)]	1442.035
ϕ, fractional pore volume	0.190
open space / Å^3/uc	231.4
Pore volume / cm^3/g	0.097
Surface area /m^2/g	253.0
DeLaunay diameter /Å	4.88

MgMOF-74 pore landscapes

The structural information on MgMOF-74 (= Mg_2(dobdc) = Mg\(dobdc = CPO-27-Mg) with dobdc = ($dobdc^{4-}$ = 2,5-dioxido-1,4-benzenedicarboxylate)) were obtained from

A.Ö. Yazaydın, R.Q. Snurr, T.H. Park, K. Koh, J. Liu, M.D. LeVan, A.I. Benin, P. Jakubczak, M. Lanuza, D.B. Galloway, J.J. Low, R.R. Willis, Screening of Metal-Organic Frameworks for Carbon Dioxide Capture from Flue Gas using a Combined Experimental and Modeling Approach, J. Am. Chem. Soc. 131 (2009) 18198-18199.

D. Britt, H. Furukawa, B. Wang, T.G. Glover, O.M. Yaghi, Highly efficient separation of carbon dioxide by a metal-organic framework replete with open metal sites, Proc. Natl. Acad. Sci. U.S.A. 106 (2009) 20637-20640.

N.L. Rosi, J. Kim, M. Eddaoudi, B. Chen, M. O'Keeffe, O.M. Yaghi, Rod Packings and Metal-Organic Frameworks Constructed from Rod-Shaped Secondary Building Units, J. Am. Chem. Soc. 127 (2005) 1504-1518.

P.D.C. Dietzel, B. Panella, M. Hirscher, R. Blom, H. Fjellvåg, Hydrogen adsorption in a nickel based coordination polymer with open metal sites in the cylindrical cavities of the desolvated framework, Chem. Commun. (2006) 959-961.

P.D.C. Dietzel, V. Besikiotis, R. Blom, Application of metal–organic frameworks with coordinatively unsaturated metal sites in storage and separation of methane and carbon dioxide, J. Mater. Chem. 19 (2009) 7362-7370.

S.R. Caskey, A.G. Wong-Foy, A.J. Matzger, Dramatic Tuning of Carbon Dioxide Uptake via Metal Substitution in a Coordination Polymer with Cylindrical Pores, J. Am. Chem. Soc. 130 (2008) 10870-10871.

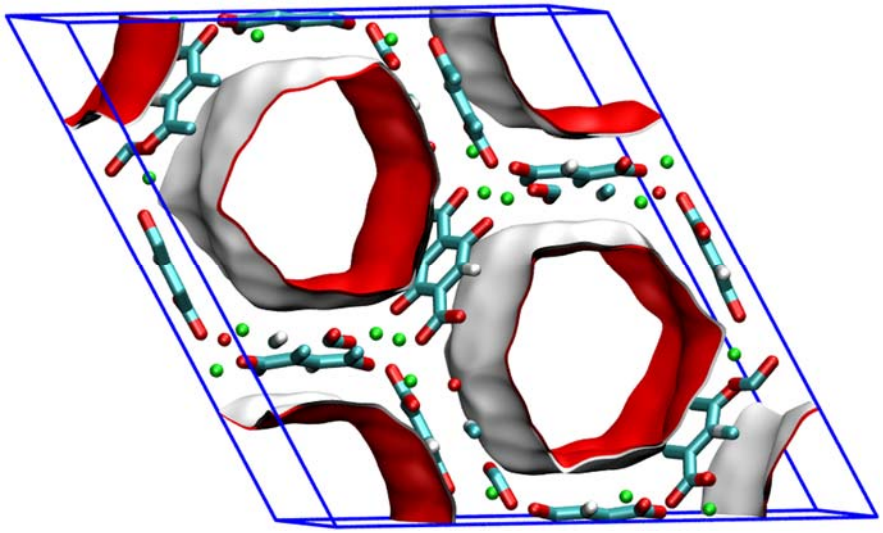

MgMOF-74 pore dimensions

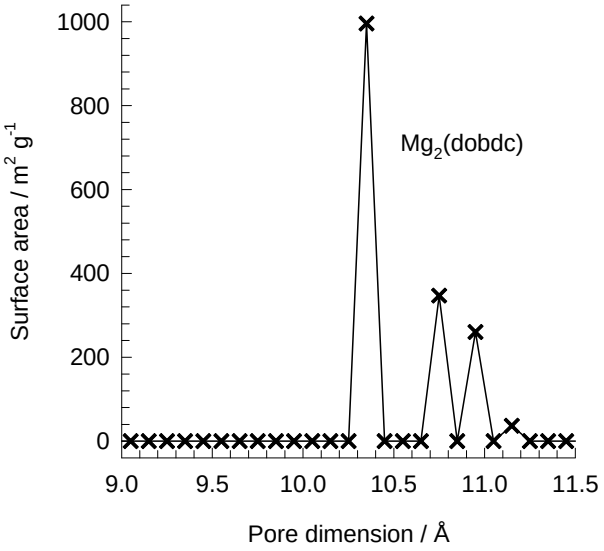

This plot of surface area versus pore dimension is determined using a combination of the DeLaunay triangulation method for pore dimension determination, and the procedure of Düren for determination of the surface area.

	MgMOF-74
a /Å	25.8621
b /Å	25.8621
c /Å	6.91427
Cell volume / Å^3	4005.019
conversion factor for [molec/uc] to [mol per kg Framework]	0.4580
conversion factor for [molec/uc] to [kmol/m^3]	0.5856
ρ [kg/m3]	905.367
MW unit cell [g/mol(framework)]	2183.601
ϕ, fractional pore volume	0.708
open space / Å^3/uc	2835.6
Pore volume / cm^3/g	0.782
Surface area /m^2/g	1640.0
DeLaunay diameter /Å	10.66

MgMOF-74 force field for framework atoms

Lennard-Jones parameters for atoms in MgMOF-74 based on the data from A.Ö. Yazaydın, R.Q. Snurr, T.H. Park, K. Koh, J. Liu, M.D. LeVan, A.I. Benin, P. Jakubczak, M. Lanuza, D.B. Galloway, J.J. Low, R.R. Willis (Screening of Metal-Organic Frameworks for Carbon Dioxide Capture from Flue Gas using a Combined Experimental and Modeling Approach, J. Am. Chem. Soc. 131 (2009) 18198-18199).

(pseudo-) atom	σ / Å	ε/k_B / K	charge
Mg	2.691	55.86	1.458
OA	3.033	48.16	-0.909
OB	3.033	48.16	-0.714
OC	3.033	48.16	-0.784
CA	3.473	47.86	0.800
CB	3.473	47.86	-0.260
CC	3.473	47.86	0.492
CD	3.473	47.86	-0.280
H	2.846	7.650	0.197

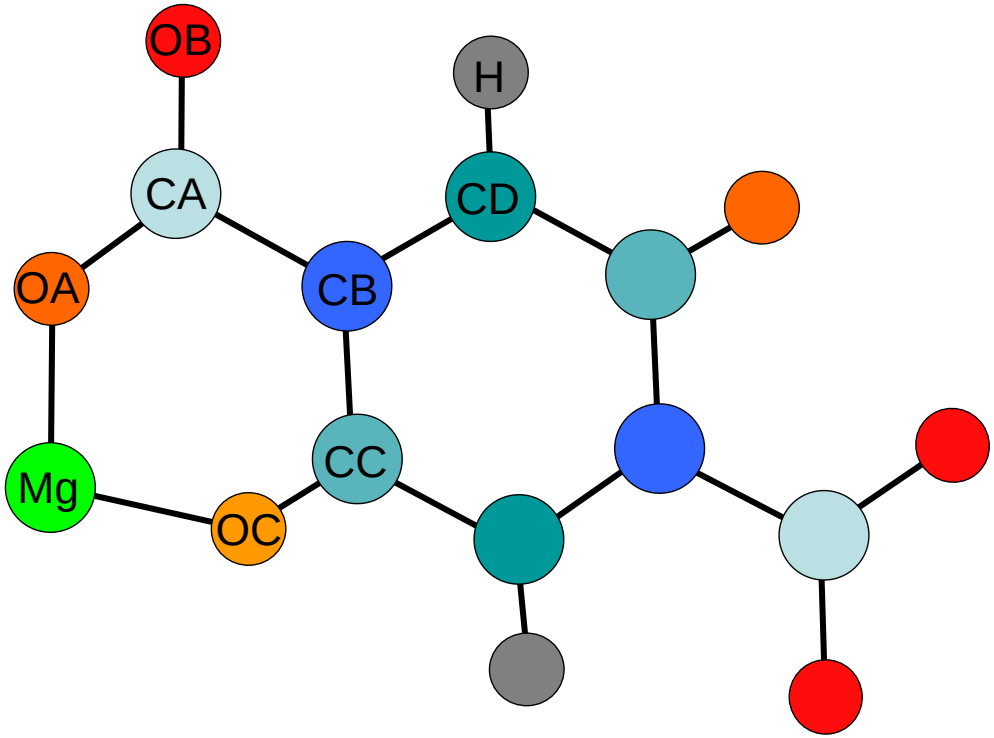

MgMOF-74 CBMC simulations of isotherms, and isosteric heats of adsorption

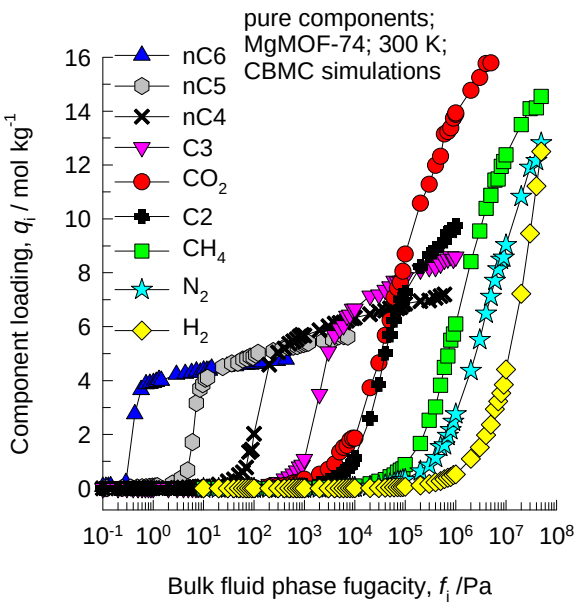

Note that C2 and C3 above refer to saturated alkanes.

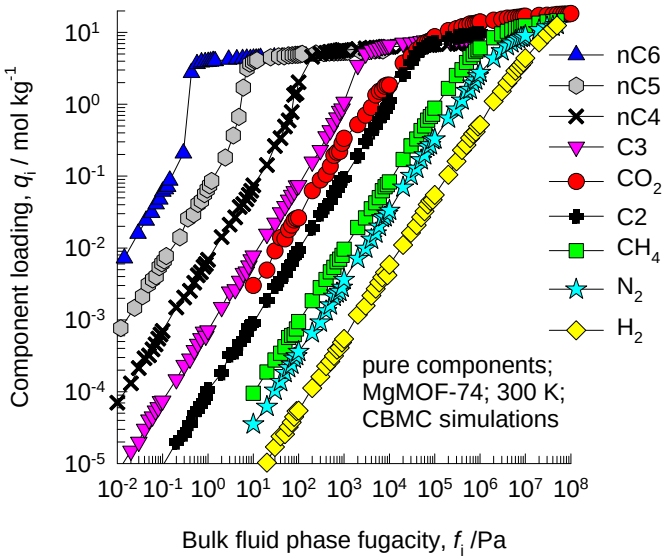

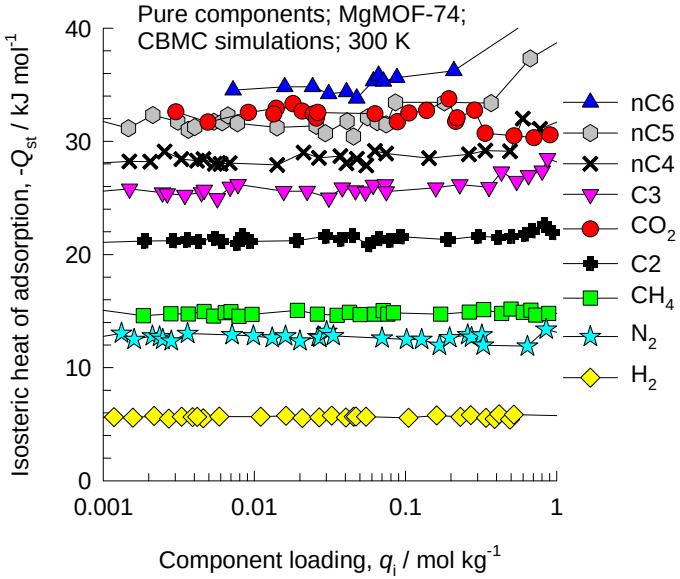

MgMOF-74 MD simulations of unary self- , and M-S diffusivities

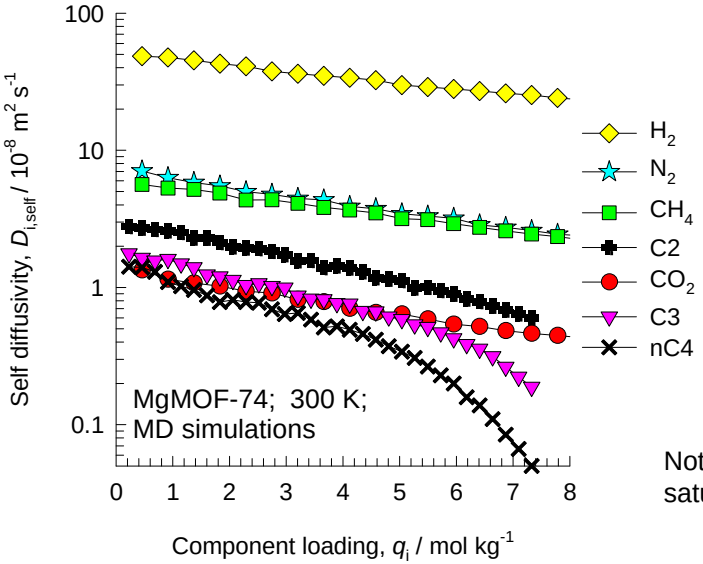

Note that C2 and C3 above refer to saturated alkanes.

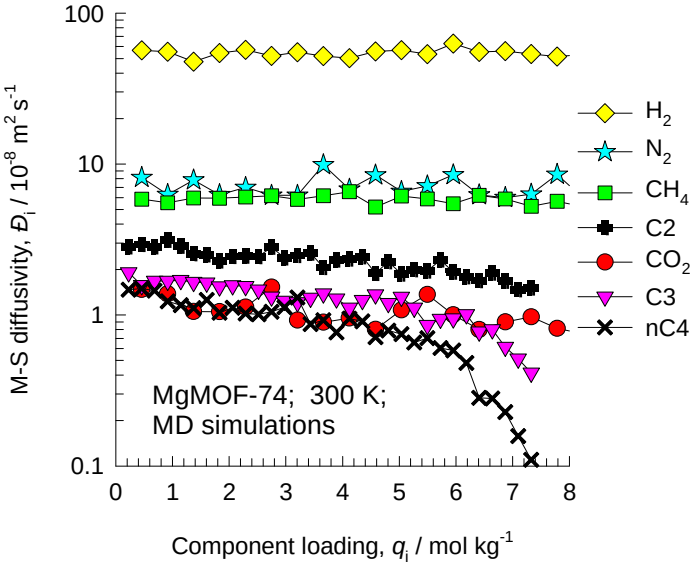

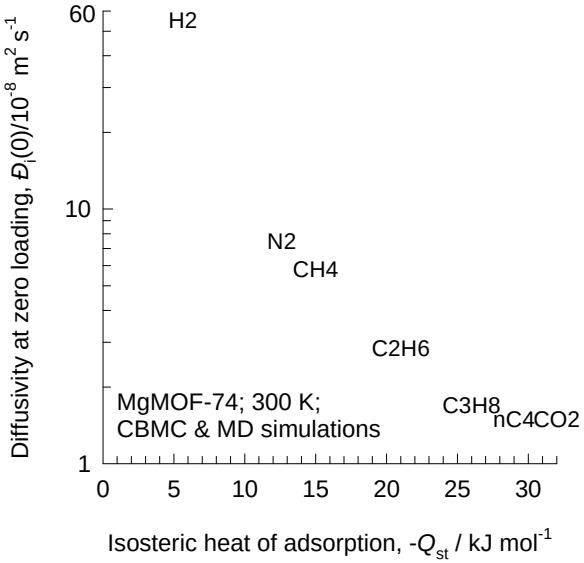

MgMOF-74 pure CO_2 isotherms; comparison with experiments

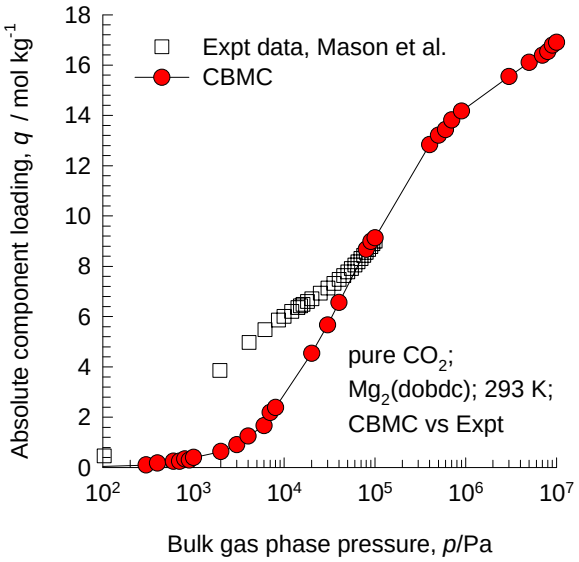

We note that for pressures exceeding 0.1 MPa, there is excellent agreement between the CBMC simulations and experiment. However, for pressures below 0.1 MPa, the experimental loadings are significantly higher than the simulated values. The reason for this deviation at pressures below 0.1 MPa can be traced to the fact that our force field implementation, following the work of Yazaydin et al.does not explicitly account for orbital interactions and polarization. Such effects are particularly strong in the low pressure region; the influence of polarization is of lesser importance at higher pressures. Put another way, we would expect the CBMC simulation results to be reasonably good for high pressure membrane operation with upstream pressures that are considerably in excess of 0.1 MPa.

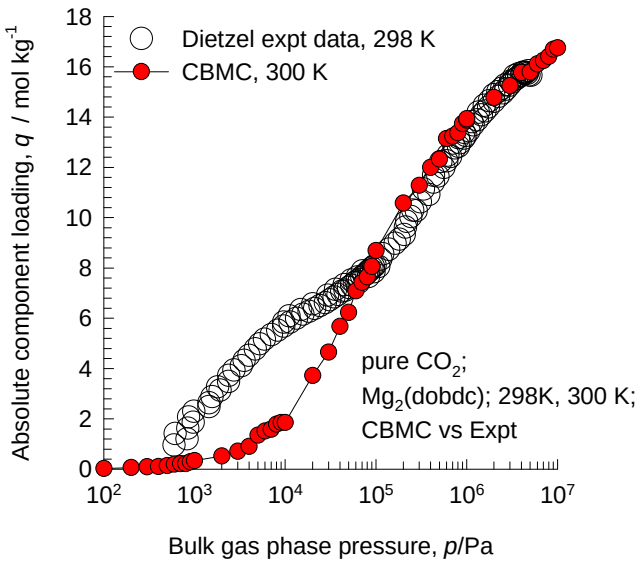

The experimental data are from:

P.D.C. Dietzel, V. Besikiotis, R. Blom, Application of metal–organic frameworks with coordinatively unsaturated metal sites in storage and separation of methane and carbon dioxide, J. Mater. Chem. 19 (2009) 7362-7370.

J.A. Mason, K. Sumida, Z.R. Herm, R. Krishna, J.R. Long, Evaluating Metal-Organic Frameworks for Post-Combustion Carbon Dioxide Capture via Temperature Swing Adsorption, Energy Environ. Sci. 4 (2011) 3030-3040.

Ab initio quantum chemical calculations are required to adequately capture the polarization effects and orbital interactions.

MgMOF-74 pure CO_2 isotherms; comparison with experiments

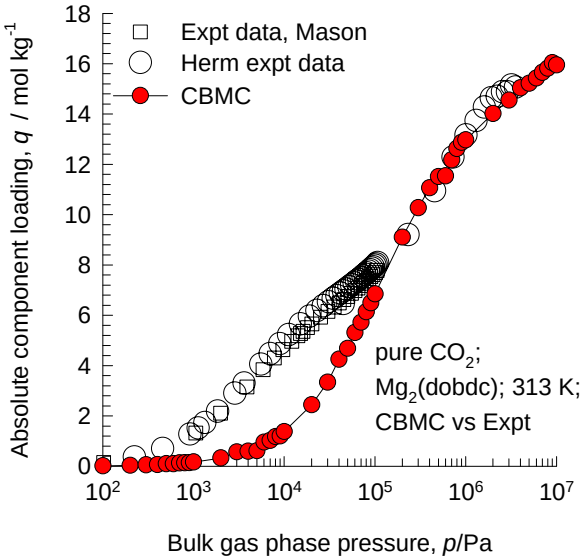

Our force field implementation, following the work of Yazaydin et al.does not explicitly account for orbital interactions and polarization. Such effects are particularly strong in the low pressure region; the influence of polarization is of lesser importance at higher pressures. Put another way, we would expect the CBMC simulation results to be reasonably good for high pressure membrane operation.

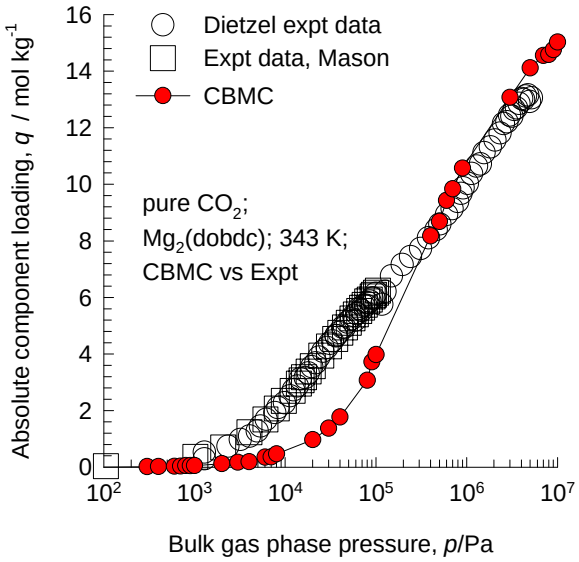

The experimental data are from:

Z.R. Herm, J.A. Swisher, B. Smit, R. Krishna, J.R. Long, Metal-Organic Frameworks as Adsorbents for Hydrogen Purification and Pre-Combustion Carbon Dioxide Capture, J. Am. Chem. Soc. 133 (2011) 5664-5667.

P.D.C. Dietzel, V. Besikiotis, R. Blom, Application of metal–organic frameworks with coordinatively unsaturated metal sites in storage and separation of methane and carbon dioxide, J. Mater. Chem. 19 (2009) 7362-7370.

J.A. Mason, K. Sumida, Z.R. Herm, R. Krishna, J.R. Long, Evaluating Metal-Organic Frameworks for Post-Combustion Carbon Dioxide Capture via Temperature Swing Adsorption, Energy Environ. Sci. 4 (2011) 3030-3040.

MgMOF-74 pure CO_2 isotherms; comparison with experiments

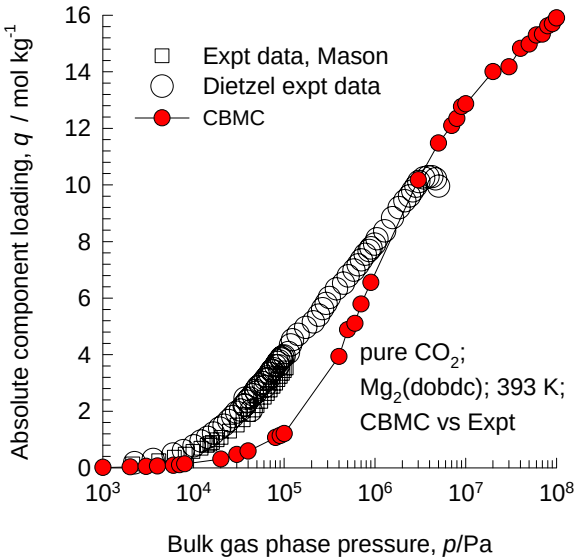

Our force field implementation, following the work of Yazaydin et al. does not explicitly account for orbital interactions and polarization. Such effects are particularly strong in the low pressure region; the influence of polarization is of lesser importance at higher pressures. Put another way, we would expect the CBMC simulation results to be reasonably good for high pressure membrane operation.

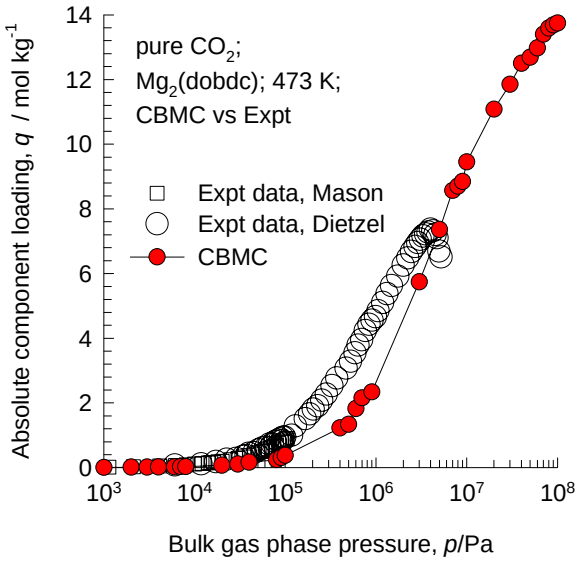

The experimental data are from:

P.D.C. Dietzel, V. Besikiotis, R. Blom, Application of metal–organic frameworks with coordinatively unsaturated metal sites in storage and separation of methane and carbon dioxide, J. Mater. Chem. 19 (2009) 7362-7370.

J.A. Mason, K. Sumida, Z.R. Herm, R. Krishna, J.R. Long, Evaluating Metal-Organic Frameworks for Post-Combustion Carbon Dioxide Capture via Temperature Swing Adsorption, Energy Environ. Sci. 4 (2011) 3030-3040.

MgMOF-74 pure CH_4 isotherms; comparison with experiments

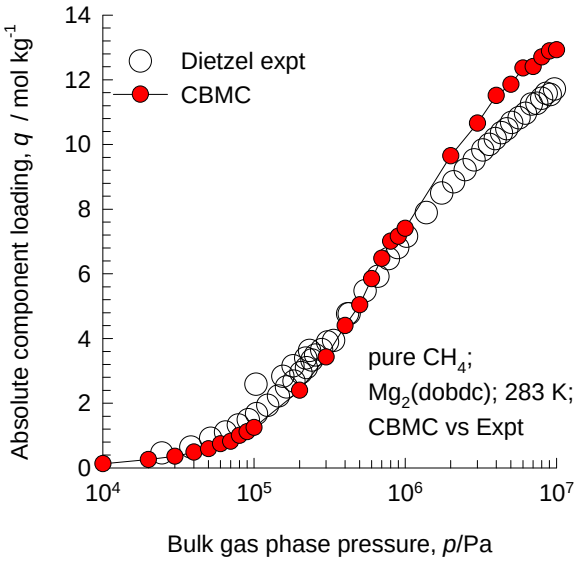

When the guest species do not have orbital interactions with the Mg atoms, as is the case with CH_4, the predictions of the CBMC simulations can be expected to be good.

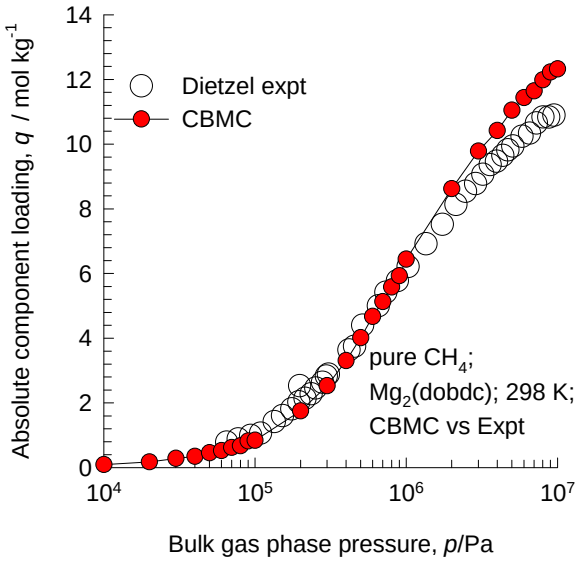

The experimental data are from:

P.D.C. Dietzel, V. Besikiotis, R. Blom, Application of metal–organic frameworks with coordinatively unsaturated metal sites in storage and separation of methane and carbon dioxide, J. Mater. Chem. 19 (2009) 7362-7370.

MgMOF-74 pure CH_4 isotherms; comparison with experiments

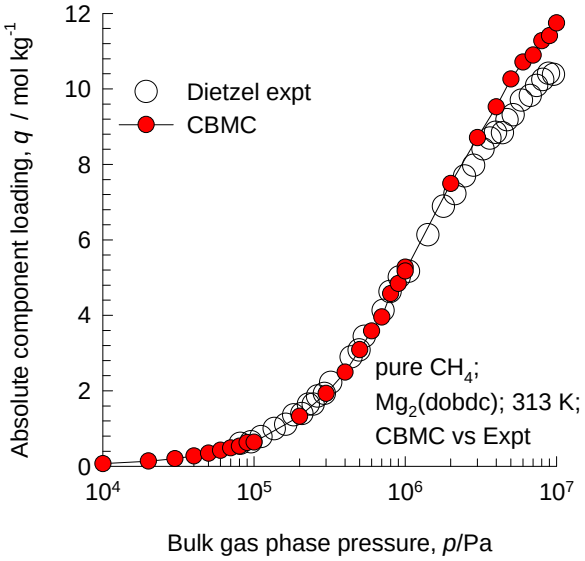

When the guest species do not have orbital interactions with the Mg atoms, as is the case with CH_4, the predictions of the CBMC simulations can be expected to be good.

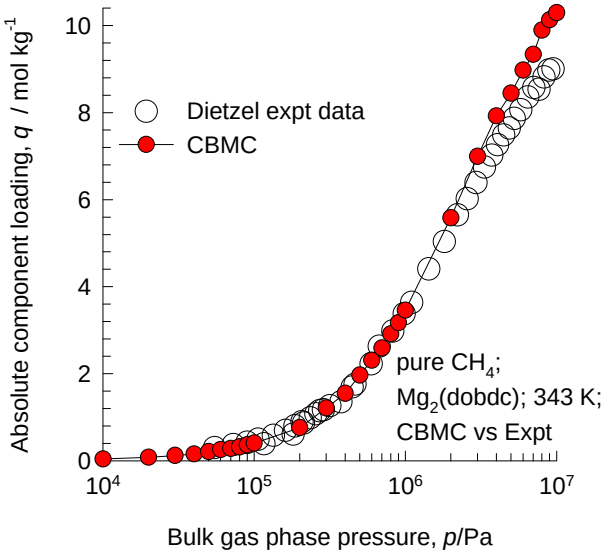

The experimental data are from:

P.D.C. Dietzel, V. Besikiotis, R. Blom, Application of metal–organic frameworks with coordinatively unsaturated metal sites in storage and separation of methane and carbon dioxide, J. Mater. Chem. 19 (2009) 7362-7370.

MgMOF-74 fits of experimental isotherms for CO_2, CH_4, ethene, ethane, propene, propane

Dual-Langmuir-Freundlich parameter fits for MgMOF-74 (= Mg_2(dobdc) = CPO-27-Mg).

$$q = q_{A,sat}\frac{b_A p^{\nu_A}}{1+b_A p^{\nu_A}} + q_{B,sat}\frac{b_B p^{\nu_B}}{1+b_B p^{\nu_B}};\quad b_A = b_{A0}\exp\left(\frac{E_A}{RT}\right);\quad b_B = b_{B0}\exp\left(\frac{E_B}{RT}\right)$$

Since our force field implementation, following the work of Yazaydin et al. does not explicitly account for orbital interactions and polarization the available experimental data for various temperatures were fitted.

	Site A				Site B			
	$q_{A,sat}$ mol kg^{-1}	b_{A0} Pa$^{-\nu_i}$	E_A kJ mol^{-1}	ν_A dimensionless	$q_{B,sat}$ mol kg^{-1}	b_{B0} Pa$^{-\nu_i}$	E_B kJ mol^{-1}	ν_B dimensionless
C_2H_4	3.1	2.15×10^{-12}	28	1.3	6.4	2.11×10^{-12}	45.2	1.07
C_2H_6	8.4	3.28×10^{-12}	34.5	1.2				
CH_4	11	7.48×10^{-10}	18.2	1	5	1.64×10^{-11}	18.2	1
C_3H_6	7.1	6.32×10^{-13}	55	1.04	1.7	2.17×10^{-14}	40	1.44
C_3H_8	1.9	2.22×10^{-11}	42	0.73	5.9	7.84×10^{-13}	42	1.41
CO_2	6.8	5.63×10^{-4}	42	1	9.9	2.23×10^{-6}	24	1

The isotherm fit parameters are on the basis of experimental data for variety of temperatures from:

Z.R. Herm, J.A. Swisher, B. Smit, R. Krishna, J.R. Long, Metal-Organic Frameworks as Adsorbents for Hydrogen Purification and Pre-Combustion Carbon Dioxide Capture, J. Am. Chem. Soc. 133 (2011) 5664-5667.

P.D.C. Dietzel, V. Besikiotis, R. Blom, Application of metal–organic frameworks with coordinatively unsaturated metal sites in storage and separation of methane and carbon dioxide, J. Mater. Chem. 19 (2009) 7362-7370.

J.A. Mason, K. Sumida, Z.R. Herm, R. Krishna, J.R. Long, Evaluating Metal-Organic Frameworks for Post-Combustion Carbon Dioxide Capture via Temperature Swing Adsorption, Energy Environ. Sci. 4 (2011) 3030-3040.

Bao, Z.; Yu, L.; Ren, Q.; Lu, X.; Deng, S. Adsorption of CO_2 and CH_4 on a magnesium-based metal organic framework, *J. Colloid Interface Sci.* **2011**, *353*, 549-556.

Bao, Z.; Alnemrat, S.; Vasiliev, I.; Ren, Q.; Yu, L.; Lu, X.; Deng, S. Adsorption of Ethane, Ethylene, Propane and Propylene on a Magnesium-Based Metal-Organic Framework, *Langmuir* **2011**, *27*, 13554-13562.

Y. He, R. Krishna, B. Chen, Metal-Organic Frameworks with Potential for Energy-Efficient Adsorptive Separation of Light Hydrocarbons, Energy Environ. Sci. 5 (2012) 9107-9120.

MgMOF-74: isosteric heats of adsorption determined from experimental data

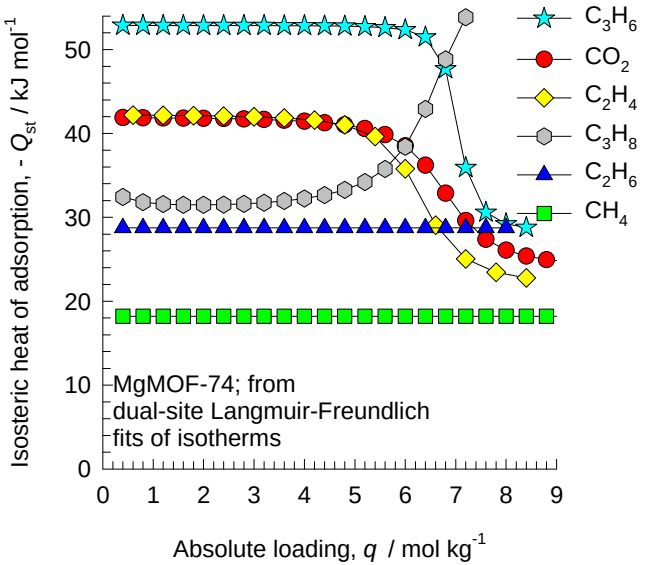

These calculations of $-Q_{st}$ are based on the isotherm fits provided in the previous slide. The values were determined by numerical differentiation and use of the Clausius-Clapeyron equation.

Ab initio quantum chemical calculations are required to adequately capture the polarization effects and orbital interactions.

MgMOF-74 isosteric heats of adsorption, comparison with experiments

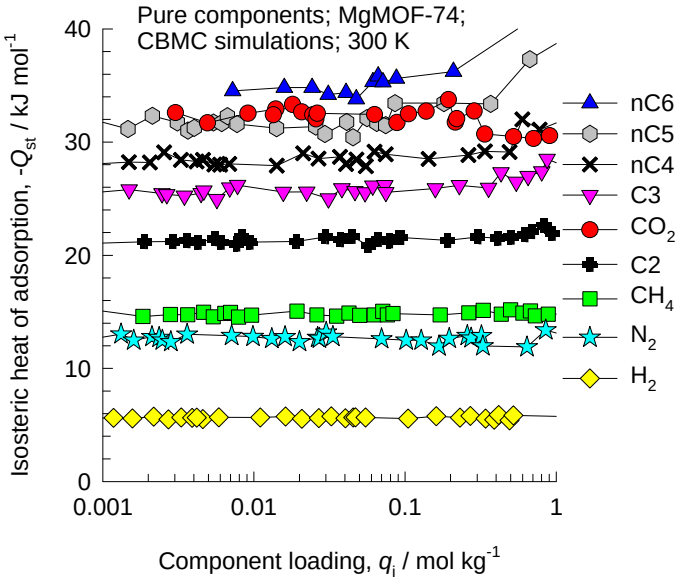

These are simulated values of -Q_{st}

Note that C2 and C3 above refer to saturated alkanes.

The differences in the two sets are severe for CO_2, for which the polarization effects are not included. Ab initio quantum chemical calculations are required to adequately capture the polarization effects and orbital interactions.

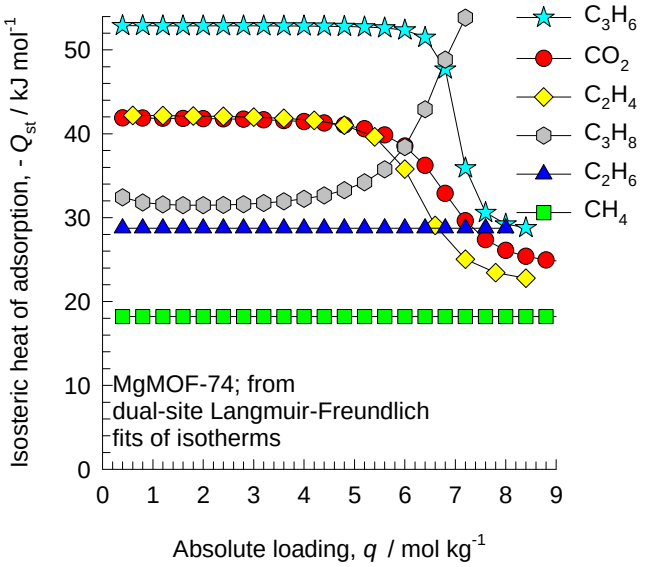

These are values of –Q_{st} obtained from the experimental isotherm fits.

ZnMOF-74 pore landscapes

The structural information on ZnMOF-74 (= Zn_2(dobdc) = Zn\(dobdc= CPO-27-Zn) with dobdc = ($dobdc^{4-}$ = 2,5-dioxido-1,4-benzenedicarboxylate)) were obtained from

A.Ö. Yazaydın, R.Q. Snurr, T.H. Park, K. Koh, J. Liu, M.D. LeVan, A.I. Benin, P. Jakubczak, M. Lanuza, D.B. Galloway, J.J. Low, R.R. Willis, Screening of Metal-Organic Frameworks for Carbon Dioxide Capture from Flue Gas using a Combined Experimental and Modeling Approach, J. Am. Chem. Soc. 131 (2009) 18198-18199.

D. Britt, H. Furukawa, B. Wang, T.G. Glover, O.M. Yaghi, Highly efficient separation of carbon dioxide by a metal-organic framework replete with open metal sites, Proc. Natl. Acad. Sci. U.S.A. 106 (2009) 20637-20640.

N.L. Rosi, J. Kim, M. Eddaoudi, B. Chen, M. O'Keeffe, O.M. Yaghi, Rod Packings and Metal-Organic Frameworks Constructed from Rod-Shaped Secondary Building Units, J. Am. Chem. Soc. 127 (2005) 1504-1518.

P.D.C. Dietzel, B. Panella, M. Hirscher, R. Blom, H. Fjellvåg, Hydrogen adsorption in a nickel based coordination polymer with open metal sites in the cylindrical cavities of the desolvated framework, Chem. Commun. (2006) 959-961.

P.D.C. Dietzel, V. Besikiotis, R. Blom, Application of metal–organic frameworks with coordinatively unsaturated metal sites in storage and separation of methane and carbon dioxide, J. Mater. Chem. 19 (2009) 7362-7370.

S.R. Caskey, A.G. Wong-Foy, A.J. Matzger, Dramatic Tuning of Carbon Dioxide Uptake via Metal Substitution in a Coordination Polymer with Cylindrical Pores, J. Am. Chem. Soc. 130 (2008) 10870-10871.

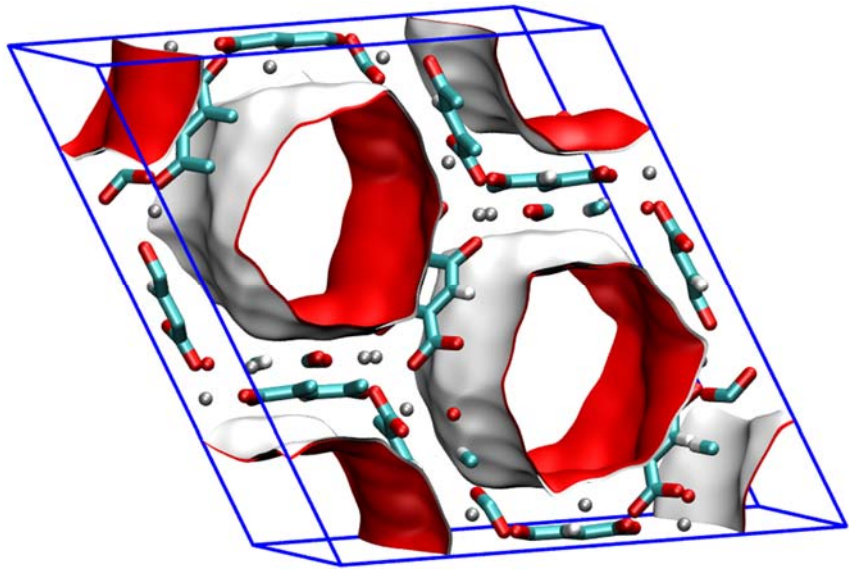

ZnMOF-74 pore dimensions

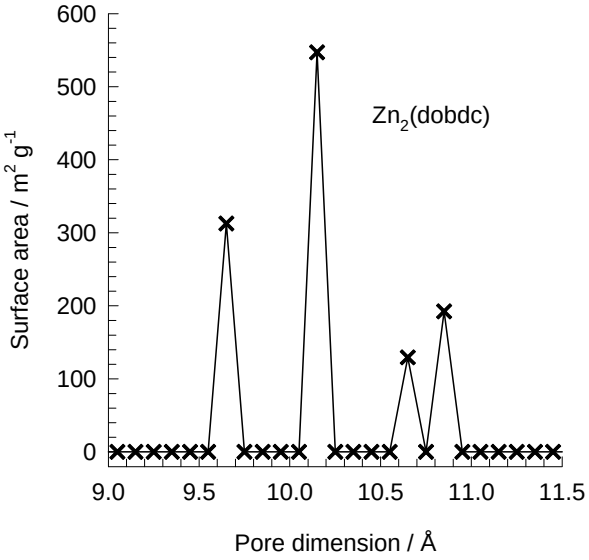

This plot of surface area versus pore dimension is determined using a combination of the DeLaunay triangulation method for pore dimension determination, and the procedure of Düren for determination of the surface area.

	ZnMOF-74
a /Å	25.9322
b /Å	25.9322
c /Å	6.8365
Cell volume / Å^3	3981.467
conversion factor for [molec/uc] to [mol per kg Framework]	0.3421
conversion factor for [molec/uc] to [kmol/m^3]	0.5881
ρ [kg/m3]	1219.304
MW unit cell [g/mol(framework)]	2923.473
ϕ, fractional pore volume	0.709
open space / Å^3/uc	2823.8
Pore volume / cm^3/g	0.582
Surface area /m^2/g	1176.0
DeLaunay diameter /Å	9.49

ZnMOF-74 force field for framework atoms

Lennard-Jones parameters for atoms in ZnMOF-74 based on the data from A.Ö. Yazaydın, R.Q. Snurr, T.H. Park, K. Koh, J. Liu, M.D. LeVan, A.I. Benin, P. Jakubczak, M. Lanuza, D.B. Galloway, J.J. Low, R.R. Willis (Screening of Metal-Organic Frameworks for Carbon Dioxide Capture from Flue Gas using a Combined Experimental and Modeling Approach, J. Am. Chem. Soc. 131 (2009) 18198-18199).

(pseudo-) atom	σ / Å	ε/k_B / K	charge
Zn	4.045	27.68	1.206
OA	3.033	48.16	-0.670
OB	3.033	48.16	-0.659
OC	3.033	48.16	-0.702
CA	3.473	47.86	0.767
CB	3.473	47.86	-0.292
CC	3.473	47.86	0.325
CD	3.473	47.86	-0.147
H	2.846	7.650	0.172

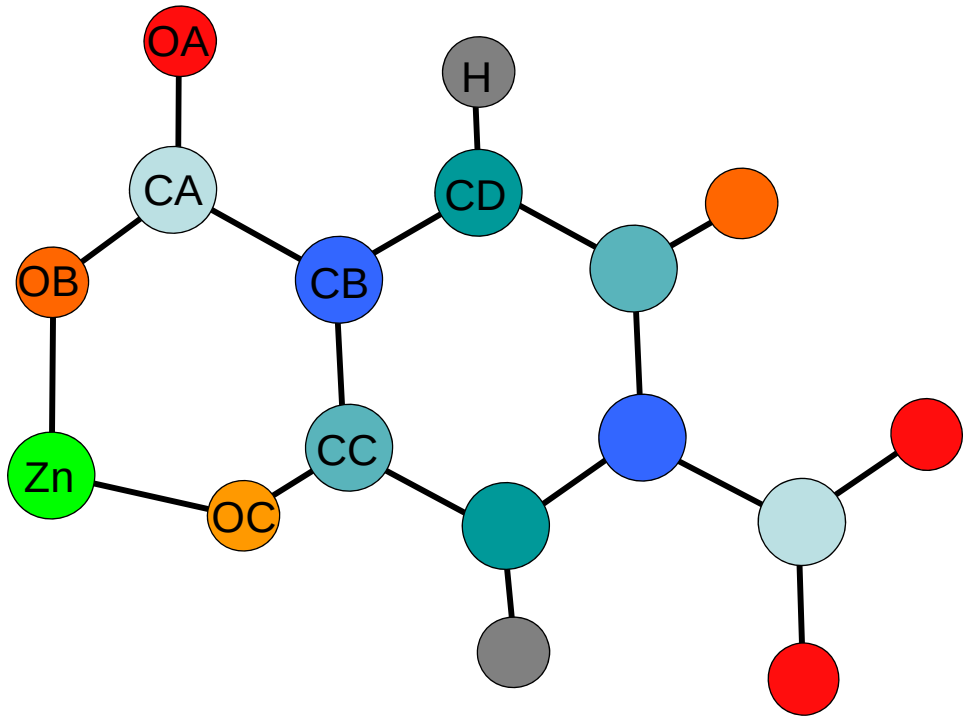

ZnMOF-74 CBMC simulations of isotherms, and isosteric heats of adsorption

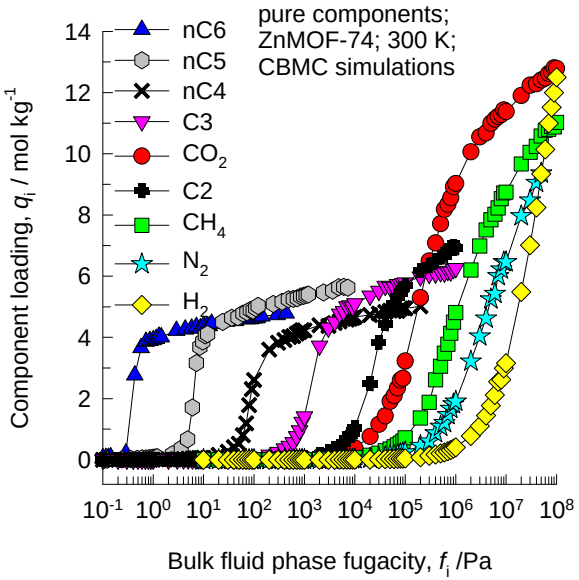

Note that C2 and C3 above refer to saturated alkanes.

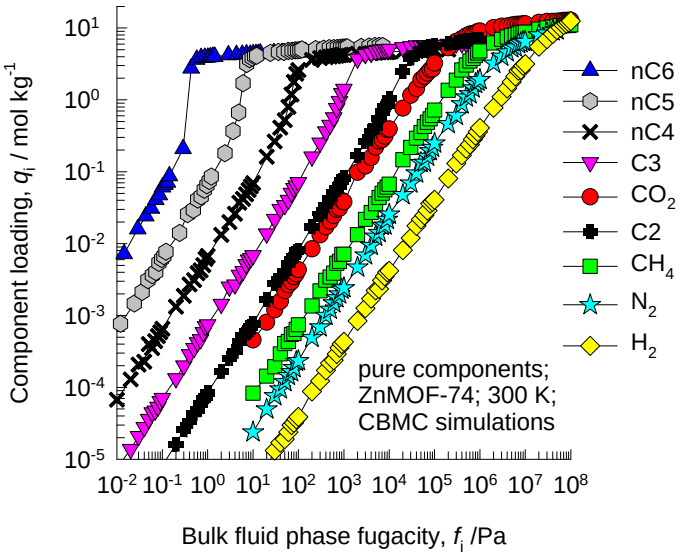

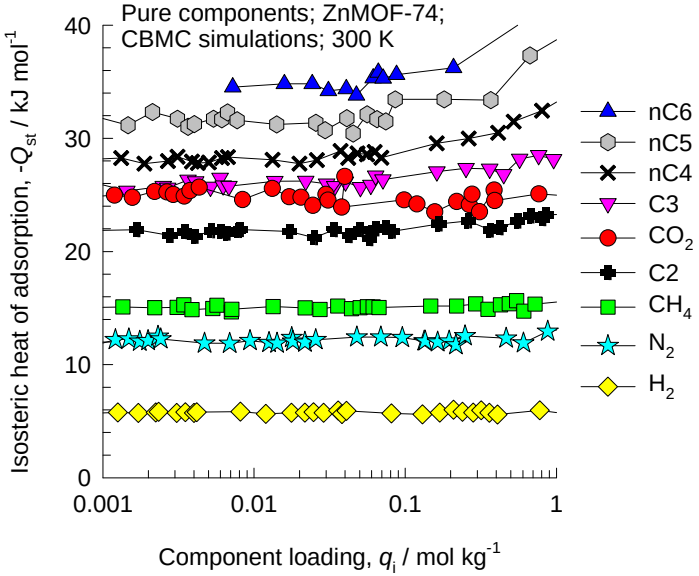

ZnMOF-74 MD simulations of unary self- , and M-S diffusivities

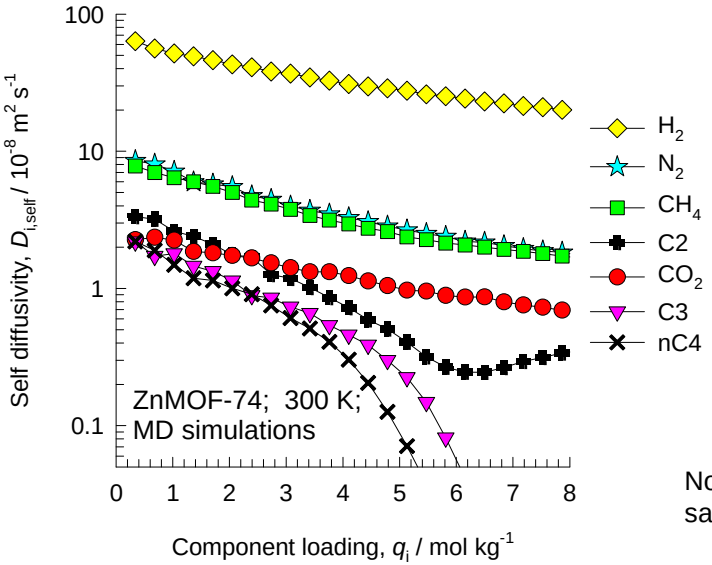

Note that C2 and C3 above refer to saturated alkanes.

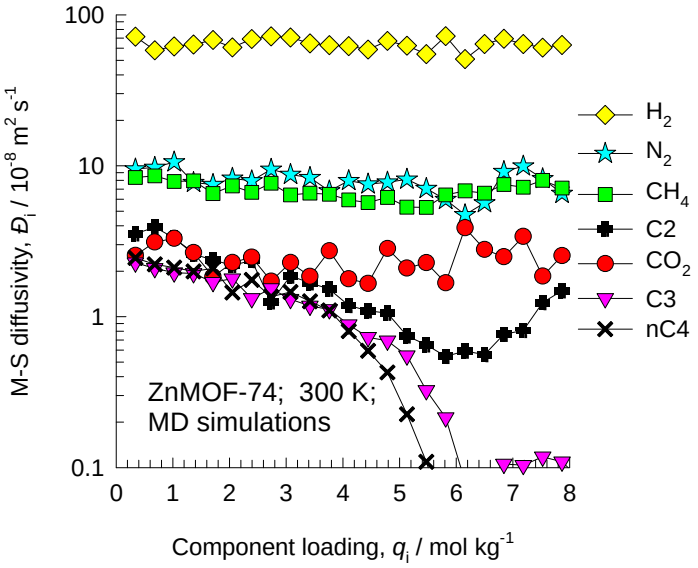

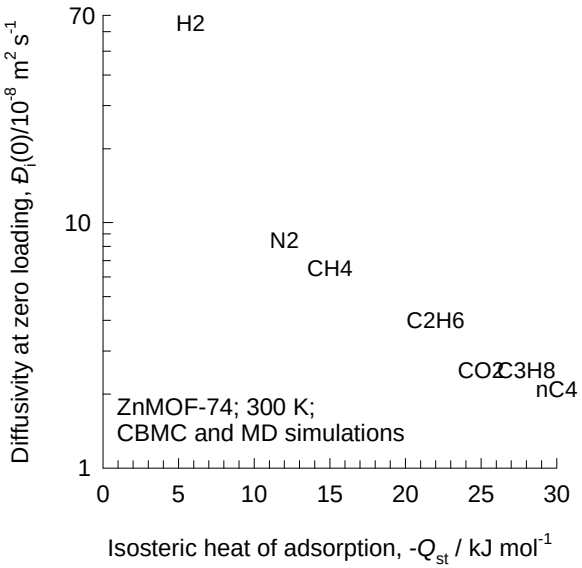

NiMOF-74 pore landscapes

The structural information on NiMOF-74 (= Ni_2(dobdc) = Ni\(dobdc = CPO-27-Ni) with dobdc = ($dobdc^{4-}$ = 2,5-dioxido-1,4-benzenedicarboxylatee)) were obtained from

A.Ö. Yazaydın, R.Q. Snurr, T.H. Park, K. Koh, J. Liu, M.D. LeVan, A.I. Benin, P. Jakubczak, M. Lanuza, D.B. Galloway, J.J. Low, R.R. Willis, Screening of Metal-Organic Frameworks for Carbon Dioxide Capture from Flue Gas using a Combined Experimental and Modeling Approach, J. Am. Chem. Soc. 131 (2009) 18198-18199.
D. Britt, H. Furukawa, B. Wang, T.G. Glover, O.M. Yaghi, Highly efficient separation of carbon dioxide by a metal-organic framework replete with open metal sites, Proc. Natl. Acad. Sci. U.S.A. 106 (2009) 20637-20640.
N.L. Rosi, J. Kim, M. Eddaoudi, B. Chen, M. O'Keeffe, O.M. Yaghi, Rod Packings and Metal-Organic Frameworks Constructed from Rod-Shaped Secondary Building Units, J. Am. Chem. Soc. 127 (2005) 1504-1518.
P.D.C. Dietzel, B. Panella, M. Hirscher, R. Blom, H. Fjellvåg, Hydrogen adsorption in a nickel based coordination polymer with open metal sites in the cylindrical cavities of the desolvated framework, Chem. Commun. (2006) 959-961.
P.D.C. Dietzel, V. Besikiotis, R. Blom, Application of metal–organic frameworks with coordinatively unsaturated metal sites in storage and separation of methane and carbon dioxide, J. Mater. Chem. 19 (2009) 7362-7370.
S.R. Caskey, A.G. Wong-Foy, A.J. Matzger, Dramatic Tuning of Carbon Dioxide Uptake via Metal Substitution in a Coordination Polymer with Cylindrical Pores, J. Am. Chem. Soc. 130 (2008) 10870-10871.

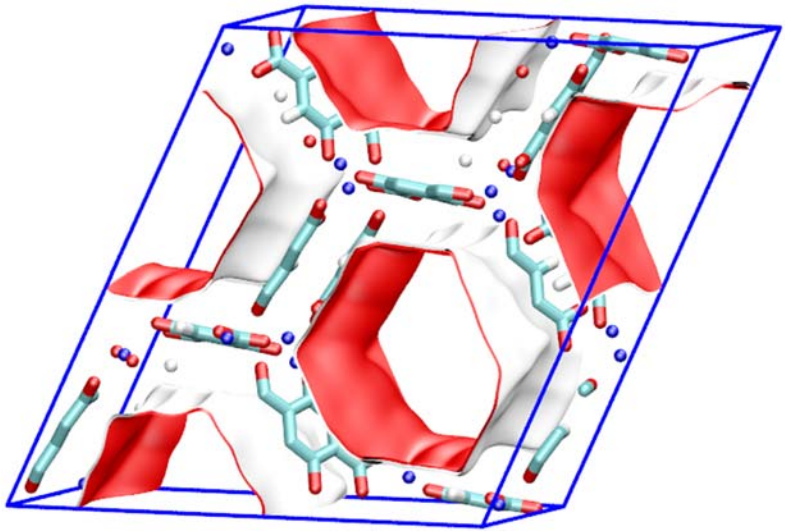

NiMOF-74 pore dimensions

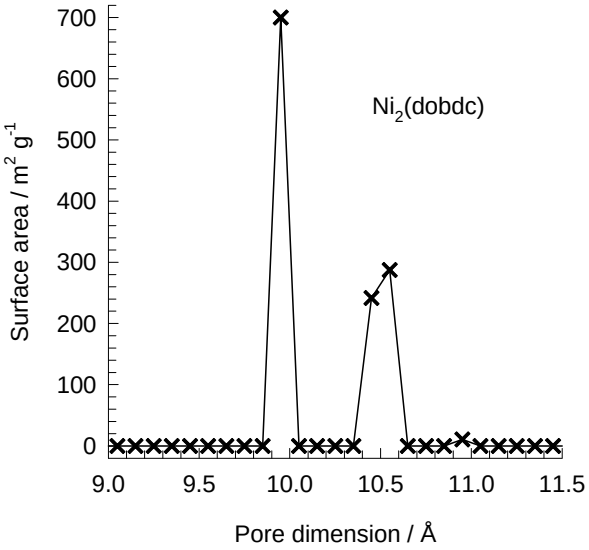

This plot of surface area versus pore dimension is determined using a combination of the DeLaunay triangulation method for pore dimension determination, and the procedure of Düren for determination of the surface area.

	NiMOF-74
a /Å	25.7856
b /Å	25.7856
c /Å	6.7701
Cell volume / Å^3	3898.344
conversion factor for [molec/uc] to [mol per kg Framework]	0.3568
conversion factor for [molec/uc] to [kmol/m^3]	0.6133
ρ [kg/m3]	1193.811
MW unit cell [g/mol(framework)]	2802.592
ϕ, fractional pore volume	0.695
open space / Å^3/uc	2707.6
Pore volume / cm^3/g	0.582
Surface area /m^2/g	1239.0
DeLaunay diameter /Å	9.80

NiMOF-74 fits of experimental isotherms for CO_2, CH_4, N_2, and H_2

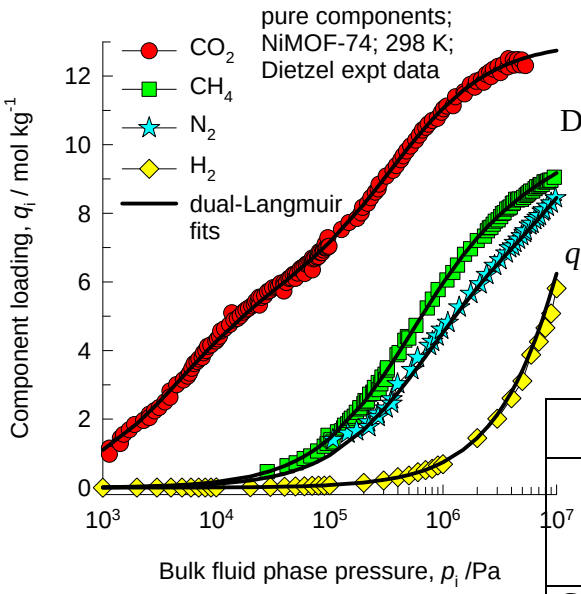

Dual-Langmuir-Freundlich parameter fits for NiMOF-74 (= Ni_2(dobdc) = CPO-27-Ni).

$$q = q_{A,sat}\frac{b_A p^{\nu_A}}{1+b_A p^{\nu_A}} + q_{B,sat}\frac{b_B p^{\nu_B}}{1+b_B p^{\nu_B}}; \quad b_A = b_{A0}\exp\left(\frac{E_A}{RT}\right); \quad b_B = b_{B0}\exp\left(\frac{E_B}{RT}\right)$$

	Site A				Site B			
	$q_{A,sat}$ mol kg^{-1}	b_{A0} Pa$^{-\nu_i}$	E_A kJ mol^{-1}	ν_A dimensionless	$q_{B,sat}$ mol kg^{-1}	b_{B0} Pa$^{-\nu_i}$	E_B kJ mol^{-1}	ν_B dimensionless
CO_2	7.1	1.22×10^{-10}	24.8	1	5.9	4.89×10^{-11}	38	1
CH_4	9	3.92×10^{-10}	21	1	2	9.52×10^{-12}	21	1
N_2	9.76	2.71×10^{-10}	10.6	1	7.35	6.57×10^{-10}	19.1	1
H_2	36	2.1×10^{-8}		1				

The isotherm fit parameters for CO_2, CH_4, and N_2 are on the basis of experimental data for variety of temperatures from:

P.D.C. Dietzel, V. Besikiotis, R. Blom, Application of metal–organic frameworks with coordinatively unsaturated metal sites in storage and separation of methane and carbon dioxide, J. Mater. Chem. 19 (2009) 7362-7370.

The isotherm fit parameters for H_2 are on the basis of experimental data from:
Yaghi, O. M. Hydrogen Storage in Metal Organic Frameworks, www.hydrogen.energy.gov/pdfs/review11/st049_yaghi_2011_p.pdf, University of California Los Angeles, California, 2011.

These data were supplemented with CBMC simulations.

NiMOF-74: isosteric heats of adsorption determined from experimental data

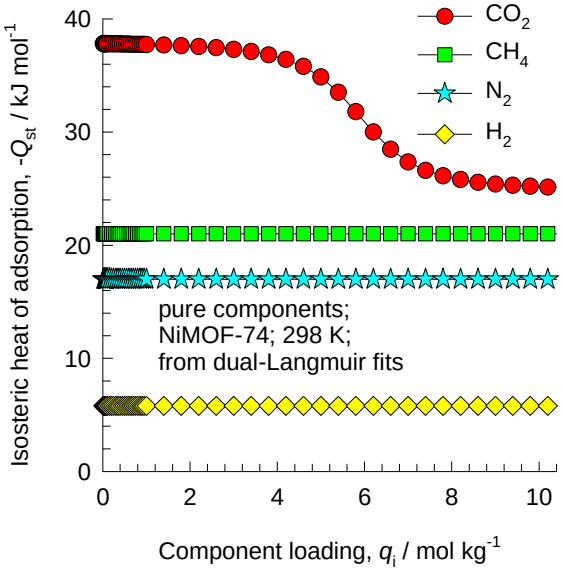

These calculations of $-Q_{st}$ are based on the isotherm fits provided in the previous slide. The values were determined by numerical differentiation and use of the Clausius-Clapeyron equation.

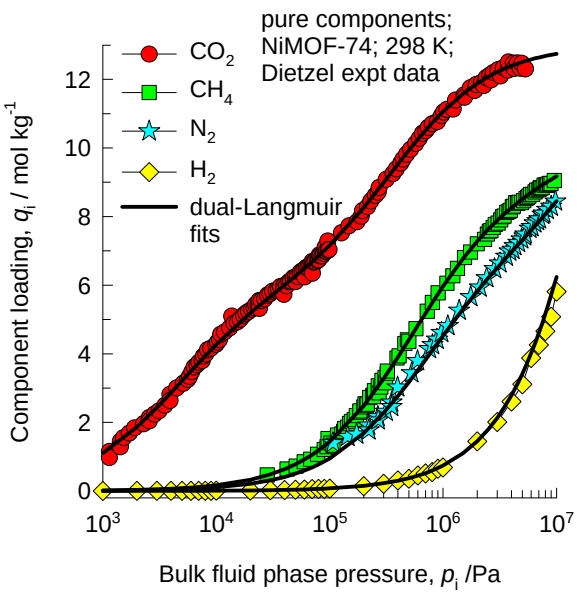

From the pure component isotherm fits, we determine the molar loadings for CO_2, CH_4, N_2, and H_2 to be 7.16, 1.43, 0.95, and 0.075 mol kg^{-1} at 100 kPa. The corresponding values of $-Q_{st}$ are determined to be 27.3, 21, 17, and 5.8 kJ mol^{-1}, respectively. These are the $-Q_{st}$ values plotted on the x-axis in the following slide.

NiMOF-74: Analysis of membrane permeation experiments

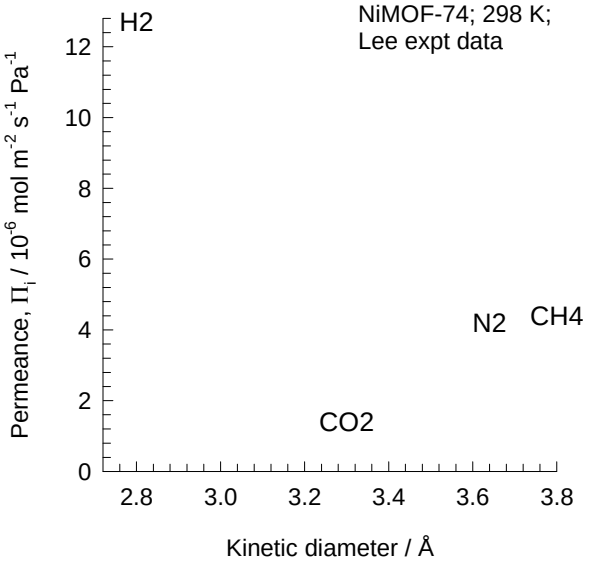

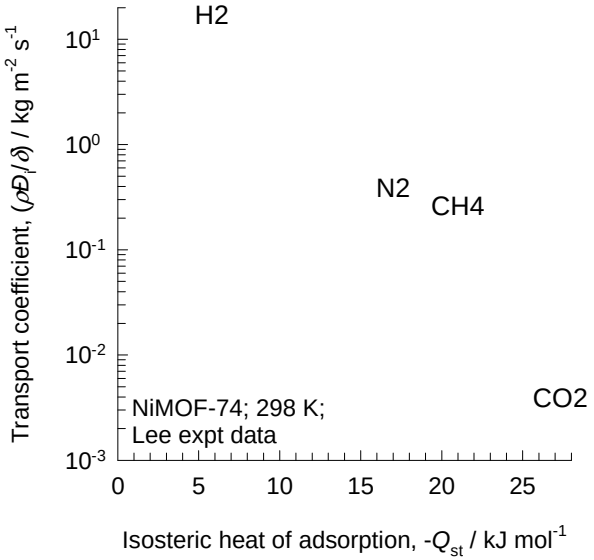

The data on membrane permeances are obtained from:

Lee, D. J.; Li, Q.; Kim, H.; Lee, K. Preparation of Ni-MOF-74 membrane for CO_2 separation by layer-by-layer seeding technique, *Microporous Mesoporous Mater.* **2012**, *163*, 169-177.

The transport coefficients are calculated from

$$\frac{\rho Đ_i}{\delta} = \frac{\Pi_i}{\Gamma_i \frac{q_i}{p_i}}$$

with the molar loadings q_i and thermodynamic correction factor Γ_i at the upstream face determined from pure component isotherm fits evaluated at p_i = 100 kPa

FeMOF-74 pore landscapes

The structural information on FeMOF-74 (= Fe_2(dobdc) = Fe\(dobdc = CPO-27-Fe) with dobdc = ($dobdc^{4-}$ = 2,5-dioxido-1,4-benzenedicarboxylate)) was obtained from

Bloch et al. E.D. Bloch, L. Murray, W.L. Queen, S.M. Chavan, S.N. Maximoff, J.P. Bigi, R. Krishna, V.K. Peterson, F. Grandjean, G.J. Long, B. Smit, S. Bordiga, C.M. Brown, J.R. Long, Selective Binding of O_2 over N_2 in a Redox-Active Metal-Organic Framework with Open Iron(II) Coordination Sites, J. Am. Chem. Soc. 133 (2011) 14814-14822.

E.D. Bloch, W.L. Queen, R. Krishna, J.M. Zadrozny, C.M. Brown, J.R. Long, Hydrocarbon Separations in a Metal-Organic Framework with Open Iron(II) Coordination Sites, Science 335 (2012) 1606-1610.

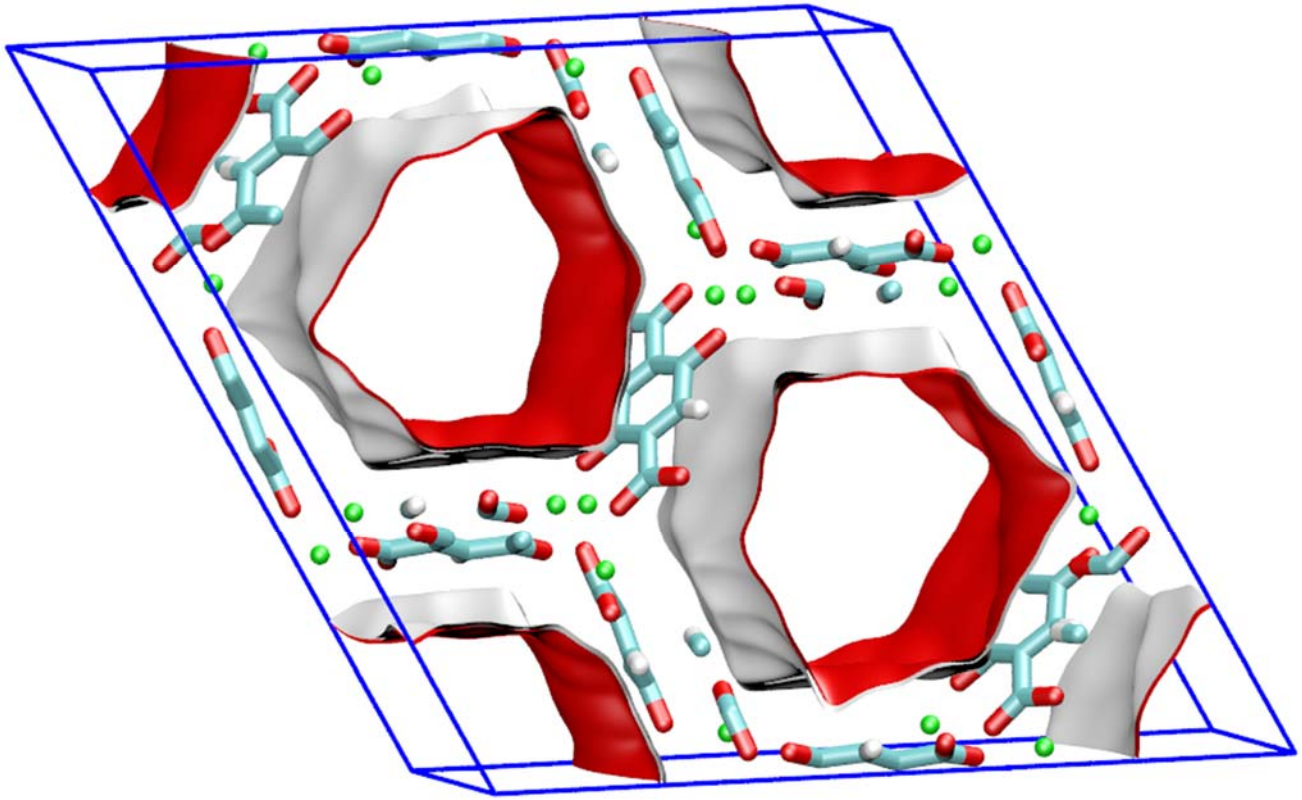

FeMOF-74 pore dimensions

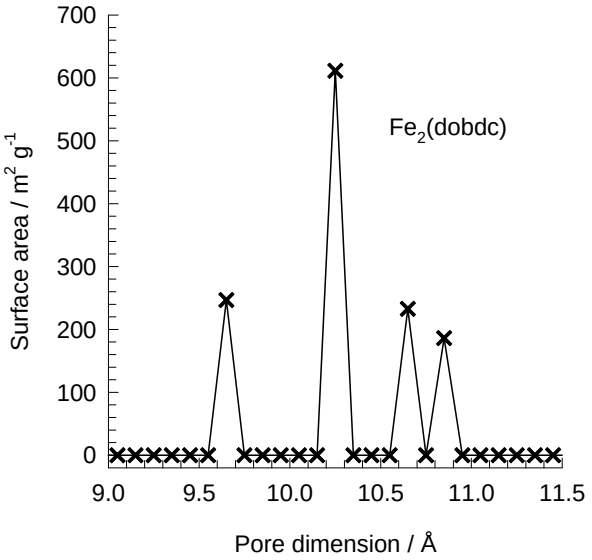

This plot of surface area versus pore dimension is determined using a combination of the DeLaunay triangulation method for pore dimension determination, and the procedure of Düren for determination of the surface area.

	FeMOF-74
a /Å	26.1627
b /Å	26.1627
c /Å	6.8422
Cell volume / Å^3	4055.94
conversion factor for [molec/uc] to [mol per kg Framework]	0.3635
conversion factor for [molec/uc] to [kmol/m^3]	0.5807
ρ [kg/m3]	1126.434
MW unit cell [g/mol (framework)]	2751.321
ϕ, fractional pore volume	0.705
open space / Å^3/uc	2859.7
Pore volume / cm^3/g	0.626
Surface area /m^2/g	1277.4
DeLaunay diameter /Å	11.12

FeMOF-74 fit parameters for alkanes, alkenes, and ethyne

Dual-site Langmuir-Freundlich parameters for pure ethyne, ethene, ethane, methane, propene, and propane isotherms in Fe_2(dobdc) obtained by re-fitting the experimental isotherms of Bloch measured at 318 K, 333 K, and 353 K. These parameters are valid only within the temperature range of 318 K – 353 K; extrapolation to temperatures outside this range is not justified.

$$q = q_{A,sat}\frac{b_A p^{\nu_A}}{1+b_A p^{\nu_A}} + q_{B,sat}\frac{b_B p^{\nu_B}}{1+b_B p^{\nu_B}}; \quad b_A = b_{A0}\exp\left(\frac{E_A}{RT}\right); \quad b_B = b_{B0}\exp\left(\frac{E_B}{RT}\right)$$

	Site A				Site B			
	$q_{A,sat}$ mol kg^{-1}	b_{A0} Pa$^{-\nu_i}$	E_A kJ mol^{-1}	ν_A dimensionless	$q_{B,sat}$ mol kg^{-1}	b_{B0} Pa$^{-\nu_i}$	E_B kJ mol^{-1}	ν_B dimensionless
C_2H_2	4.8	2.42×10^{-12}	51.4	1.1	3.2	2.07×10^{-10}	33.4	0.89
C_2H_4	1.74	6.51×10^{-12}	38	1.12	4.9	4.16×10^{-13}	53	1.12
C_2H_6	8.42	4.47×10^{-11}	31	1.1				
CH_4	6.7	8.06×10^{-10}	19.6	1				
C_3H_6	5.3	1.42×10^{-20}	97	1.76	1.7	1.29×10^{-10}	33	1.13
C_3H_8	2.1	5.95×10^{-12}	48	0.83	4.3	6.15×10^{-15}	53	1.63

The experimental isotherm data for variety of temperatures from:

Bloch, E. D.; Queen, W. L.; Krishna, R.; Zadrozny, J. M.; Brown, C. M.; Long, J. R. Hydrocarbon Separations in a Metal-Organic Framework with Open Iron(II) Coordination Sites, *Science* **2012**, *335*, 1606-1610.

FeMOF-74 experimental isotherms fits at 318 K for alkanes, alkenes, and ethyne

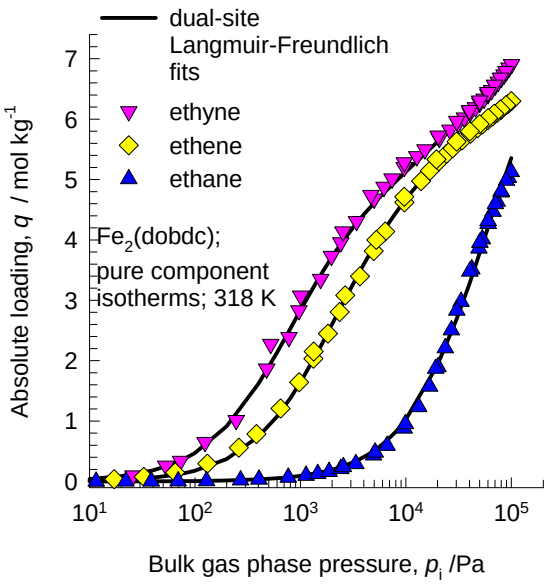

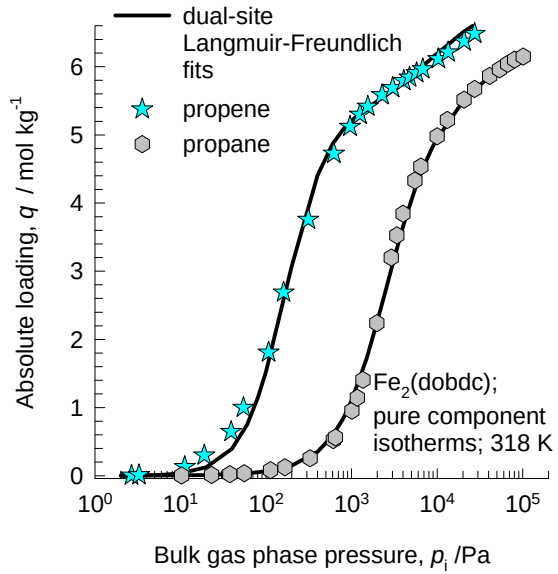

The experimental for variety of temperatures from:

Bloch, E. D.; Queen, W. L.; Krishna, R.; Zadrozny, J. M.; Brown, C. M.; Long, J. R. Hydrocarbon Separations in a Metal-Organic Framework with Open Iron(II) Coordination Sites, *Science* **2012**, *335*, 1606-1610.

FeMOF-74: isosteric heats of adsorption determined from experimental data

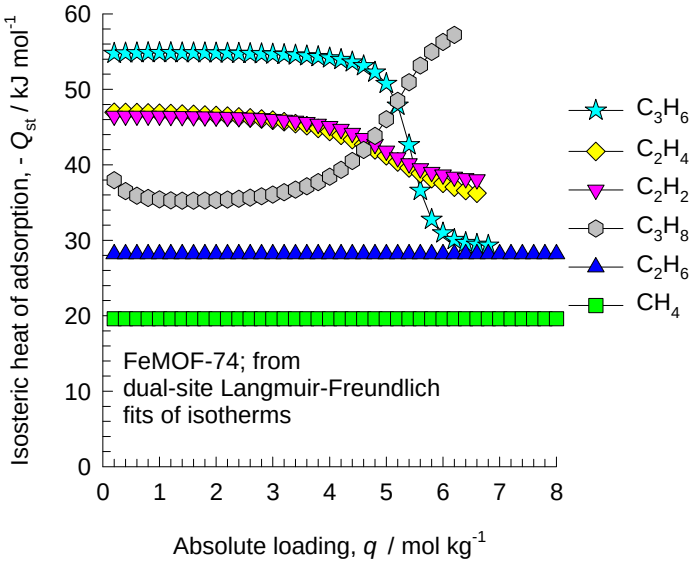

These calculations of $-Q_{st}$ are based on the isotherm fits provided in the previous slide. The values were determined by numerical differentiation and use of the Clausius-Clapeyron equation.

MIL–47 pore landscape

The structural information for MIL-47 was taken from

L. Alaerts, C.E.A. Kirschhock, M. Maes, M. van der Veen, V. Finsy, A. Depla, J.A. Martens, G.V. Baron, P.A. Jacobs, J.F.M. Denayer, D. De Vos, Selective Adsorption and Separation of Xylene Isomers and Ethylbenzene with the Microporous Vanadium(IV) Terephthalate MIL-47, Angew. Chem. Int. Ed. 46 (2007) 4293-4297.

V. Finsy, H. Verelst, L. Alaerts, D. De Vos, P.A. Jacobs, G.V. Baron, J.F.M. Denayer, Pore-Filling-Dependent Selectivity Effects in the Vapor-Phase Separation of Xylene Isomers on the Metal-Organic Framework MIL-47, J. Am. Chem. Soc. 130 (2008) 7110-7118.

K. Barthelet, J. Marrot, D. Riou, G. Férey, A Breathing Hybrid Organic - Inorganic Solid with Very Large Pores and High Magnetic Characteristics, Angew. Chem. Int. Ed. 41 (2007) 281-284.

Snapshot of CO_2/CH_4 mixture

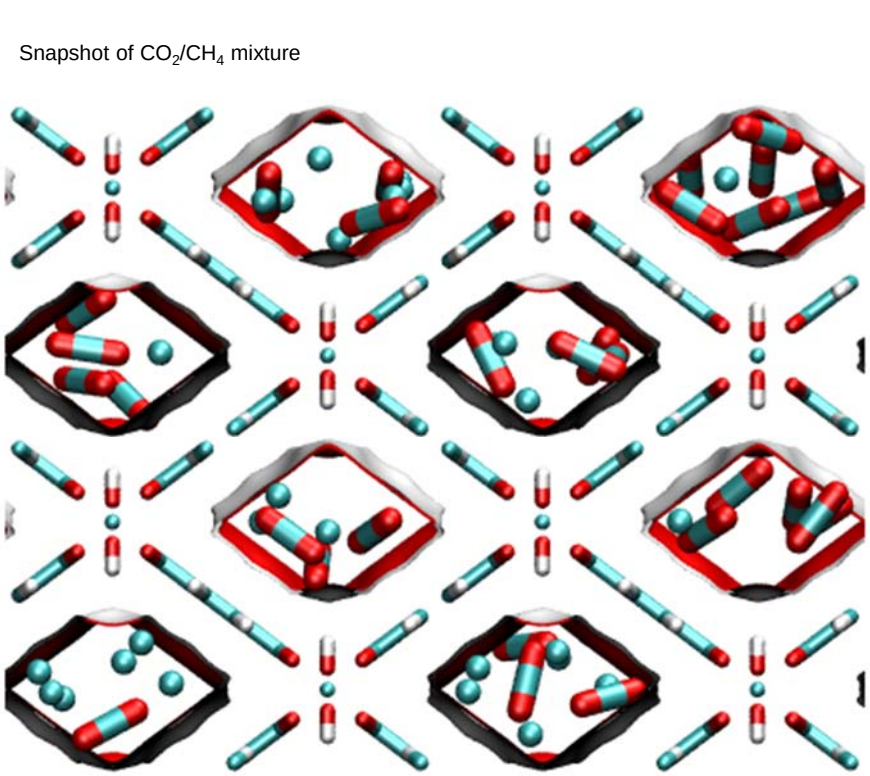

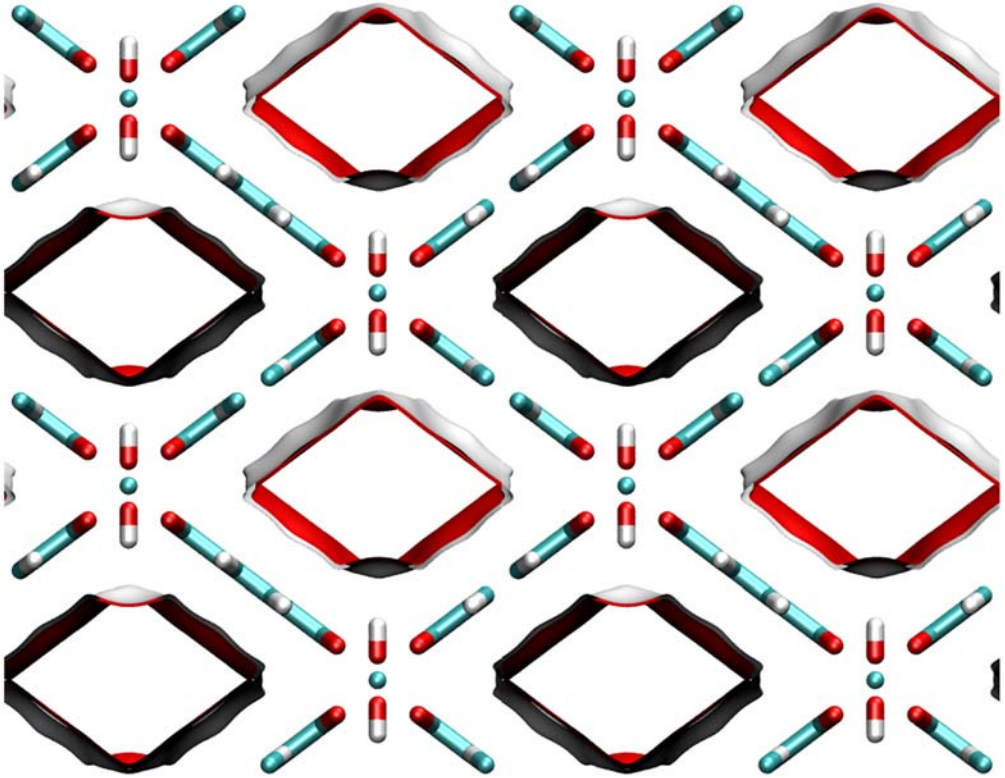

MIL–47 dimensions

	MIL-47
a /Å	6.808
b /Å	16.12
c /Å	13.917
Cell volume / Å^3	1527.321
conversion factor for [molec/uc] to [mol per kg Framework]	1.0824
conversion factor for [molec/uc] to [kmol/m^3]	1.7868
ρ [kg/m3]	1004.481
MW unit cell [g/mol(framework)]	923.881
ϕ, fractional pore volume	0.608
open space / Å^3/uc	929.3
Pore volume / cm^3/g	0.606
Surface area /m^2/g	1472.8
DeLaunay diameter /Å	8.03

One-dimensional diamond-shaped channels with free internal diameter of 8Å

MIL–47 force field for framework atoms

Lennard-Jones parameters for atoms in MIL-47. The information on charges is taken from the work of N. Rosenbach, H. Jobic, A. Ghoufi, F. Salles, G. Maurin, S. Bourrelly, P.L. Llewellyn, T. Devic, C. Serre, G. Férey (Quasi-Elastic Neutron Scattering and Molecular Dynamics Study of Methane Diffusion in Metal Organic Frameworks MIL-47(V) and MIL-53(Cr), Angew. Chem. Int. Ed. 47 (2008) 6611-6615)

(pseudo-) atom	σ / Å	ε/k_B / K	charge
V	2.8	8.05	1.208
Oa	3.03	48.2	-0.596
Ob	3.03	48.2	-0.496
Ca	3.47	47.9	0.604
Cb	3.47	47.9	-0.071
Cc	3.47	47.9	-0.068
H	2.85	7.65	0.146

MIL-47 (V)

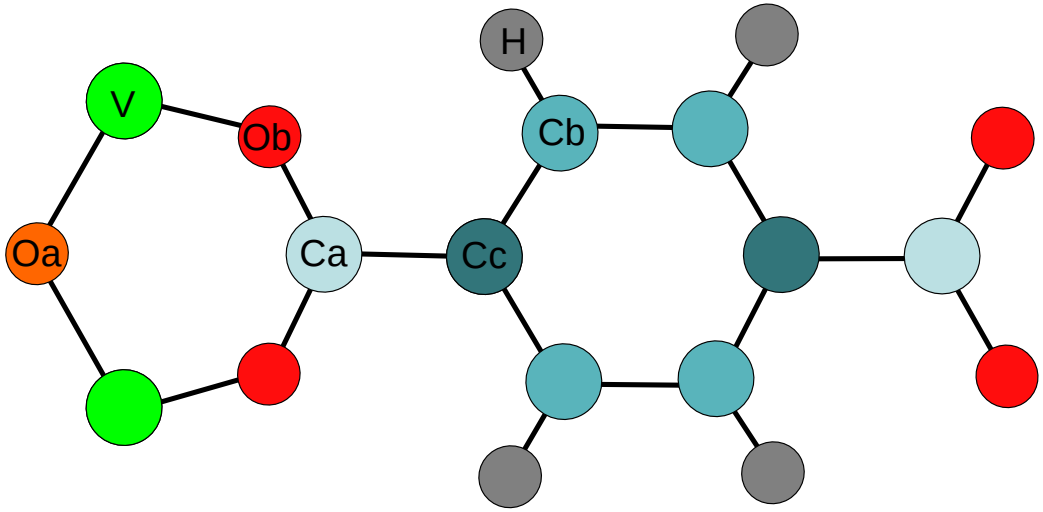

MIL-47 CBMC simulations of isotherms, and isosteric heats of adsorption

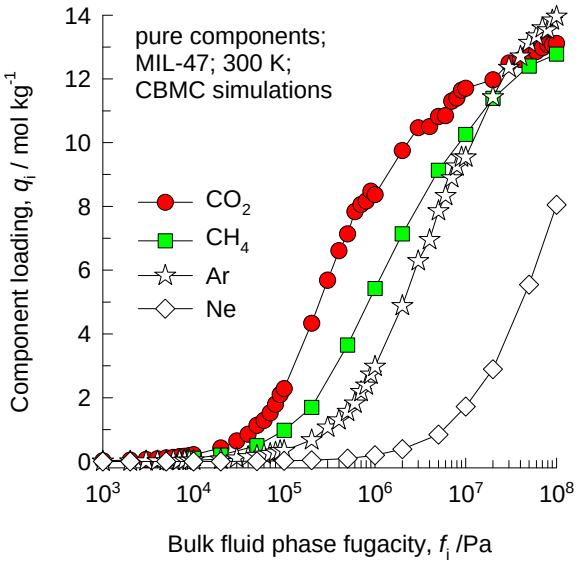

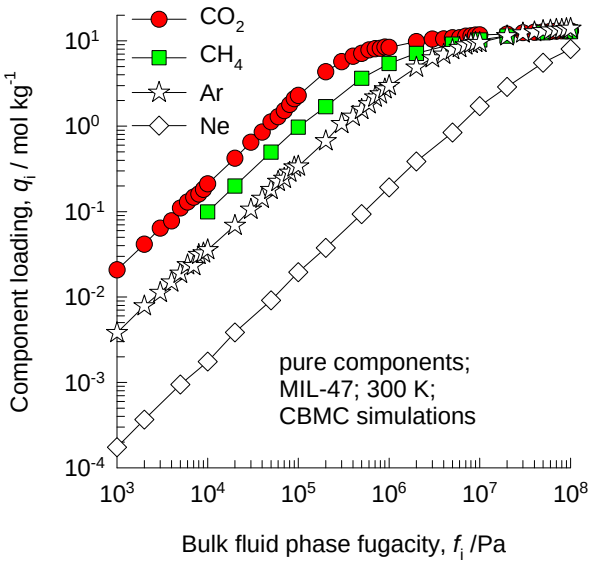

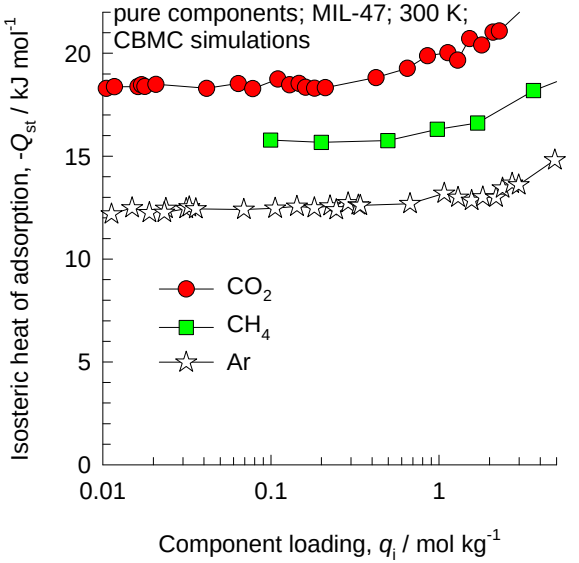

MIL-47 MD simulations of unary self- , and M-S diffusivities

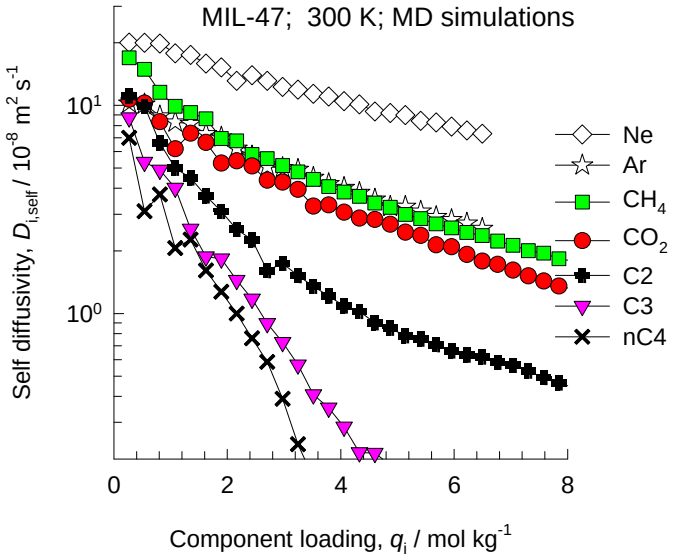

Note that C2 and C3 refer to saturated alkanes

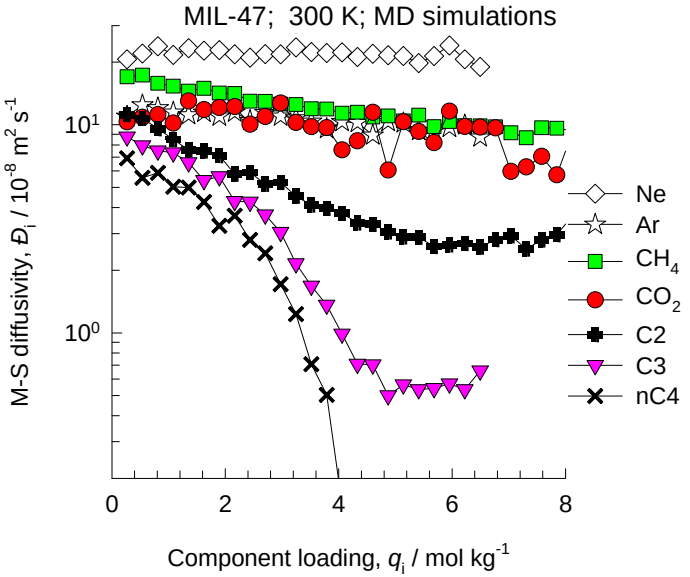

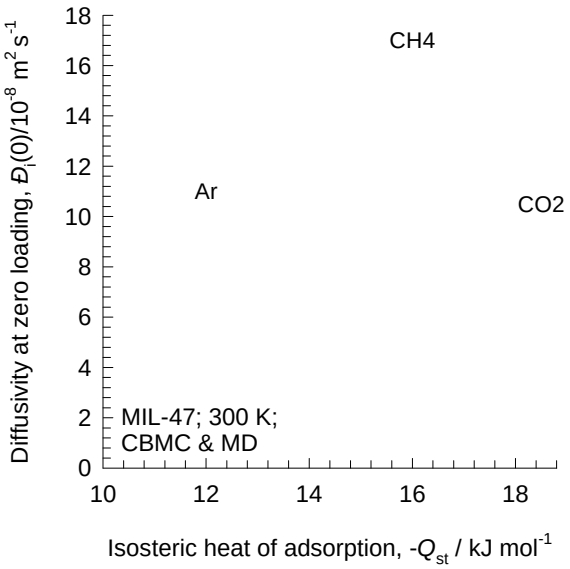

MIL – 53 (Cr) pore landscape

The structural data for MIL-53 (Cr) = $Cr(OH)(O_2C\text{-}C_6H_4\text{-}CO_2)$ was taken from

D.S. Coombes, F. Corà, C. Mellot-Draznieks, R.G. Bell, Sorption-Induced Breathing in the Flexible Metal Organic Framework CrMIL-53: Force-Field Simulations and Electronic Structure Analysis, J. Phys. Chem. C 113 (2009) 544-552.

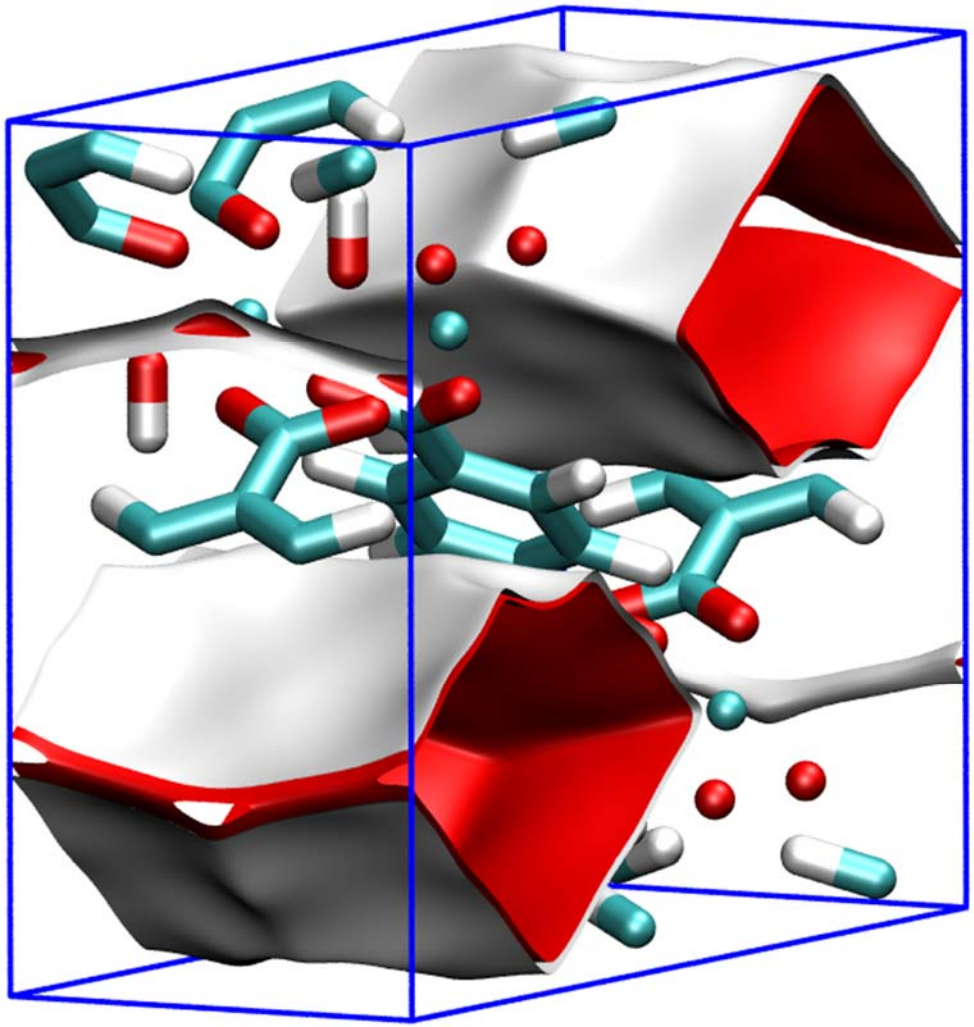

Simulation results presented are for –lp structure, i.e. large pore

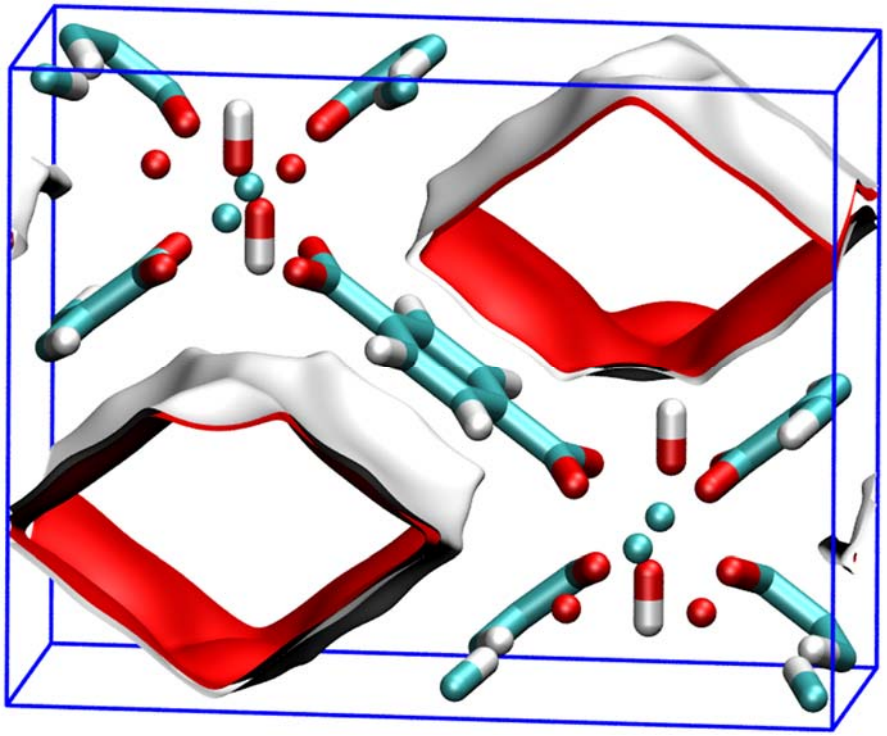

MIL–53 (Cr) pore dimensions

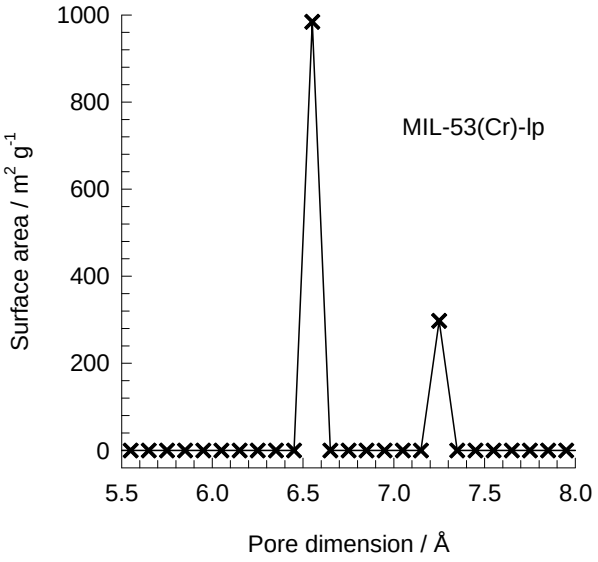

This plot of surface area versus pore dimension is determined using a combination of the DeLaunay triangulation method for pore dimension determination, and the procedure of Düren for determination of the surface area.

	MIL53(Cr)-lp
a /Å	16.733
b /Å	13.038
c /Å	6.812
Cell volume / Å^3	1486.139
conversion factor for [molec/uc] to [mol per kg Framework]	1.0728
conversion factor for [molec/uc] to [kmol/m^3]	2.0716
ρ [kg/m3]	1041.534
MW unit cell [g/mol(framework)]	932.1312
ϕ, fractional pore volume	0.539
open space / Å^3/uc	801.6
Pore volume / cm^3/g	0.518
Surface area /m^2/g	1280.5
DeLaunay diameter /Å	7.40

One-dimensional lozenge-shaped channels

MIL–53 (Cr) force field for framework atoms

Lennard-Jones parameters for atoms in MIL-53(Cr)-lp. The information on charges is taken from the work of F. Salles, A. Ghoufi, G. Maurin, R.G. Bell, C. Mellot-Draznieks, G. Férey (Molecular Dynamics Simulations of Breathing MOFs: Structural Transformations of MIL-53(Cr) upon Thermal Activation and CO2 Adsorption, Angew. Chem. Int. Ed. 47 (2008) 8487-8491.)

(pseudo-) atom	σ / Å	ε/k_B / K	charge
Cr	2.69	7.55	1.032
Oa	3.03	48.2	-0.506
Ob	3.03	48.2	-0.637
Ca	3.47	47.9	-0.074
Cb	3.47	47.9	0.613
Ha	2.85	7.65	0.139
Hb	2.85	7.65	0.291

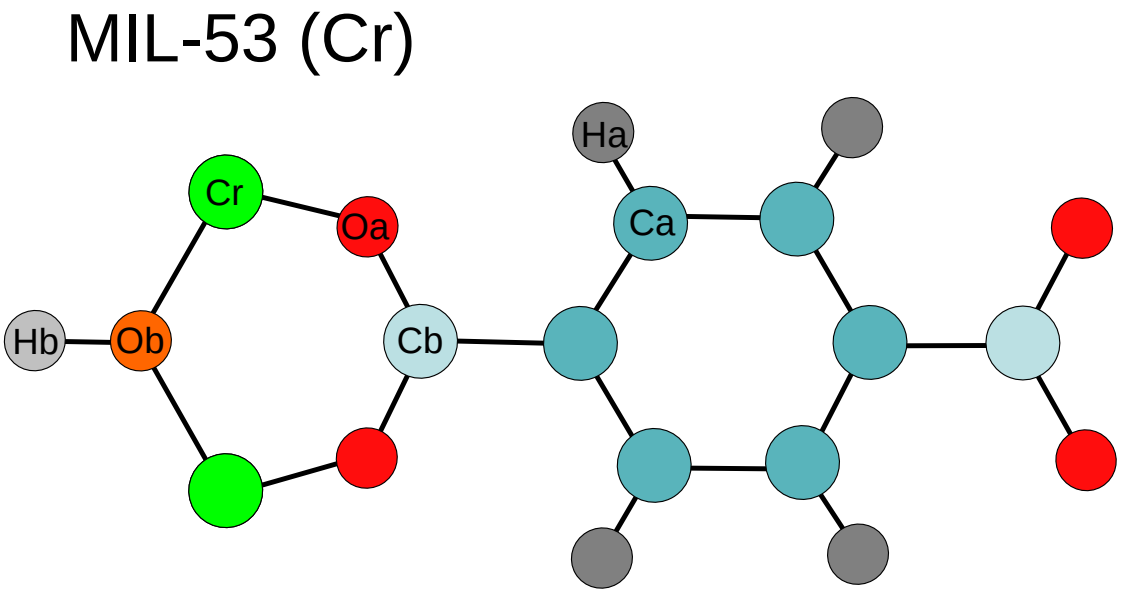

MIL-53(Cr)-lp CBMC simulations of isotherms, and isosteric heats of adsorption

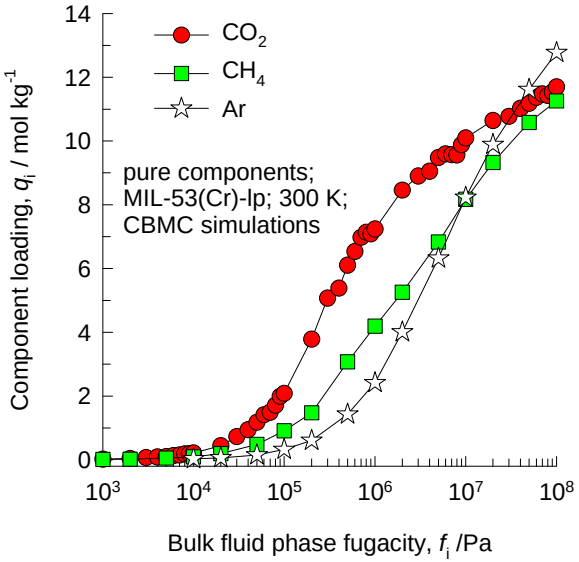

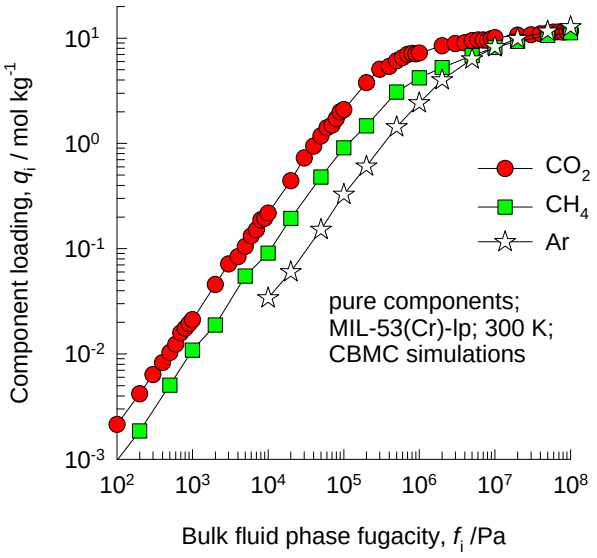

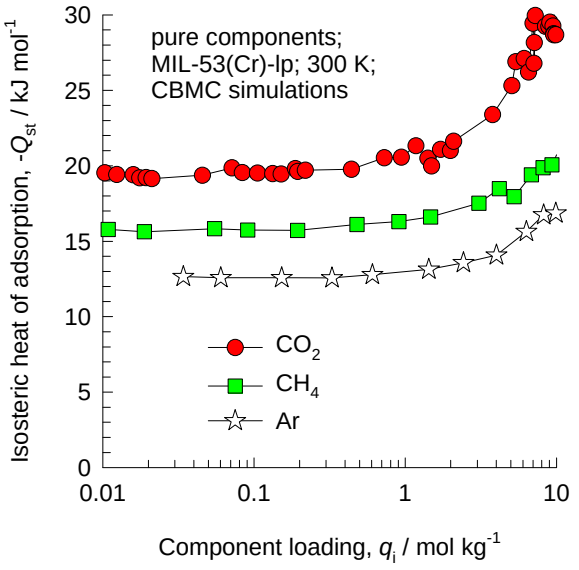

MIL-53(Cr)-lp MD simulations of unary self- , and M-S diffusivities

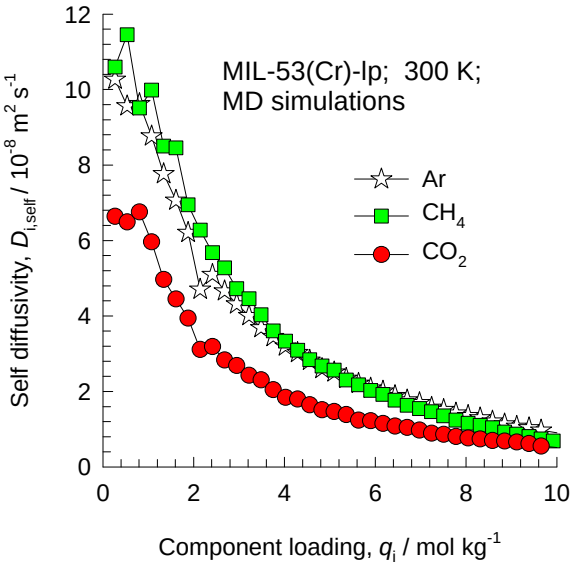

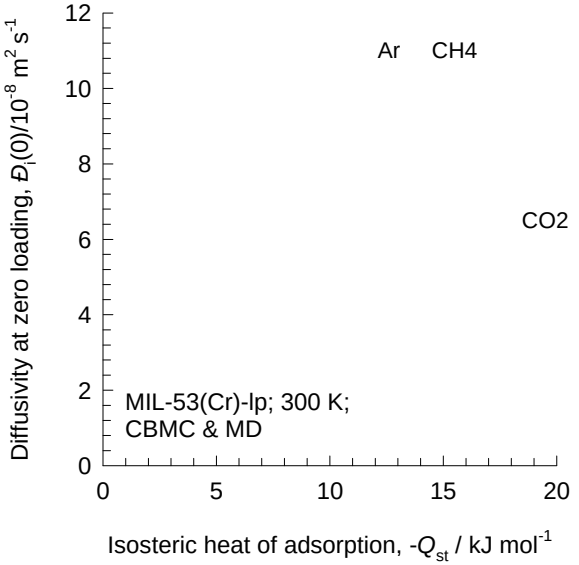

1D micro-porous channels
With side pockets

FER pore landscape

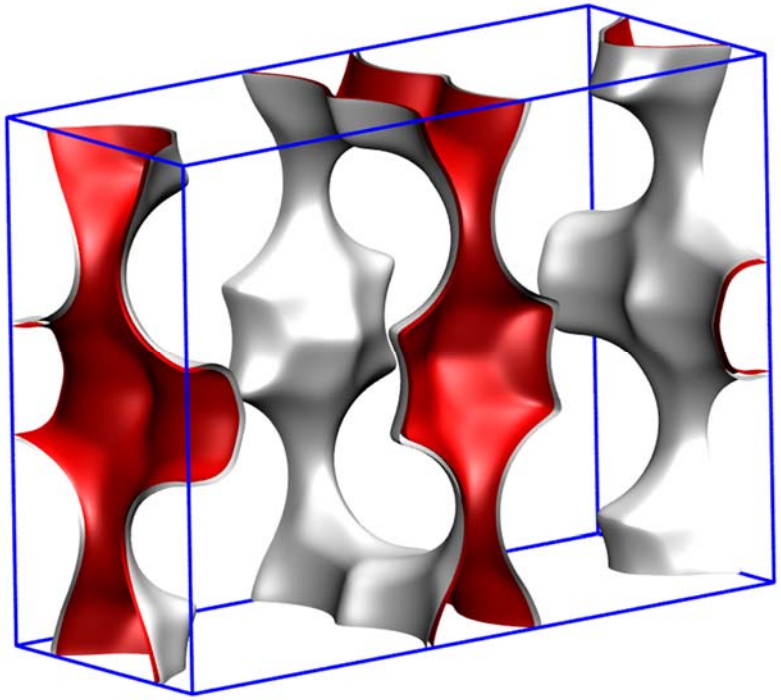

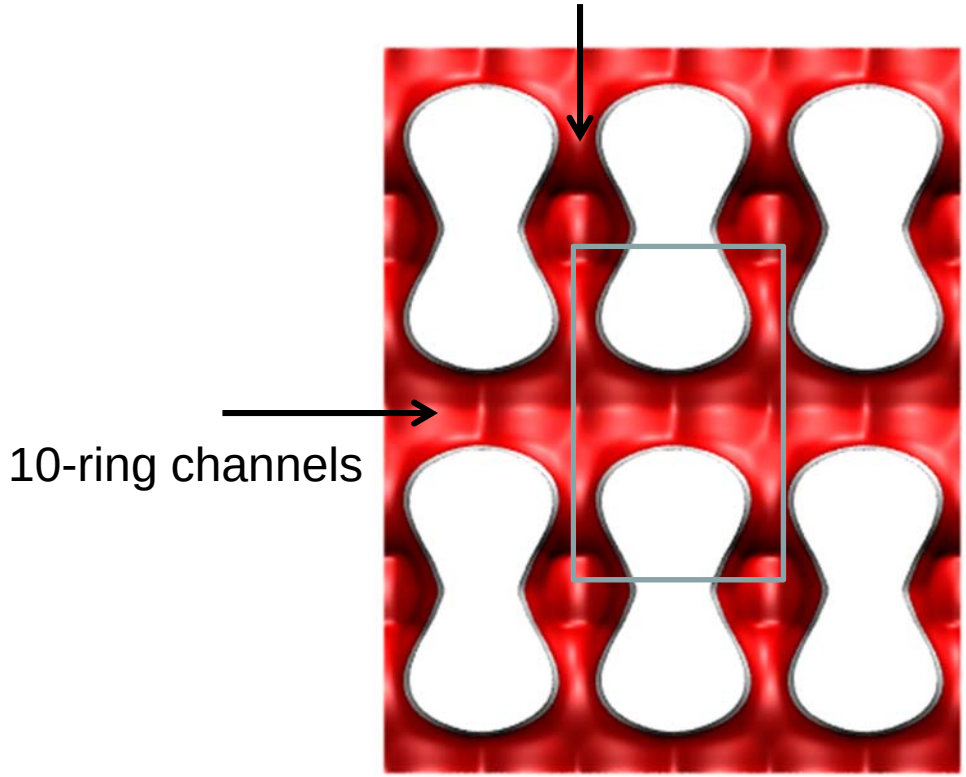

This is one unit cell

There are two 10-ring channels
There are two 8-ring channels

Structural information from: C. Baerlocher, L.B. McCusker, Database of Zeolite Structures, International Zeolite Association, http://www.iza-structure.org/databases/

FER pore landscape

8-ring channels

10-ring channels

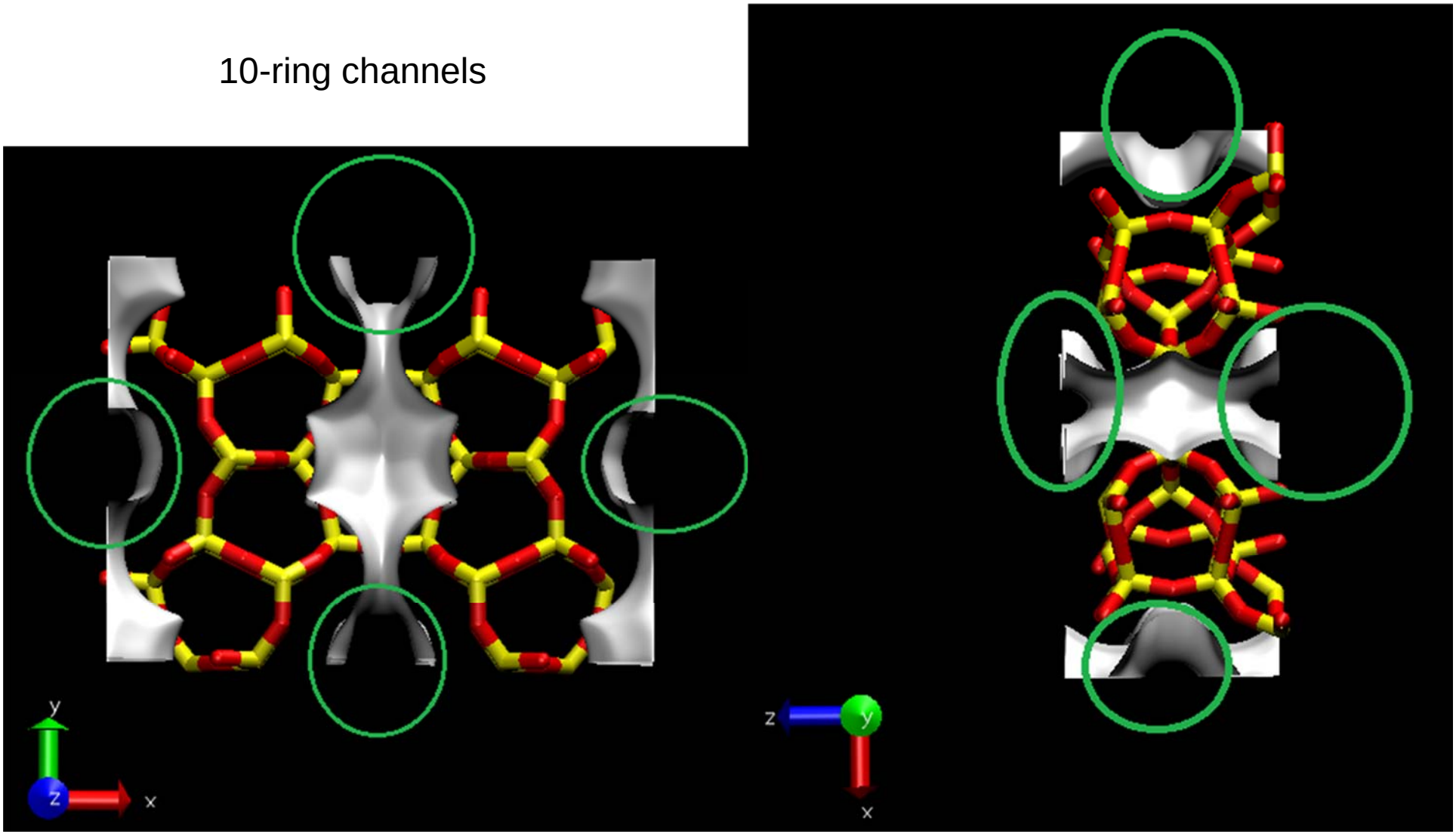

FER pore dimensions

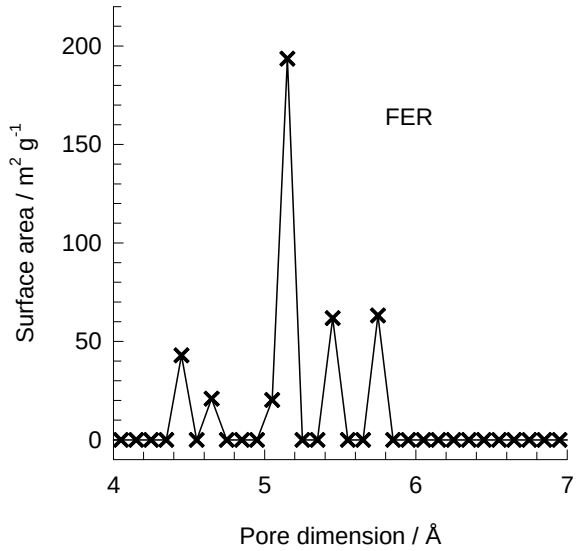

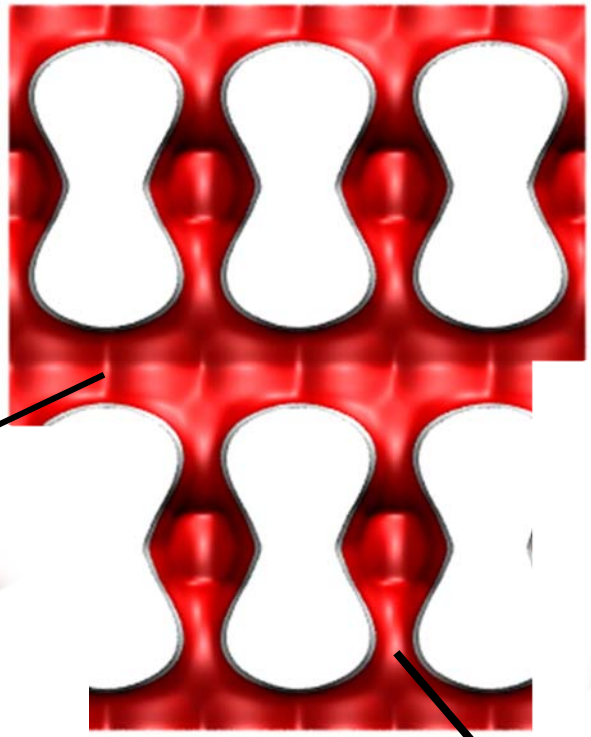

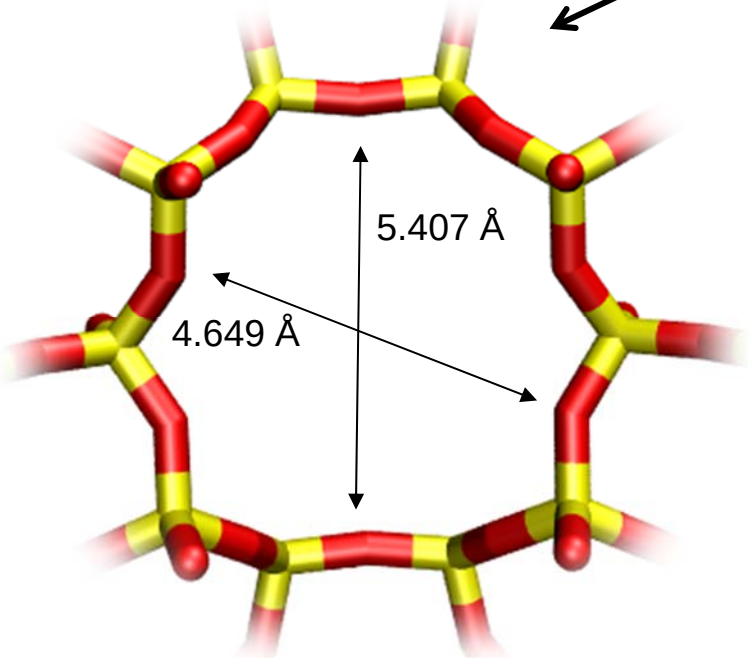

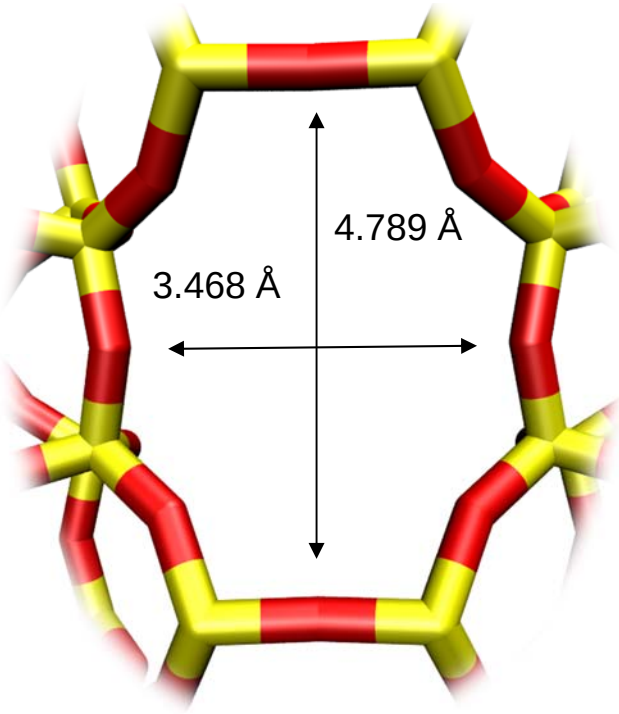

FER channel [0 0 1]

FER [0 1 0]

FER pore landscape

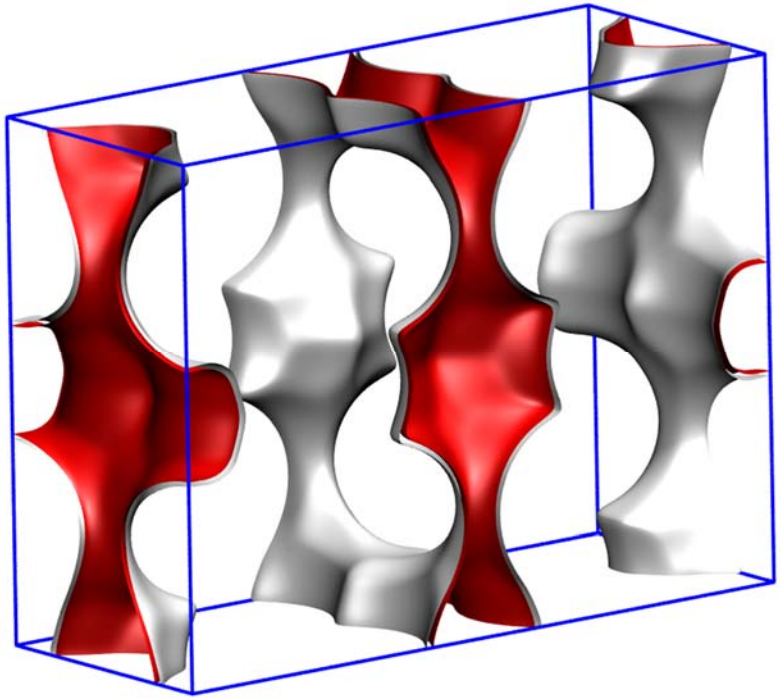

	FER
a /Å	19.156
b /Å	14.127
c /Å	7.489
Cell volume / Å^3	2026.649
conversion factor for [molec/uc] to [mol per kg Framework]	0.4623
conversion factor for [molec/uc] to [kmol/m^3]	2.8968
ρ [kg/m3]	1772.33
MW unit cell [g/mol (framework)]	2163.053
ϕ, fractional pore volume	0.283
open space / Å^3/uc	573.2
Pore volume / cm^3/g	0.160
Surface area /m^2/g	403.0
DeLaunay diameter /Å	4.65

FER CBMC simulations of isotherms, and -Q_{st}; MD simulations of diffusivities

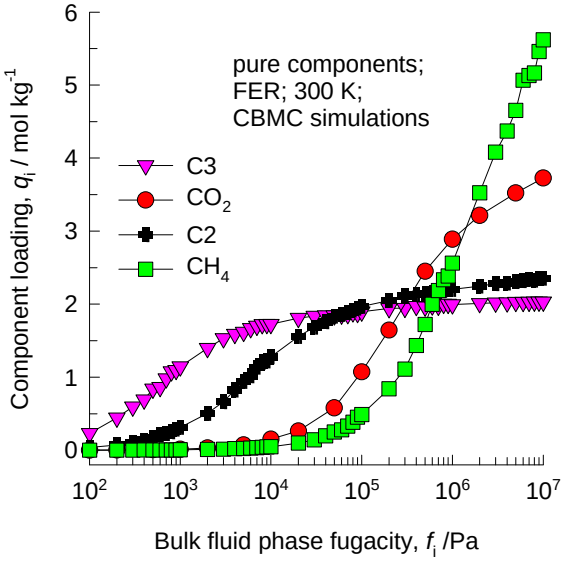

Note that C2 and C3 above refer to saturated alkanes.

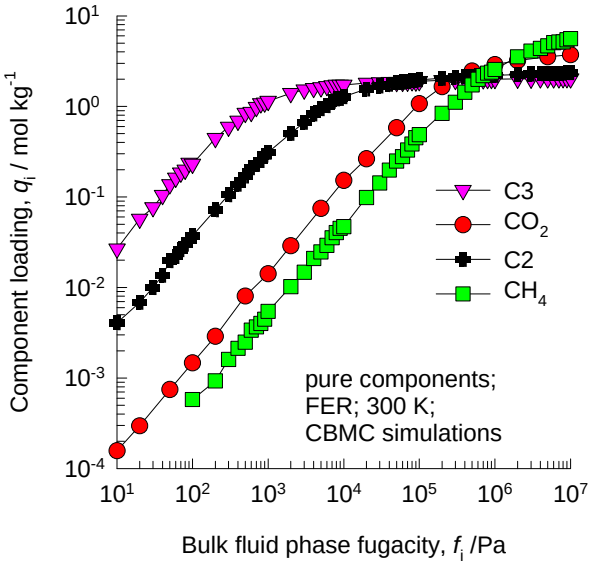

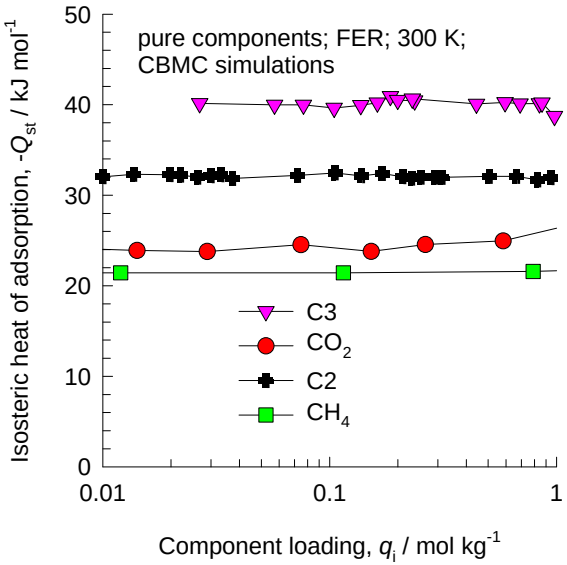

FER MD simulations of unary diffusivities

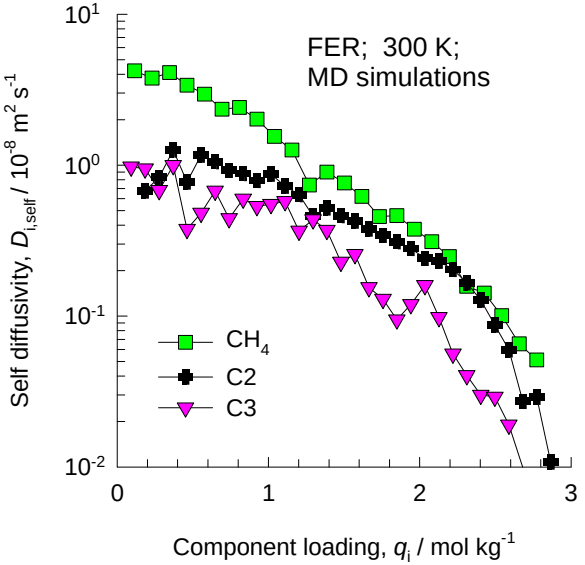

Note that C2 and C3 above refer to saturated alkanes.

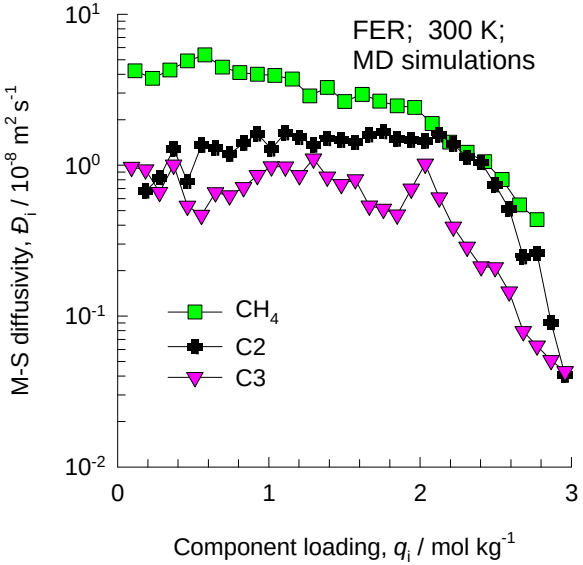

MOR pore landscape

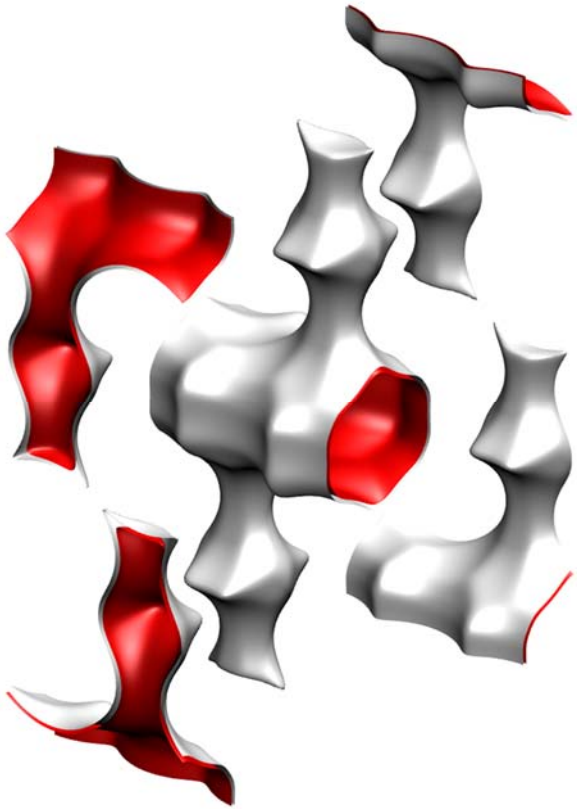

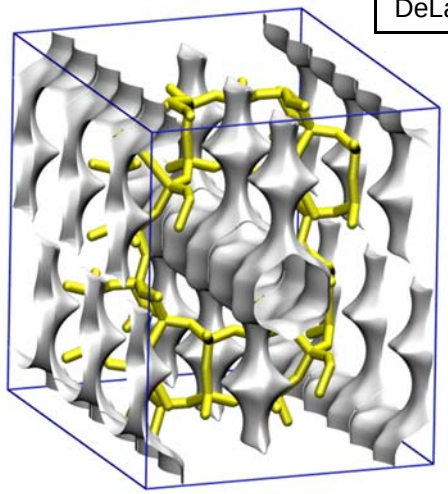

	MOR
a /Å	18.094
b /Å	20.516
c /Å	7.524
Cell volume / Å^3	2793.033
conversion factor for [molec/uc] to [mol per kg Framework]	0.3467
conversion factor for [molec/uc] to [kmol/m^3]	2.0877
ρ [kg/m3]	1714.691
MW unit cell [g/mol(framework)]	2884.07
ϕ, fractional pore volume	0.285
open space / Å^3/uc	795.4
Pore volume / cm^3/g	0.166
Surface area /m^2/g	417.0
DeLaunay diameter /Å	6.44

Structural information from: C. Baerlocher, L.B. McCusker, Database of Zeolite Structures, International Zeolite Association, http://www.iza-structure.org/databases/

MOR pore dimensions

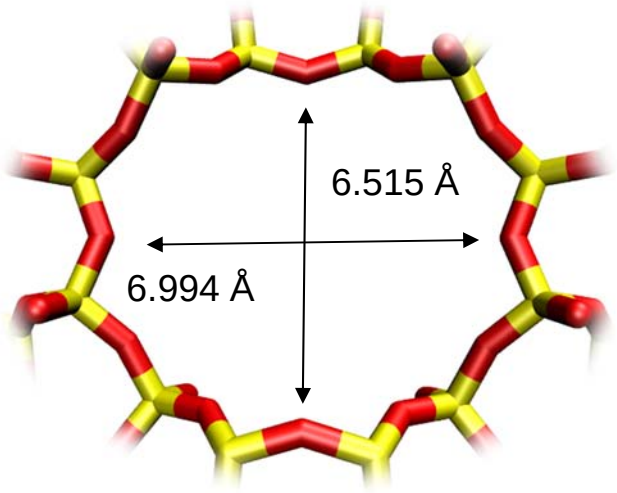

MOR Channel [1 0 0]

12-ring
main channels

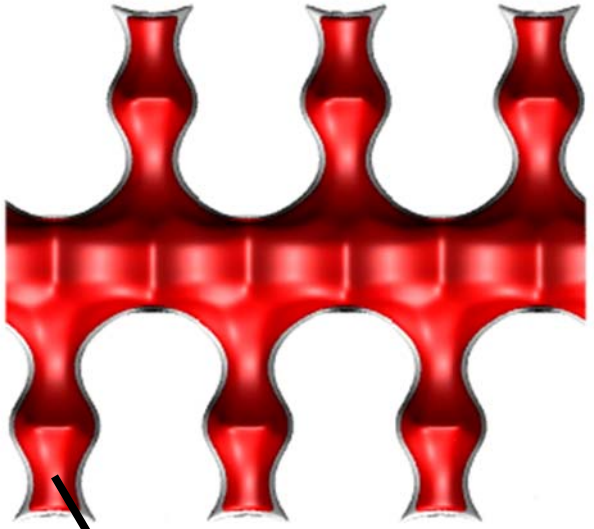

8-ring

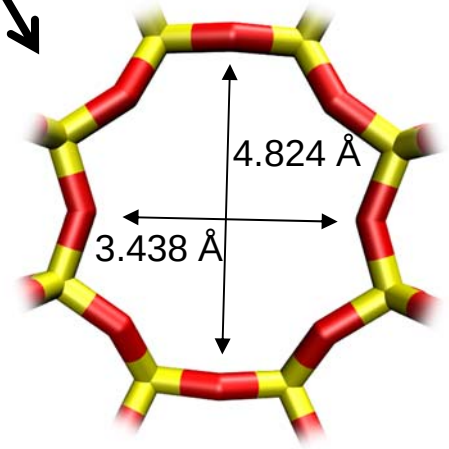

MOR [0 1 0]

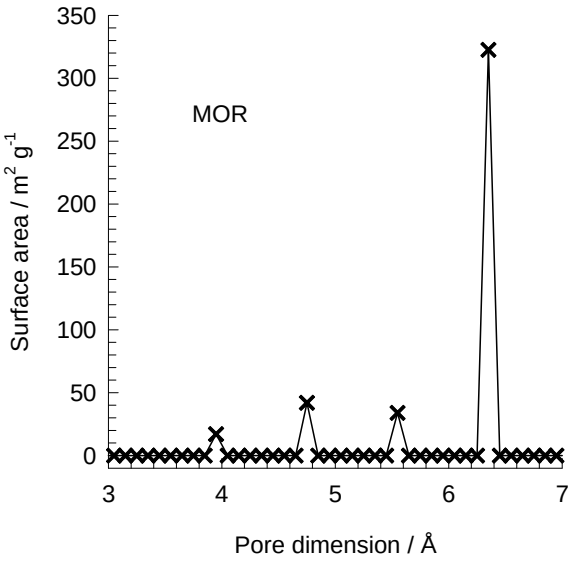

This plot of surface area versus pore dimension is determined using a combination of the DeLaunay triangulation method for pore dimension determination, and the procedure of Düren for determination of the surface area.

MOR CBMC simulations of isotherms, and -Q_{st}; MD simulations of diffusivities

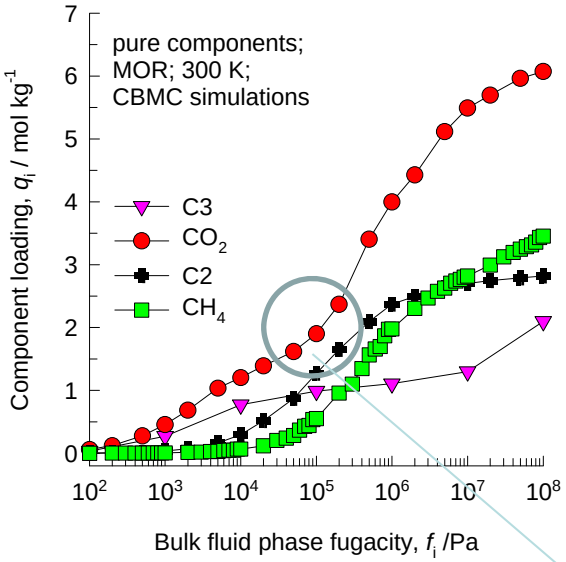

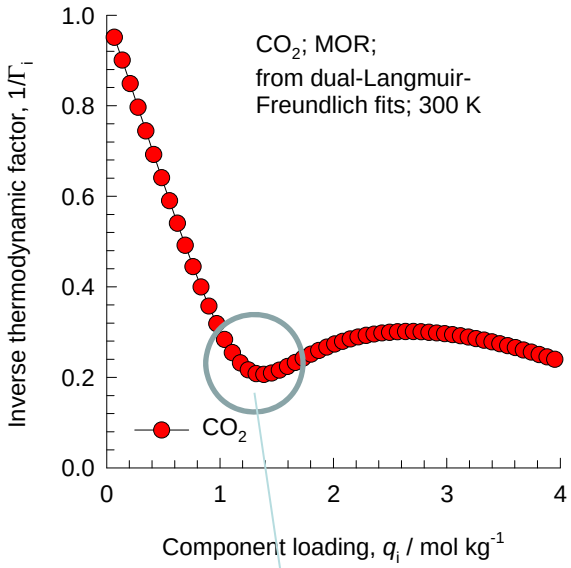

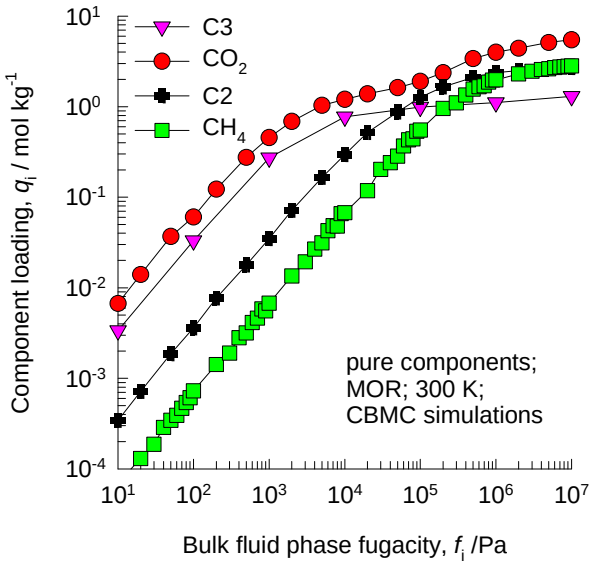

Note that C2 and C3 above refer to saturated alkanes.

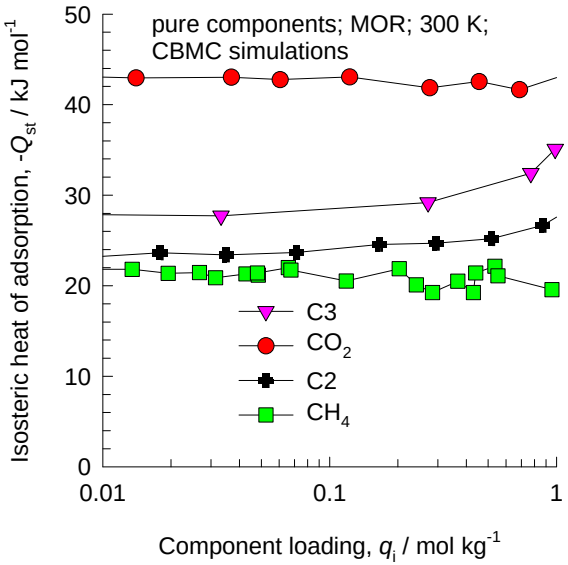

Side pockets

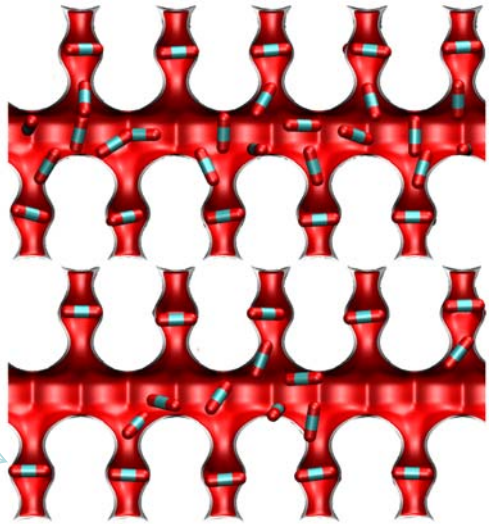

CO_2 preferentially locates in the side pockets as shown in snapshot. At a loading of 4/uc = 1.39 mol/kg, the pockets are full. This causes an infection. This also explains the high heat of adsorption due to snug fits in the side pockets

MOR MD simulations of unary diffusivities

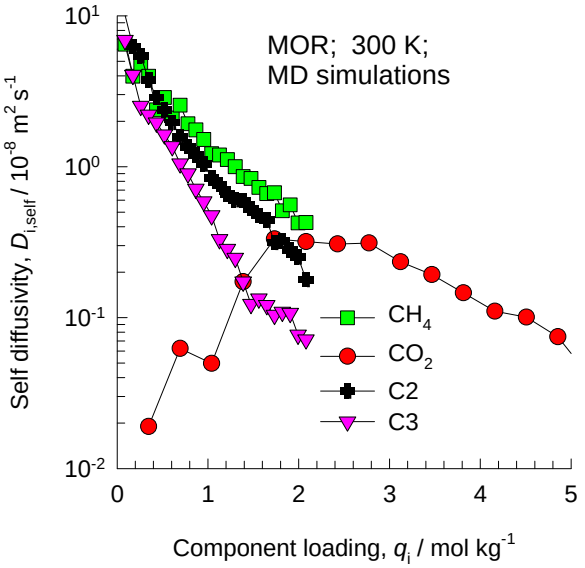

Note that C2 and C3 above refer to saturated alkanes.

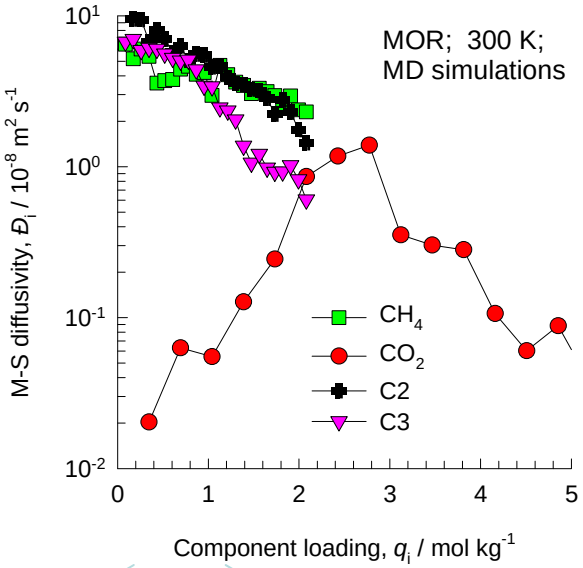

CO_2 preferentially locates in the side pockets in this loading range. This explains the low diffusivities.

Side pockets

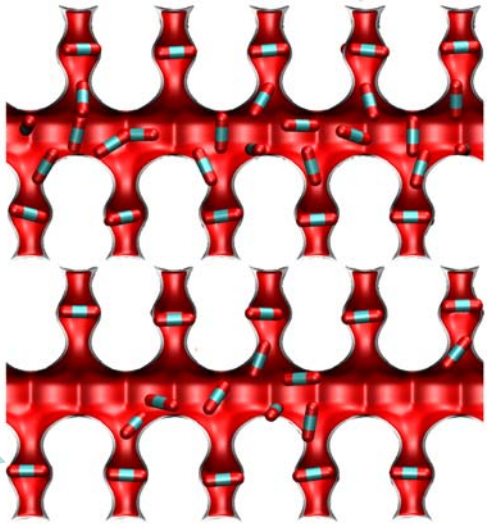

“Open” structures with large cavities

FAU-Si pore landscape

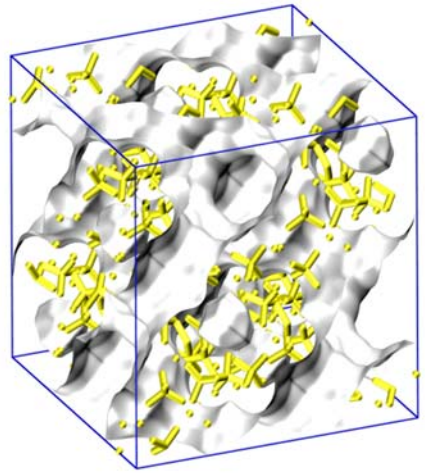

The sodalite cages are blocked in simulations and are not accessible to guest molecules; these are excluded for pore volume determination.

12-ring
window of FAU

There are 8 cages per unit cell. The volume of one FAU cage is 786 Å^3, larger in size than that of LTA (743 Å^3) and DDR (278 Å^3).

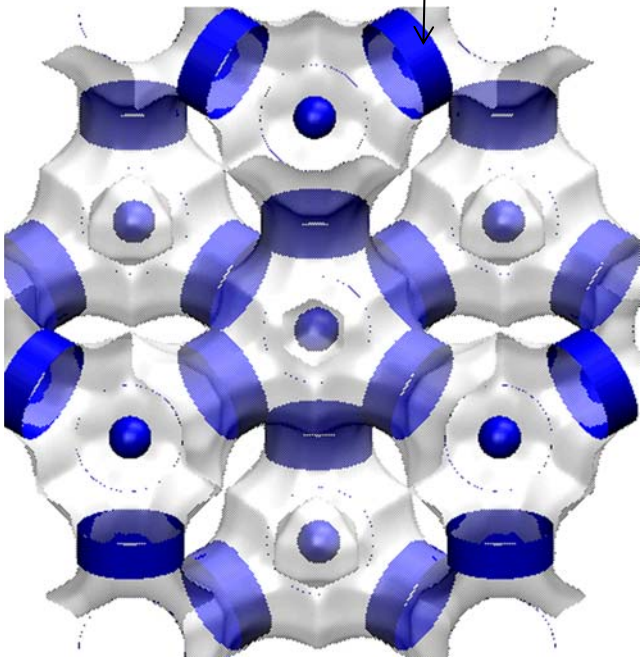

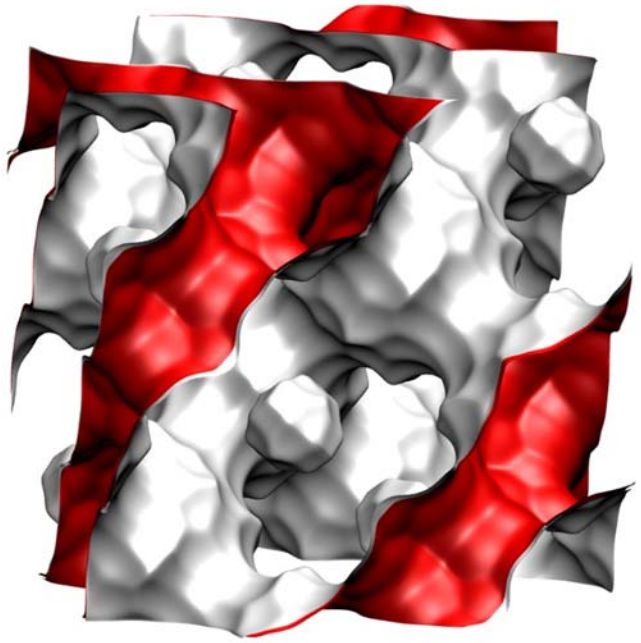

Structural information from: C. Baerlocher, L.B. McCusker, Database of Zeolite Structures, International Zeolite Association, http://www.iza-structure.org/databases/

FAU-Si window and pore dimensions

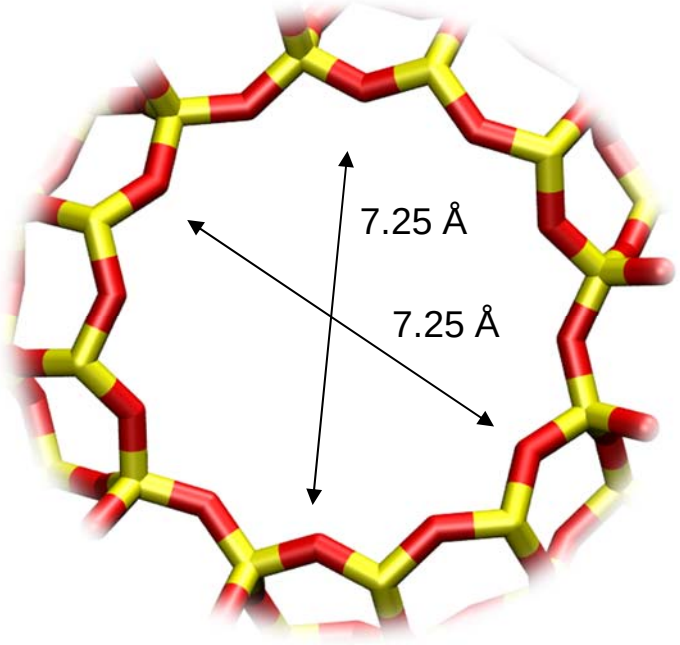

This plot of surface area versus pore dimension is determined using a combination of the DeLaunay triangulation method for pore dimension determination, and the procedure of Düren for determination of the surface area.

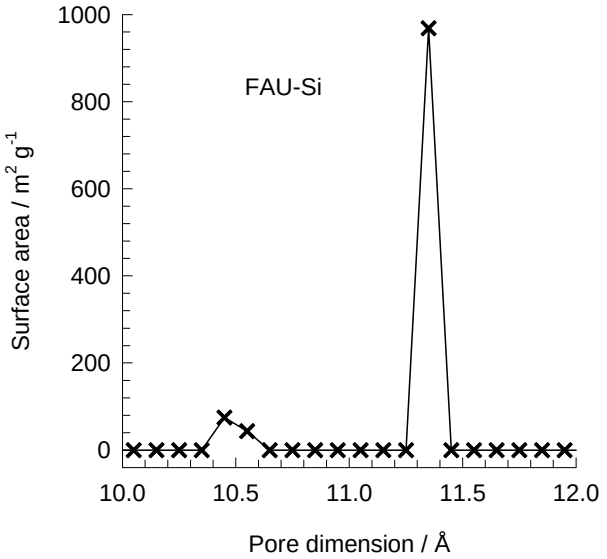

	FAU-Si
a /Å	24.28
b /Å	24.28
c /Å	24.28
Cell volume / Å^3	14313.51
conversion factor for [molec/uc] to [mol per kg Framework]	0.0867
conversion factor for [molec/uc] to [kmol/m^3]	0.2642
ρ [kg/m3]	1338.369
MW unit cell [g/mol (framework)]	11536.28
ϕ, fractional pore volume	0.439
open space / Å^3/uc	6285.6
Pore volume / cm^3/g	0.328
Surface area /m^2/g	1086.0
DeLaunay diameter /Å	7.37

FAU-Si CBMC simulations of isotherms, and isosteric heats of adsorption

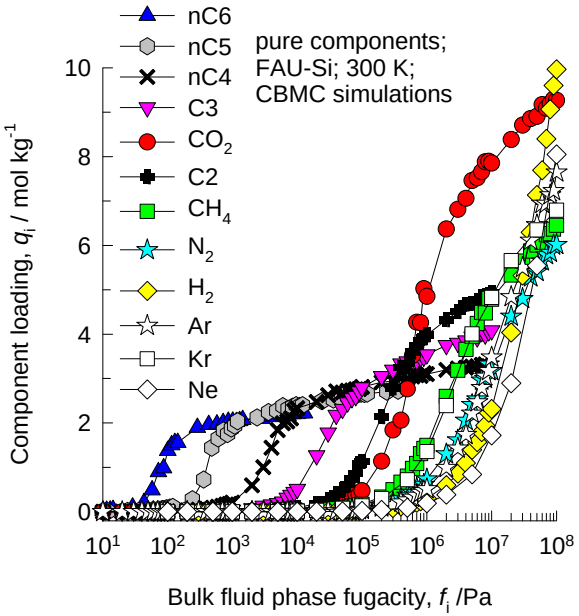

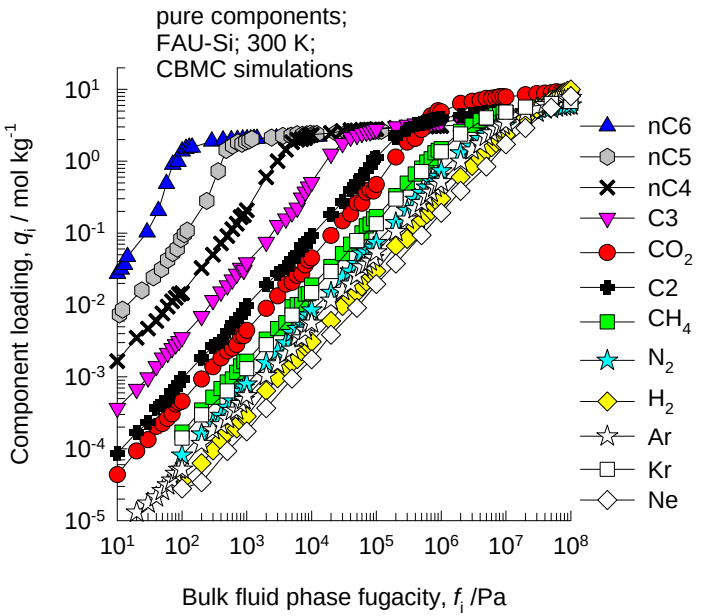

Note that C2 and C3 above refer to saturated alkanes

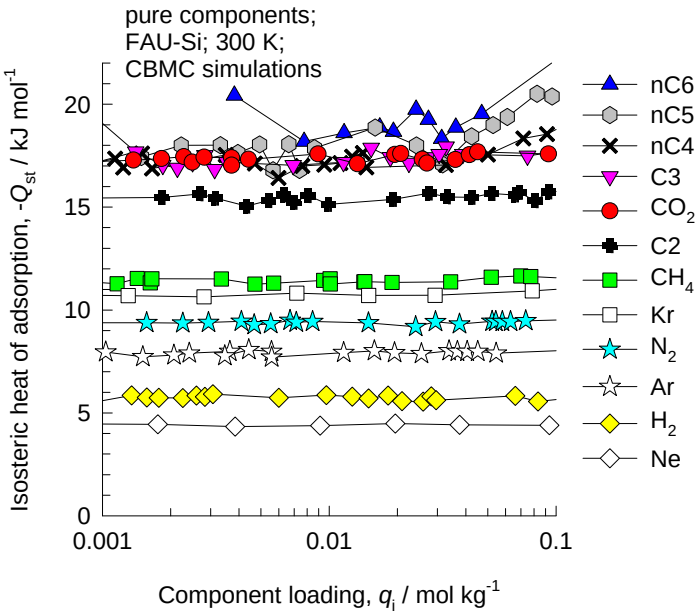

FAU-Si MD simulations of unary self- , and M-S diffusivities

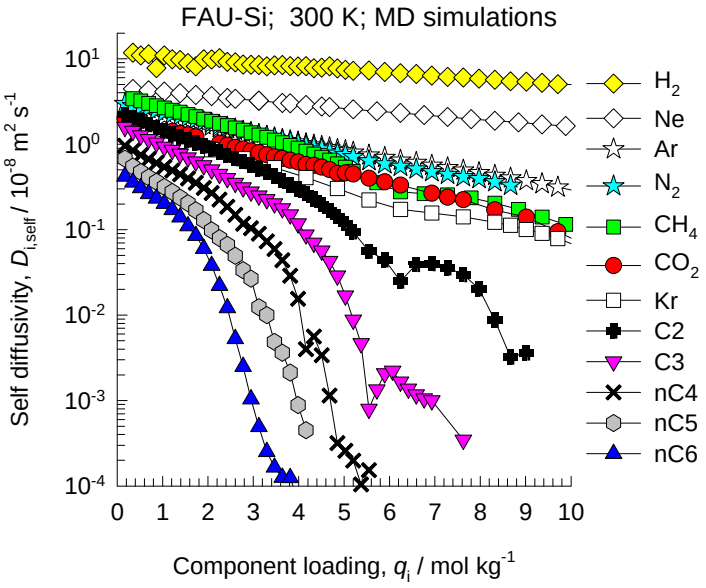

Note that C2 and C3 above refer to saturated alkanes

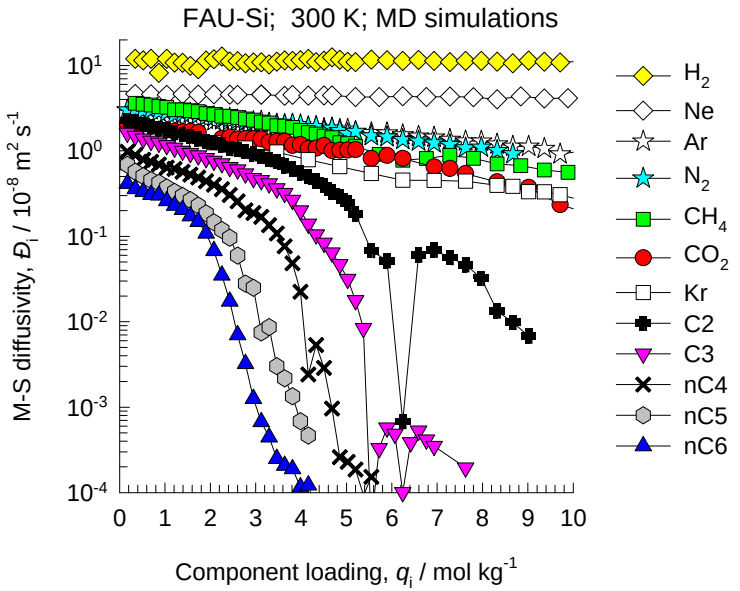

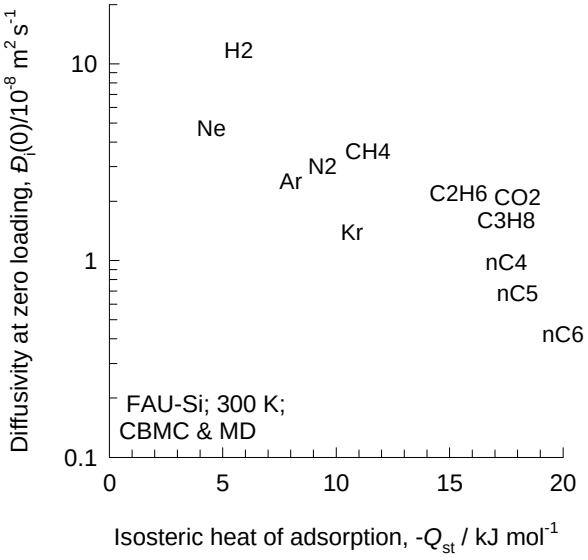

NaY (138 Si, 54 Al, 54 Na+, Si/Al=2.55)

Blue spheres are cations

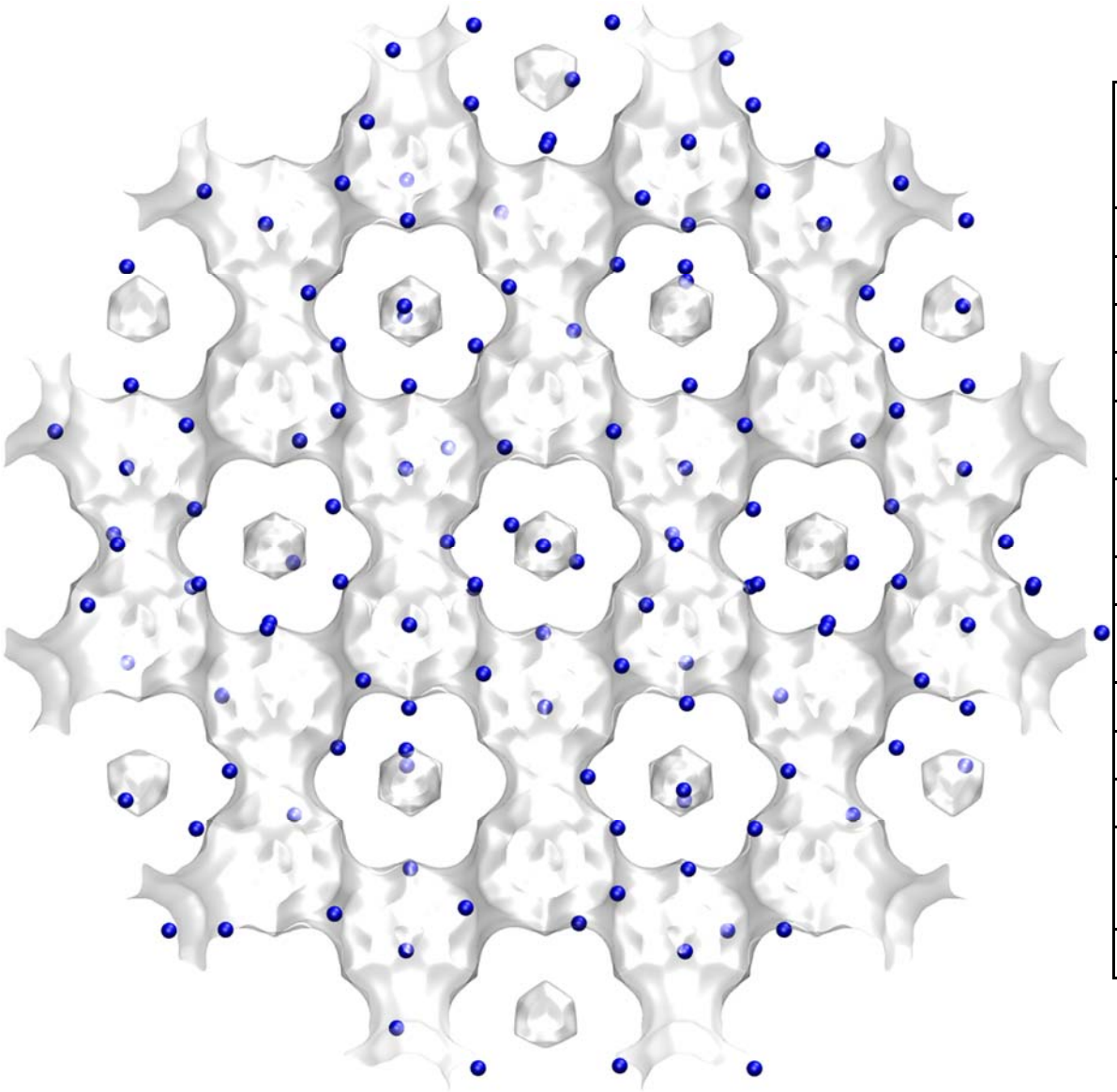

	FAU-54Al
a /Å	25.028
b /Å	25.028
c /Å	25.028
Cell volume / Å^3	15677.56
conversion factor for [molec/uc] to [mol per kg Framework]	0.0786
conversion factor for [molec/uc] to [kmol/m^3]	0.2596
ρ [kg/m3] (with cations)	1347.1
MW unit cell [g/mol(framework+cations)]	12718.08
ϕ, fractional pore volume	0.408
open space / Å^3/uc	6396.6
Pore volume / cm^3/g	0.303
Surface area /m^2/g	
DeLaunay diameter /Å	7.37

NaY CBMC simulations of isotherms, and isosteric heats of adsorption

Unary self-, and Maxwell-Stefan diffusivities

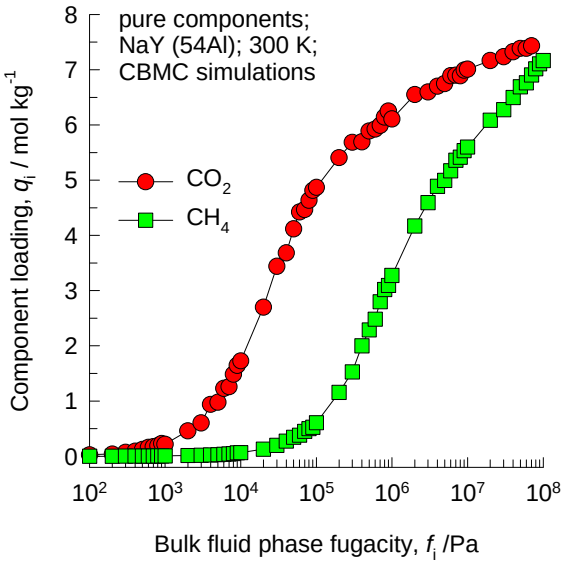

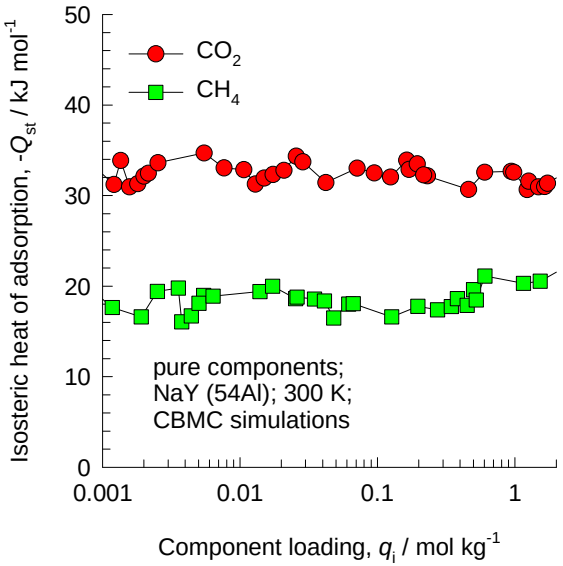

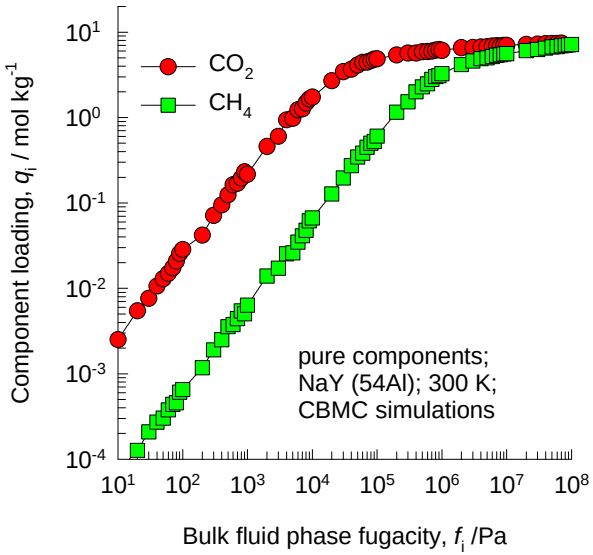

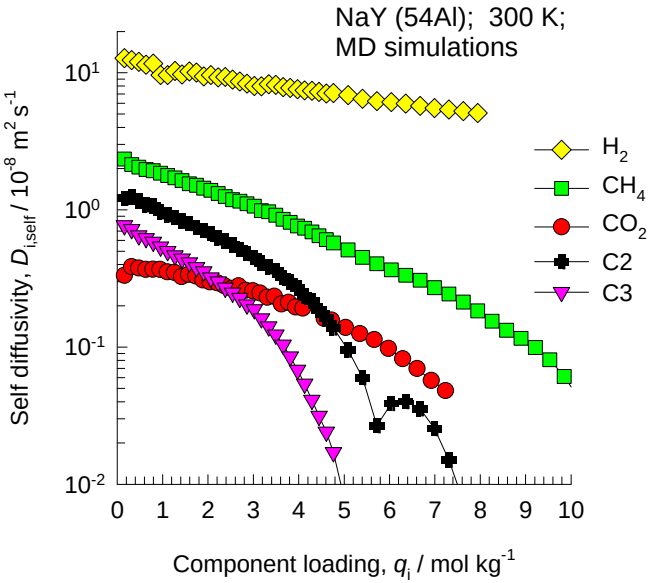

Note that C2 and C3 above refer to saturated alkanes

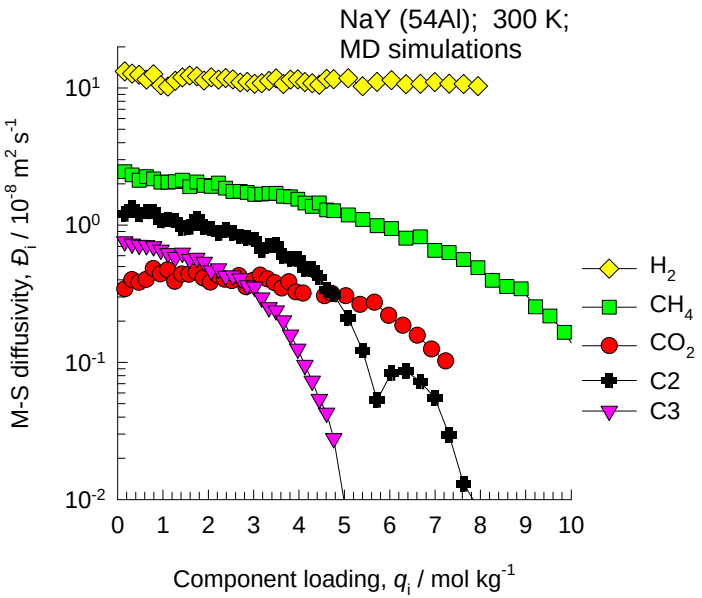

NaX (106 Si, 86 Al, 86 Na+, Si/Al=1.23)

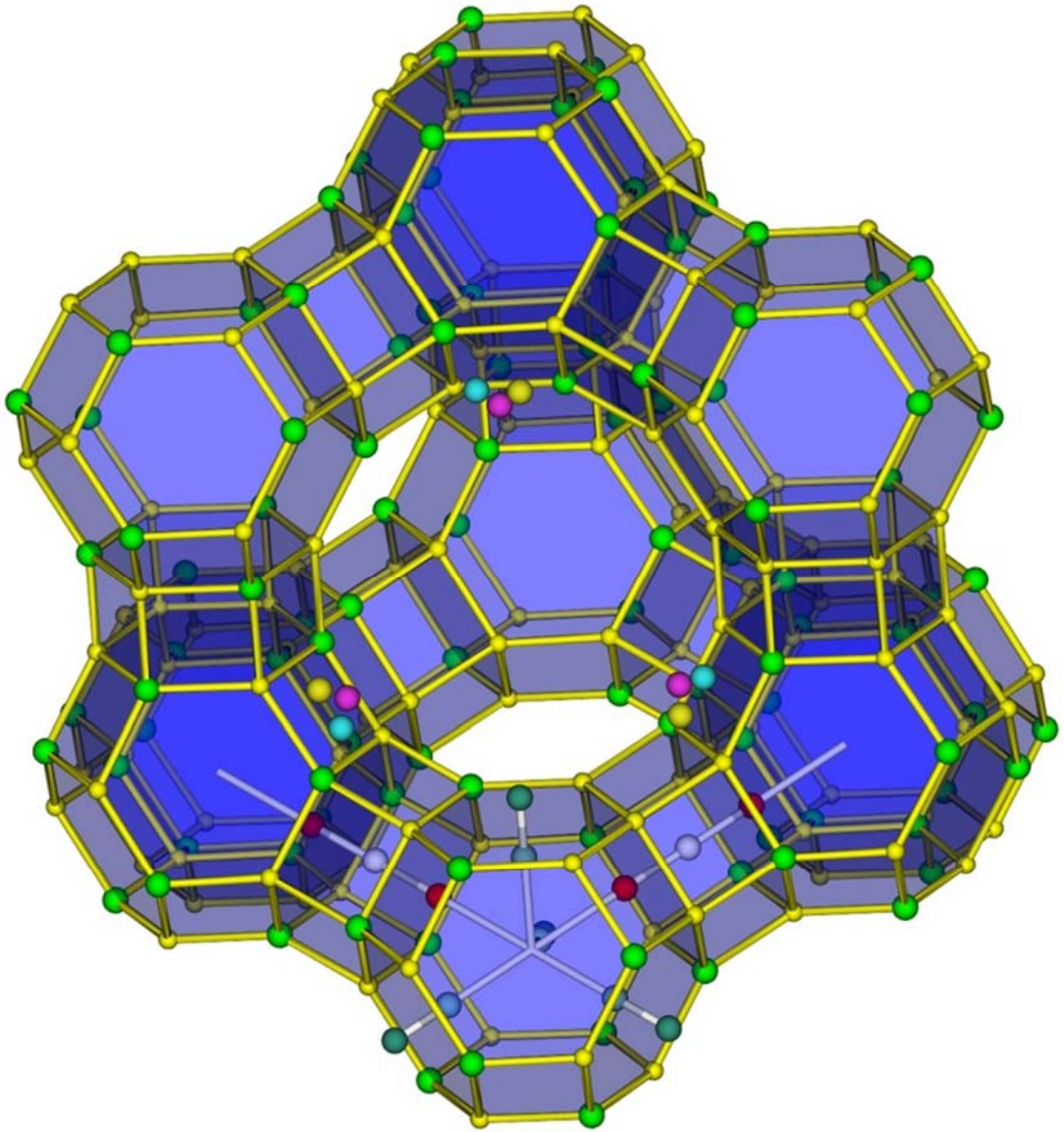

NaX (106 Si, 86 Al, 86 Na+, Si/Al=1.23)

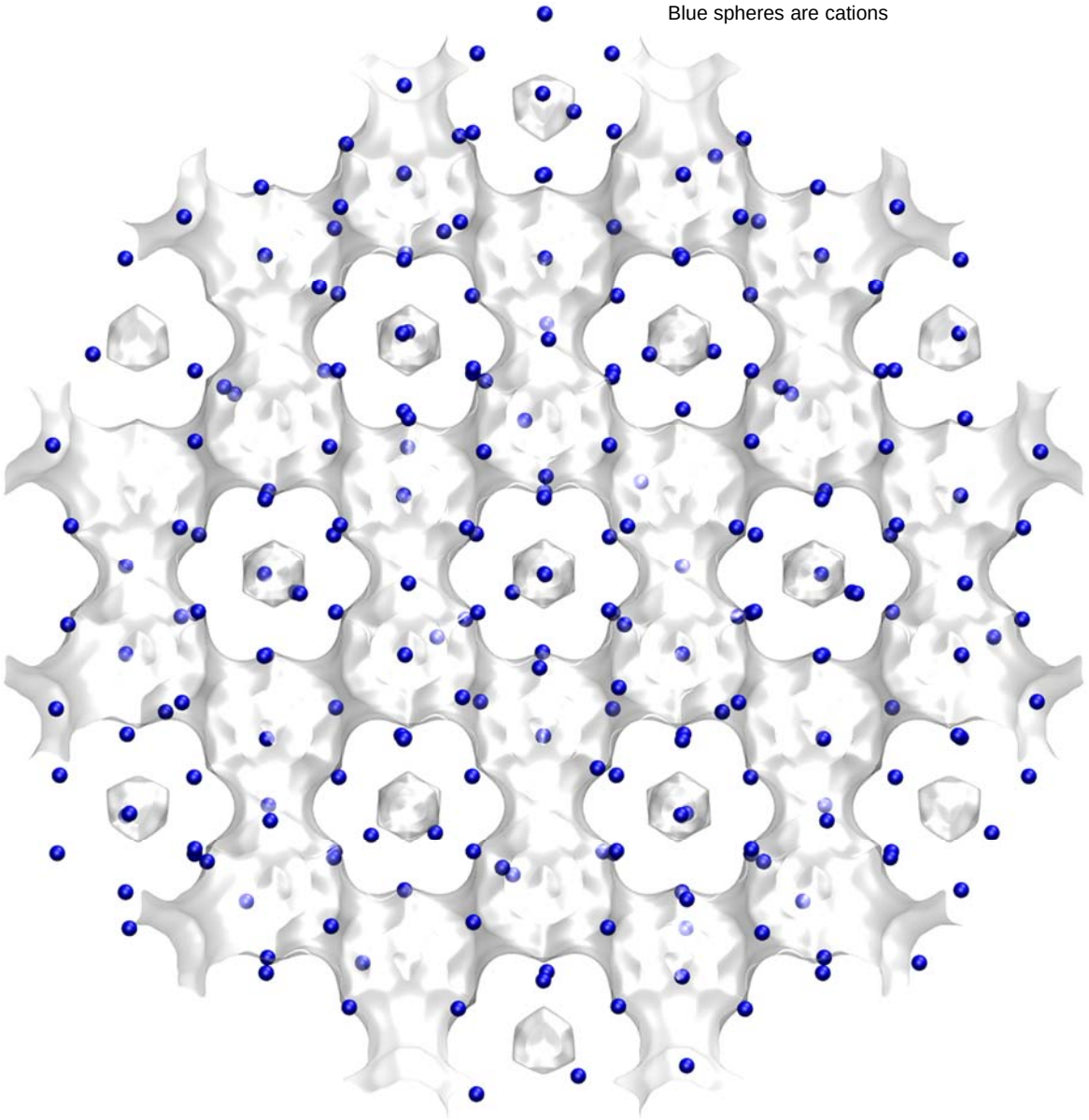

	FAU-86Al
a /Å	25.028
b /Å	25.028
c /Å	25.028
Cell volume / Å^3	15677.56
conversion factor for [molec/uc] to [mol per kg Framework]	0.0745
conversion factor for [molec/uc] to [kmol/m^3]	0.2658
ρ [kg/m3] (with cations)	1421.277
MW unit cell [g/mol(framework+cations)]	13418.42
ϕ, fractional pore volume	0.399
open space / Å^3/uc	6248.0
Pore volume / cm^3/g	0.280
Surface area /m^2/g	
DeLaunay diameter /Å	7.37

NaX CBMC simulations of isotherms, and isosteric heats of adsorption

Unary self-, and Maxwell-Stefan diffusivities

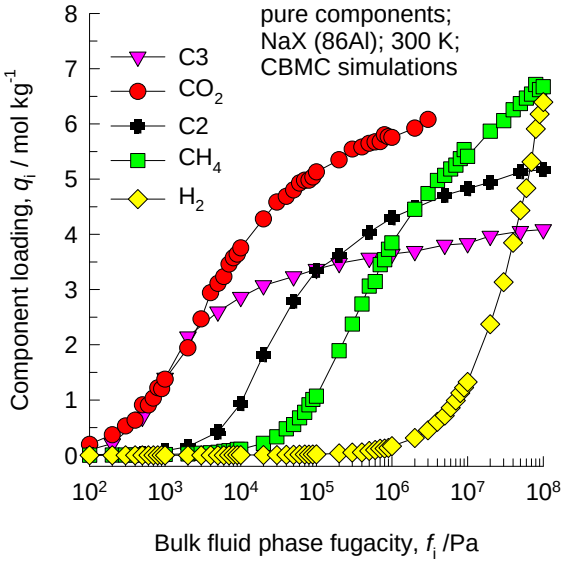

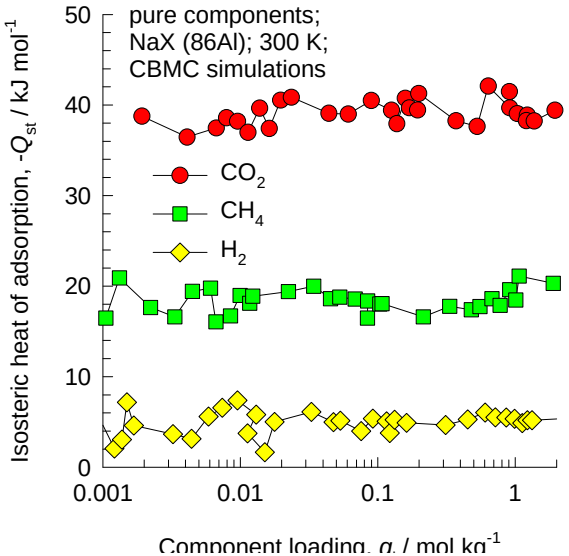

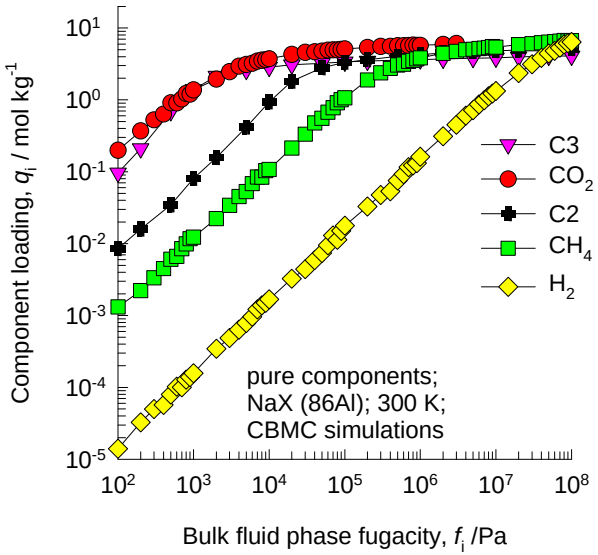

Note that C2 and C3 above refer to saturated alkanes

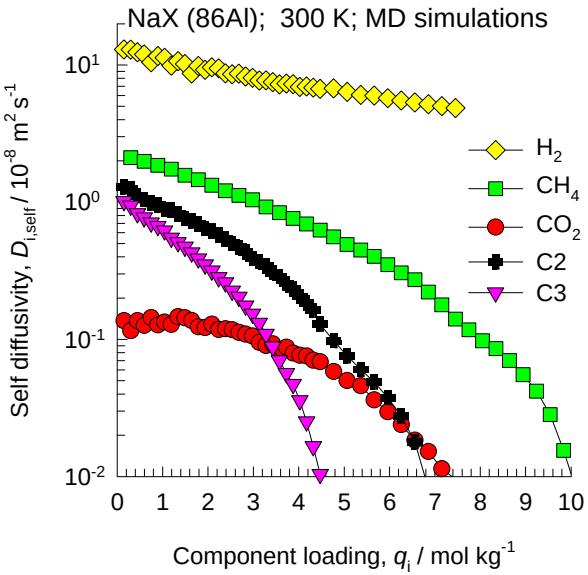

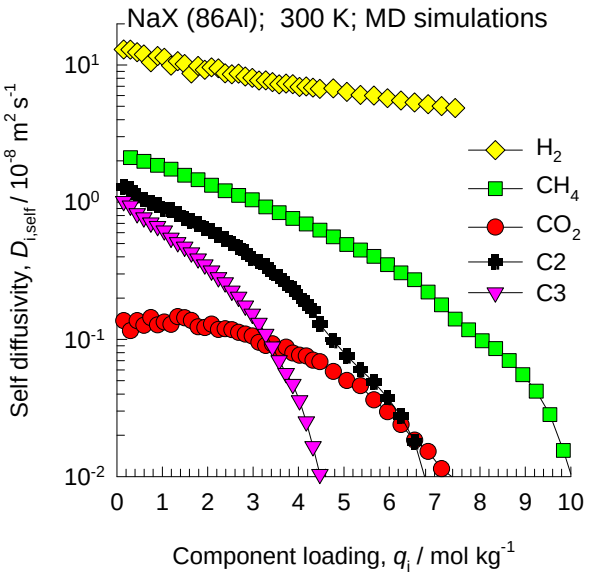

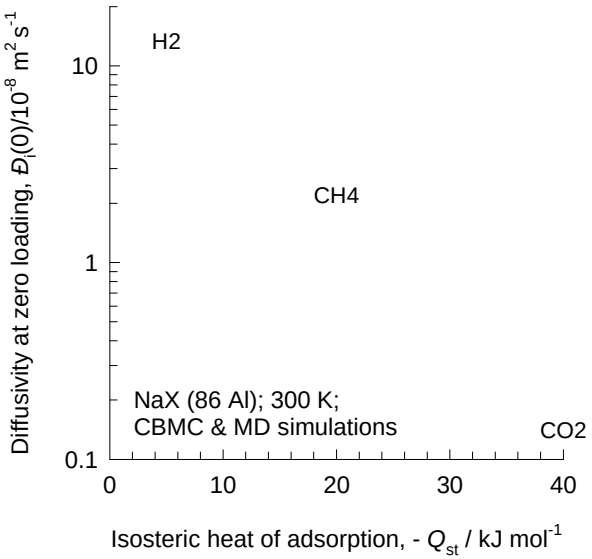

NaX zeolite: experimental isotherm data fitting

Dual-site Langmuir parameters for guest molecules in NaX zeolite.

$$q = q_{A,sat}\frac{b_A p^{\nu_A}}{1+b_A p^{\nu_A}} + q_{B,sat}\frac{b_B p^{\nu_B}}{1+b_B p^{\nu_B}};\quad b_A = b_{A0}\exp\left(\frac{E_A}{RT}\right);\quad b_B = b_{B0}\exp\left(\frac{E_B}{RT}\right)$$

	Site A				Site B			
	$q_{A,sat}$ mol kg^{-1}	b_{A0} Pa$^{-\nu_i}$	E_A kJ mol^{-1}	ν_A dimensionless	$q_{B,sat}$ mol kg^{-1}	b_{B0} Pa$^{-\nu_i}$	E_B kJ mol^{-1}	ν_B dimensionless
CO_2	3.5	3.64×10^{-13}	35	1	5.2	6.04×10^{-11}	35	1
CH_4	4	3.66×10^{-10}	14	1	5	3.75×10^{-9}	14	1
C_2H_4	0.75	2.09×10^{-10}	40	1	2.15	9.28×10^{-11}	35	1
C_2H_6	2.95	3.07×10^{-10}	28.7	1				

The isotherm fit parameters are on the basis of experimental data for variety of temperatures from:

Belmabkhout, Y.; Pirngruber, G.; Jolimaitre, E.; Methivier, A. A complete experimental approach for synthesis gas separation studies using static gravimetric and column breakthrough experiments, *Adsorption* **2007**, *13*, 341-349.

Cavenati, S.; Grande, C. A.; Rodrigues, A. E. Adsorption Equilibrium of Methane, Carbon Dioxide, and Nitrogen on Zeolite 13X at High Pressures, *J. Chem. Eng. Data* **2004**, *49*, 1095-1101.

Hyun, S. H.; Danner, R. P. Equiilbrium Adsorption of Ethane, Ethylene, Isobutane, Carbon Dioxide, and Their Binary Mixtures on 13X Molecular Sieves, *J. Chem. Eng. Data* **1982**, *27*, 196-200.

Bao, Z.; Yu, L.; Ren, Q.; Lu, X.; Deng, S. Adsorption of CO_2 and CH_4 on a magnesium-based metal organic framework, *J. Colloid Interface Sci.* **2011**, *353*, 549-556.

He, Y.; Krishna, R.; Chen, B. Metal-Organic Frameworks with Potential for Energy-Efficient Adsorptive Separation of Light Hydrocarbons, *Energy Environ. Sci.* **2012**, *XXX*, XXX-XXX. http://dx.doi.org/doi:10.1039/C2EE22858K.

NaX zeolite: isosteric heats of adsorption

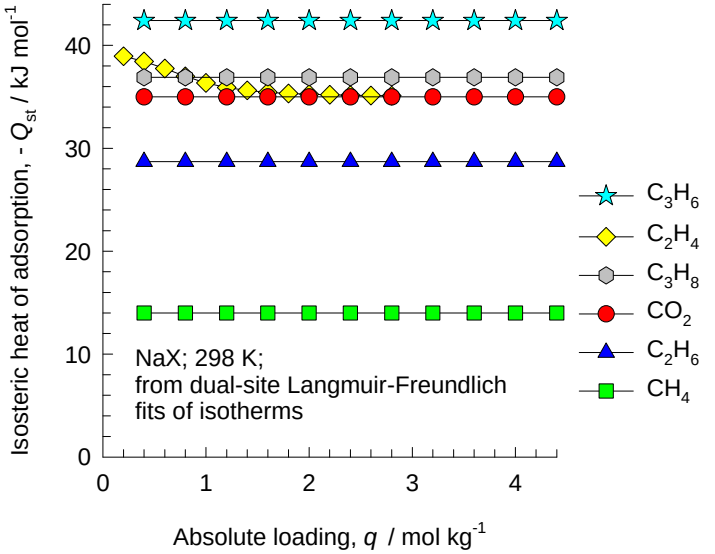

These calculations of $-Q_{st}$ are based on the isotherm fits provided in the previous slide. The values were determined by numerical differentiation and use of the Clausius-Clapeyron equation.

These values of $-Q_{st}$ for propene and propane plotted above are from
Lamia, N.; Granato, M. A.; Gomes, P. S. A.; Grande, C. A.; Wolff, L.; Leflaive, P.; Leinekugel-le-Cocq, D.; Rodrigues, A. E. Propane/Propylene Separation by Simulated Moving Bed II. Measurement and Prediction of Binary Adsorption Equilibria of Propane, Propylene, Isobutane, and 1-Butene on 13X Zeolite, *Sep. Sci. and Technol.* **2009**, *44*, 1485-1509.

Compare CO_2 in FAU-Si vs NaY vs NaX

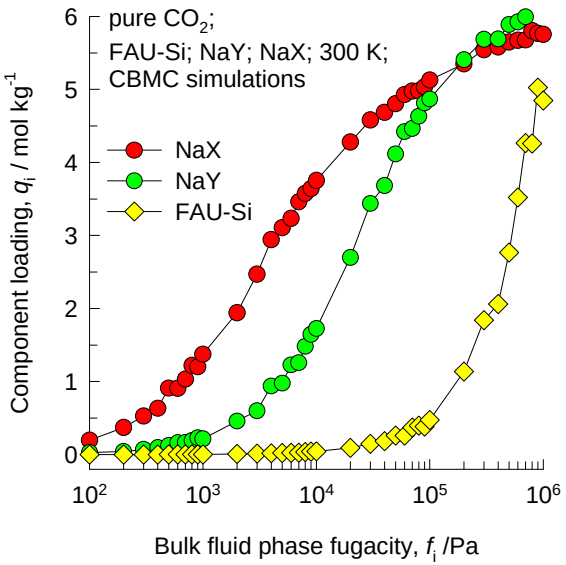

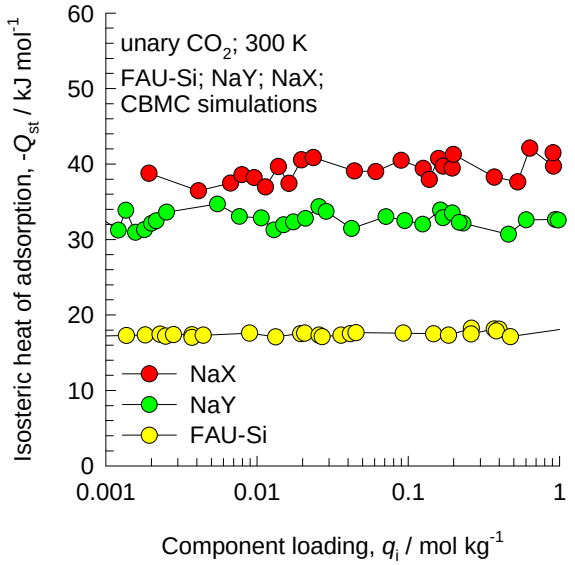

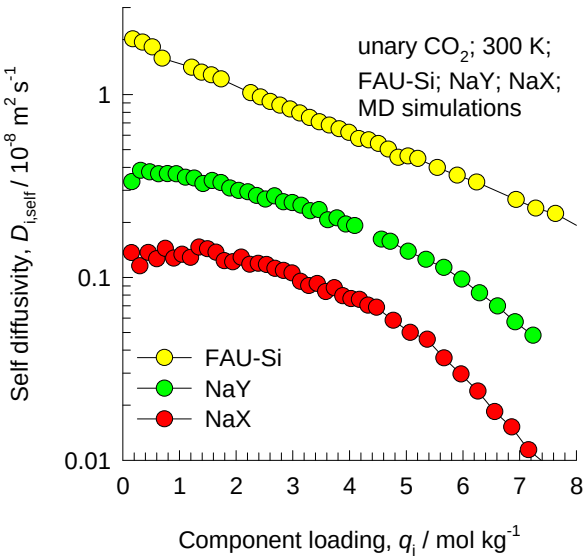

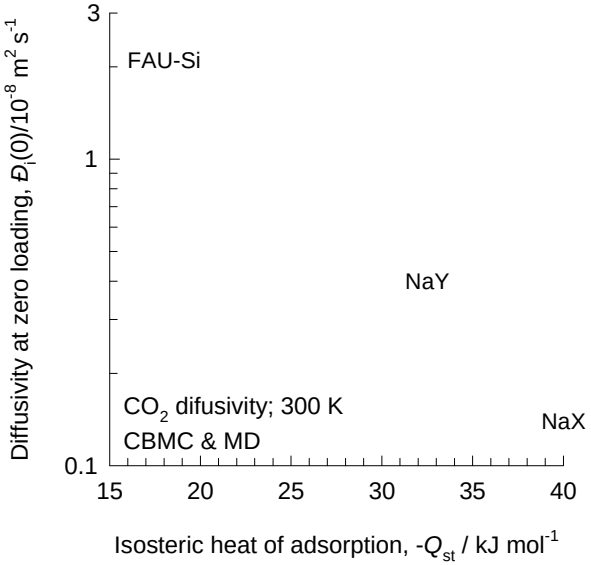

CuBTC pore landscapes

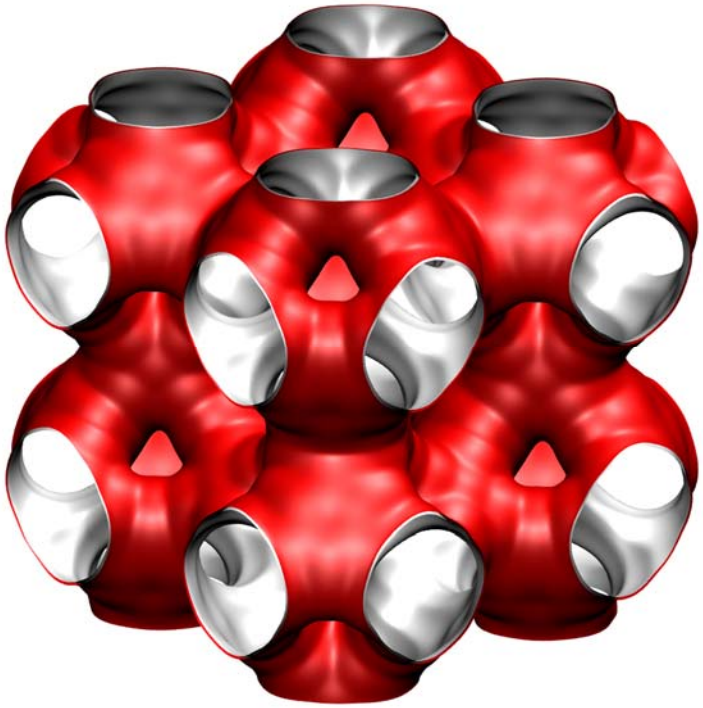

The structural information for CuBTC (= $Cu_3(BTC)_2$ with BTC = 1,3,5-benzenetricarboxylate) have been taken from

S.S.Y. Chui, S.M.F. Lo, J.P.H. Charmant, A.G. Orpen, I.D. Williams, A chemically functionalizable nanoporous material $[Cu_3(TMA)_2(H2O)_3]_n$, Science 283 (1999) 1148-1150.
The crystal structure of Chui et al. includes axial oxygen atoms weakly bonded to the Cu atoms, which correspond to water ligands. Our simulations have been performed on the dry CuBTC with these oxygen atoms removed.

Q. Yang, C. Zhong, Electrostatic-Field-Induced Enhancement of Gas Mixture Separation in Metal-Organic Frameworks: A Computational Study, ChemPhysChem 7 (2006) 1417-1421.

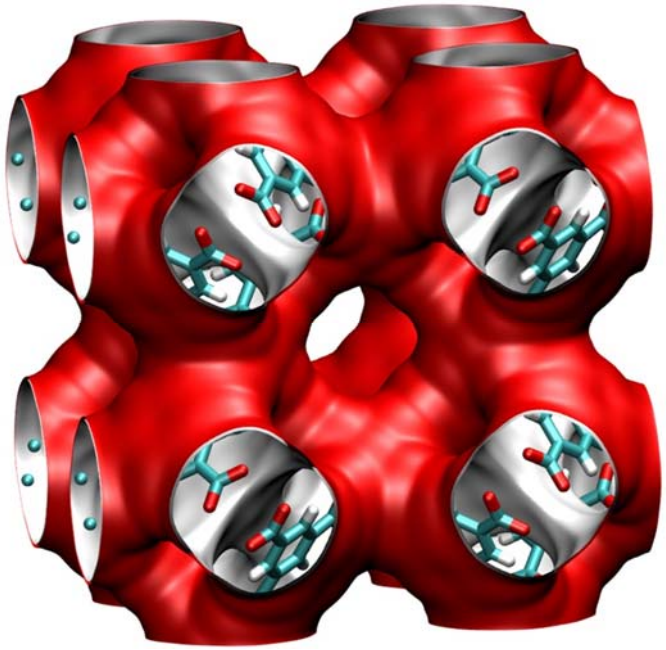

Snapshot of CO_2/CH_4 mixture

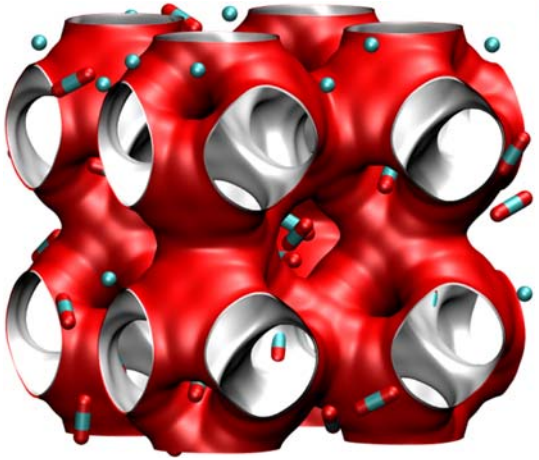

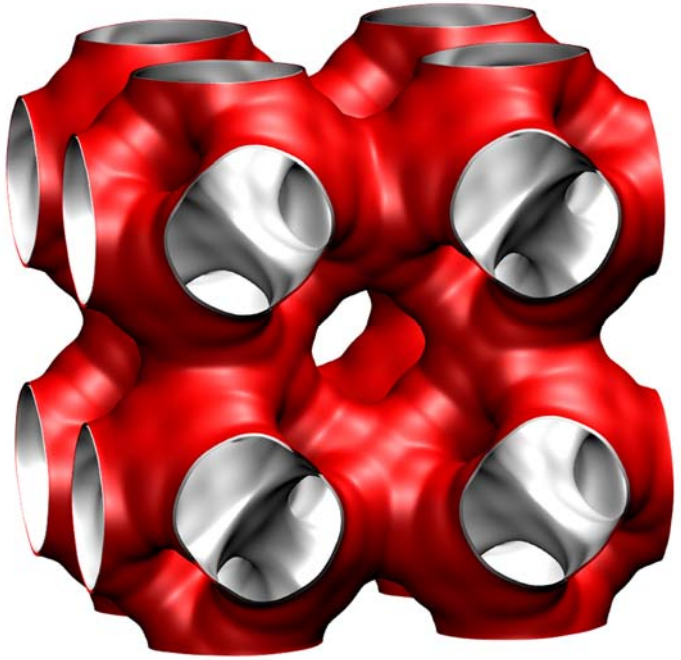

CuBTC pore dimensions

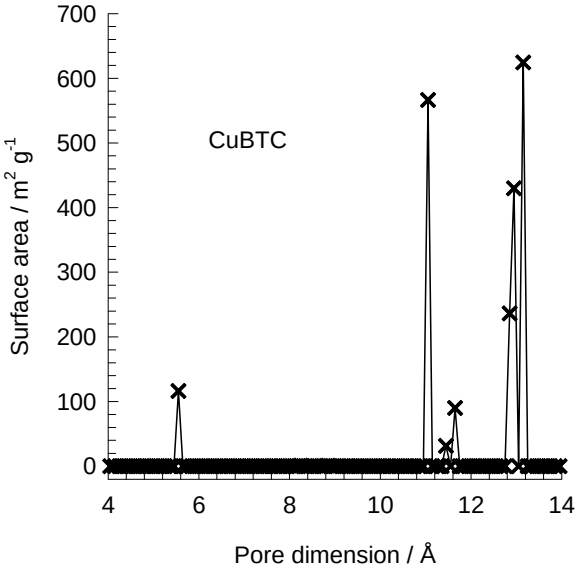

This plot of surface area versus pore dimension is determined using a combination of the DeLaunay triangulation method for pore dimension determination, and the procedure of Düren for determination of the surface area.

	CuBTC
a /Å	26.343
b /Å	26.343
c /Å	26.343
Cell volume / Å^3	18280.82
conversion factor for [molec/uc] to [mol per kg Framework]	0.1034
conversion factor for [molec/uc] to [kmol/m^3]	0.1218
ρ [kg/m3]	878.8298
MW unit cell [g/mol(framework)]	9674.855
ϕ, fractional pore volume	0.746
open space / Å^3/uc	13628.4
Pore volume / cm^3/g	0.848
Surface area /m^2/g	2097.0
DeLaunay diameter /Å	6.23

The CuBTC structure consists of two types of “cages” and two types of “windows” separating these cages. Large cages are inter-connected by 9 Å windows of square cross-section. The large cages are also connected to tetrahedral-shaped pockets of ca. 6 Å size through triangular-shaped windows of ca. 4.6 Å size

CuBTC force field for framework atoms

Lennard-Jones parameters for atoms in CuBTC. The information on charges is taken from the work of A. Martín-Calvo, E. García-Pérez, S. Calero (Molecular simulations for adsorption and separation of natural gas in IRMOF-1 and Cu-BTC metal-organic frameworks, Phys. Chem. Chem. Phys. 10 (2008) 7085-7091)

(pseudo-) atom	σ / Å	ε/k_B / K	charge
Cu	3.114	2.518	1.098
O	3.03	48.2	-0.665
Ca	3.47	47.9	0.778
Cb	3.47	47.9	-0.092
Cc	3.47	47.9	-0.014
H	2.85	7.65	0.109

CuBTC

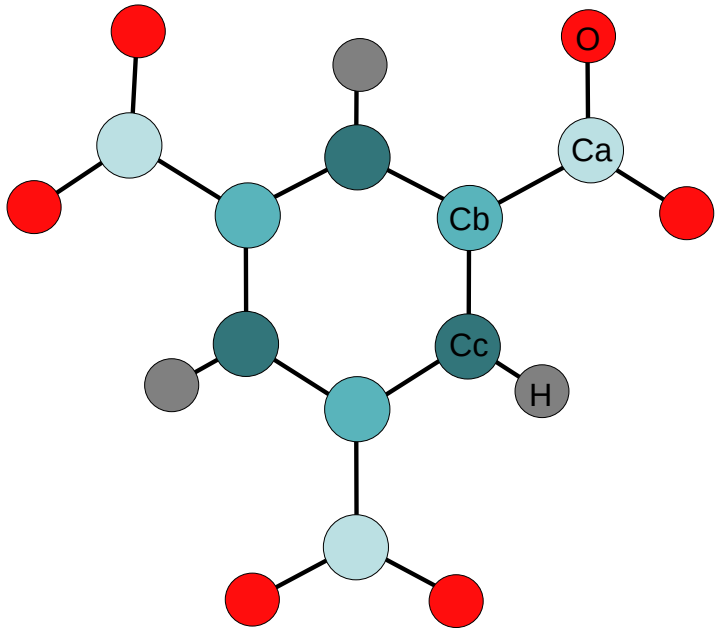

CuBTC CBMC simulations of isotherms, and isosteric heats of adsorption

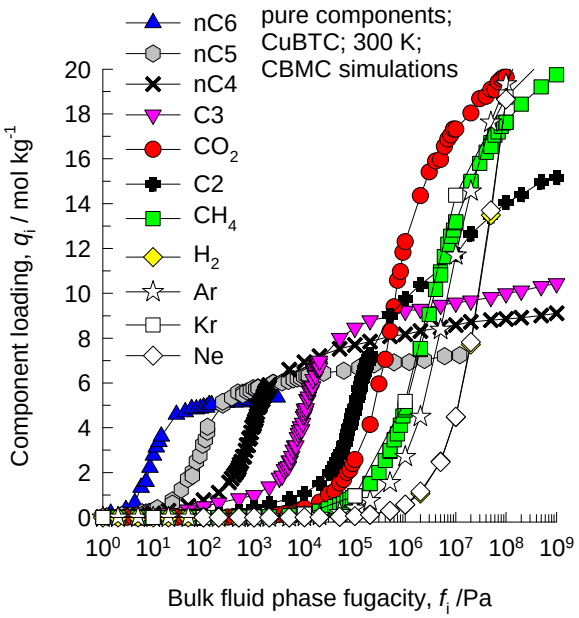

Note that C2 and C3 refer to saturated alkanes

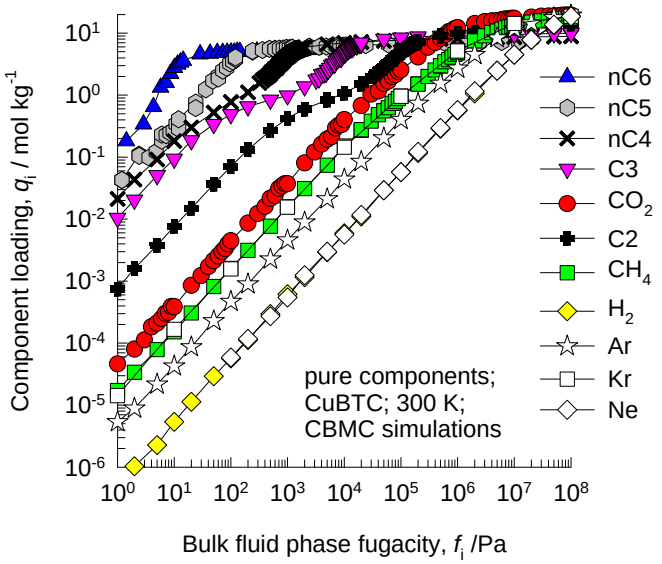

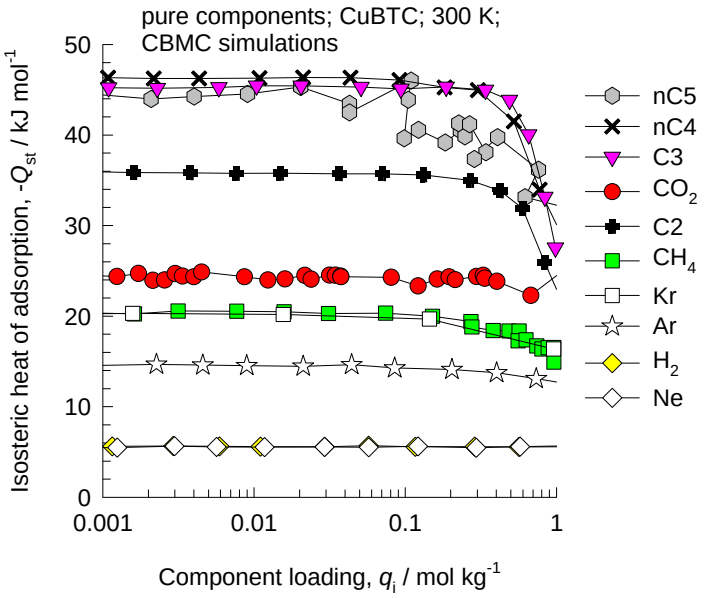

CuBTC MD simulations of unary self- , and M-S diffusivities

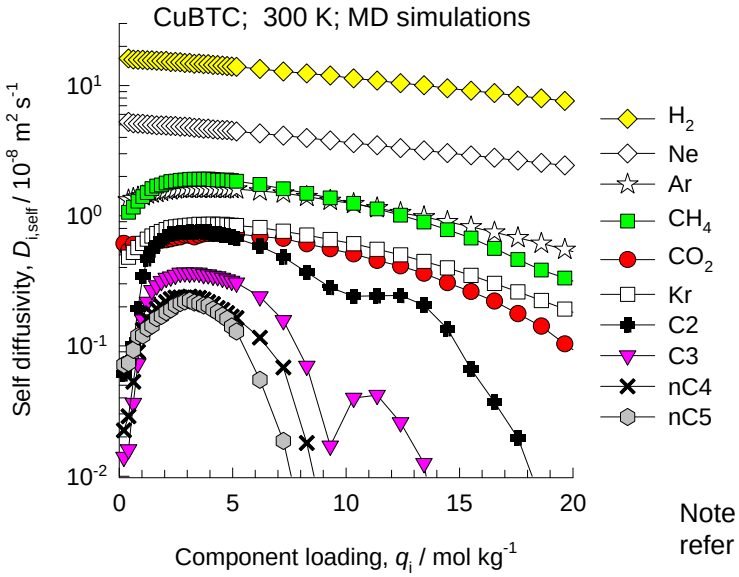

Note that C2 and C3 refer to saturated alkanes

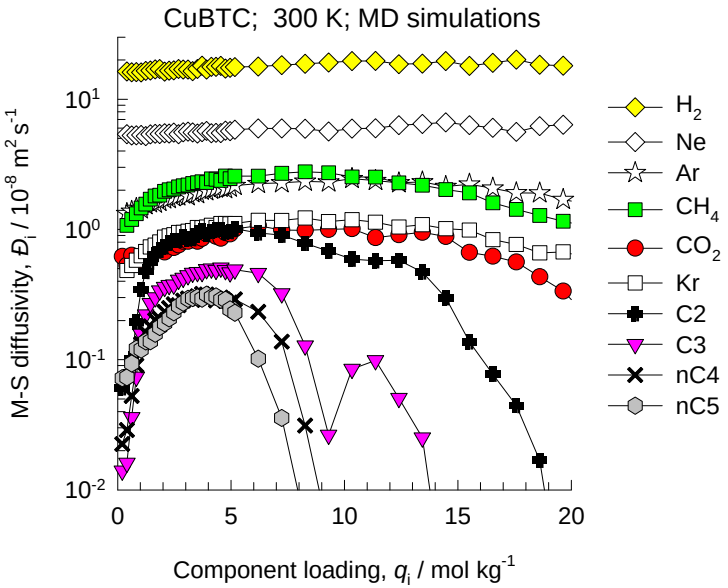

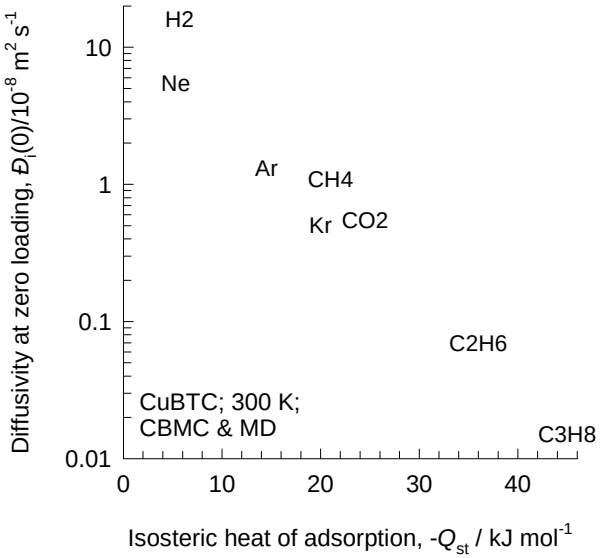

IRMOF-1 pore landscape

For IRMOF-1 (= MOF 5 = $Zn_4O(BDC)_3$ with BDC^{2-} = 1-4 benzenedicarboxylate) the structural information was obtained from

D. Dubbeldam, K.S. Walton, D.E. Ellis, R.Q. Snurr, Exceptional Negative Thermal Expansion in Isoreticular Metal–Organic Frameworks, Angew. Chem. Int. Ed. 46 (2007) 4496-4499.

D. Dubbeldam, H. Frost, K.S. Walton, R.Q. Snurr, Molecular simulation of adsorption sites of light gases in the metal-organic framework IRMOF-1, Fluid Phase Equilib. 261 (2007) 152-161.

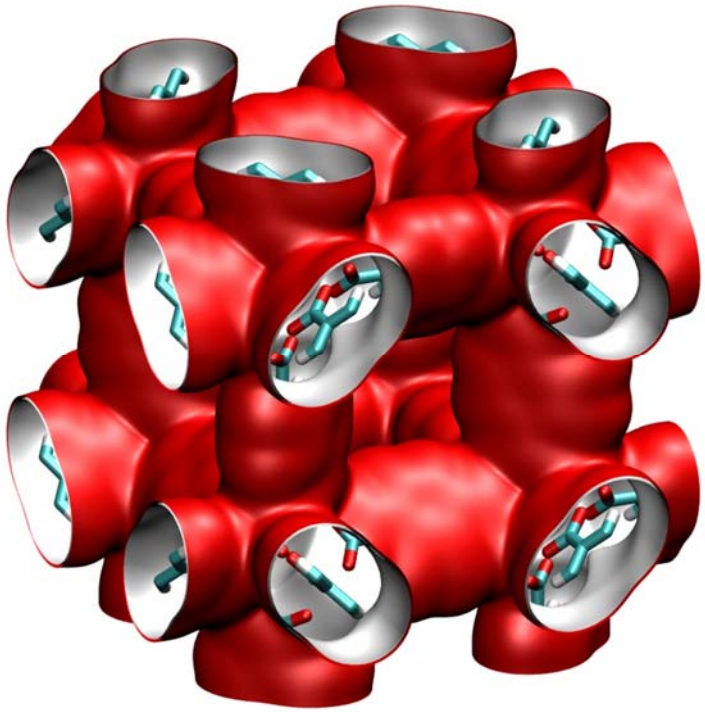

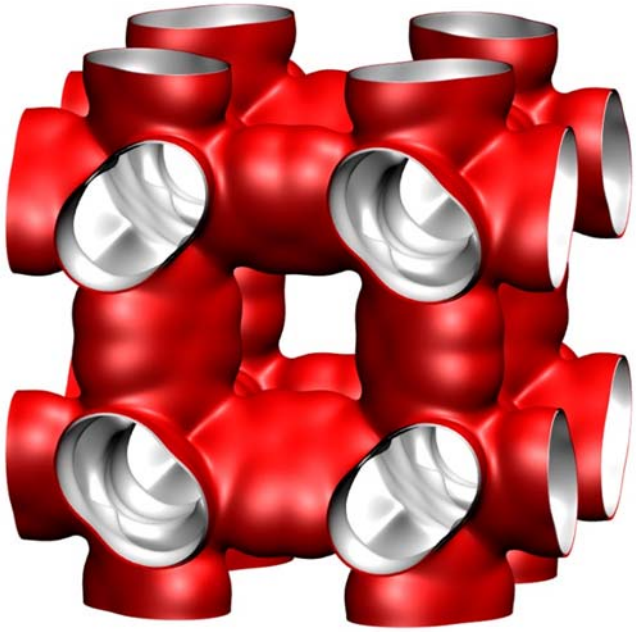

Snapshot of CO_2/CH_4 mixture

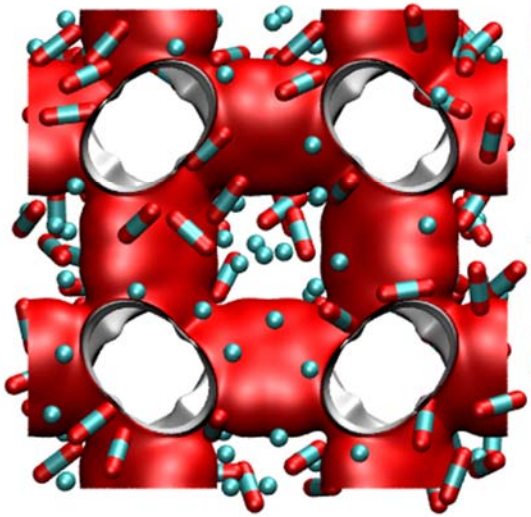

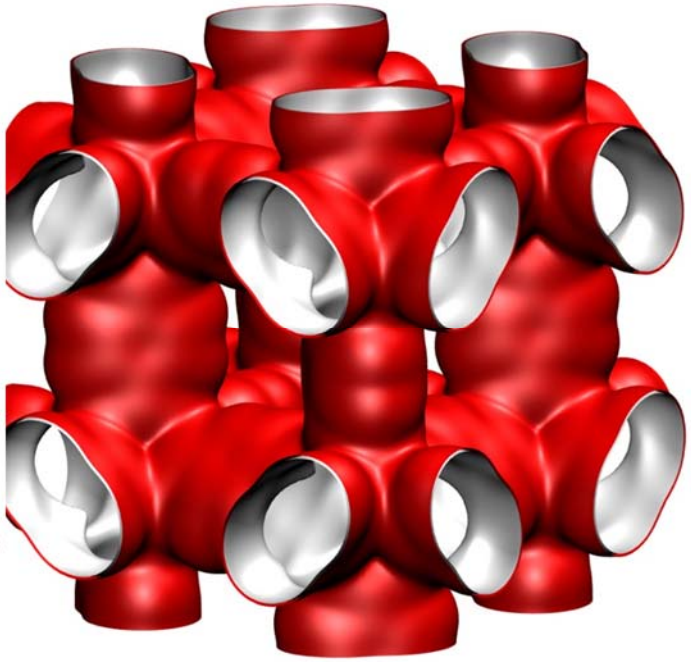

IRMOF-1 pore dimensions

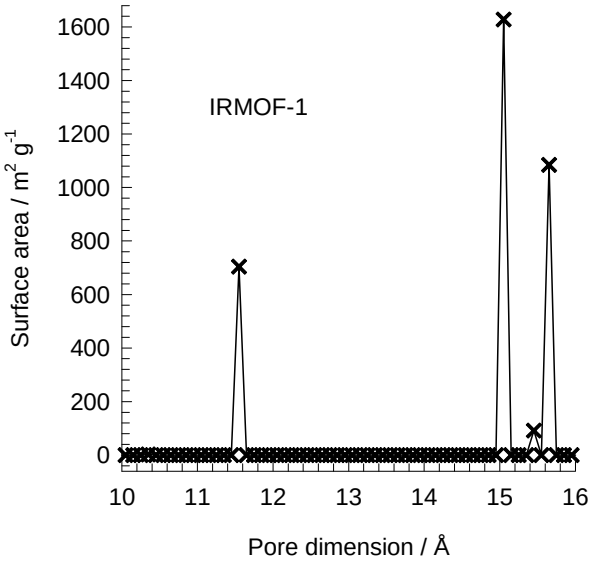

This plot of surface area versus pore dimension is determined using a combination of the DeLaunay triangulation method for pore dimension determination, and the procedure of Düren for determination of the surface area.

	IRMOF-1
a /Å	25.832
b /Å	25.832
c /Å	25.832
Cell volume / Å^3	17237.49
conversion factor for [molec/uc] to [mol per kg Framework]	0.1624
conversion factor for [molec/uc] to [kmol/m^3]	0.1186
ρ [kg/m3]	593.2075
MW unit cell [g/mol(framework)]	6157.788
ϕ, fractional pore volume	0.812
open space / Å^3/uc	13996.3
Pore volume / cm^3/g	1.369
Surface area /m^2/g	3522.2
DeLaunay diameter /Å	7.38

Two alternating, inter-connected, cavities of 11 Å and 15 Å with window size of 8 Å.

IRMOF-1 force field for framework atoms

Lennard-Jones parameters for atoms in IRMOF-1. The force field corresponds to that presented in the papers by K.S. Walton, A.R. Millward, D. Dubbeldam, H. Frost, J.J. Low, O.M. Yaghi, R.Q. Snurr (Understanding Inflections and Steps in Carbon Dioxide Adsorption Isotherms in Metal-Organic Frameworks, J. Am. Chem. Soc. 130 (2008) 406-407.) and D. Dubbeldam, H. Frost, K.S. Walton, R.Q. Snurr (Molecular simulation of adsorption sites of light gases in the metal-organic framework IRMOF-1, Fluid Phase Equilib. 261 (2007) 152-161.)

(pseudo-) atom	σ / Å	ε/k_B / K	charge
Zn	2.69	0.41	1.275
Oa	2.98	700	-1.5
Ob	3.11	70.5	-0.6
Ca	3.74	47	0.475
Cb	3.47	47.9	0.125
Cc	3.47	47.9	-0.15
H	2.85	7.65	0.15

IRMOF-1

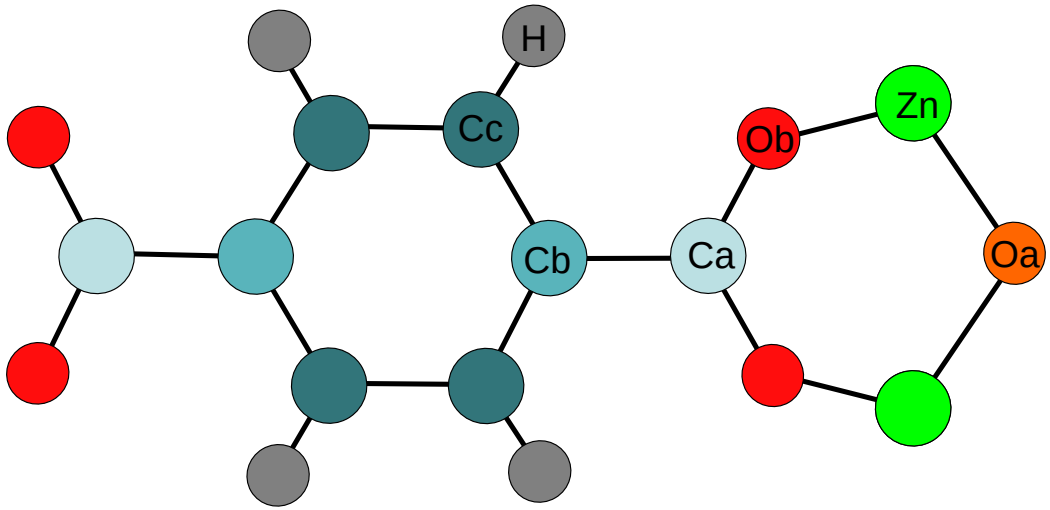

IRMOF-1 CBMC simulations of isotherms, and isosteric heats of adsorption

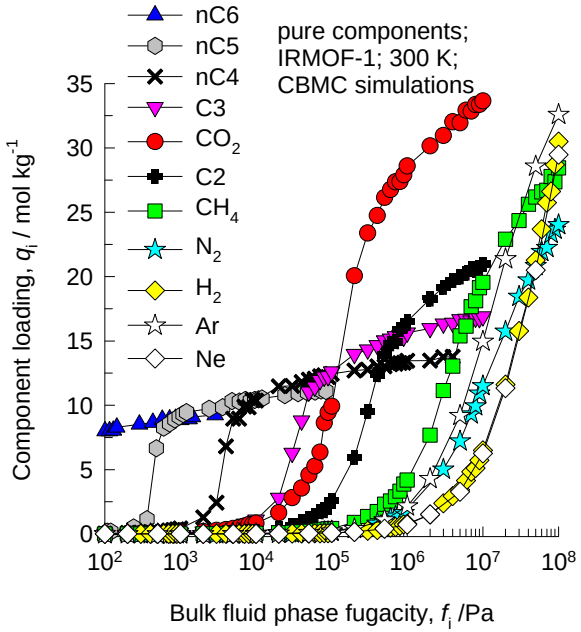

Note that C2 and C3 refer to saturated alkanes

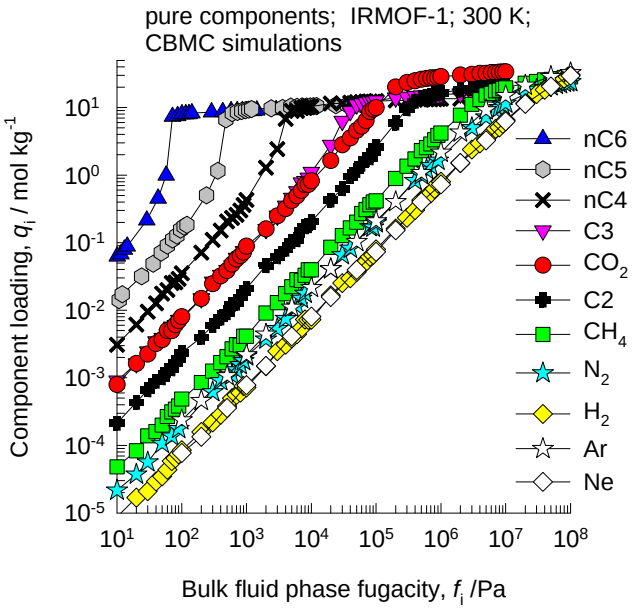

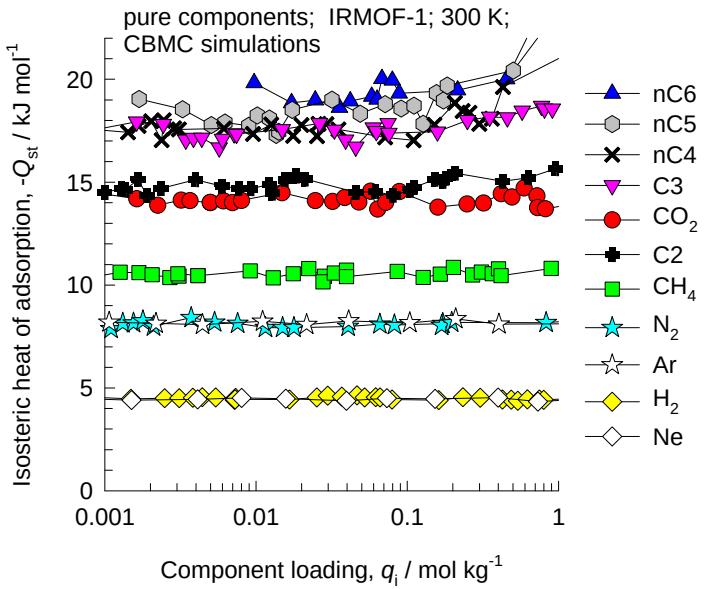

IRMOF-1 MD simulations of unary self- , and M-S diffusivities

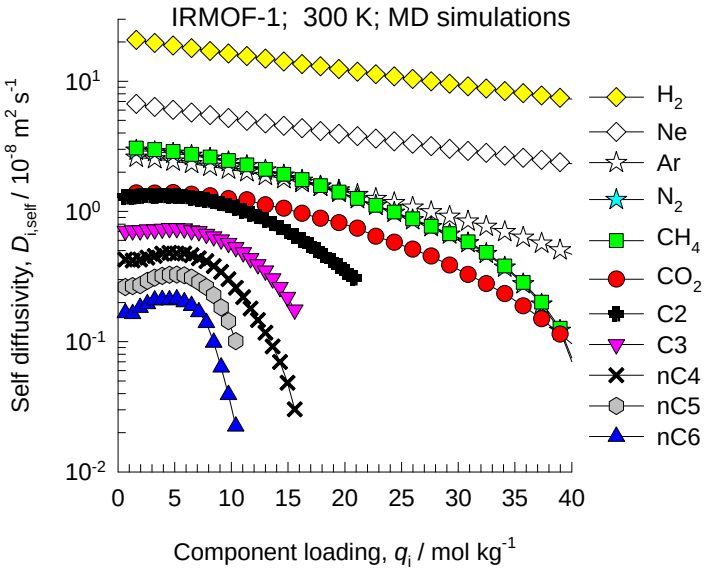

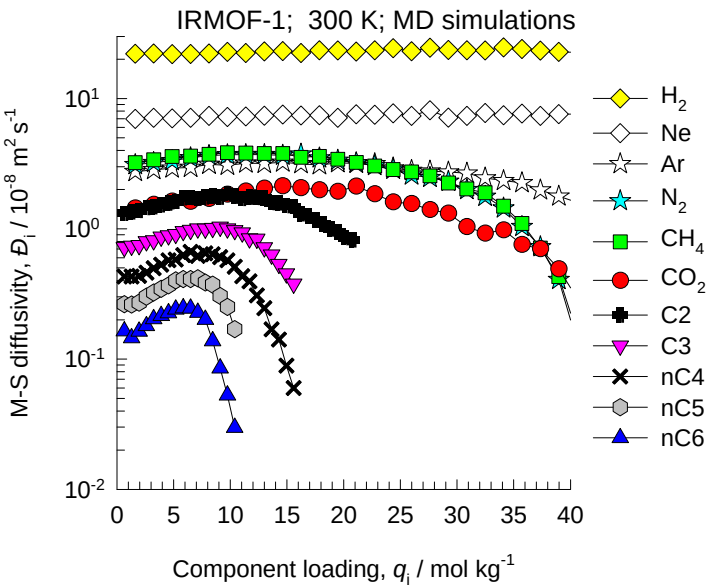

Note that C2 and C3 refer to saturated alkanes

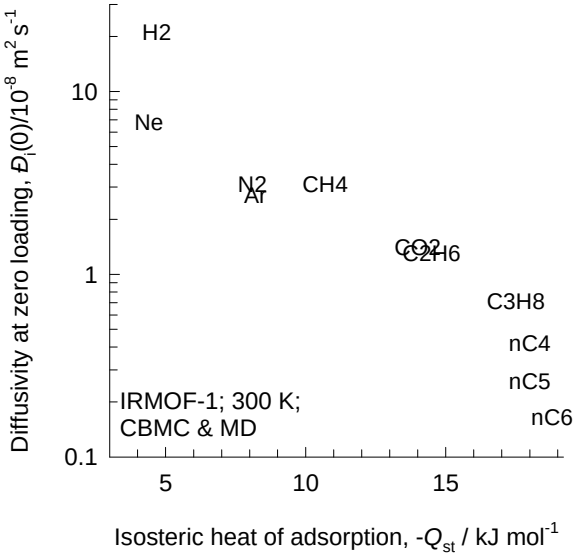

MOF-177 pore landscape

The structural information for MOF-177 (= $Zn_4O(BTB)_2$ with (BTB^{3-} = 1,3,5-benzenetribenzoate)) is provided by

H.K. Chae, D.Y. Siberio-Pérez, J. Kim, Y.B. Go, M. Eddaoudi, A.J. Matzger, M. O'Keeffe, O.M. Yaghi, A route to high surface area, porosity and inclusion of large molecules in crystals, Nature 427 (2004) 523-527.

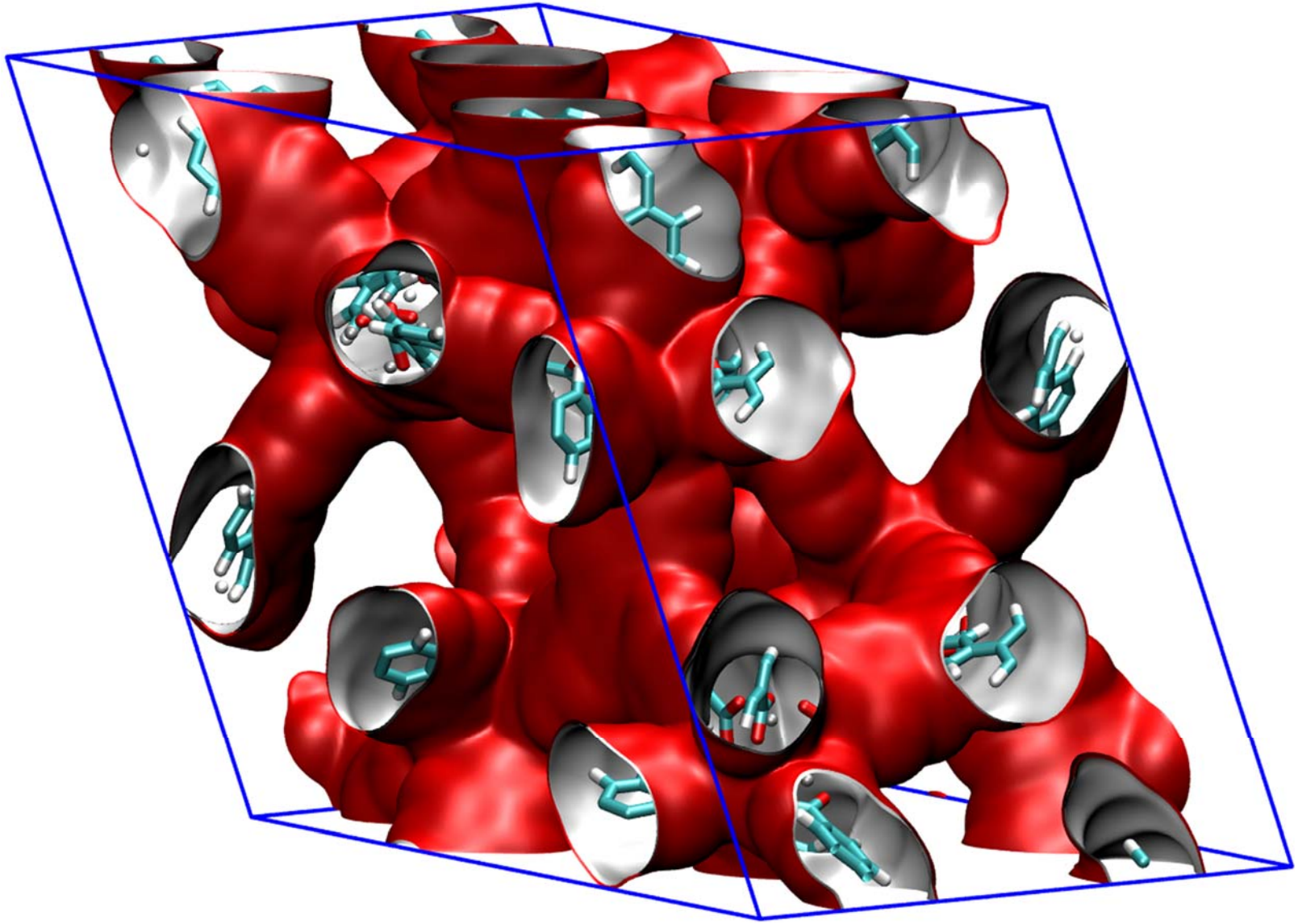

MOF-177 pore dimensions

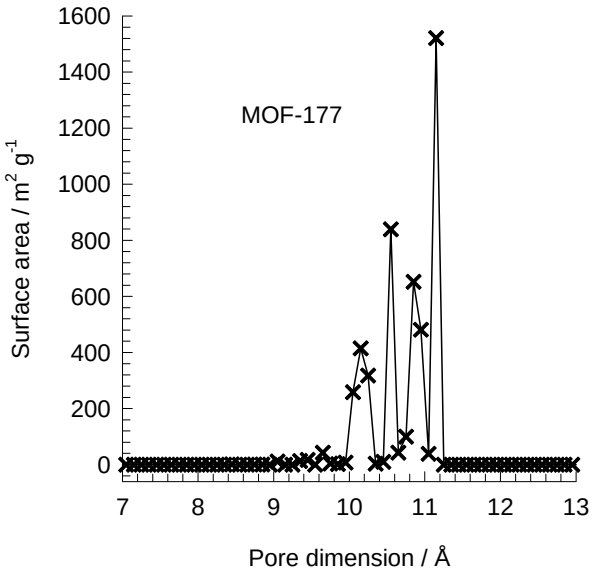

This plot of surface area versus pore dimension is determined using a combination of the DeLaunay triangulation method for pore dimension determination, and the procedure of Düren for determination of the surface area.

	MOF-177
a /Å	37.072
b /Å	37.072
c /Å	30.033
Cell volume / Å^3	35745.5
conversion factor for [molec/uc] to [mol per kg Framework]	0.1089
conversion factor for [molec/uc] to [kmol/m^3]	0.0553
ρ [kg/m3]	426.5952
MW unit cell [g/mol(framework)]	9182.931
ϕ, fractional pore volume	0.840
open space / Å^3/uc	30010.9
Pore volume / cm^3/g	1.968
Surface area /m^2/g	4781.0
DeLaunay diameter /Å	10.1

Tetrahedral $[Zn_4O]^{6+}$ units are linked by large, triangular tricarboxylate ligands. Six diamond-shaped channels (upper) with diameter of 10.8 Å surround a pore containing eclipsed BTB^{3-} moieties.

MOF-177 force field for framework atoms

Lennard-Jones parameters for the framework atoms of MOF-177. The framework charges of MOF-177 were estimated using the group-contribution procedure based on quantum mechanical calculations described by Q. Xu, C. Zhong (A General Approach for Estimating Framework Charges in Metal-Organic Frameworks, J. Phys. Chem. C 114 (2010) 5035-5042).

(pseudo-) atom	σ / Å	ε/k_B / K	charge
CA	3.473	47.86	0.8056
CB	3.473	47.86	0.0496
CC	3.473	47.86	-0.1304
H	2.846	7.650	0.1086
OA	3.033	48.16	-1.9214
OB	3.033	48.16	-0.7934
Zn	4.044	27.68	1.5916

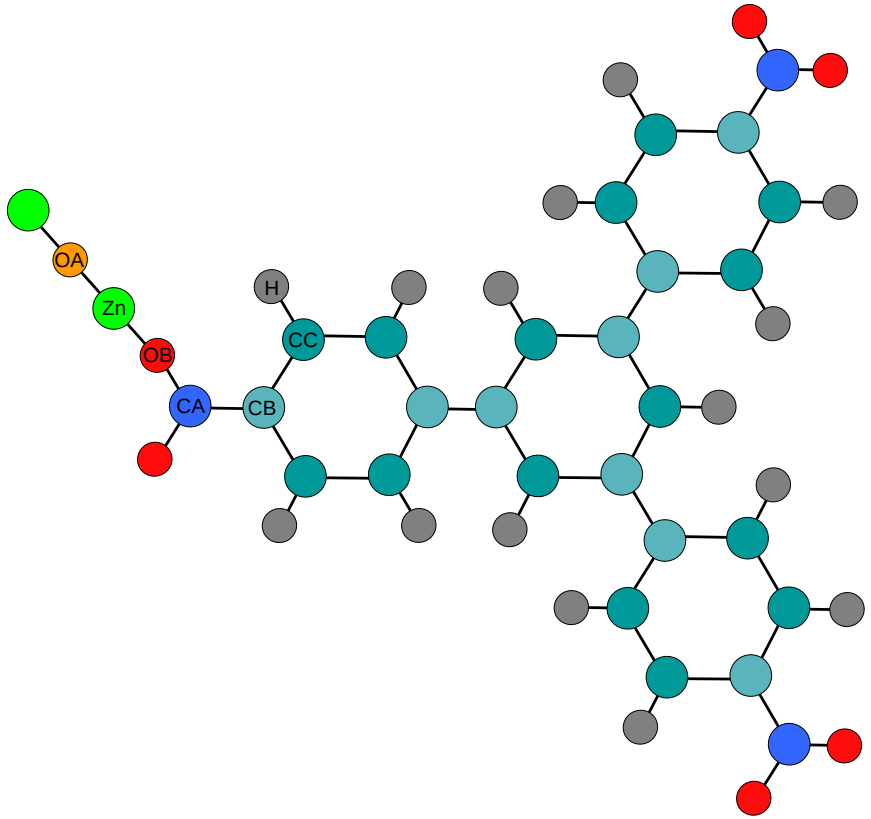

MOF-177 CBMC simulations of isotherms, and isosteric heats of adsorption

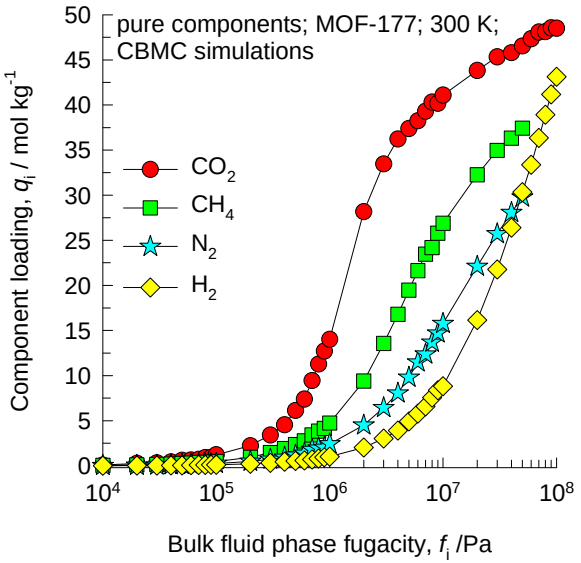

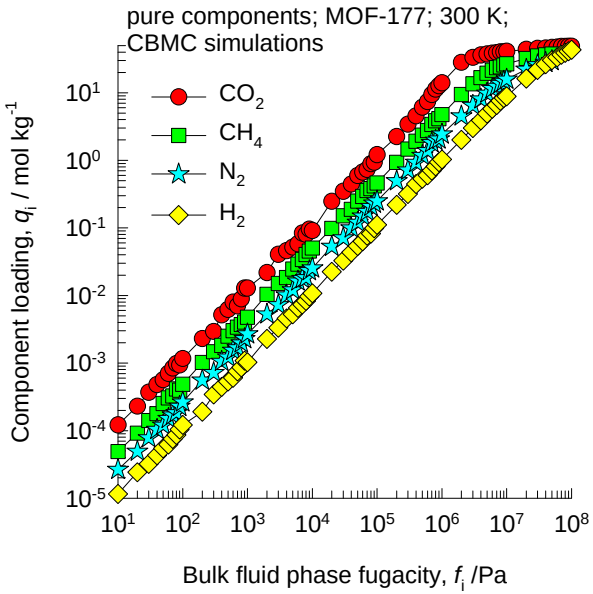

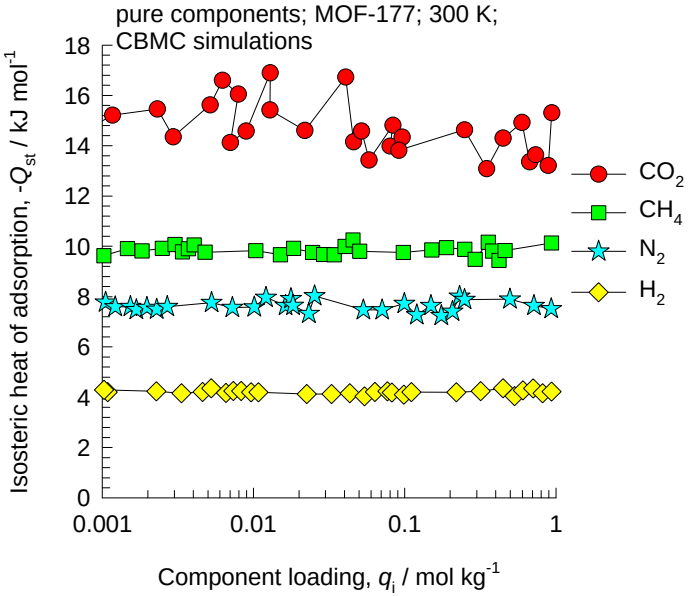

MOF-177 MD simulations of unary self- , and M-S diffusivities

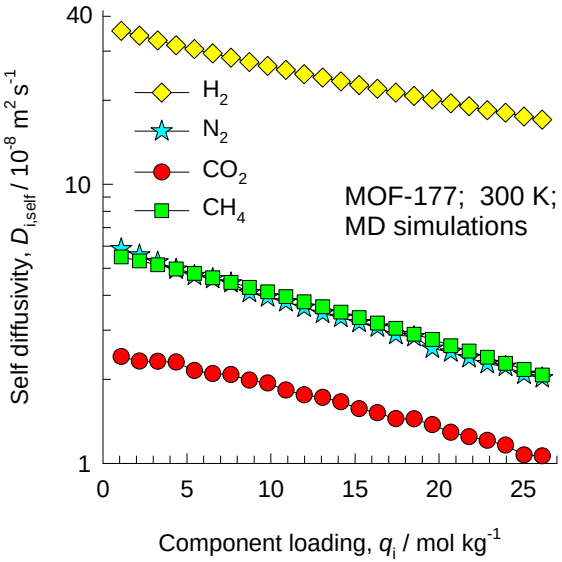

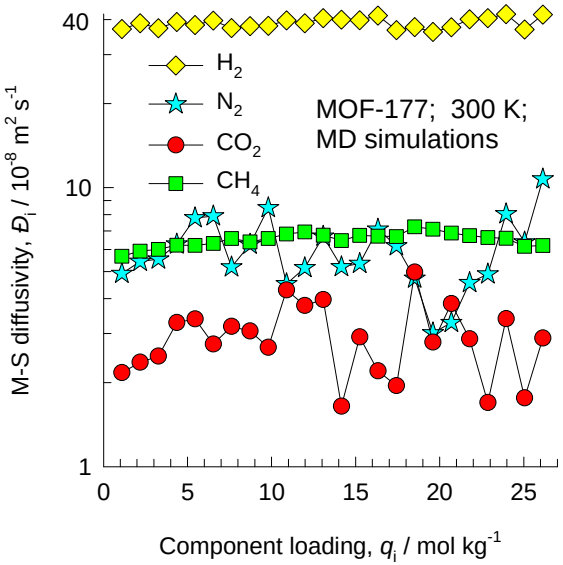

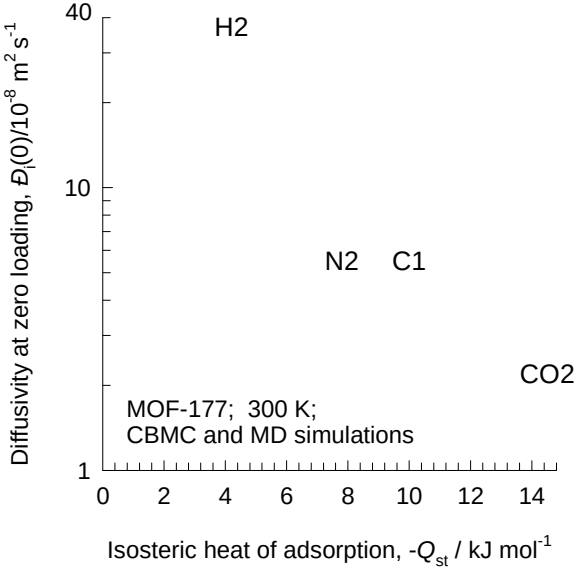

1D intersecting channels

BEA pore landscape

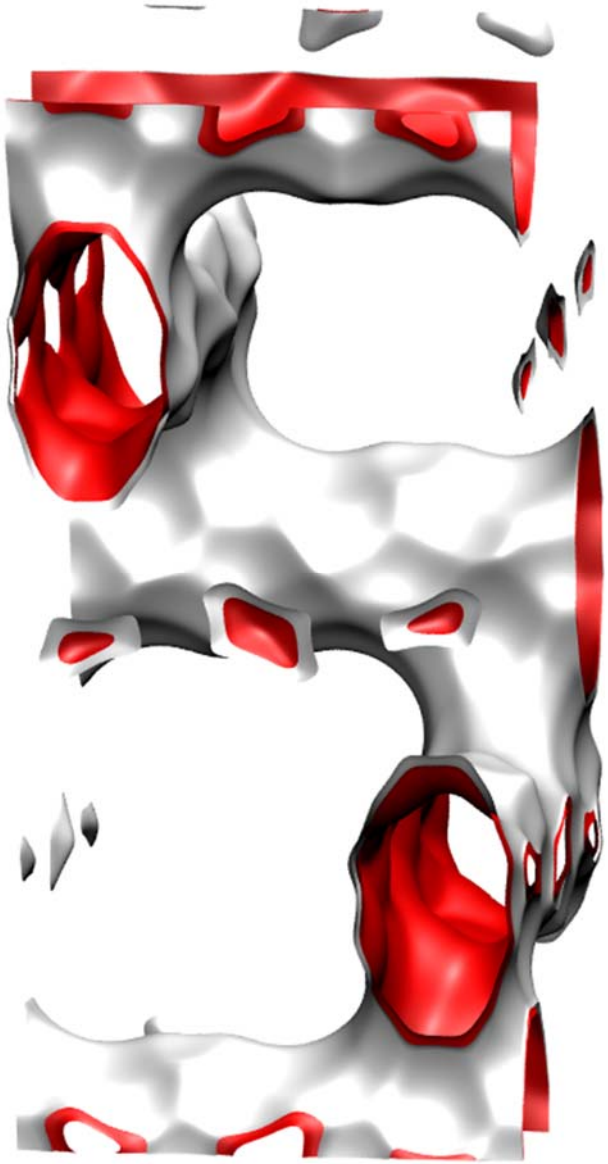

Intersecting channels of two sizes:
12-ring and 10-ring

	BEA
a /Å	12.661
b /Å	12.661
c /Å	26.406
Cell volume / Å^3	4232.906
conversion factor for [molec/uc] to [mol per kg Framework]	0.2600
conversion factor for [molec/uc] to [kmol/m^3]	0.9609
ρ [kg/m3]	1508.558
MW unit cell [g/mol(framework)]	3845.427
ϕ, fractional pore volume	0.408
open space / Å^3/uc	1728.1
Pore volume / cm^3/g	0.271
Surface area /m^2/g	923.0
DeLaunay diameter /Å	5.87

Structural information from: C. Baerlocher, L.B. McCusker, Database of Zeolite Structures, International Zeolite Association, http://www.iza-structure.org/databases/

BEA pore dimensions

This plot of surface area versus pore dimension is determined using a combination of the DeLaunay triangulation method for pore dimension determination, and the procedure of Düren for determination of the surface area.

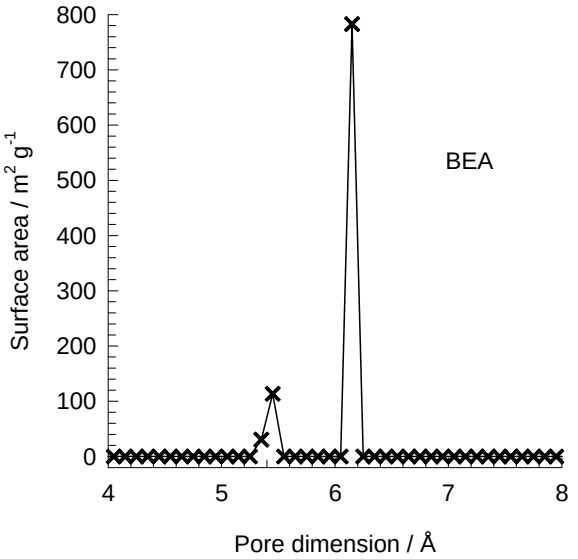

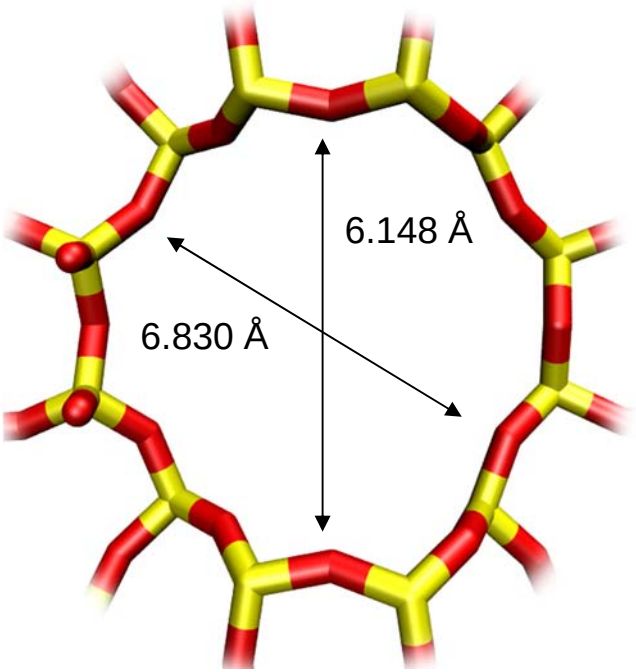

BEA [1 0 0]

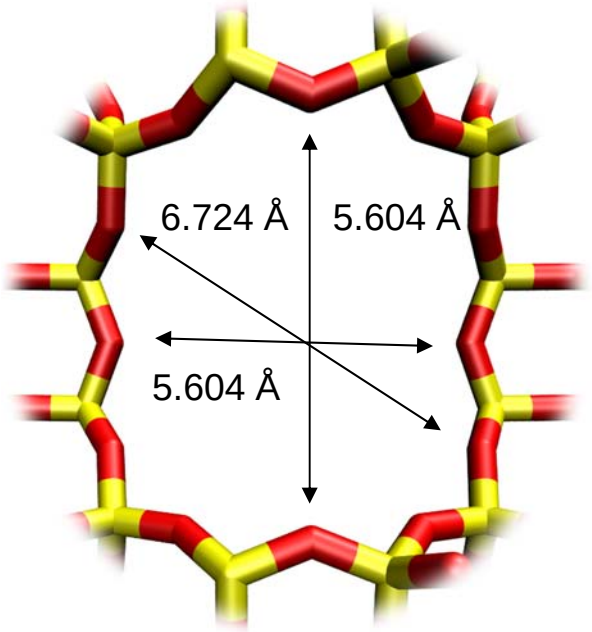

BEA [0 0 1]

BEA MD simulations of unary self- , and M-S diffusivities

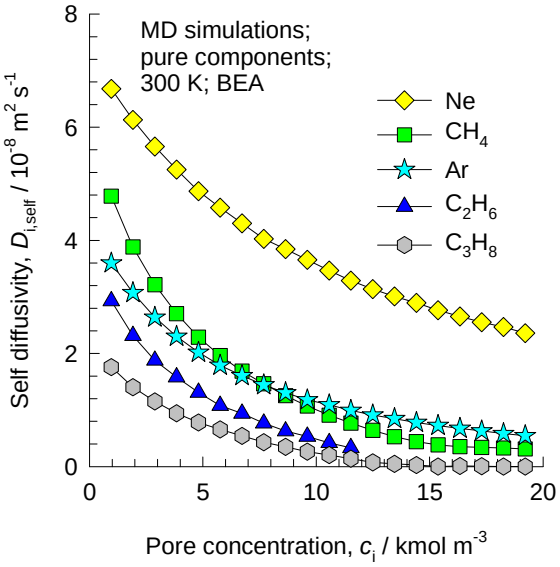

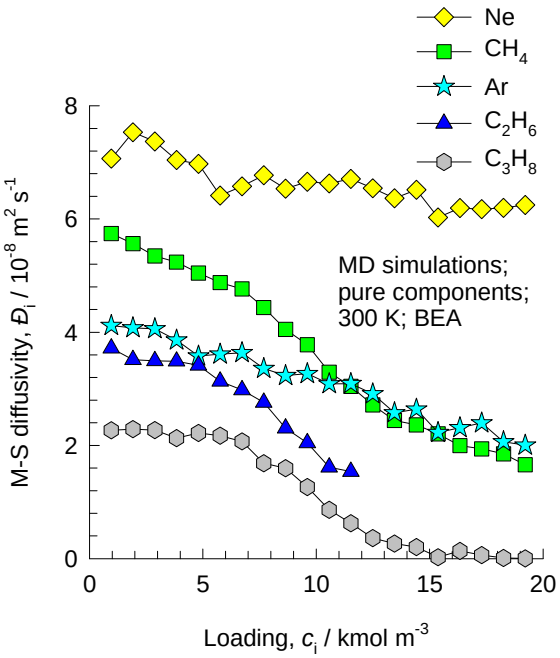

BOG pore landscape

Intersecting channels:
12-ring and 10-ring

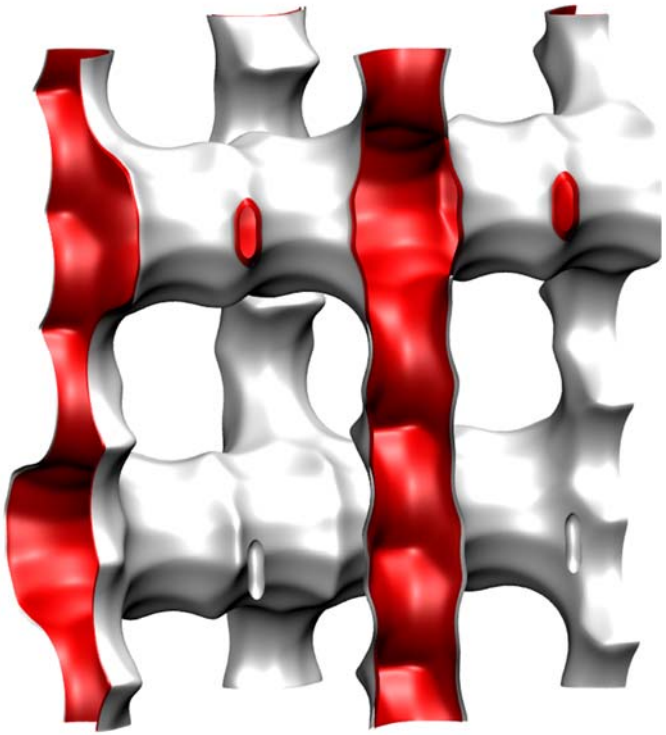

	BOG
a /Å	20.236
b /Å	23.798
c /Å	12.798
Cell volume / Å^3	6163.214
conversion factor for [molec/uc] to [mol per kg Framework]	0.1734
conversion factor for [molec/uc] to [kmol/m^3]	0.7203
ρ [kg/m3]	1995.523
MW unit cell [g/mol(framework)]	5768.141
ϕ, fractional pore volume	0.374
open space / Å^3/uc	2305.4
Pore volume / cm^3/g	0.241
Surface area /m^2/g	758.0
DeLaunay diameter /Å	5.02

Structural information from: C. Baerlocher, L.B. McCusker, Database of Zeolite Structures, International Zeolite Association, http://www.iza-structure.org/databases/

BOG pore dimensions

This plot of surface area versus pore dimension is determined using a combination of the DeLaunay triangulation method for pore dimension determination, and the procedure of Düren for determination of the surface area.

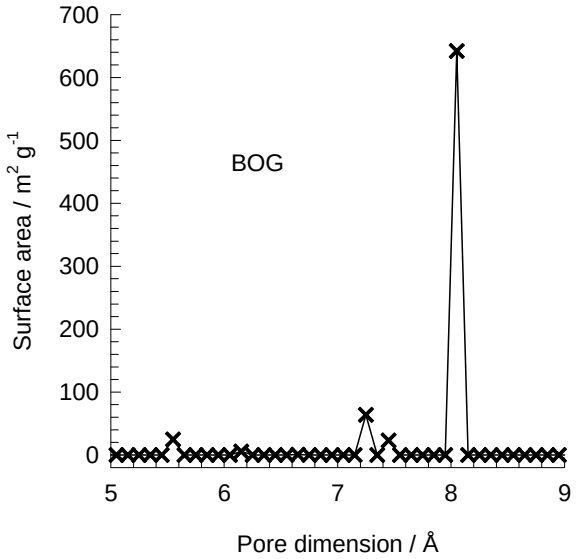

BOG has an intersecting channel system:
12-ring channels intersecting with 10-ring channels

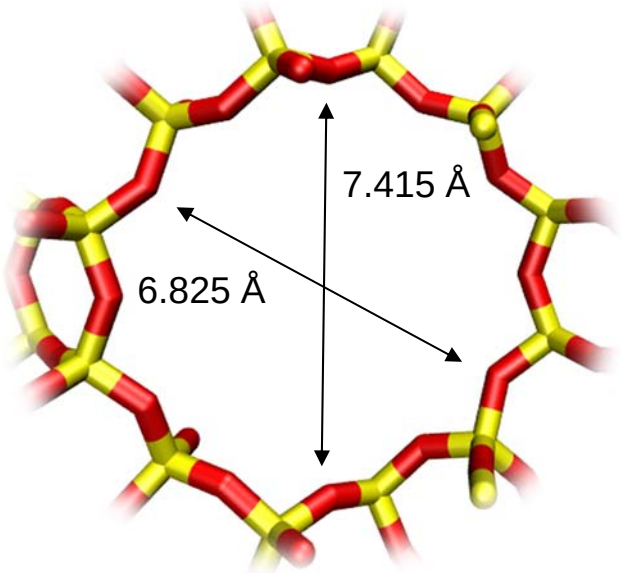

BOG [1 0 0]

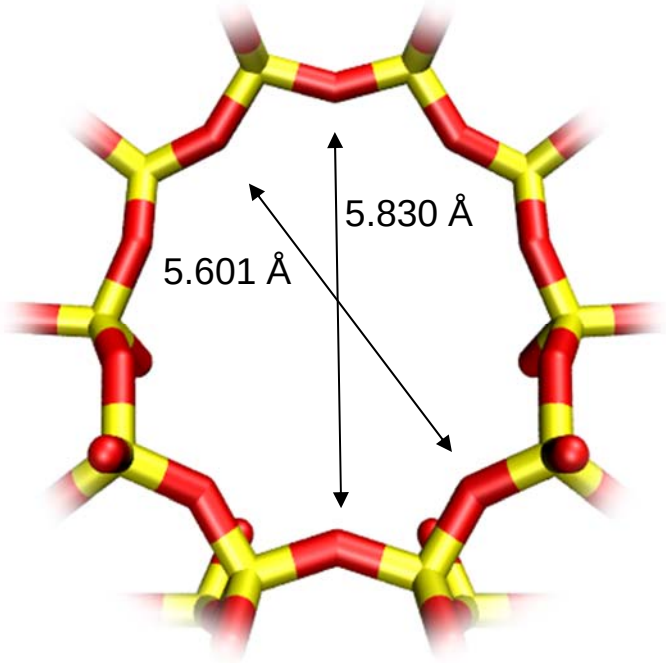

BOG [0 1 0]

BOG MD simulations of unary self- , and M-S diffusivities

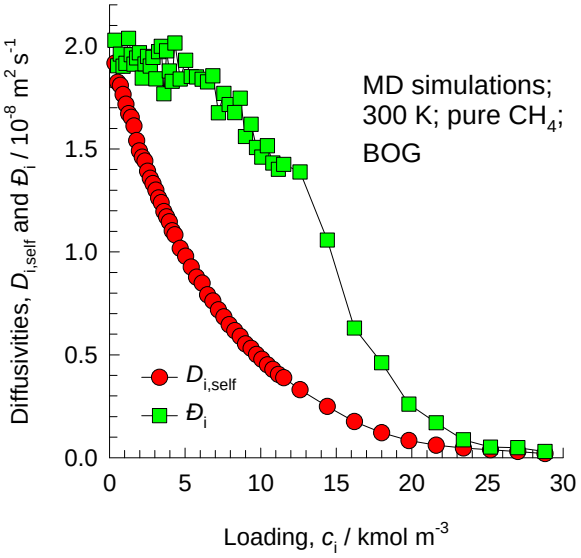

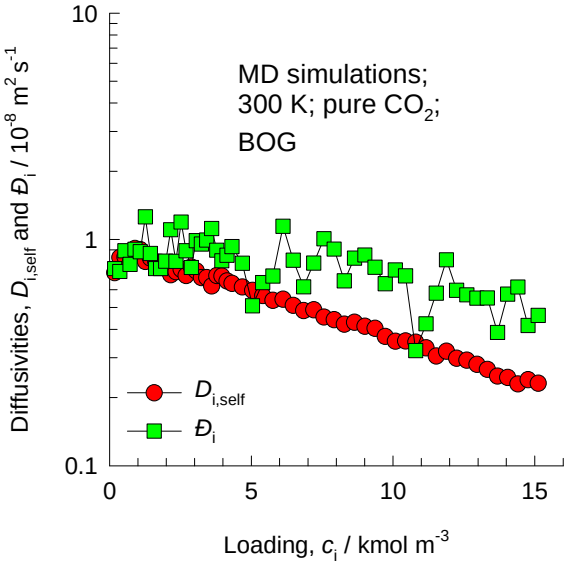

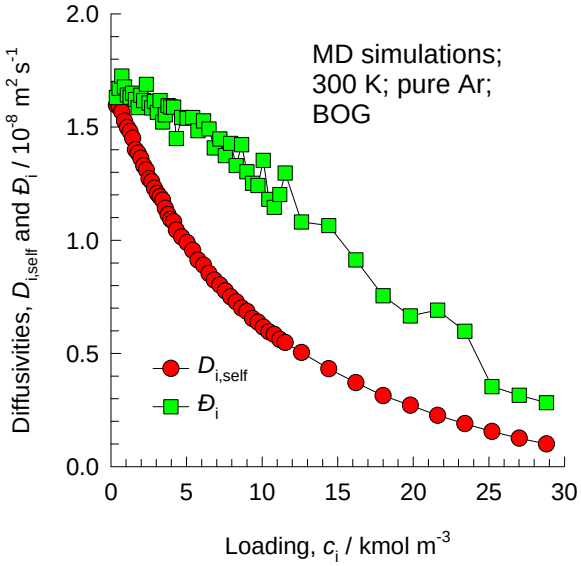

ISV pore landscape

Intersecting 12-ring channels structure

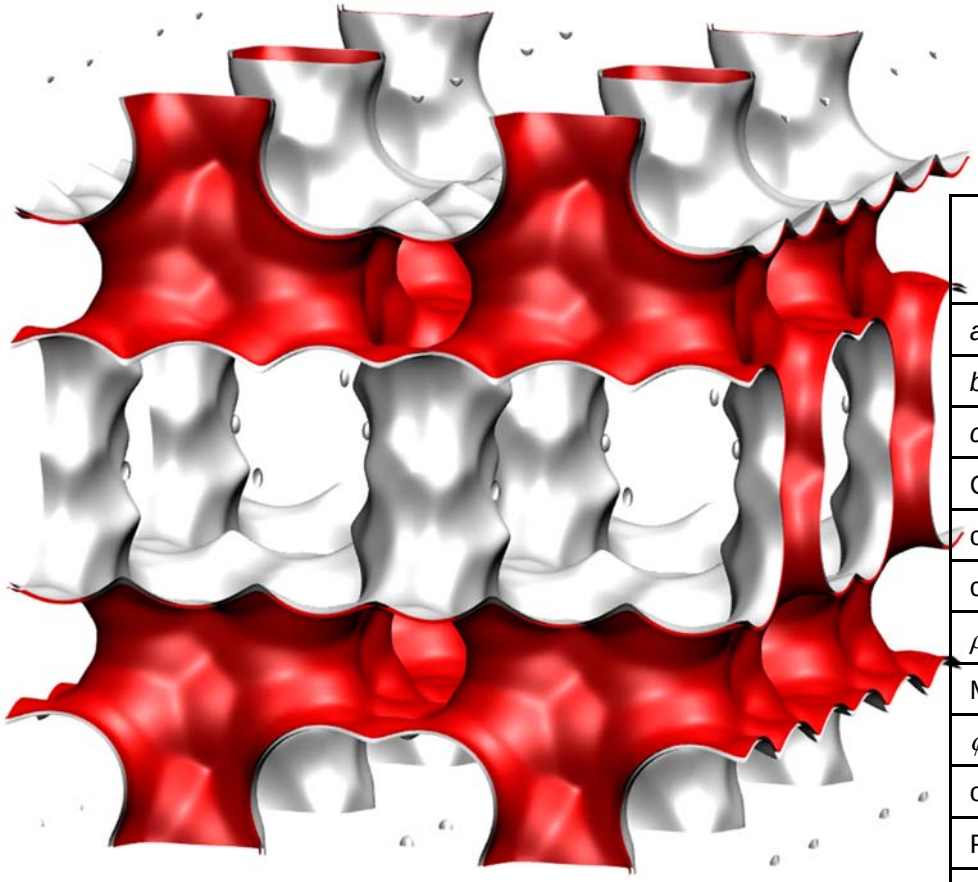

	ISV
a /Å	12.853
b /Å	12.853
c /Å	25.214
Cell volume / Å^3	4165.343
conversion factor for [molec/uc] to [mol per kg Framework]	0.2600
conversion factor for [molec/uc] to [kmol/m^3]	0.9361
ρ [kg/m3]	1533.027
MW unit cell [g/mol(framework)]	3845.427
ϕ, fractional pore volume	0.426
open space / Å^3/uc	1773.9
Pore volume / cm^3/g	0.278
Surface area /m^2/g	911.0
DeLaunay diameter /Å	5.96

Structural information from: C. Baerlocher, L.B. McCusker, Database of Zeolite Structures, International Zeolite Association, http://www.iza-structure.org/databases/

ISV MD simulations of unary self- , and M-S diffusivities

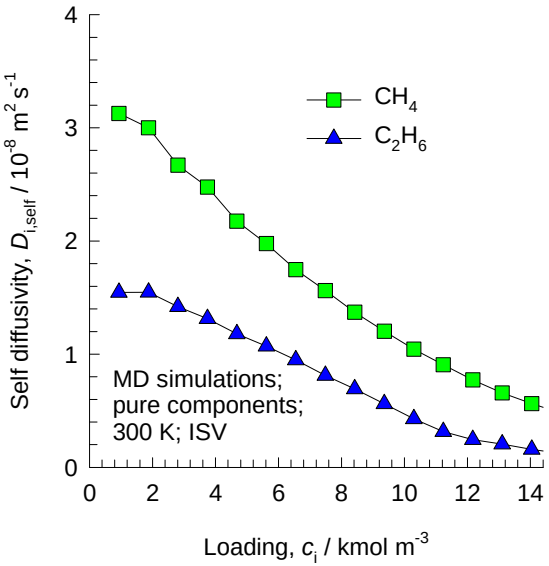

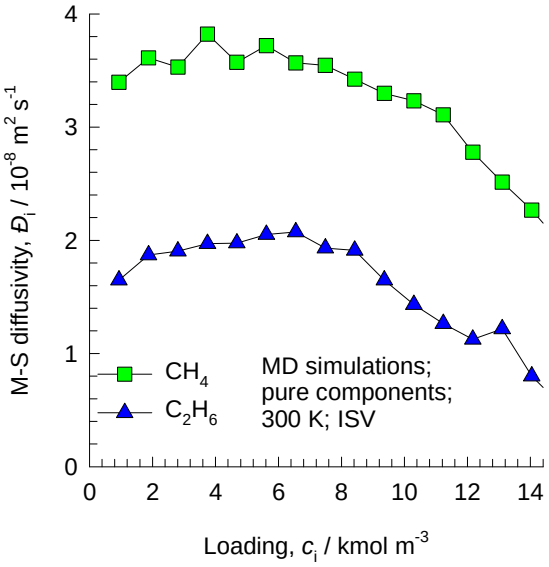

ISV pore dimensions

This plot of surface area versus pore dimension is determined using a combination of the DeLaunay triangulation method for pore dimension determination, and the procedure of Düren for determination of the surface area.

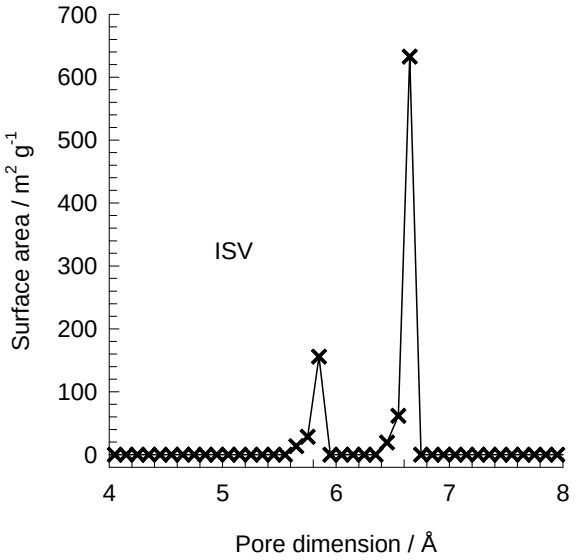

Intersecting 12-ring channels structure

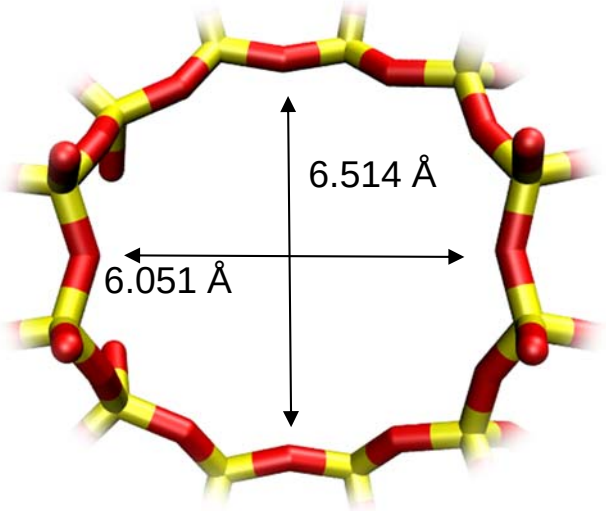

ISV [1 0 0]

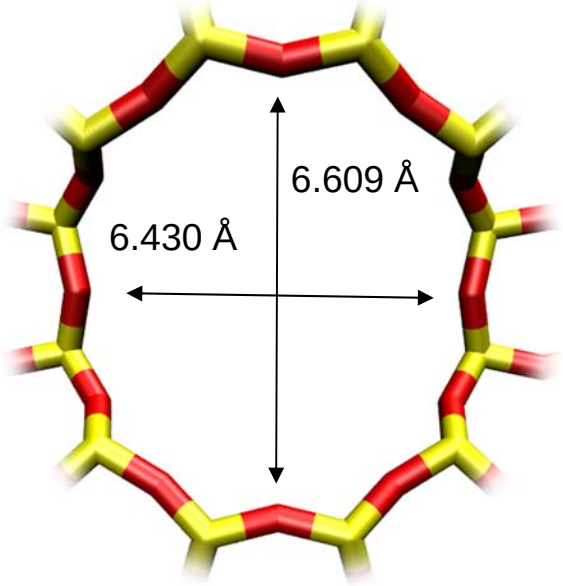

ISV [0 0 1]

ISV MD simulations of unary self- , and M-S diffusivities

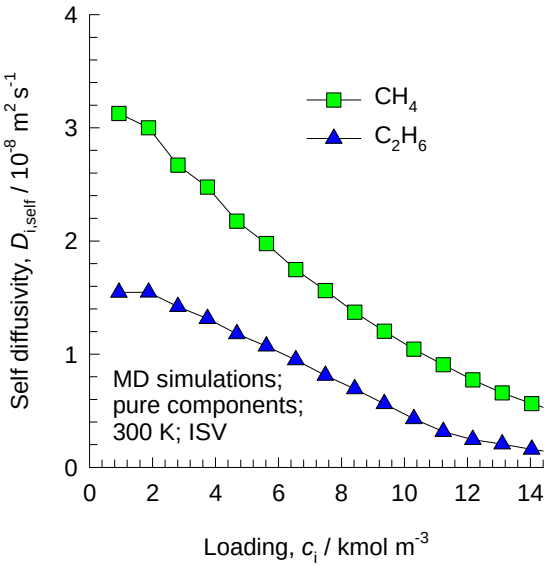

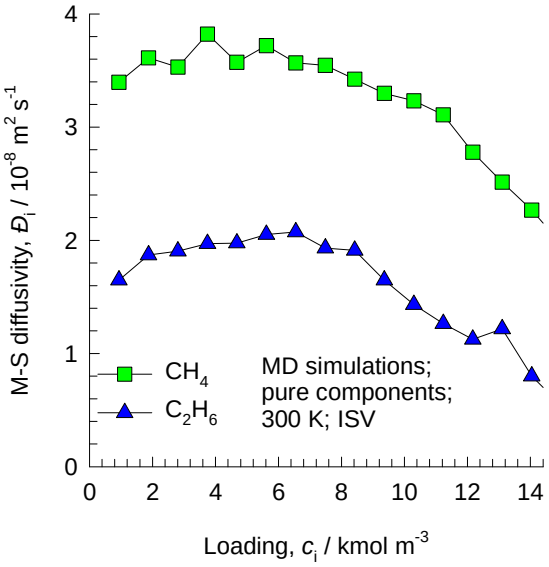

MFI pore landscape

	MFI
a /Å	20.022
b /Å	19.899
c /Å	13.383
Cell volume / Å^3	5332.025
conversion factor for [molec/uc] to [mol per kg Framework]	0.1734
conversion factor for [molec/uc] to [kmol/m^3]	1.0477
ρ [kg/m3]	1796.386
MW unit cell [g/mol(framework)]	5768.141
ϕ, fractional pore volume	0.297
open space / Å^3/uc	1584.9
Pore volume / cm^3/g	0.165
Surface area /m^2/g	487.0
DeLaunay diameter /Å	5.16

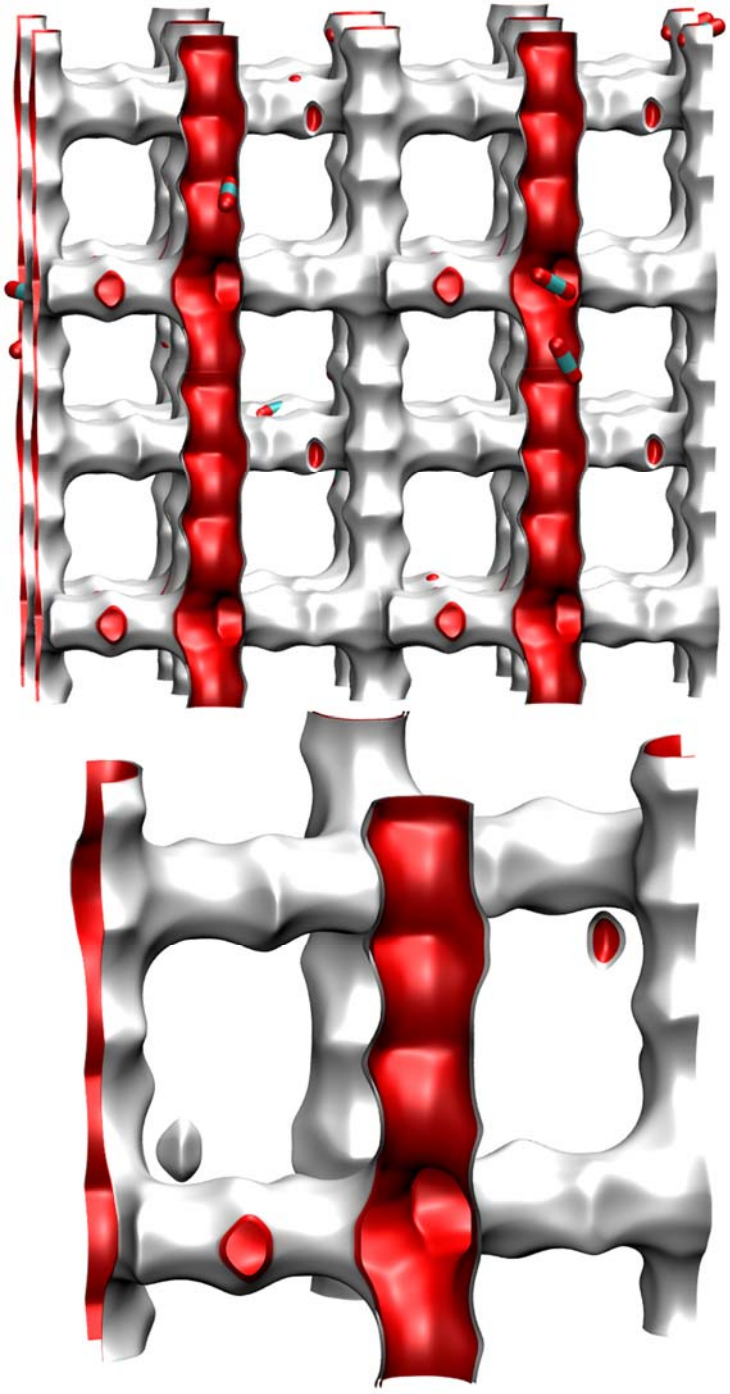

Structural information from: C. Baerlocher, L.B. McCusker, Database of Zeolite Structures, International Zeolite Association, http://www.iza-structure.org/databases/

MFI pore dimensions

10 ring channel of MFI viewed along [100]

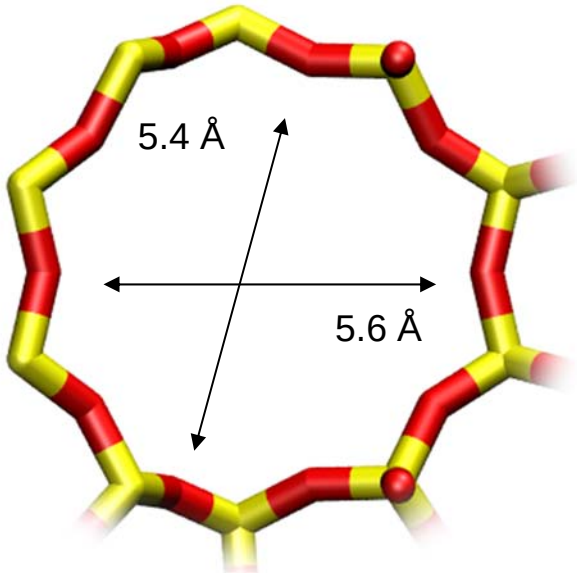

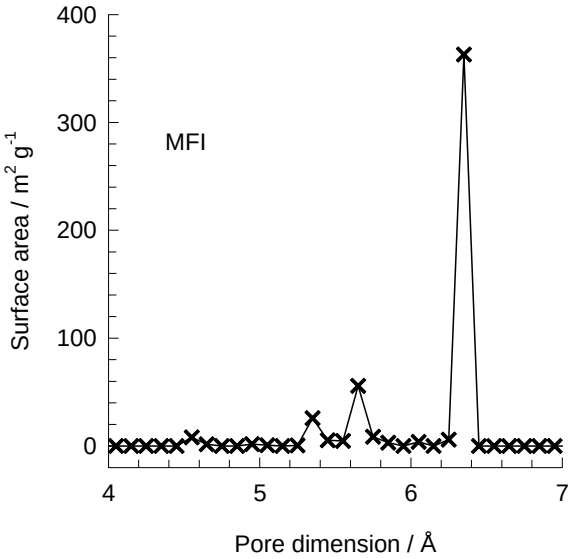

10 ring channel of MFI viewed along [010]

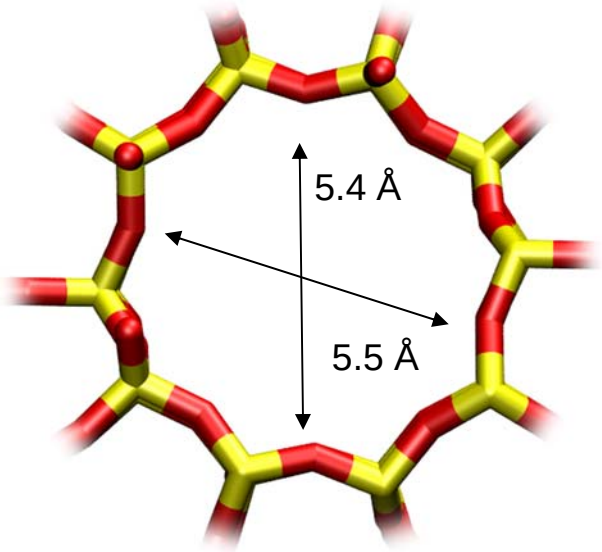

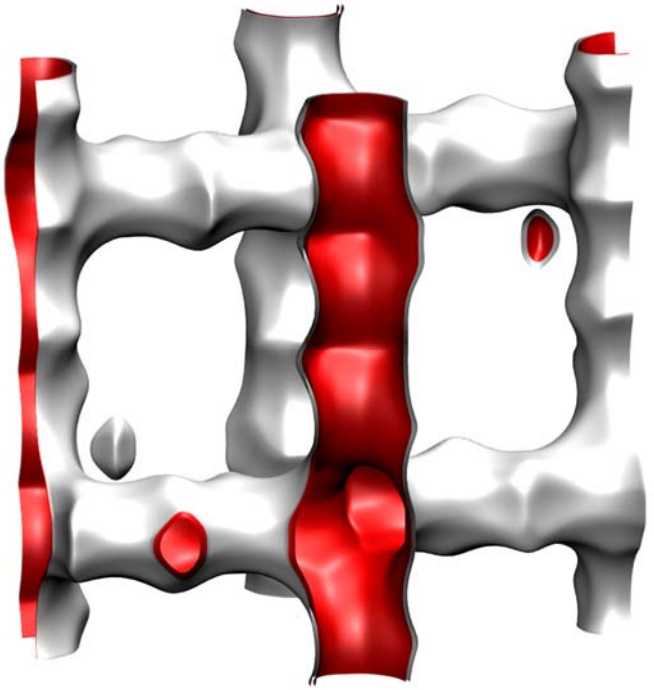

MFI pure component isotherms; comparison with experiments

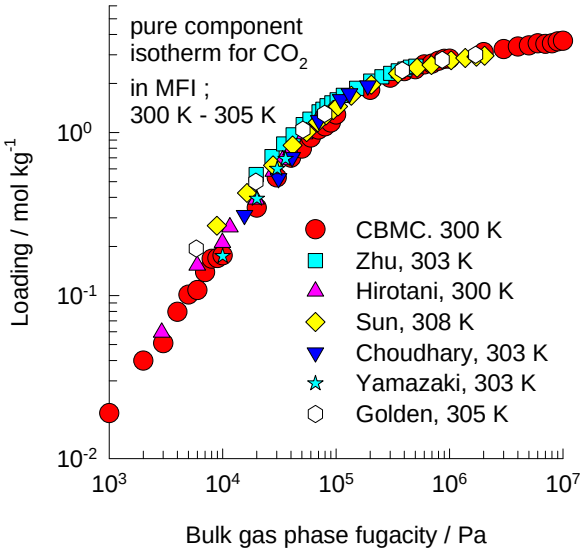

The loadings are expressed here in terms of molar loading; these can be converted to pore concentrations c_i by invoking data on the pore volume of 0.165 cm^3/g.

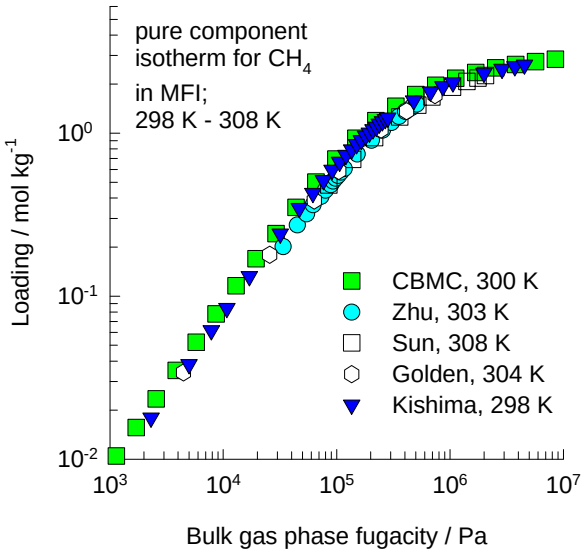

The experimental data are from the following sources:

W. Zhu, P. Hrabanek, L. Gora, F. Kapteijn, J.A. Moulijn, Role of Adsorption in the Permeation of CH4 and CO2 through a Silicalite-1Membrane, Ind. Eng. Chem. Res. 45 (2006) 767-776.

M.S. Sun, D.B. Shah, H.H. Xu, O. Talu, Adsorption equilibria of C1 to C4 alkanes, CO2, and SF6 on silicalite, J. Phys. Chem. B 102 (1998) 1466-1473.

V.R. Choudhary, S. Mayadevi, Adsorption of methane, ethane, ethylene and carbon dioxide on silicalite-1, Zeolites (1996) 501-507.

A. Hirotani, K. Mizukami, R. Miura, H. Takaba, T. Miya, A. Fahmi, A. Stirling, M. Kubo, A. Miiyamoto, Grand canonical Monte Carlo simulation of the adsorption of CO2 on silcalite and NaZSM-5, App. Surf. Sci. 120 (1997) 81-84.

T. Yamazaki, M. Katoh, S. Ozawa, Y. Ogino, Adsorption of CO2 over univalent cation-exchanged ZSM-5 zeolites, Mol. Phys. 80 (1993) 313-324.

T.C. Golden, S. Sircar, Gas Adsorption on Silicalite, J. Colloid Interface Sci. 162 (1994) 182-188.

M. Kishima, H. Mizuhata, T. Okubo, Effects of Confinement on the Adsorption Behavior of Methane in High-Silica Zeolites, J. Phys. Chem. B 110 (2006) 13889-13896.

MFI pure CO_2 isotherms; comparison with experiments

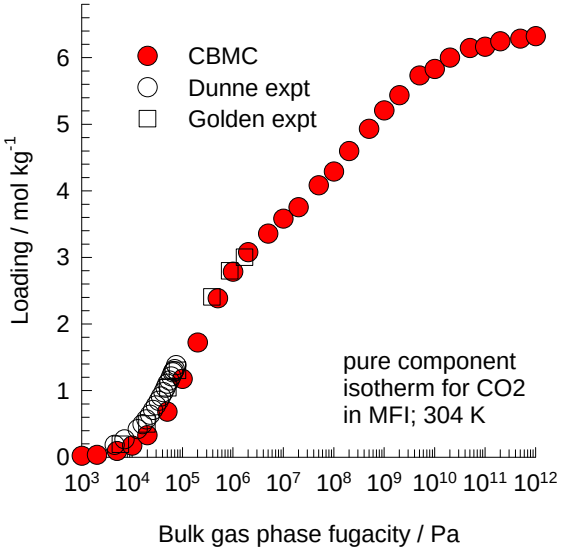

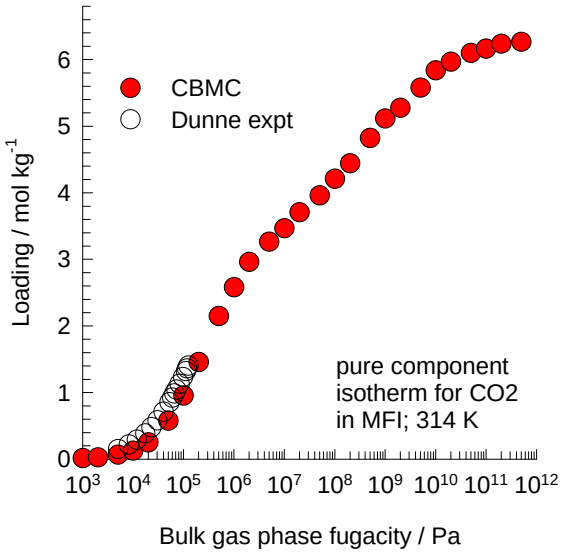

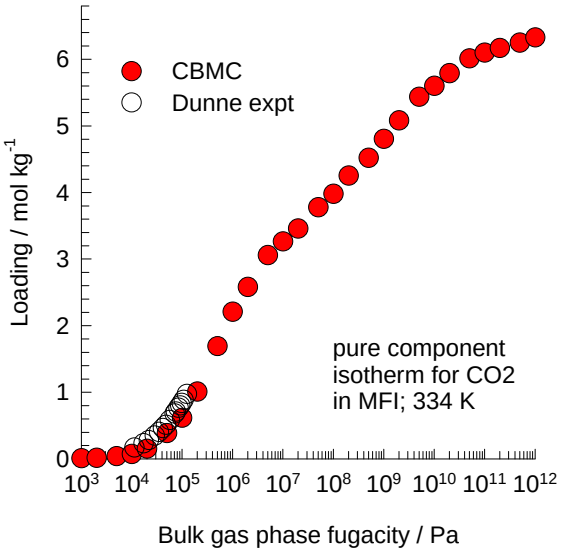

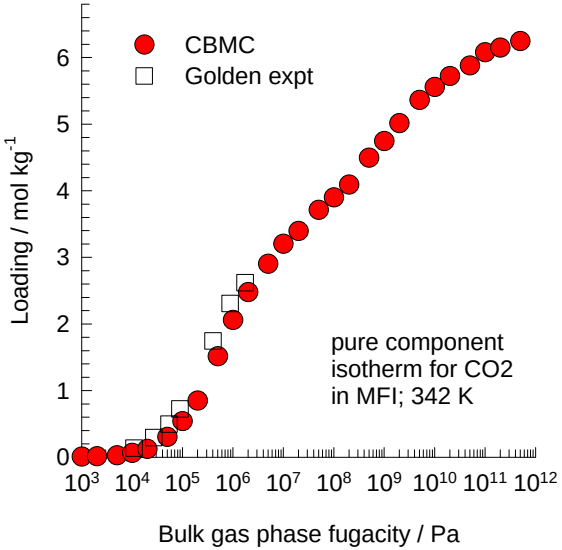

The experimental data are from the following sources:

T.C. Golden, S. Sircar, Gas Adsorption on Silicalite, J. Colloid Interface Sci. 162 (1994) 182-188.

J.A. Dunne, R. Mariwala, M. Rao, S. Sircar, R.J. Gorte, A.L. Myers, Calorimetric Heats of Adsorption and Adsorption Isotherms. 1. O2, N2, Ar, CO2, CH4, C2H6, and SF6 on Silicalite, Langmuir 12 (1996) 5888-5895.

MFI CBMC simulations of isotherms, and isosteric heats of adsorption

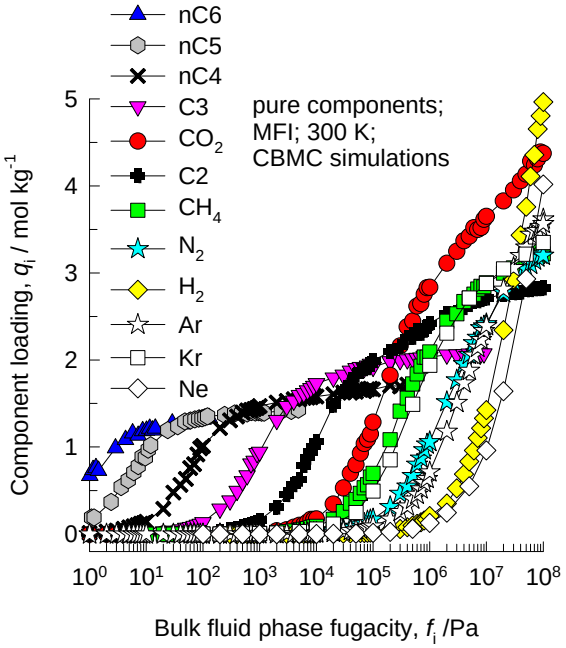

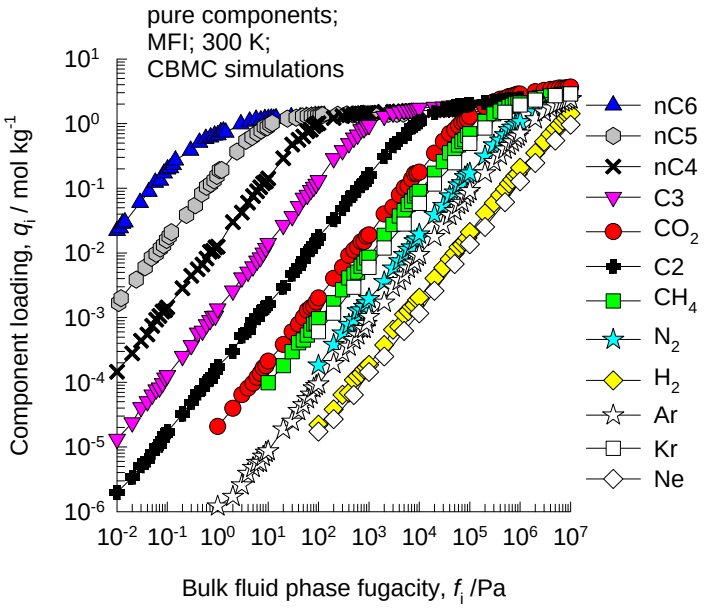

Note that C2 and C3 above refer to saturated alkanes

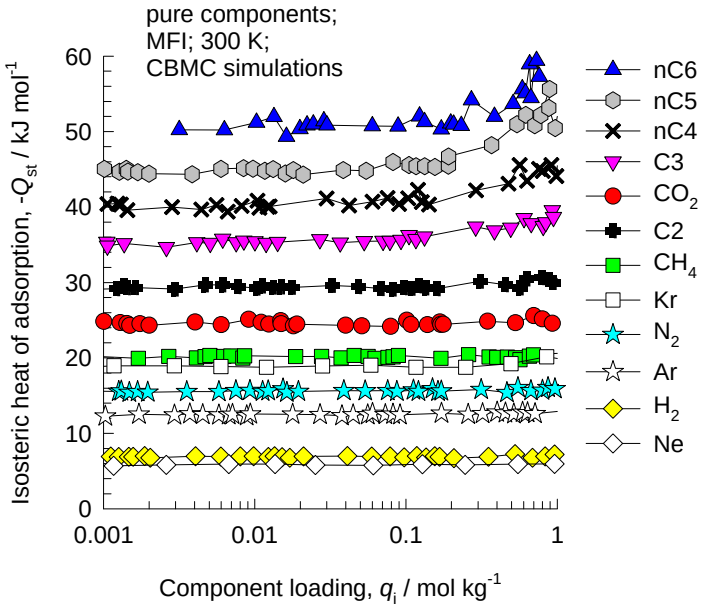

MFI MD simulations of unary self- , and M-S diffusivities

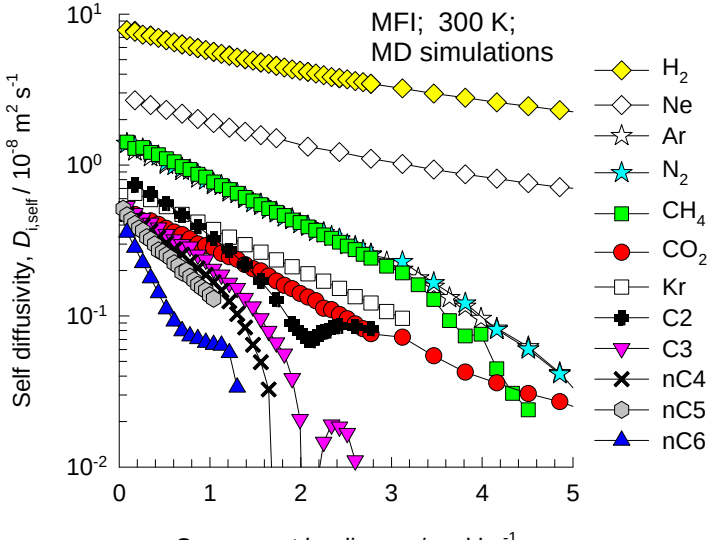

Note that C2 and C3 above refer to saturated alkanes

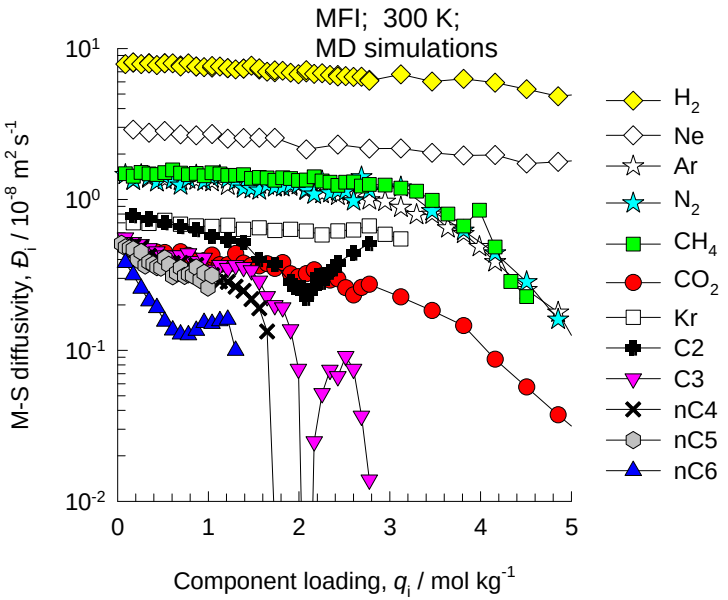

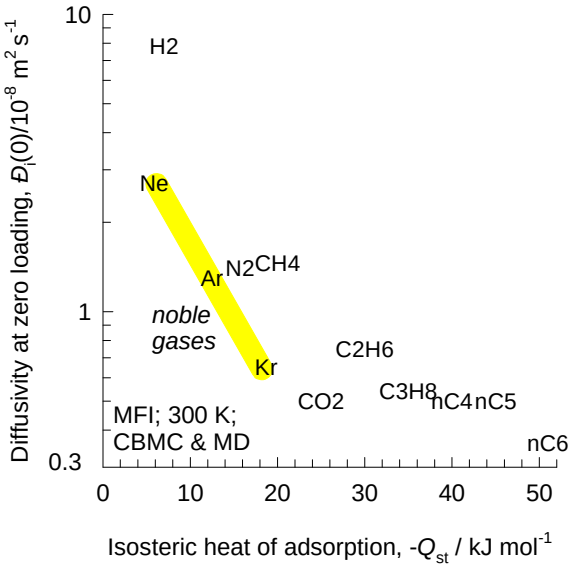

MFI membrane transport coefficients

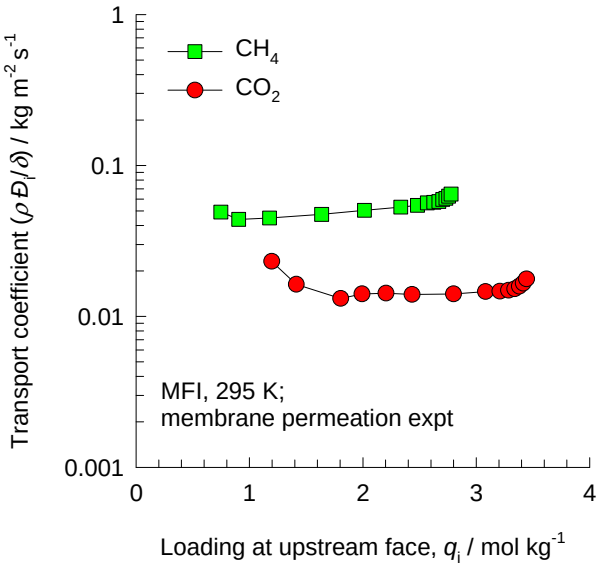

The experimental data are re-plotted using the information in:
R. Krishna, S. Li, J.M. van Baten, J.L. Falconer, R.D. Noble, Investigation of slowing-down and speeding-up effects in binary mixture permeation across SAPO-34 and MFI membranes, Sep. Purif. Technol. 60 (2008) 230-236.

Zn(bdc)dabco landscapes

The structural information for Zn(bdc)(dabco)$_{0.5}$, commonly simply referred to as Zn(bdc)dabco, is from

P.S. Bárcia, F. Zapata, J.A.C. Silva, A.E. Rodrigues, B. Chen, Kinetic Separation of Hexane Isomers by Fixed-Bed Adsorption with a Microporous Metal-Organic Framework, J. Phys. Chem. B 111 (2008) 6101-6103.

J.Y. Lee, D.H. Olson, L. Pan, T.J. Emge, J. Li, Microporous Metal–Organic Frameworks with High Gas Sorption and Separation Capacity, Adv. Funct. Mater. 17 (2007) 1255-1262.

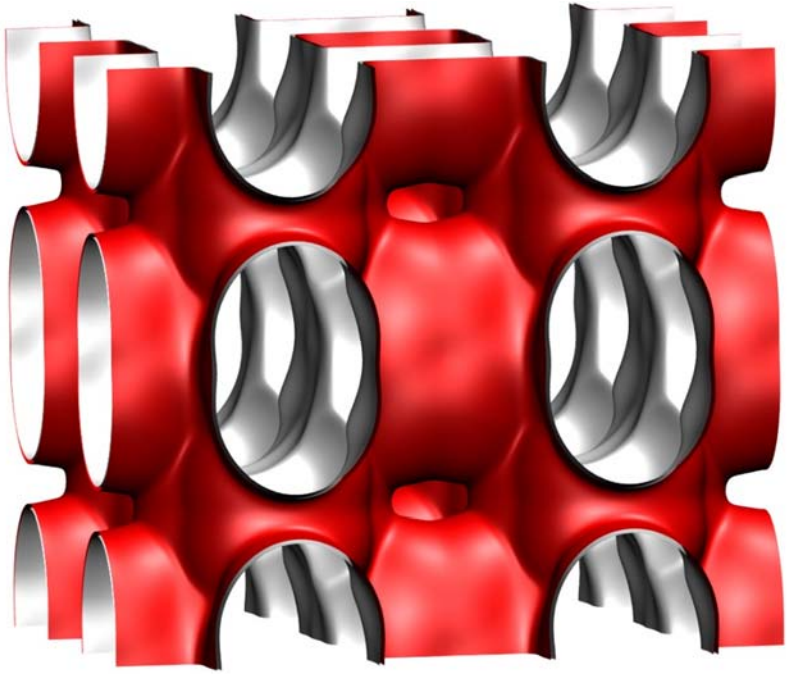

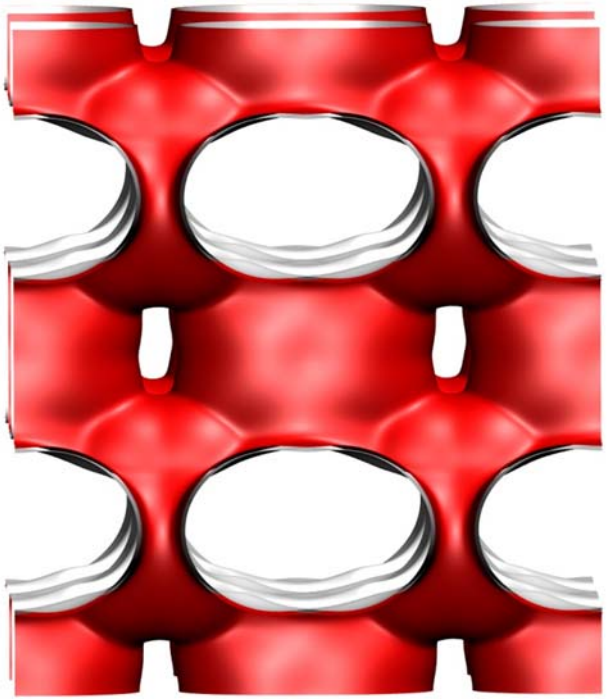

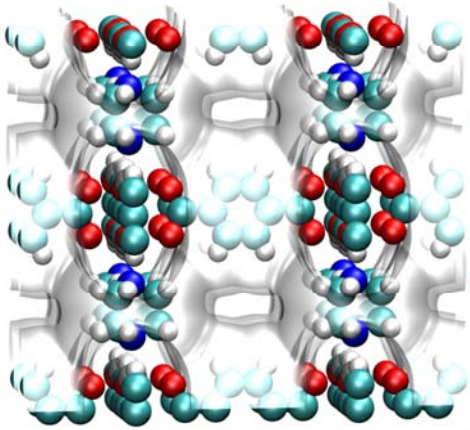

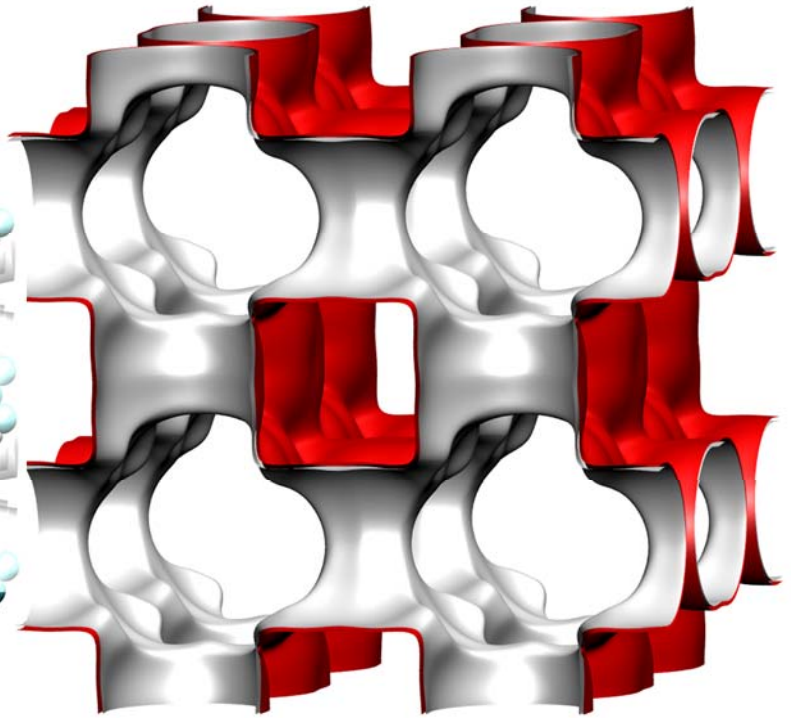

Zn(bdc)dabco

landscapes

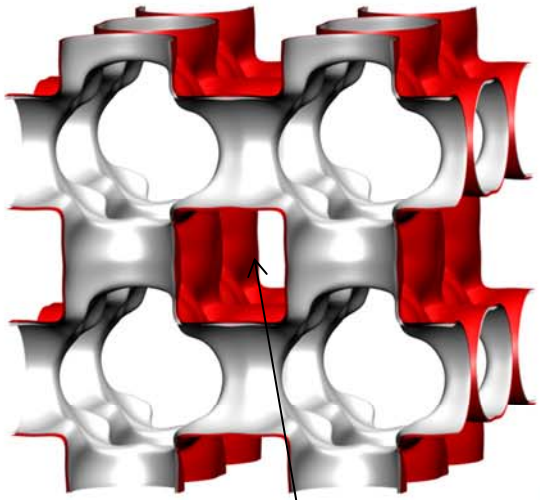

3D intersecting channels

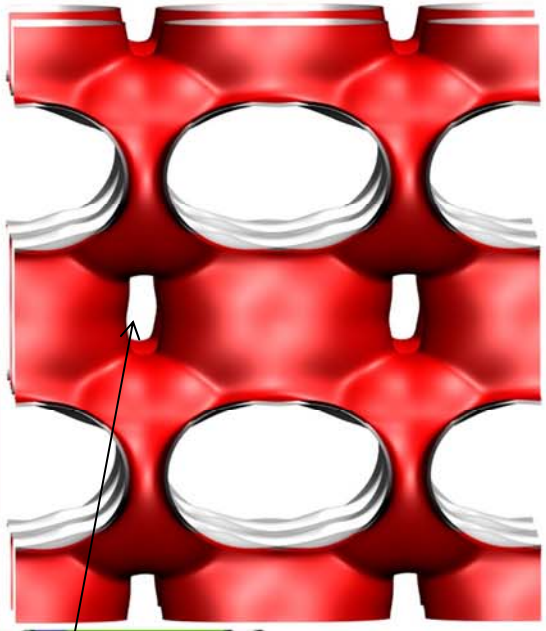

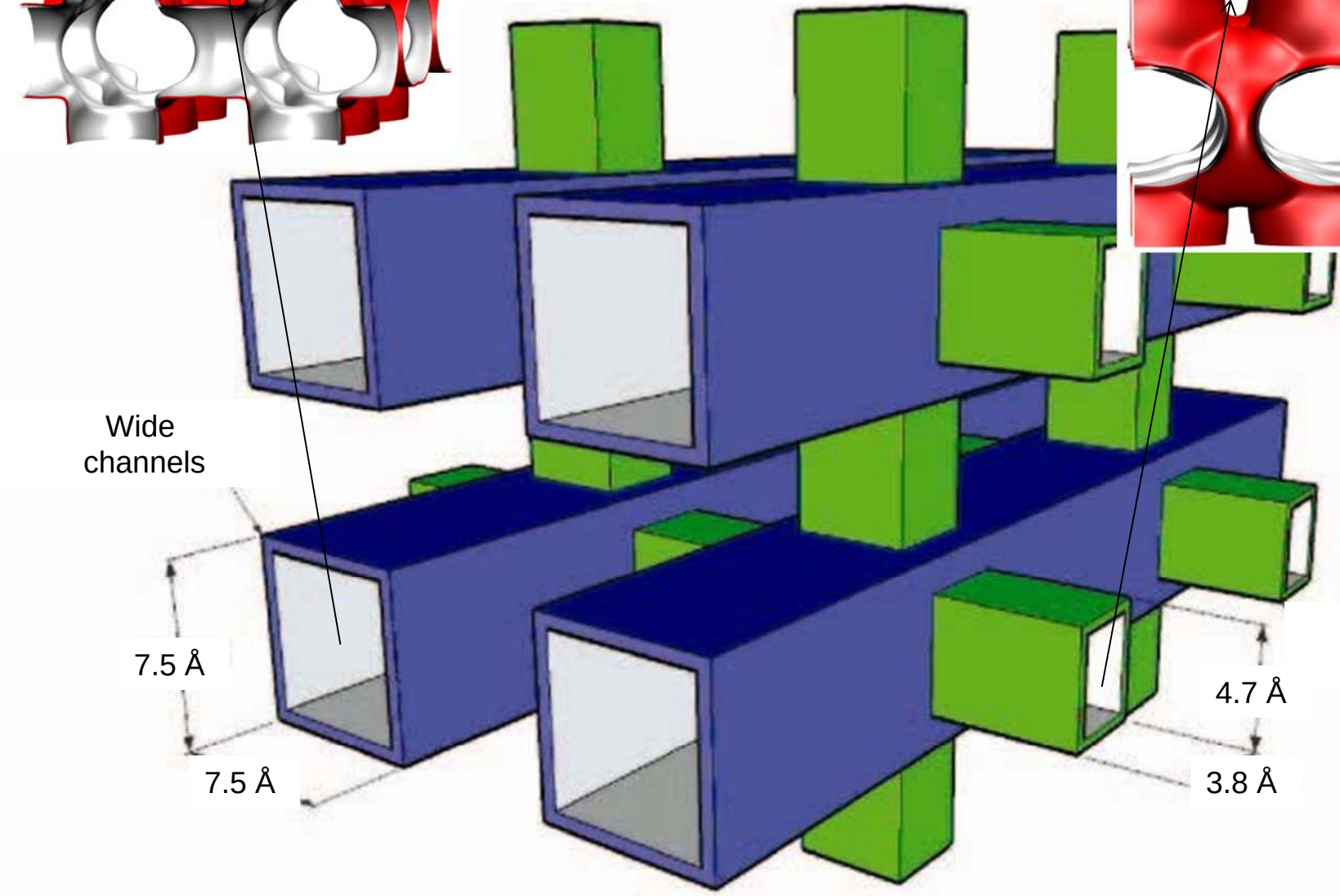

There exist two types of intersecting channels of about 7.5 Å × 7.5 Å along the *x*-axis and channels of 3.8 Å × 4.7 Å along *y* and *z* axes.

Narrow channels

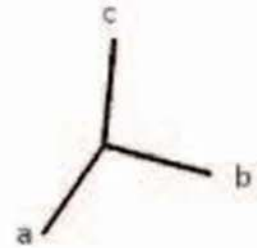

Zn(bdc)dabco pore dimensions

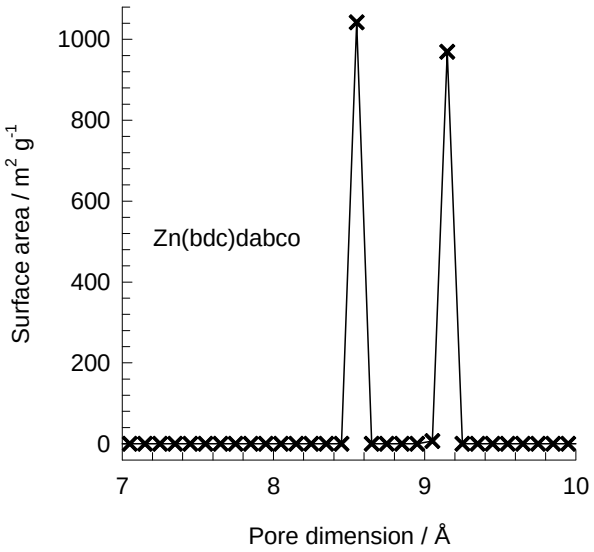

This plot of surface area versus pore dimension is determined using a combination of the DeLaunay triangulation method for pore dimension determination, and the procedure of Düren for determination of the surface area.

	Zn(bdc)dabco
a /Å	10.9288
b /Å	10.9288
c /Å	9.6084
Cell volume / Å^3	1147.615
conversion factor for [molec/uc] to [mol per kg Framework]	1.7514
conversion factor for [molec/uc] to [kmol/m^3]	2.1867
ρ [kg/m3]	826.1996
MW unit cell [g/mol(framework)]	570.9854
ϕ, fractional pore volume	0.662
open space / Å^3/uc	759.4
Pore volume / cm^3/g	0.801
Surface area /m^2/g	2022.5
DeLaunay diameter /Å	8.32

Zn(bdc)dabco force field for framework atoms

Lennard-Jones parameters for the framework atoms of Zn(bdc)dabco.

(pseudo-) atom	σ / Å	ε/k_B / K
Zn	2.46	62.41
O	3.03	48.19
C	3.47	47.86
N	3.26	38.95
H	2.85	7.65

Zn(bdc)dabco MD simulations of unary self- , and M-S diffusivities

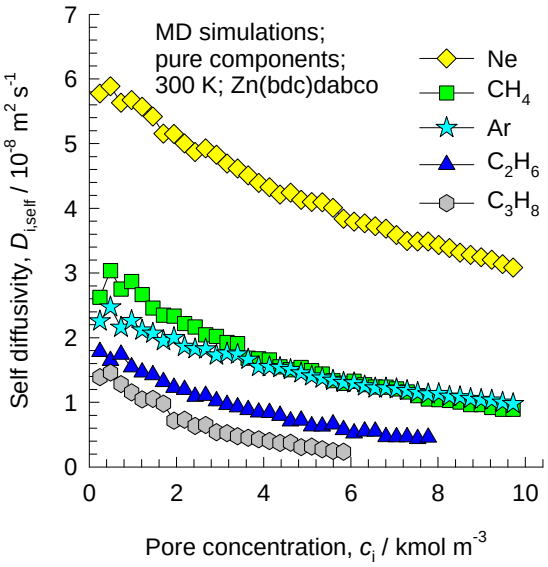

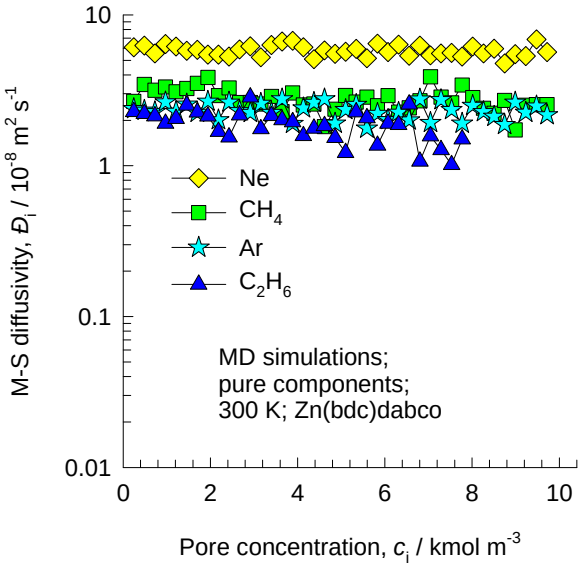

Characterization of Ordered Nanoporous Crystalline Materials by Determination of the Surface Areas as a function of the corresponding Pore Dimensions

Rajamani Krishna*, and Jasper M. van Baten

Van 't Hoff Institute for Molecular Sciences, University of Amsterdam, Science Park 904,

1098 XH Amsterdam, The Netherlands

Tel +31 20 6270990; Fax: + 31 20 5255604;

email: r.krishna@uva.nl

1. Methodology

From a Delaunay triangulation using the framework atom centre coordinates, a set of spheres is determined that represents the pore space in the structure. Connectivities between the spheres are determined that lead to determination of the diffusion sizes along each of the framework axes. In addition, the connectivity information provides information on framework locations that are blocked (not accessible to adsorbents). A reduced set of spheres is assembled representing the open space in the structure. For each accessible location in the structure, this set provides information regarding the local pore size. Subsequently, the surface area is sampled using a Monte-Carlo approach. A pore size is attributed to each accessible surface sample, leading to a distribution of surface area over pore size. The following paragraphs will describe the algorithm in more detail.

Figure 1 shows an example 2D unit cell; this is an imaginary example and only serves to demonstrate the algorithm in 2D; the actual implementation is in 3D, using unit cell lengths, angles and framework atom diameters (taken from the Dreiding force field [1] value for the Lennard-Jones σ parameter), and atomic masses. The example unit cell is orthogonal, but this is not a restriction; the actual implementation deals also with non-orthogonal isoclinic periodicity.

Following Foster [2], we start with a Delaunay triangulation of the coordinates of the framework atom centres. For the Delaunay triangulation, the public-domain software package *qdelaunay* was used [3]. This software does not account for periodic boundary conditions. To account for boundary effects, all framework atoms are echoed to fill the unit cell coordinates [-0.5, 1.5] in all directions. This is depicted in Figure 2.

In 2D, the Delaunay triangulation results a set of three 2D locations each. Each triangle of three points corresponds to a circle in 2D space exactly enclosing the triangle (each of the points is located on the circle's circumference). In 3D, the Delaunay triangulation results a set of four 3D locations; each polyhedron of four points defines a sphere exactly enclosing the polyhedron (each of the points is located on the sphere's surface). The resulting spheres for the example 2D unit cell are shown in Figure 3.

Although the unit cell is extended to [-0.5, 1.5] dimensions, boundary effects are still present. Boundary circles (or spheres) are detected by the fact that echoes of atom locations are contained within them, and they are removed from the collection. In addition, degenerate circles or spheres can result from the Delaunay triangulation (three co-linear points define a degenerate circle, a degenerate sphere follows four co-planar points). Degenerate circles (spheres) are removed from the collection. The remainder of this section will refer to circles in 2D space and spheres in 3D space as *spheres*, corresponding to the actual 3D implementation.

Finally, as we are interested in adsorption and diffusion in feasible areas of the framework, we are not interested in spheres with a size smaller than the smallest adsorbent of interest. We take Ne as the smallest molecule of interest; we presume that the O framework atom is a representative framework atom. We have taken r_{min} as $(d_O + d_{Ne}) / 2 = 2.911$ Å; to be on the safe side we pick a size somewhat smaller and define r_{min} as 2.75 Å. All spheres with $r < r_{min}$ are discarded. The remaining set of spheres, after removal of boundary artifacts, too small spheres and degenerate spheres, is shown in Figure 4. The spheres are translated back to the unit cell, as shown in Figure 5. Several echoes of the same space will now be present, that have to be removed. In addition, as the framework centre locations are known with a finite precision (at best machine precision, but usually following from a textual limitation in input files), some spheres that should be equal, are nearly equal in size and location. Spheres for which the radius is contained for more than 99% inside another sphere are removed, taking care of exactly and nearly overlapping spheres. The resulting sphere set is shown in Figure 6.

For determination of the spatial distribution of pore size, it is useful to know which of the regions (spheres) of the framework are inaccessible. A region is inaccessible if no diffusion path exists into the region, across a unit cell boundary (a periodic diffusion path). A diffusion path is a periodic series of connected spheres connected by apertures large enough for an adsorbent to pass through by diffusion. For determining accessible regions, finding any periodic diffusion path is sufficient condition. We extend the search somewhat to obtain some other useful characteristics of the diffusion paths; in each

direction we determine the radius of the maximum hard sphere that can pass through the framework (fitting in between the framework atom centres).

As a first step in the diffusion path search, the connectivity between each of the spheres is determined. The radius of the aperture of two overlapping spheres characterizes the size of the diffusion path. If we take sphere 1 with radius r_1 at the original of a coordinate system (origin is point A, $x_A = 0$, $y_A = 0$), as shown in Figure 7, we can place another sphere 2 with radius r_2 at a point B, where B is offset by a distance d_{AB} along the x-direction ($x_B = d_{AB}$, $y_B = 0$). We then define r_{ap} as the aperture radius, which is the y-location of point C in Figure 7; we then have two unknowns x_C, and $y_C = r_{ap}$. As point C is located at the circumference of sphere 1, we know that

$$x_C^2 + y_C^2 = r_1^2$$

We also know that point C is on the circumference of sphere 2, so that

$$(x_B - x_C)^2 + y_C^2 = r_2^2$$

Solving these two equations results the positive solution

$$r_{ap} = y_C = \frac{\sqrt{2d_{AB}^2\left(r_1^2 + r_2^2\right) + 2r_1^2 r_2^2 - r_1^4 - r_2^4 - d_{AB}^4}}{2d_{AB}^2}$$

and the negative solution is $-y_C$.

For each overlapping sphere with each of its echoes, the aperture can be calculated. Here it is important to consider each periodic echo of each sphere. Two spheres can have multiple connections, across different cell boundaries, and a larger sphere can even connect with itself across a cell boundary. Overlaps are discarded if the aperture does not allow for diffusion, or $r_{ap} < r_{min}$, unless the spheres are largely overlapping themselves (to prevent many unconnected spheres forming satellites we are not interested in analyzing separately); apertures of $r_{ap} < r_{min}$ are accepted if 70% of the radius of a sphere lies inside the connecting sphere. All resulting apertures from such a calculation are shown in Figure 8. For each accepted aperture, a connection is added to each of the spheres, while keeping track of which cell boundaries are crossed.

Based upon connectivity information (defined by the accepted apertures), spheres now divide into *sphere groups*. Spheres that connect, directly or via other spheres, are in the same sphere group.

For each sphere group, a path search is performed to find the maximum value of the minimum aperture for a diffusion path along each of the cell axes. The path searching scales poorly with the amount of spheres and amount of connections per sphere, and computational effort can be reduced drastically by smart ways to reduce the search directions. As noted earlier, if diffusion path sizes are not required, the search can be stopped as soon as a single periodic path is found.

We presume that the largest sphere in the group is part of the diffusion path, and the largest sphere is used as the starting point. Before the search is started, each of the connections for each sphere are sorted from large to small aperture, so that paths connecting through larger apertures are attempted first. The search starts with a path of one sphere, the largest sphere. The path is grown until the search directions have exhausted. In case of a dead end (no more connections to search) the path is shrunk until it is no longer at a dead end. The next sphere in the path is the next untried connection for the last sphere in the path, where the next untried connection is set to the first connection at the moment a sphere is added to the path. While adding spheres to the path, crossed cell boundaries in each direction are tracked (using stored boundary crossing information for each connection), as well as the hard sphere diameter that can diffuse through the path (minimum of all apertures passed). We do not follow paths that effectively cross a cell boundary twice in the same direction (keeping track of crossing that cell boundary in the opposite direction) without ending up at the starting sphere. As we are only interested in the diffusion paths with the largest aperture, a sphere is not added to the path if it has been visited before with a larger value of the minimum aperture. If the path leads back to the starting sphere and crosses at least one cell boundary (effectively, reverse crossings accounted for), a periodic path is found for the direction of the cell boundaries that are crossed. The maximum value of the minimum aperture of such paths are stored as r_X, r_Y and r_Z (radius of a hard sphere that can diffuse along the X, Y or Z axis of the unit cell). As periodic paths are found, all connections with apertures less than $\min(r_X,r_Y,r_Z)$ are ignored (these will not lead to better diffusion paths).

After the search has completed for a sphere group, the group is marked as a blocked region in case no periodic paths have been found, or as accessible in case at least one periodic path has been found.

The example leads to finding two sphere groups. The smaller sphere group is shown in Figure 9 with all its apertures. It has no periodic path and is marked as blocked. Figure 10 shows the other sphere group with all its apertures. This group has a periodic path along the x direction of the unit cell; the path with the maximum value of the minimum aperture is shown in Figure 11.

The restricting minimum aperture is indicated by the thick red line. Note that this aperture does not take into account the size of the atoms (also not that not all end points of apertures need to correspond to atom locations in 2D, and an aperture represents the circumference of a circle in 3D).

A new collection of spheres is constructed, consisting of all spheres in all sphere groups marked as accessible, sorted from large radius to small radius. For each arbitrary point in the unit cell, the pore size can now be identified (before correction for the framework atom diameters) by finding the largest sphere (the first in the reconstructed sorted list of spheres) that contains the point or any periodic echo thereof. The division of pore size resulting from such an analysis is shown for the entire example unit cell in Figure 12. The dark blue regions correspond to the single large sphere (and its echo), the middle blue regions correspond to the middle sized spheres and the light blue regions correspond to the smallest spheres. The white regions correspond to inaccessible space.

For the last step of the analysis, the determination of surface area and its distribution over pore size, requires sampling the surface area of the framework atoms. For the atoms in the host metal organic framework, the generic DREIDING [1], if available, or the UFF [4] force fields were used for the Lennard-Jones parameter. The surface area sampling follows to a large extent that of Düren et al [5]. A probe size is defined (we use d_{probe} = 3.681 Å for comparison with earlier results; a probe size of d_{probe} = 0 Å would result the framework atom hard sphere surface). For each framework atom i, a list is constructed of all other framework atoms that could block a sample around atom i. This list contains all framework atoms j for which the distance to the nearest echo is less than $r_i + r_j + d_{probe}$. A total of n_{sample} = 5000 random points around framework atom i are inspected. The points are taken as a random unit sphere vector, multiplied by length $r_i + d_{probe}/2$. For all spheres j in the constructed list of possible overlaps, it is checked whether the sample point falls within a distance of $r_j + d_{probe}/2$ of the nearest echo

of atom *j*. If it does for any atom *j*, the sample is not accepted. All accepted samples are shown as a red line in Figure 13.

Each accepted sample corresponds to a surface area of $\pi(r_i+d_{probe}/2)^2/\ n_{sample}$ Å/uc (in 2D), or $4\pi(r_i+d_{probe}/2)^2/\ n_{sample}$ Å^2/uc (in 3D). The surface area corresponding to accepted samples is binned in a surface area distribution histogram versus pore diameter. The pore diameter of the sample is taken as the diameter of the largest containing sphere (cf. Figure 12) minus the diameter framework atom *i* (implicitly assuming that the pore is delimited on all sides by framework atoms corresponding in size to atom *i*). Accepted samples that fall in inaccessible regions (red lines in white area in Figure 13) are recorded separately as blocked surface area.

The total unit cell volume V_{uc} is calculated from the cell dimensions. The unit cell molar mass MW_{uc} is calculated from the sum of all framework atom molecular weights. The unit cell mass density follows from $\rho_{uc} = MW_{uc}/(N_{av}V_{uc})$. The area per unit cell is converted to area per mass or area per volume using V_{uc} and ρ_{uc}.

2. References

[1] S.L. Mayo, B.D. Olafson, W.A. Goddard, DREIDING: A Generic Force Field for Molecular Simulations, J. Phys. Chem. 94 (1990) 8897-8909.

[2] M.D. Foster, I. Rivin, M.M.J. Treacy, O.D. Friedrichs, A geometric solution to the largest-free-sphere problem in zeolite frameworks, Microporous Mesoporous Mater. 90 (2006) 32-38.

[3] C.B. Barber, D.P. Dobkin, H.T. Huhdanpaa, The Quickhull Algorithm for Convex Hulls, ACM Transactions on Mathematical Software 22 (1996) 469-483.

[4] A.K. Rappé, C.J. Casewit, K.S. Colwel, W.A. Goddard, W.M. Skiff, UFF, a Full Periodic Table Force Field for Molecular Mechanics and Molecular Dynamics Simulations, J. Am. Chem. Soc. 114 (1992) 10024-10035.

[5] T. Düren, F. Millange, G. Férey, K.S. Walton, R.Q. Snurr, Calculating Geometric Surface Areas as a Characterization Tool for Metal-Organic Frameworkss, J. Phys. Chem. C 111 (2007) 15350-15356.

Figure 1. Unit cell.

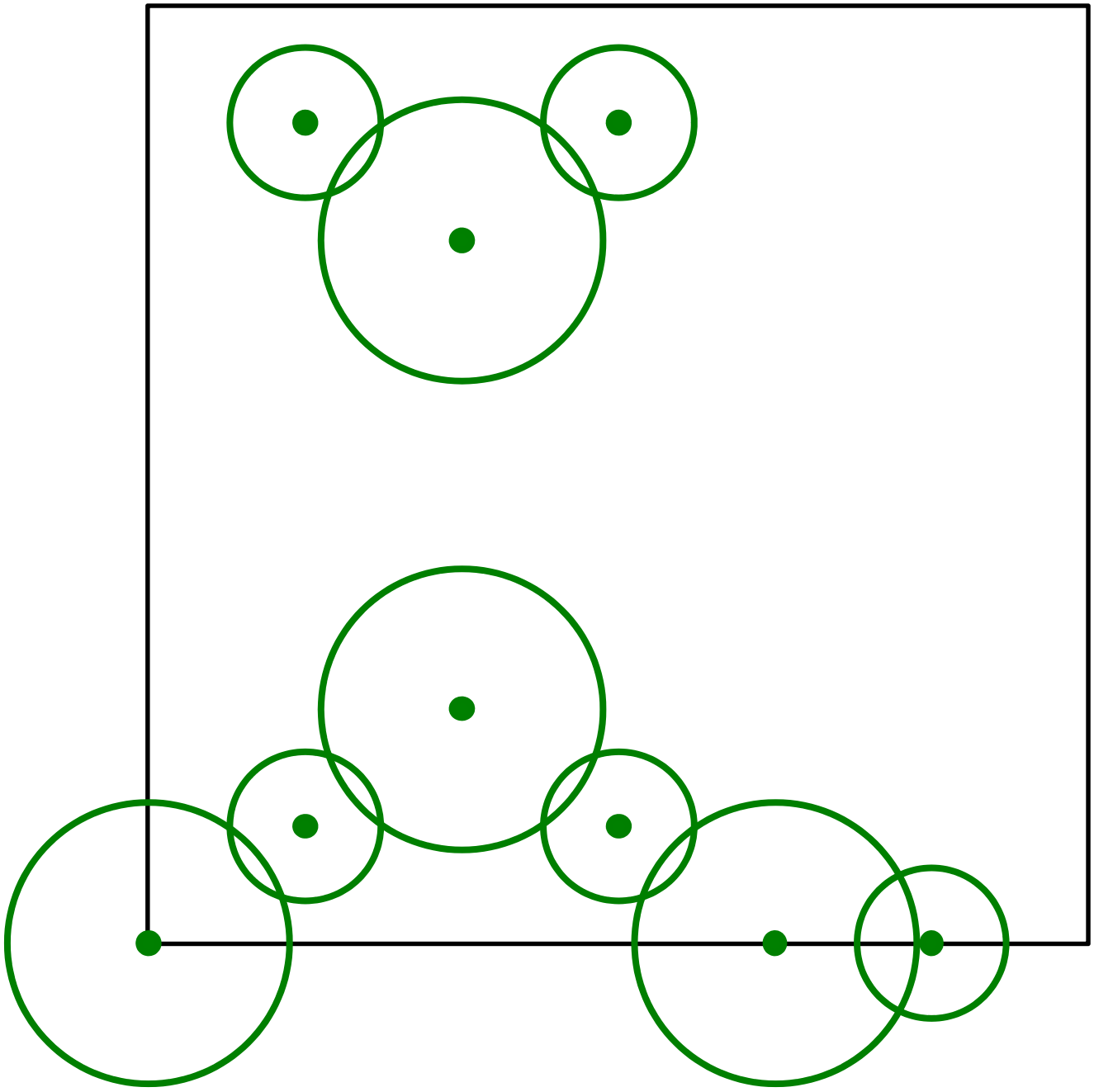

Figure 2. Duplicated atoms.

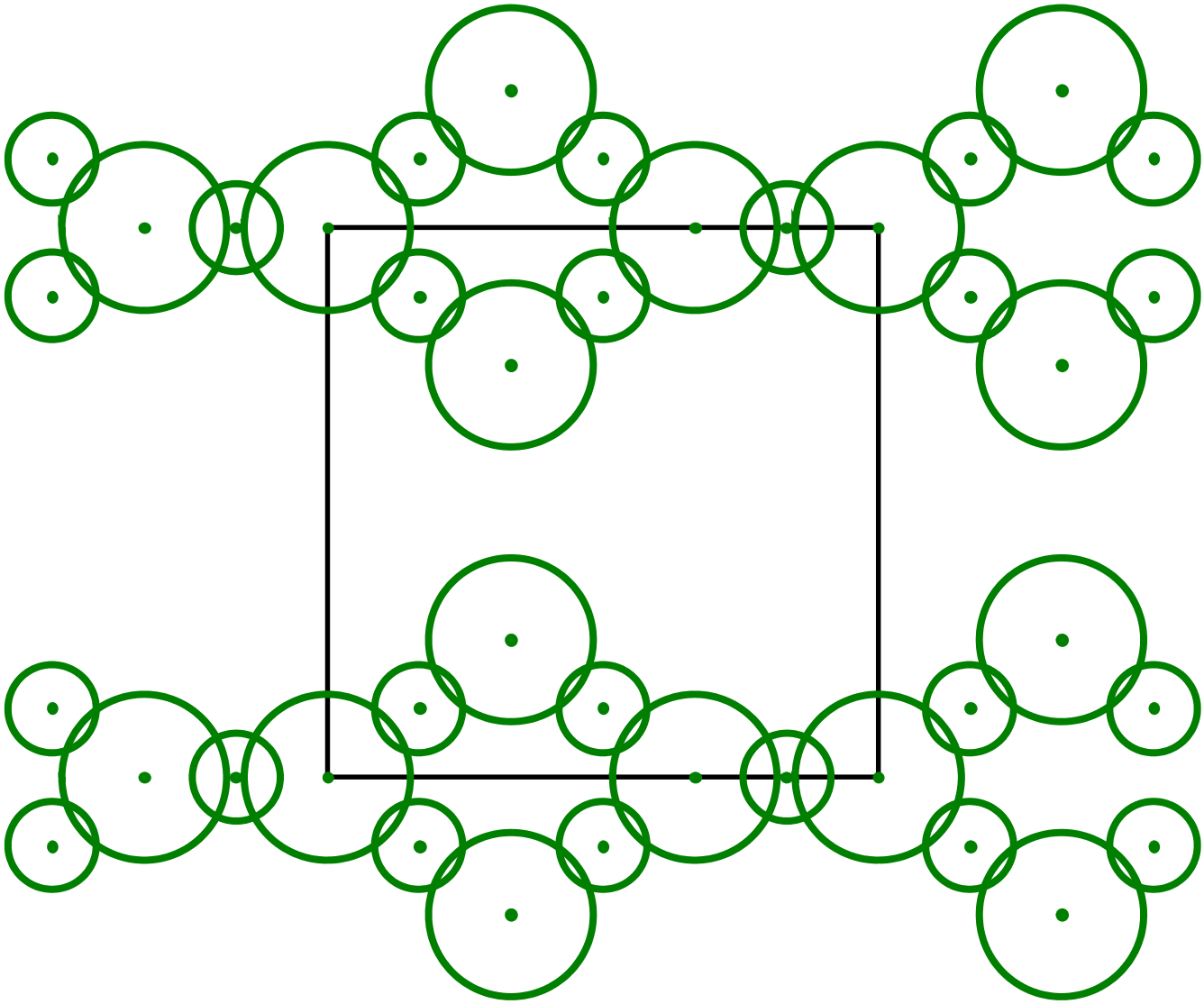

Figure 3. Delaunay spheres.

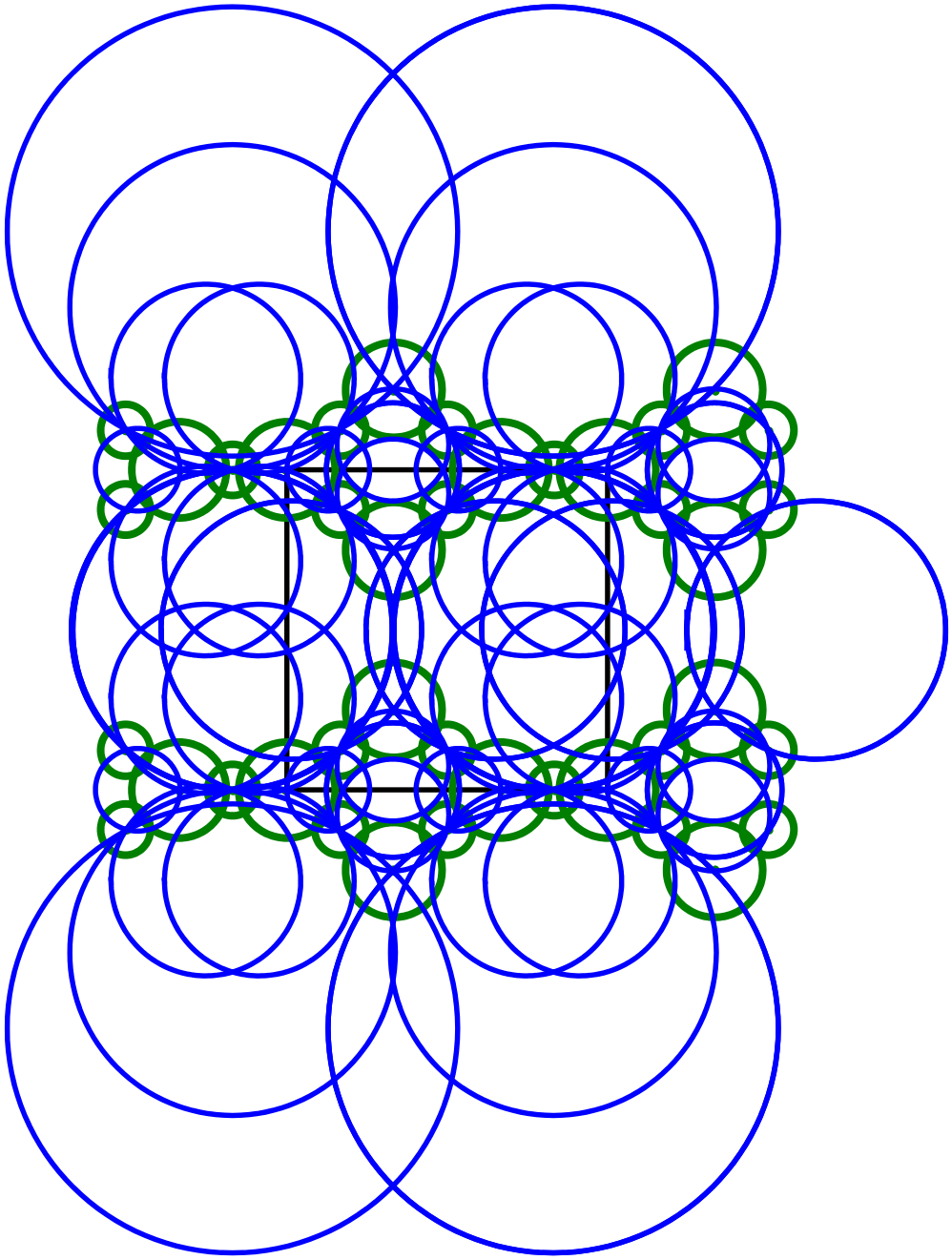

Figure 4. Removal of too small, boundary and degenerate spheres.

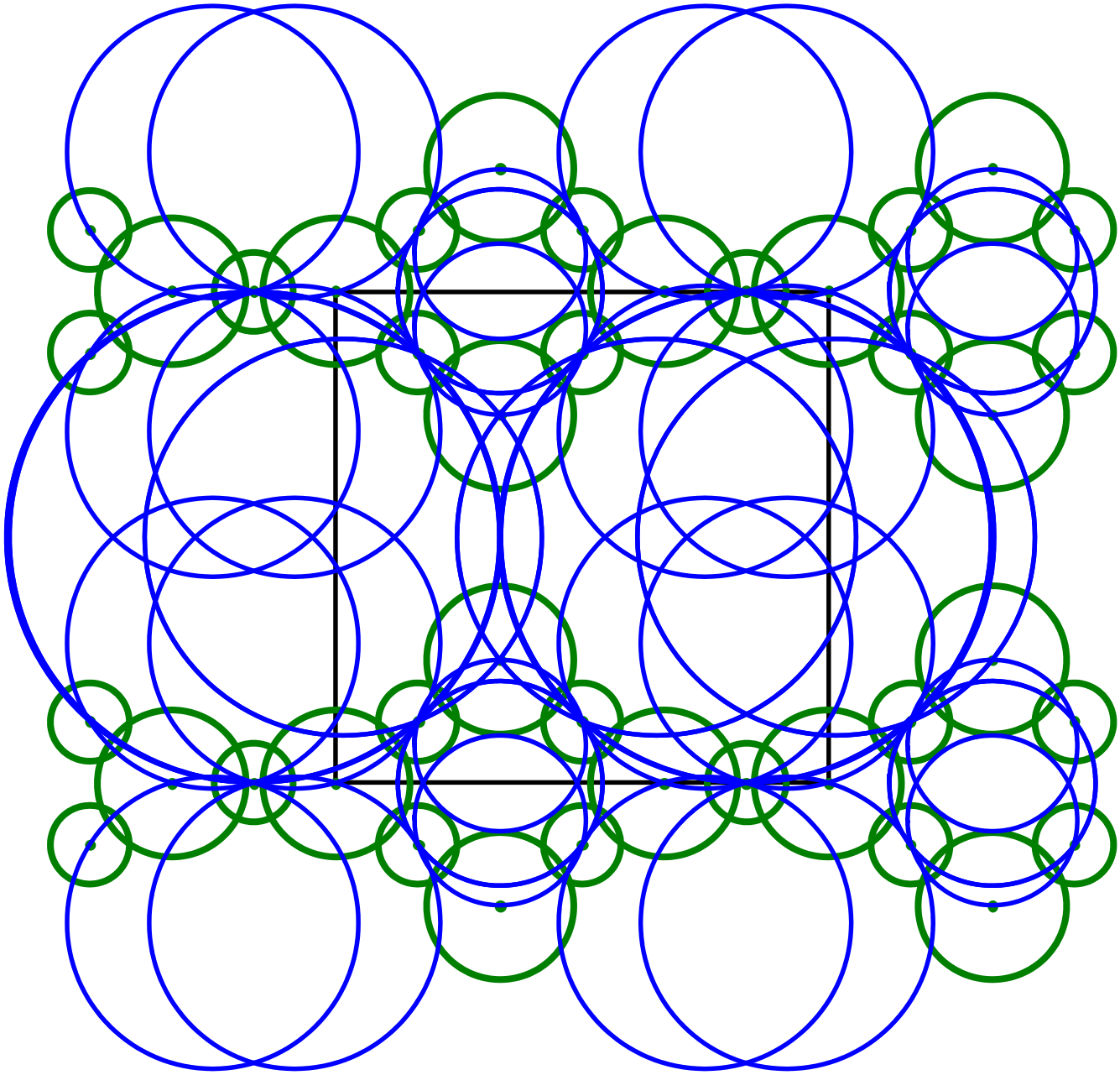

Figure 5. Placing spheres back into the unit cell.

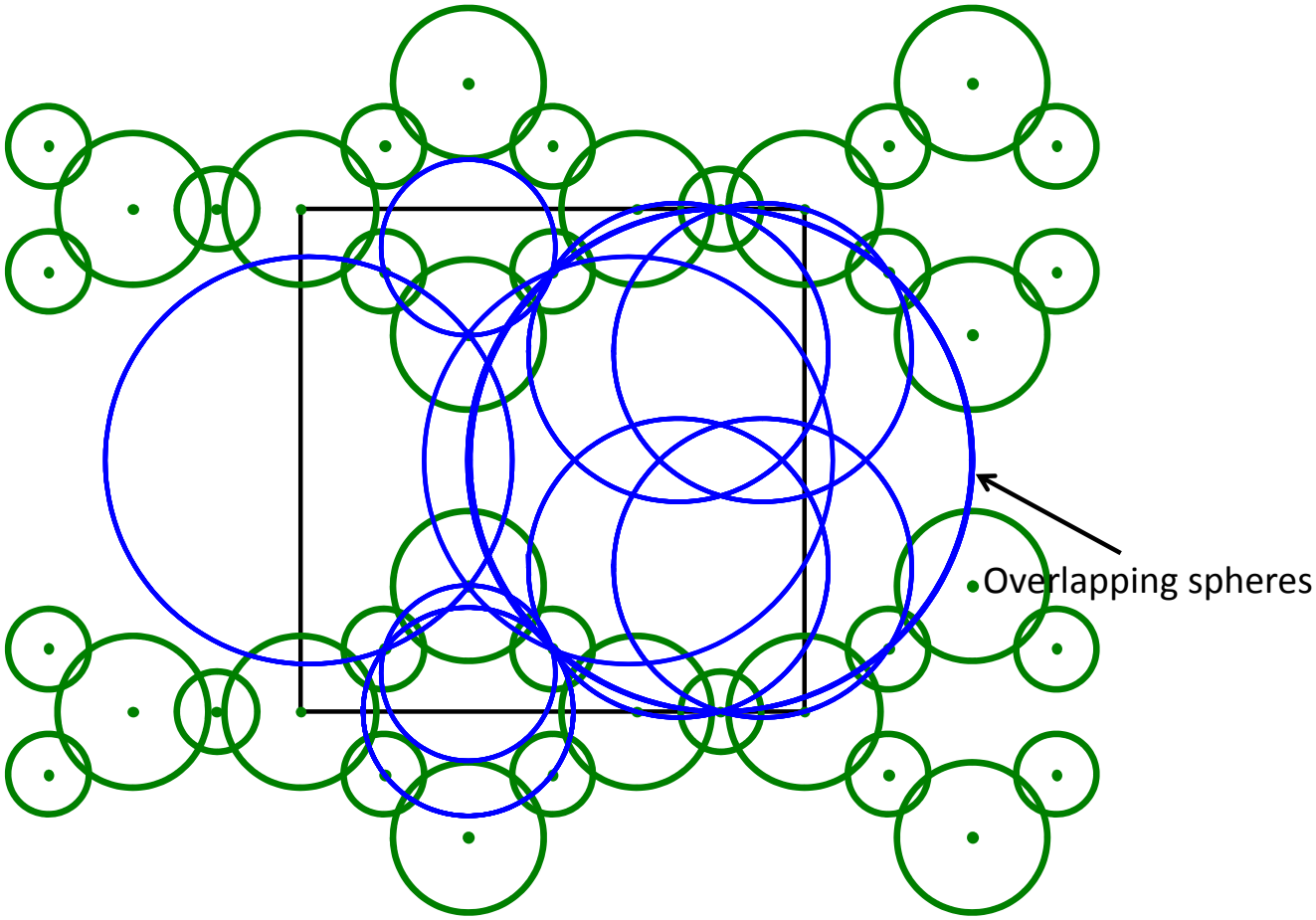

Figure 6. Removal of spheres with more than 90% overlap.

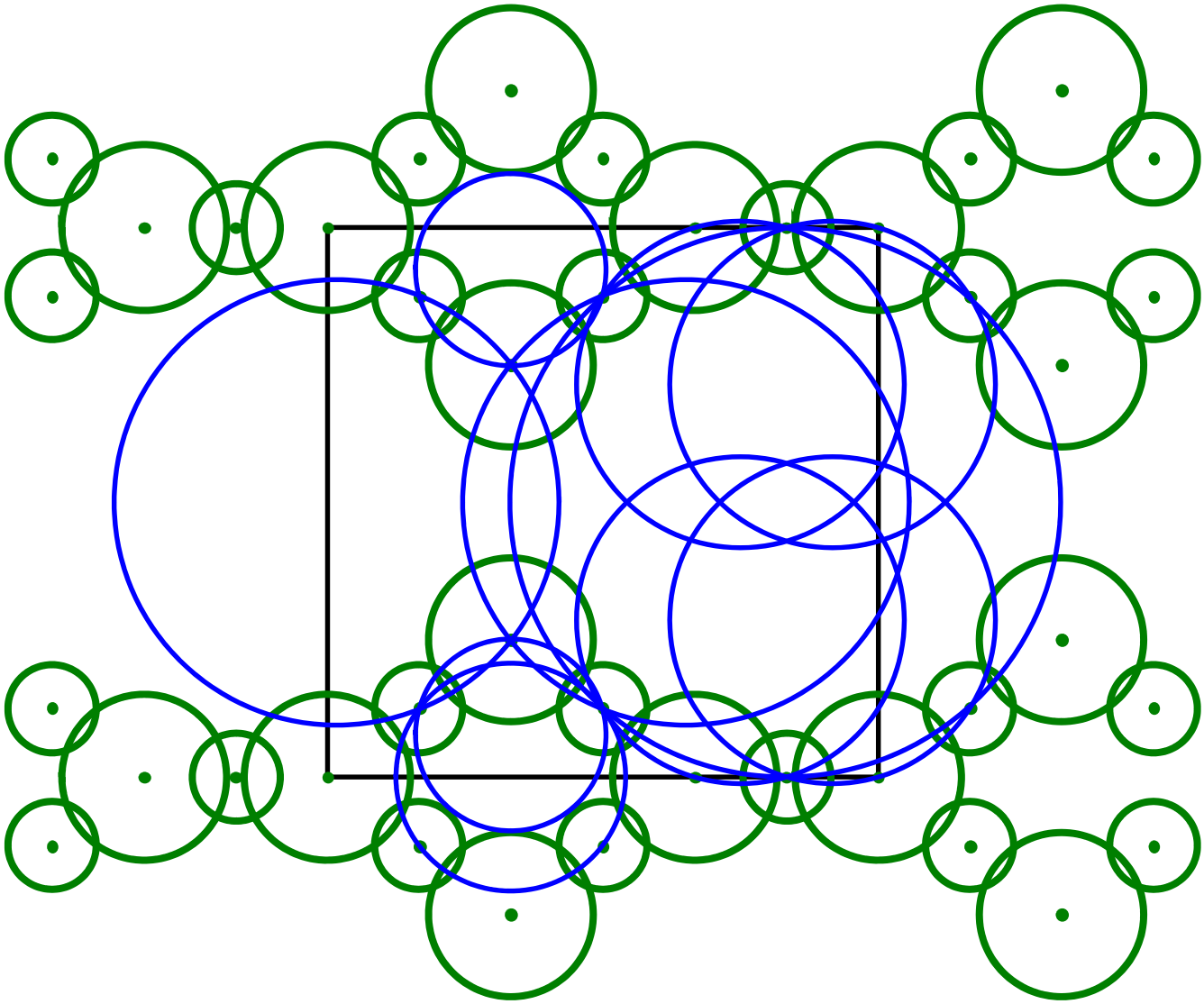

Figure 7. Aperture calculation.

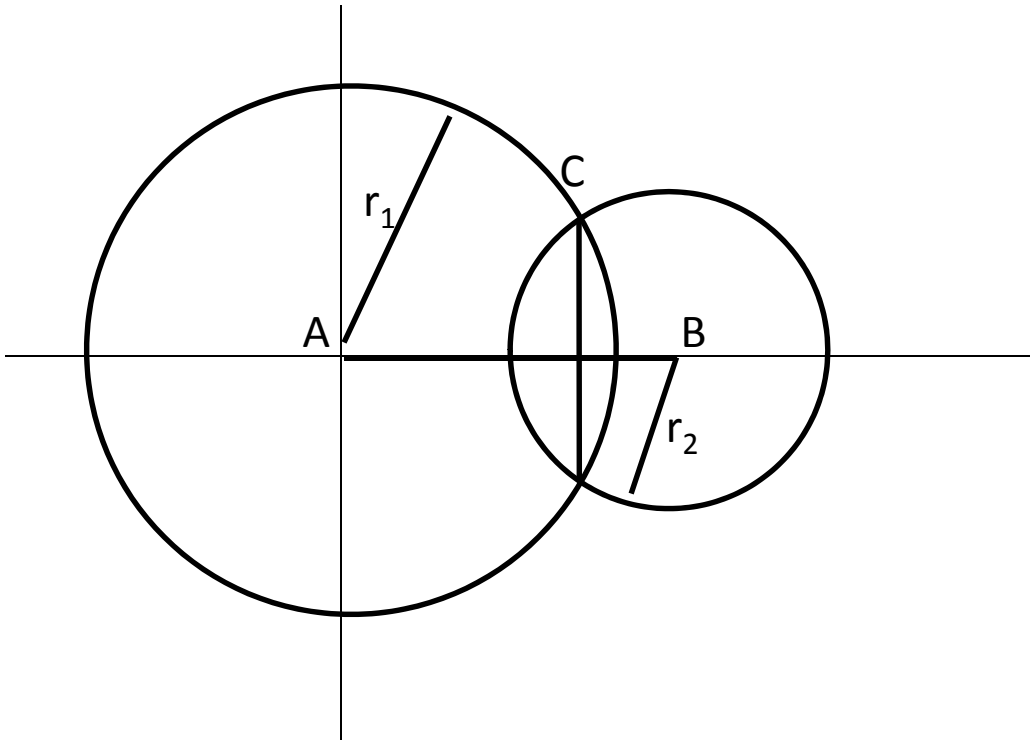

Figure 8. Selected apertures of all reflections (also the connections) (this figure will be broken down in Figures 9, 10, 11, 12, and 13)

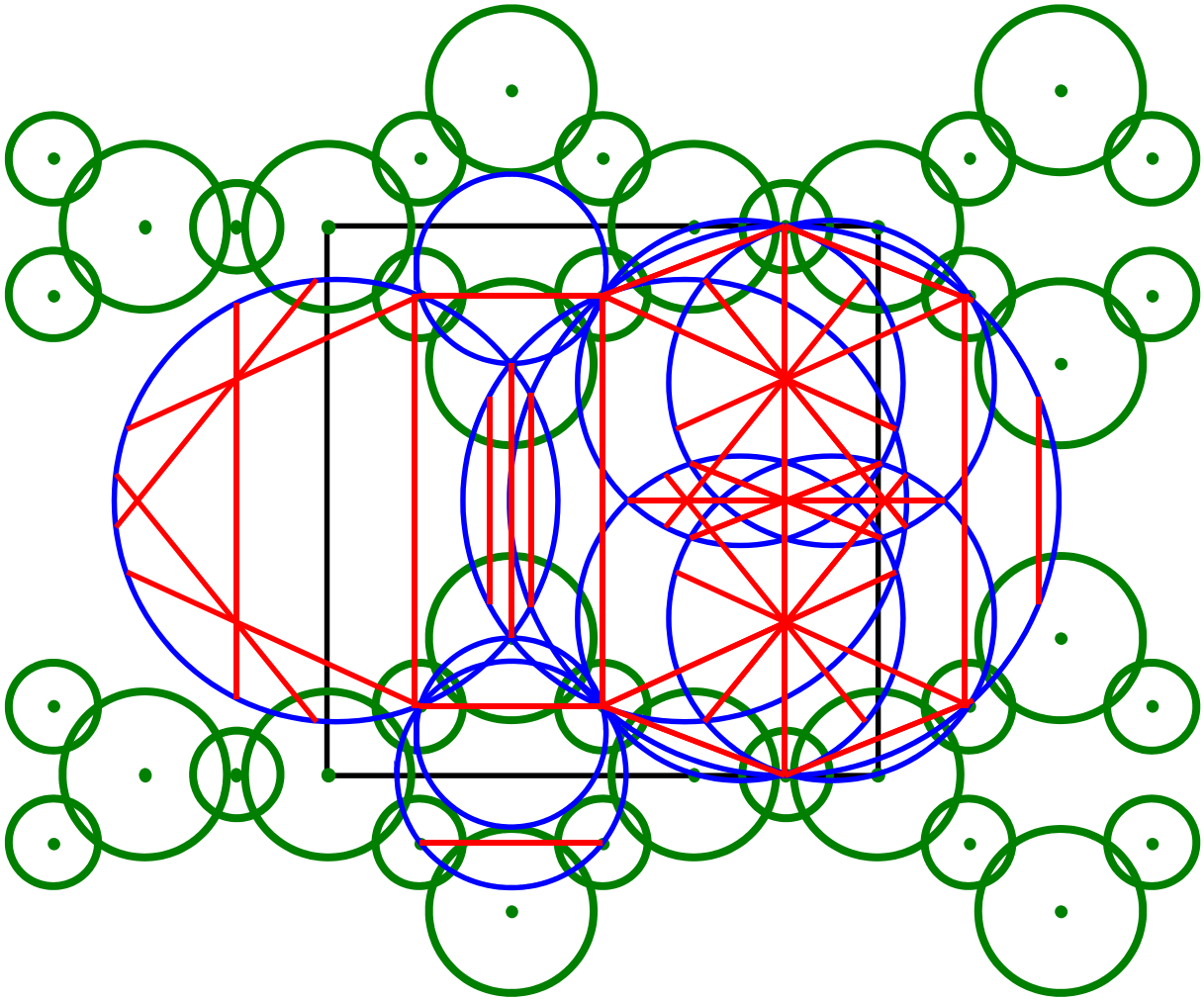

Figure 9. Blocked group.

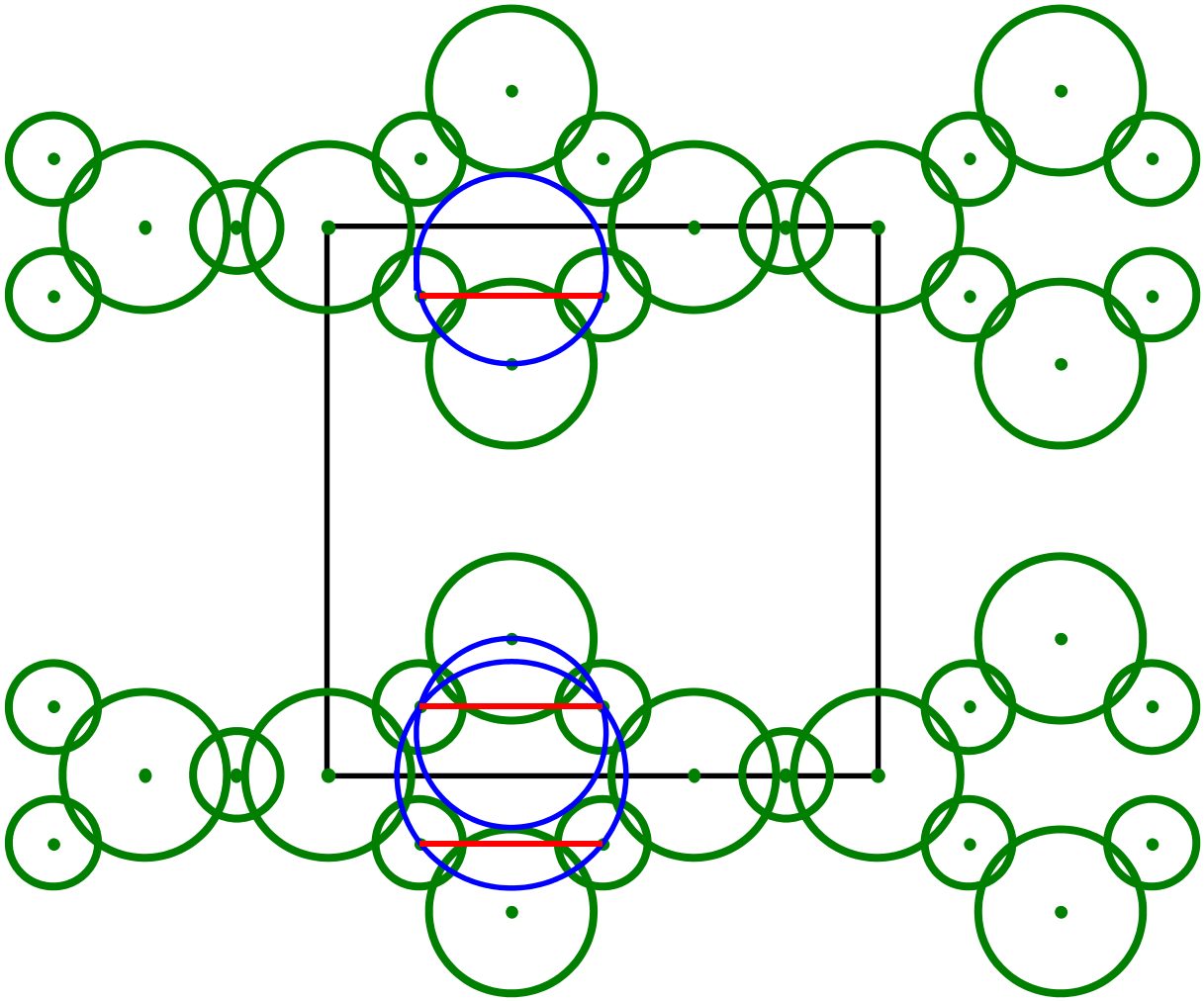

Figure 10. Non-blocked group.

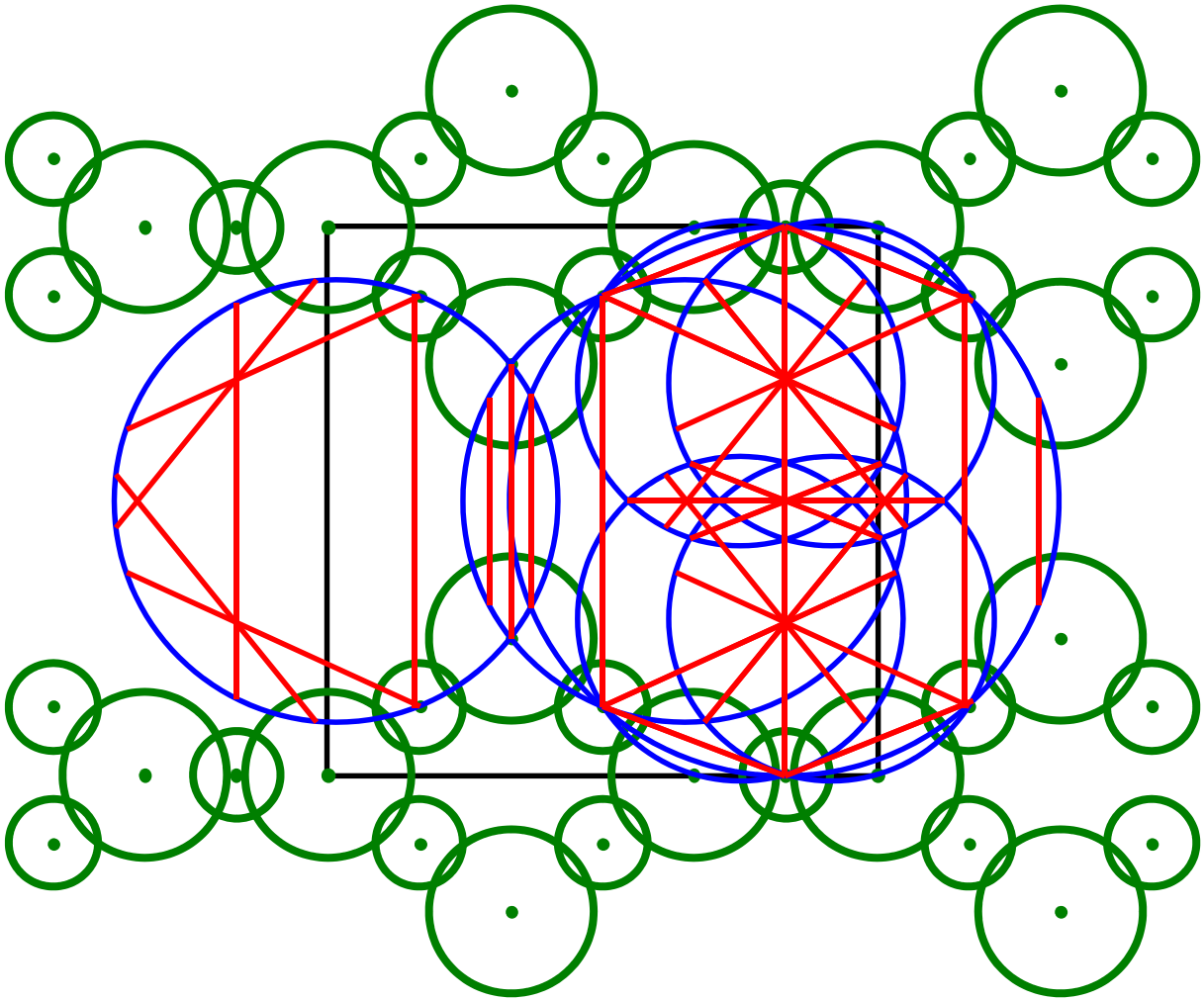

Figure 11.Max path in x-direction and apertures passed (restrictive aperture wide line).

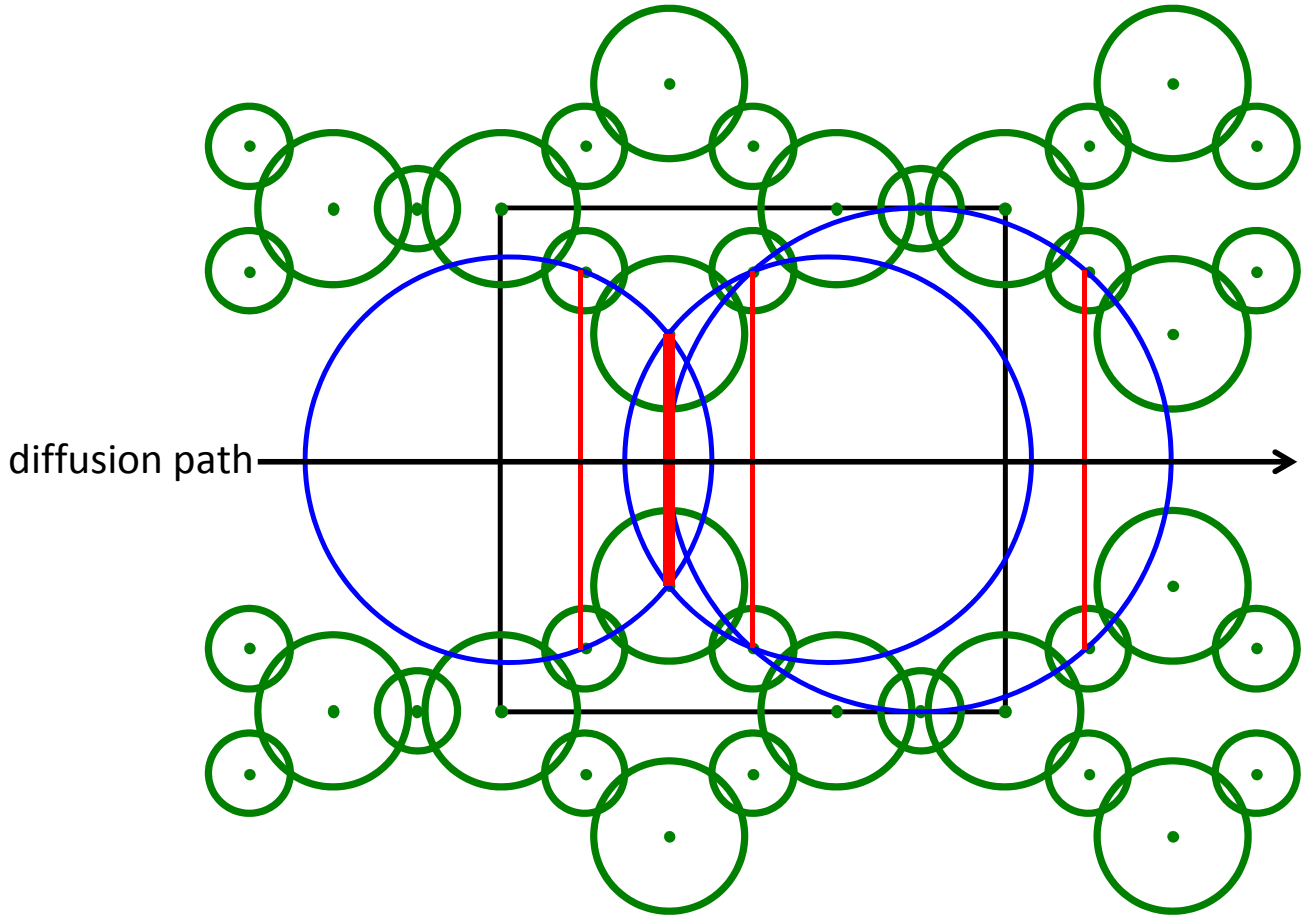

Figure 12. Non-blocked groups, and space division of sphere volume.

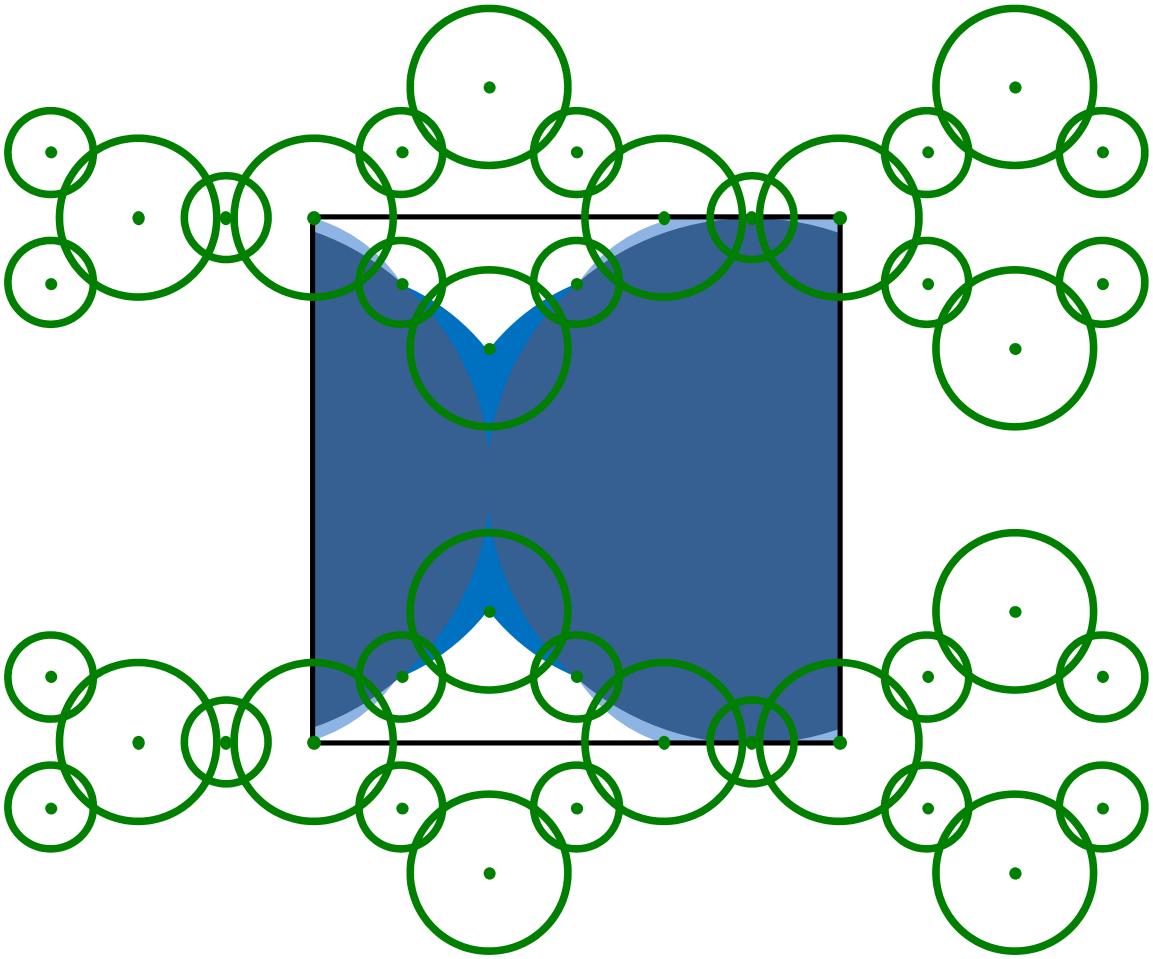

Figure 13. Surface area indicated in red.